3-D Satellite Interferometry for Interseismic Velocity Fields

Pawan Piromthong

Submitted in accordance with the requirements for the degree of
Doctor of Philosophy

The University of Leeds
School of Earth and Environment

May, 2021

The candidate confirms that the work submitted is their own, except where work which has formed part of jointly authored publications has been included. The contribution of the candidate and the other authors to this work has been explicitly indicated below. The candidate confirms that appropriate credit has been given within the thesis where reference has been made to the work of others.

The candidate used a script from Karsten Spaan to extract pixels in the burst overlap region of TOPS Sentinel-1 images in image processing in this thesis.

For the work in Chapter 3, the candidate used a script from Karsten Spaans to generate split-spectrum SAR images. The candidate worked on the data processing, methodology developments, and discussion. Andy Hooper provided comments and suggestions on the work.

The candidate carried out the work in Chapter 4 of the thesis. Andy Hooper and John Elliott provided comments and suggestions on the work.

The candidate carried out the work in Chapter 5 of the thesis. Andy Hooper provided comments and suggestions on the work.

Acknowledgements

Very first of all, I would like to express sincere thanks to my primary supervisor, Prof. Andy Hooper, for his incredible patience, immense knowledge, and valuable guidance. The suggestions are not only for this thesis but for how to be a good researcher. He gave me these great learning opportunities. I will never forget this.

I would like to give a special thanks to my co-supervisor, Dr. John Elliott, for his great support, throughout my Ph.D. study. He was always willing to help and offer encouragement. I really appreciate all things he has done and given to me.

Overall of my thesis got help and support from many people. Processing scripts from Karsten Spaans helped and guided me to start the work much more manageable. I would like to thank Milan Lazecky, Yu Morishita, and Jonathan Weiss, who develop and take care of LiCSAR/LiCBAS software which makes my life get along with InSAR processing much easier. Moreover, they always give me full supports every time I needed it. I am grateful to the people in Centre for Observation and Modelling of Earthquakes, volcanoes and Tectonics (COMET) and the COMET itself for kindly offering me great experiences in the UK. I also would like to thank my colleague in office 8.153, Hardianshah Bin Saleh, Lin Shen, Matthew Gaddes, Huw Goodall, Jeanne Giniaux, Ita Alvarez for the great working environment.

Finally, I would like to thank my parents and family, who always support me wherever I am.

The study of Ph.D. degree is sponsored by the Thai Ministry of Science and Technology.

Abstract

The global interseismic strain rate map is being accomplished rapidly with measurements of the space-based geodetic technique of InSAR. High-resolution measurements of crustal deformation from InSAR can provide crucial constraints on a region's active tectonics, geodynamics, and seismic hazard. However, space-based InSAR usually only provides good constraints on horizontal displacement in the east-west direction, with the north-south component typically provided by low-resolution GNSS measurements. Sentinel-1, on the other hand, has the potential to provide measurements that are sensitive to north-south motion, through exploitation of the burst overlap areas produced by the TOPS acquisition mode. However, the significant noise contributions from decorrelation and propagation through the ionosphere make it challenging to detect surface displacements associated with interseismic deformation needing millimeters per year accuracy.

The ionospheric phase advance is a significant nuisance term that can bias InSAR measurements. Although methods have been developed to mitigate the effect, they are not always routinely applied when processing C-band SAR images, for which the effect is generally expected to be small. Nevertheless, the effect can be significant, especially when analyzing low deformation gradients over large areas using time-series analysis. Here, the work in Chapter 3 presents a time-series approach to ionospheric noise mitigation, which improves on existing methods. Firstly, I estimate the ionospheric contribution for each individual acquisition from multiple interferograms, which reduces noise. Secondly, this work improved the identification of unwrapping errors, which can bias the estimation. Thirdly, I introduce a new filtering approach, which gives better results, particularly at image edges and areas with variable density of coherent measurements. Furthermore, the approach is applicable when estimating along-track motion in burst overlap areas. The results show that applying the correction improves velocity accuracy significantly for both conventional line-of-sight and burst overlap interferometry techniques.

The application of measuring long-term tectonic signals that concentrate in the north-south component with millimeters per year accuracy is essential to constrain interseismic strain globally. In Chapter 4, I also demonstrate a time-series approach

with the burst overlap interferometry appropriate for extracting subtle long-term displacements. The approach includes mitigation of ionospheric noise, and I investigate different filtering approaches to optimize the reduction of decorrelation noise. I present the mean ground velocity in the azimuth direction from data acquired between 2014 and 2019 along the West-Lut Fault, a north-south striking fault in eastern Iran. The chi-square statistic defines a good agreement between the results and independent GNSS measurements. Moreover, the denser coverage of the technique allows to detect the variation in strain accumulation between northern and southern segments of the fault, with our modeling indicating a variation of slip rate from 9.2±0.5 mm/yr in the south to 4.3±0.5 mm/yr in the north. With current efforts to use InSAR to constrain strain rates globally, along-track measurements can fill a crucial gap in north-south sensitivity.

With the achievement of that the burst overlap InSAR technique can measure azimuth motions across a slowly deforming area where the surface displacements are concentrated in the north-south component, this results in that, in the TOPS burst overlap region, the number of observations for a ground displacement can reach 3-4 times with different observational components. Measurement redundancy allows for the decomposition of observed velocities into three-dimensional components. In Chapter 5, I apply InSAR observations to estimate a deformation across the Chaman fault in both line-of-sight and along-track components using images from ascending and descending passes. I demonstrate an inversion to estimate the decomposed velocities. The algorithm employs a sparse GNSS network across the region to transform InSAR velocities to the GNSS reference frame. The results show that constraining the long-wavelength signal across the InSAR observations using GNSS data can mitigate the long-wavelength ionospheric disturbance that remains in the observations. The variation in slip rates across the Chaman fault is depicted by two transect profiles. The mean velocity profile at latitude 31°N, where the Chaman fault is the only tectonic structure to accommodate strain, is consistent with 10.4±0.4 mm/yr of slip rate derived from the interseismic modeling. The optimal fault slip rate to fit with the mean velocity of the southern profile at latitude 29°N is 5.5±0.8 mm/yr across the Chaman fault and 15.5±0.9 mm/yr across the parallel fault (the Ghazaband fault). I also demonstrate the benefits of high temporal sampling of InSAR observations with TOPS acquisition mode to study time-dependent surface deformation. I present the evolution of fault creeps, including seismic and aseismic fault slip along the Chaman fault during 2014-2018.

Contents

List of Figures

List of Tables

Nomenclature

List of acronyms

DEM	Digital Elevation Model
ECMWF	European Centre for Medium-Range Weather Forecasts
ESA	European Space Agency
ESD	Enhanced Spectral Diversity
EW	Extra Wideswath mode
GACOS	Generic Atmospheric Correction Online Service for InSAR
GNSS	Global Navigation Satellite System
GSRM	Global Strain Rate Model
IERS	International Earth Rotation and Reference Systems
InSAR	Interferometric Synthetic Aperture Radar
ITRF	IERS Terestial Reference Frame
ITRS	International Terrestial Reference System
IW	Interferometric Wideswath mode
MAI	Multiple Aperture Interferometry
MCF	Minimum Cost Function
PS	Persistent Scatter
SAR	Synthetic Aperture Radar
SLC	Single Look Complex
SLR	Satellite Laser Ranging
SM	Stripmap Mode
SRTM	Shuttle Radar Topography Mission
SVD	Singular Value Decomposition
TEC	Total Electron Content
TOPS	Terrain Observation Progressive Scanning
UAVSAR	Unmanned Aerial Vehicle Synthetic Aperture Radar
VLBI	Very Long Baseline Interferometry
WM	Wave Mode
ZHD	Zenith Hydrostratic Delay

List of symbols

$\Delta\phi_{ovl}$	Double-difference phase (rad)
$\Delta\phi_{ion}$	Ionospheric difference phase (rad)
Δt_{az}	Azimuth sampling time per SAR pixel (s)
Δx_{az}	Azimuth shift (m)
α	Satellite platform's heading (degree)
γ	Coherence
ϕ	Interferometric phase (rad)
μ	Mean value
σ	Standard deviation
θ	Look angle (degree)
c	Speed of light (m/s^2)
d	Locking depth (km)
f_c	Central Doppler frequency (Hz)
f_H	Sub-band high frequency signal
f_L	Sub-band low frequency signal
M	Primary image signal (Master image signal)
N	Number of points in a specific multilooking window/ Number of looks
s	Slip rate (mm/yr)
S	Secondary image signal (Slave image signal)
uwh	High-frequency unwrap signal
uwl	Low-frequency unwrap signal

Chapter 1

Introduction

1.1 Toward measuring tectonic strain accumulation globally

Earthquakes result from the sudden release of the long-term build-up of tectonic strain, which accumulates over 10–100s years, a slip deficit that is recovered in the seconds of rupture. Capturing the entire earthquake cycle, including interseismic, coseismic, and postseismic phases, typically requires data over at least 100 years, whereas advanced geodetic observations have only been available for about three decades or less. Therefore, extrapolating from short-term knowledge to long-term conclusions relies on a number of models, which require as many cases of data as possible, as well as the study of multiple fault systems at different stages of the earthquake cycle to try to understand the underlying processes. Specifically, combining the time since the last earthquake rupture with knowledge of the rate of strain accumulated in the intervening period allows an assessment of the slip deficit. If the fault rupture is assumed to occur regularly, a time-dependent seismic hazard model can be assessed. Therefore, to determine where and how fast the strain is accumulating within the crust is necessary to assess the potential level of seismic hazard and consequent risk if exposed populations are nearby.

Although geodetic techniques cannot directly measure tectonic strain rates, they can detect the relative ground deformation across large spatial scales, which can be modelled as the present-day strain accumulation. Analysing a ground velocity associated with interseismic deformation for a single fault can be examined with a 1-D elastic screw dislocation model (Savage and Burford, 1973)

$$v = \frac{s}{\pi} \arctan \frac{x}{d} \tag{1.1}$$

where v is a fault-parallel surface velocity, s is the slip rate, d is a locking depth, and x is a distance from the fault trace. The rate of change of velocity with distance ($\frac{dv}{dx}$) represents the strain due to the shear zone of the active fault (Weiss et al., 2020).

$$\frac{dv}{dx} = \frac{sd}{\pi(x^2 + d^2)} \tag{1.2}$$

At present, there are two geodetic techniques that can effectively measure crustal deformation in active tectonic areas. Firstly, the Global Navigation Satellite System (GNSS) can reach the precision levels of measurement to 1 mm (Misra and Enge, 2006). A GNSS instrument is installed at a fixed point for a period of time to receive transmissions from GNSS satellites. The duration can be hours to days as part of a survey campaign up to many years and decades for fixed continuous GNSS sites. The stack of received data can be analysed as a function of distances between the broadcasting satellites and GNSS receiver, and consequently estimated evolutions of absolute point positions, a benchmark of the receiver on the ground surface, for the particular period of time. Therefore, a network of GNSS stations is able to provide a measurement of the amount of deformation across fault zones. Currently, there are many global tectonic models, especially the Global Strain Rate Model (GSRM) (Kreemer et al., 2014), using data from many thousands of GNSS sites around the globe, freely provided.

However, due to a requirement to access areas that are typically difficult to reach and maintain instruments, the technique cannot be used to provide dense measurements spatially or be comprehensive in its degree of spatial coverage. Therefore, the number of currently available GNSS observations is still inadequate to measure the strain rate globally. According to Kreemer et al. (2014), the distribution of GNSS stations is dense in well-defined areas with high risk and sparse in many active fault zones. However, Wright (2016) presented that 96% of fatalities caused by earthquakes are associated with faults that accommodate strain higher than 10^8 per year, corresponding to only 1 mm/yr distributed over 100 km. However, for many areas of the globe that are at this lower end of this strain rate threshold, the seismic hazard is less well characterized or recognized. For illustration, Elliott et al. (2016) showed that large earthquakes could occur by the slowly deforming fault. These events usually come with a long seismic cycle (large earthquake recurrence intervals), for which the last rupture was not recorded in known history. Specifically, many crucial events have occurred on the faults, which were not well-known before or underestimated. Furthermore, despite areas with dense GNSS networks, the spatial resolution is still not high enough to define the level of fault creep (aseismic slip), which directly influences the seismic risk evaluation.

Here, the second technology, Interferometric Synthetic Aperture Radar (InSAR), performs observations remotely (typically satellite-based) and moreover is analysed on

an image basis yielding dense spatial coverage on land surfaces. Since every pixel in an image can provide phase information, which is able to extract the displacement, the number of observations is highly dense without the limitation of access on the ground. The technique analyses a time delay or advance of repeat-pass SAR observations to deduce a function of change in distance (i.e., deformation) between satellite and ground using a fraction of radar wavelength and consequently enables the method to achieve a millimetre level of precision potentially. Due to being a space-based measurement, many other components to the overall path delay typically mask the displacement signal of interest. However, due to a great advance of the SAR system, particularly the Sentinel-1 mission (Elliott et al., 2016), and significantly post-processing development (Lazecky et al. (2020) and Morishita et al. (2020)), the technique recently has a high potential to measure and monitor large-scale deformation globally, with a better constraint on long-term seismic hazard than the GNSS technique for many poorly instrumented regions.

Nevertheless, compared to GNSS, space-based InSAR observations are not sensitive to the component of north-south deformation. It is mostly restricted to east-west and vertical application because of the SAR satellite being in a near-polar orbit (resulting in inclination angles with the equator of 98 degrees for Sentinel-1) and performed with side looking operation. Lacking high resolution from InSAR causes an inefficient constraint on the shear zone predominantly in the north-south direction (Hooper et al., 2020). Fortunately, burst overlap regions in images from the Terrain Observation Progressive Scan (TOPS) mode, the default operation mode of Sentinel-1, can be applied to explore a deformation in a horizontally along-track direction with greater precision than before. This flight direction can contribute a desirable constraint on the motion of the Earth's surface in the north-south direction. This analysis has proved efficient with studies of large deformation (Grandin et al. (2016) and Spaans (2016)). However, in contrast to the line-of-sight conventional InSAR, the ionospheric disturbance is the primary bias to the accuracy of relative measurement for the along-track technique as well as an unusually high sensitivity to noise, making it challenging to detect a low rate of strain accumulation. In an attempt to address this challenge, this work demonstrates an analysis of the burst overlap InSAR technique with a time-series approach using stacks of TOPS Sentinel-1 images. The ionospheric correction and decorrelation noise are also addressed to enable the method to measure slow tectonic strain accumulation (e.g., few mm/yr), dominantly in the north-south direction, aiming to achieve the global strain rate in the future.

1.2 The Earthquake cycle

The geodetic measurement of tectonic strain, the main objective of this thesis, is a principal parameter in constraining interseismic deformation. In the seismic cycle, crustal deformation behaviour around fault zones can be divided through time into

interseismic, coseismic, and postseismic phases (Thatcher et al., 1993). Non-uniform tectonic plate motions are the main force driving this quasi-cyclical process. The force causes interactions (i.e., convergence, divergence, sliding past each other, or compound with more than two processes) between plates at their boundaries and also impacts in the continental interiors as distributed strain and deformation. According to the elastic rebound model (Reid, 1910), the fault in the brittle upper crust is locked by a fault's friction, whereas the lower crust and mantle still slowly deform. This heterogeneous response causes a crustal deformation and an accumulation of elastic strain at the upper part of the crust. This building-up period, known as the interseismic period, typically ranges over hundreds to thousands of years. Due to this long-term accumulation, it is hard to tell whether the historical earthquake records we have currently are complete representative or are only a partial catalogue. The observations of surface deformation, such as from the geodetic measurements discussed here, can be used to infer the process beneath the ground through mathematical modelling (e.g., Eq. 1.1) to estimate the tectonic strain; however, their operational periods have only been broadly active for three decades or less. Moreover, one of the more powerful sets of geodetic observations, the GNSS network, often concentrates in well-defined fault zones, which we have already known that there is a fault existing in those areas. There are other areas where an earthquake could cause severe damage to people who live in high seismic risk areas where the fault has not been exposed and reported in the historical catalogue previously.

Therefore, a complete map of seismic hazards in the continents is the priority to address the challenge of earthquake risk. Although the seismicity and historical earthquake record can efficiently locate faults, they are post-processing techniques that can discover the fault only after the earthquakes. Waiting for all active faults to rupture is probably not a good choice, so an observation, which is able to detect the active fault before they rupture in an earthquake, is required. Following the clarifications in Wright (2016), mapping the complete catalogue is difficult to achieve since plate boundaries and fault zones extend very wide. Furthermore, most of the faults are not clearly single traces and usually comprise a series of complex networks of tectonic structures. Despite huge advances in analysing landscapes both from satellite images or fieldwork, the active fault map is still incomplete. Besides, although the global strain rate map (GSRM) (Kreemer et al., 2014) derived by GNSS stations can provide a tremendous recent deformation of the continent, the instrumental network, which is dense in well-defined fault, does not suit searching for an unknown fault or studying secondary faults due to the low-spatial resolution.

Nevertheless, the satellite-based geodetic InSAR observation can contribute a significant part for implementing the current map of active faults to become a complete catalogue. The measurement is now available globally with a much higher spatial resolution (i.e., typically <100 meters), which is sufficient to study the secondary faults.

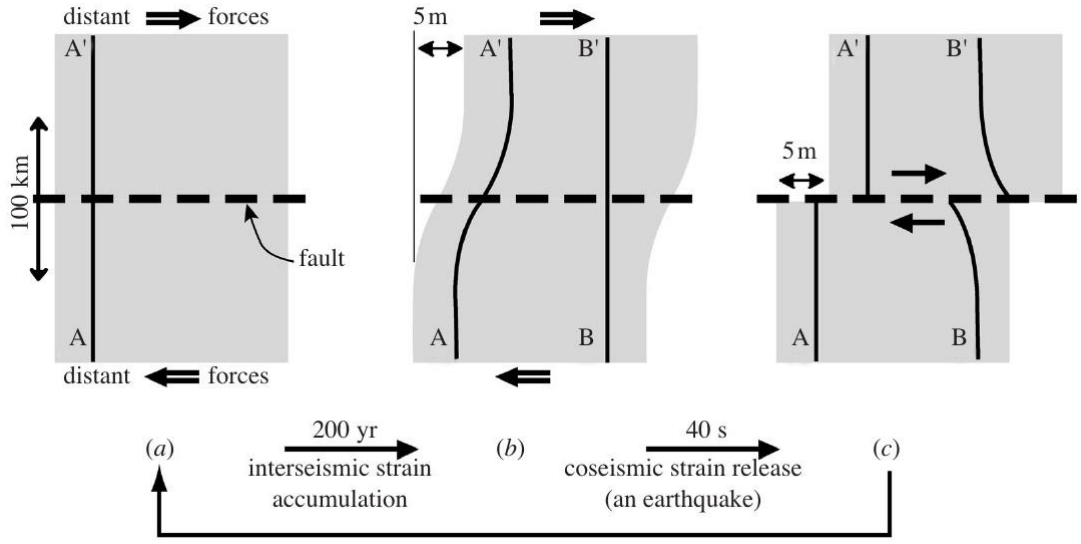

Figure 1.1: Simplified illustration of the ground displacement associated with the earthquake cycle based on Reid's elastic rebound model. The figure is reproduced with permission from Wright (2002). The dashed line is a fault trace of strike-slip fault viewed from above. a.) The profile AA' is straight and continuous. b.) After 200 years, the blocks on either side of the fault in the far-field have a displacement of 5 m due to the driving plate tectonic movement. Since the fault is locked due to the fault's friction, the profile AA' deforms to be an arctangent curve. The energy, interseismic strain, is accumulated at the fault shear zone at depth beneath this locked interface. c.) When the fault's friction is overcome by the accumulated energy, the stored elastic energy is released in a short-term scale (e.g., 40 seconds). Profile AA' is straight again, but there is a 5-meter offset at fault resulting from the permanent deformation. Profile BB', which is straight just before the rupture, also has a discontinuity at the fault trace with a 5 m maximum. The magnitude of dislocations decay as the distance from the fault increases with the wavelength determined by the depth of the locked fault.

Although the interseismic deformation is a slow-moving process, typically ranging from a few to tens mm/yr over a wide area (i.e., 100's km), a recent advance of the InSAR technique can filter out nontectonic signals and achieve the observation remotely with millimetric precision. Then, the geodetic strain rate, which is a differentiation of velocity with respect to distance, can highlight areas across which strains are concentrating. This thesis's demonstration will enable InSAR to estimate the subtle deformation in three-dimensional components, which is a limitation in conventional InSAR for a long time, without any prior assumption to be made. Furthermore, aseismic creep is a significant parameter in seismic risk evaluation. The surface creep results from low fault friction and means that the fault is not fully locked. The high-spatial resolution of the InSAR technique is compatible with detecting whether the faults are accumulating with full or partial build-up strain.

At the time that the accumulated energy exceeds the fault's friction, the energy is released in a short-time scale (i.e., seconds–minutes). The ground moves like an elastic displacement to return to a non-deform shape but with a permanent offset. The

emitted high-frequency seismic waves propagated through the ground affect a wide area and cause shaking losses. This period of rupture is known as a coseismic phase. The geodetic InSAR technique is a suitable measurement for this phenomenon and has recently become a principal tool in observing the rupture and earthquake displacement field. As a result of the great advance in the ability of InSAR and the benefit of being a remotely derived observation, the analysis of surface measurements from InSAR can capture overall the deformations, typically more than 100s km in extent for a large earthquake. The study of the coseismic period can provide the fault properties (e.g., geometry by an inversion of the surface displacement data: dislocation model based on elastic half-space model (Savage and Burford, 1973) or slip distribution on the fault plane (Okada, 1992).

After a rupture, the postseismic deformation, associated with a relaxation of the crust and mantle due to a rapid change of stress in the coseismic period, is typically found to occur (Wright et al., 2013). This transient period ranges from days to years after the earthquake. A compilation of studies of postseismic deformation (Ingleby and Wright, 2017) shows that the period can extend to 100 years. A robust boundary of the transition stage from postseismic to the longer-term accumulative interseismic phase is hardly distinguished. While the interseismic and coseismic deformation are more simply measured, the postseismic pattern is non-uniform and varies from place depending on fault properties. The pattern can be due to afterslip on extensions of the fault plane around the coseismic slip zone, viscoelastic relaxation of deeper portions of the crust, poroelastic rebound, or combined mechanisms. The studies of the postseismic deformation are significant resources to understand the rheology of the lithosphere. Even though the signal of postseismic deformation is larger than the interseismic signal (i.e., 1–10s mm/yr), the postseismic deformation is a time-dependent process. The magnitude varies inversely with time since the earthquake (Ingleby and Wright, 2017). Therefore, averaging a large stack of SAR images to enhance the deformation signal as the studies of interseismic deformation can probably not present the optimal information for postseismic deformation. However, the improvements of high-temporal resolution in recent InSAR missions (e.g. Sentinel-1) increase the tectonic phenomena more detectable by InSAR observations, for example, sequence of earthquakes (10s days interval). Furthermore, the higher frequency of acquisition increases efficiency in filtering nontectonic noise (e.g., atmospheric disturbance) and consequently enables the analysis to enhance information in sub-periods. These time-series products, which are not only an average value from a long-term estimation, should provide more knowledge on this seismic study field (e.g., postseismic deformation, variation of slip rates in the interseismic period, surface creep) and enable us to construct better tectonic models both in space and time.

1.3 The European Commission's Sentinel-1 satellite

Currently, measurements of crustal deformation are increasingly being accomplished using the InSAR technique (Elliott et al., 2016). Indeed, the Sentinel-1 mission plays a key role in this development. The comprehensive coverage with a 6–12 days revisit period could enable the InSAR technique to measure and monitor active tectonics globally. Furthermore, the current limitation that the sensitivity of surface motion that is greatest in the vertical and east-west directions, with much less constraint on the north-south motion, could be complemented by the application of the burst overlap InSAR technique, applied to the TOPS Sentinel-1 image (Grandin et al. (2016) and Spaans (2016)).

Sentinel-1 is the first SAR satellite that operates Terrain Observation with Progressive Scans (TOPS) as a standard mode. The mission is managed by the European Space Agency (ESA) and provides C-band SAR image products, with L1 level being Single Look Complex (SLC) data. The system offers four different acquisition modes (i.e., Wave Mode (WM), Stripmap Mode (SM), Interferometric WideSwath Mode (IW), Extra WideSwath mode (EW)). The IW mode is a common mode for the Sentinel-1; hence most images are acquired with a swath width of 250 km, composed of three sub-swaths, at ground resolutions of 5 m x 20 m. Sentinel-1 SAR images have been available with free access since September 2014. In the first two years of operation, only Sentinel-1A was in the constellation; the mission can reach a 12-day repeat cycle at best. Moreover, since Sentinel-1B was launched in April 2016, the shortest return period on a given ground track necessary for interferometry has been reduced to 6 days due to the compatibility of the near-identical systems and closely matched orbital paths. The mission has helped InSAR techniques developed significantly, for example, near-global coverage, decreasing decorrelation noise, reduced latency in response to hazards, and higher temporal resolution for time-series analysis to gain more knowledge of temporal tectonic processes. These reasons manifest that Sentinel-1 InSAR processing has a very high potential to measure and monitor global tectonic activities (Elliott et al., 2016).

The TOPS acquisition mode is a key success of all these benefits, as it can acquire wider images 3–4 times greater than Stripmap Mode. This is an essential factor in achieving a short revisit time of 6–12 days with 175 orbits per cycle. The system scans the surface with small discontinuous images, called bursts, approximately 20 km in along-track extent. The standard product of the IW system is three series of bursts that have a total swath width of 250 km in range direction (Fig. 1.2). Each series is called a sub-swath. During image acquisition, the sensor is continuously steered from backward- to forward-looking in an along-track direction (i.e., flight direction) to illuminate one burst. The system uses time gaps before the sensor needs to acquire the consecutive burst, to take the other two images with different look angles. After the

sensor finishes obtaining the first burst in the IW1, the nearest sub-swath, the sensor increases the look angle and repeats the steering from backward to forward to illuminate the image in IW2. Then, the sensor changes the look angle higher one more time and repeats the process for scanning the burst in IW3. After it finishes the third time, the system starts a new cycle with the smallest look angle (nearest range) for IW1 again. The system acquires images with small overlap areas in adjacent bursts and sub-swaths to avoid a gap in mosaiced images. The length of the burst overlap area in the azimuth direction is about 110 pixels, giving about 1.5 km in a ground distance. This means that the look component to illuminate the ground is not permanently perpendicular to the flight direction, but it varies along the azimuth direction. The squint angles of the steering vary between $\pm 0.4°$ and $\pm 0.7°$ (Grandin et al., 2016), depending on the sub-swath.

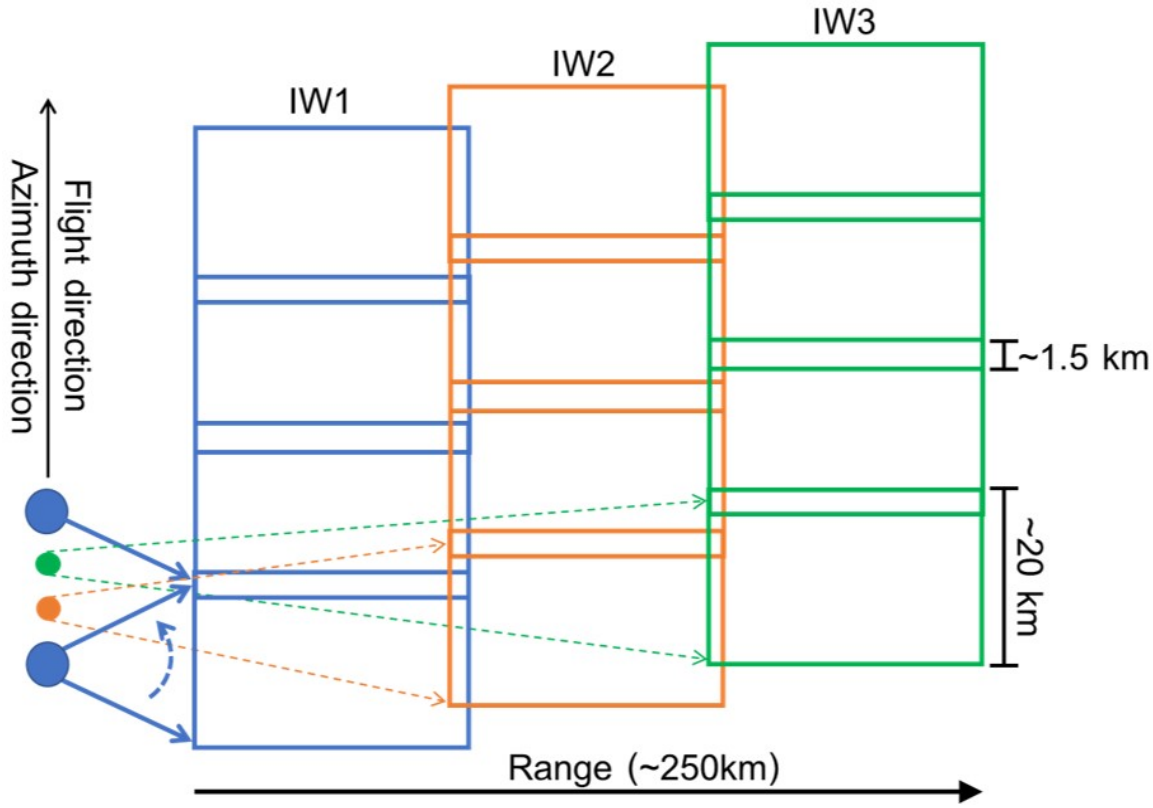

Figure 1.2: Simplification of TOPS operation from the top view looking down to the ground. The product of IW mode is three-series of discontinuous bursts. The sensor is swept from backward to forward for one burst acquisition. After it illuminates the ground with the smallest look angle (∼34°) for the first sub-swath (blue), the second (orange) and third (green) sub-swaths are scanned with the same operation with look angle ∼39° and ∼44°, respectively. The system illuminates the ground with burst overlap and sub-swath overlap to avoid a gap in the mosaiced image.

The rapid development of SAR instruments and advanced post-processing algorithms that can handle large data volumes result in a great potential to achieve global

tectonic measurements. Hussain et al. (2018) and Weiss et al. (2020) illustrate robust proof of the proposal by measuring a large-scale interseismic deformation across the North Anatolia Fault (NAF) zone. The averaged velocities in Weiss et al. (2020) are estimated from five-year stacks of Sentinel-1 images both in ascending and descending passes. They can manage and process this massive product whose volumes are uncommonly large to achieve velocity maps and strain rate fields over 800,000 km^2, covering almost all Turkey areas. However, despite this tremendous result, there is still a significant challenge in measuring an accumulated strain that dominates in the north-south component because SAR satellites are in near-polar orbits and illuminate the Earth's surface with a side-looking operation. Specifically, the observational component is perpendicular to the flight direction. The majority of line-of-sight displacement, detected by SAR satellites, is therefore likely to be due to the vertical and east-west motions (Fig. 1.3).

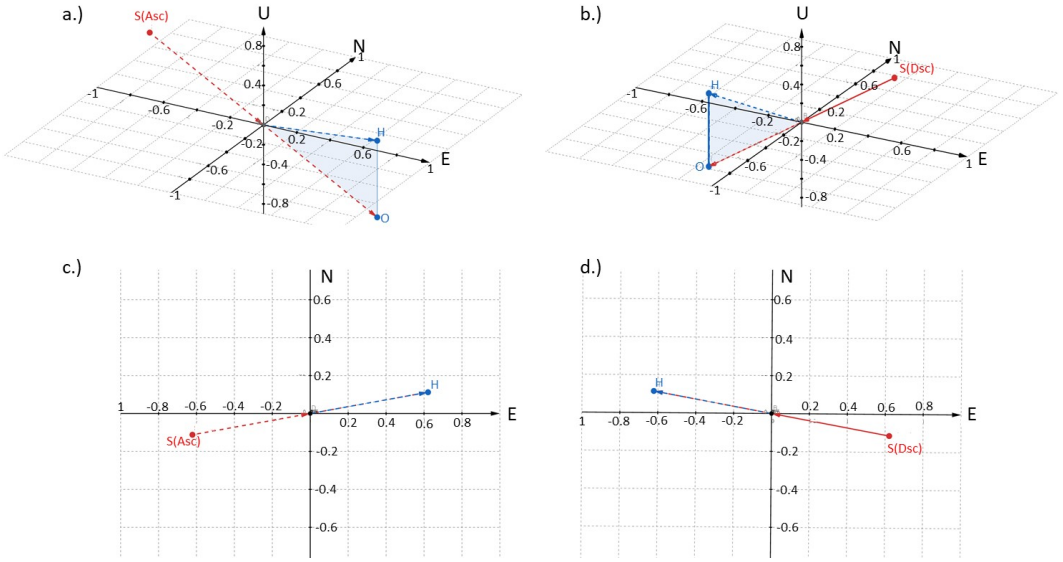

Figure 1.3: Geometry of SAR acquisition illustrated with the Sentinel-1 feature. a.) and b.) present the line-of-sight direction of the satellite in ascending (348°) and descending (192°) pass, respectively. c.) and d.) illustrate the observational components from the top view looking down to the ground. S represents the position of the Sensor looking down to the ground (grid plane). The unit vector, from the origin to point O, represents the line-of-sight observational direction. A portion of the horizontal component is presented with a vector from the origin to point H.

Defining the look angle of the Sentinel-1 as a unit vector, Fig. 1.4 presents the directional cosine or cartesian coordinates of the vector in three-dimension components. They illustrate their contributions to the SAR line-of-sight vector. As the magnitude of the unit vector is equal to 1, calculated by summation of the square of the directional cosines, the squares of directional cosine of the pixel in the middle of the scene for east, north, and up components are at 0.39, 0.01, and 0.60, respectively. These values show that the observational component is sensitive only to east and vertical directions.

Therefore, Hussain et al. (2018) and Weiss et al. (2020) applied smoothed estimates of northward deformation derived from GNSS data to constrain the north-south part in the decomposition of InSAR observations to three-dimensional velocity maps. However, for tectonic strain dominated in north-south component, we cannot implement such smoothed data, derived from a sparse network, to define strain accumulation which is estimated from the gradient of velocity in a function of distance. Hooper et al. (2020) also presents the necessity of north-south high-spatial-resolution strain measurement from InSAR to improve the strain rate map in areas where deformation concentrates in the north-south direction.

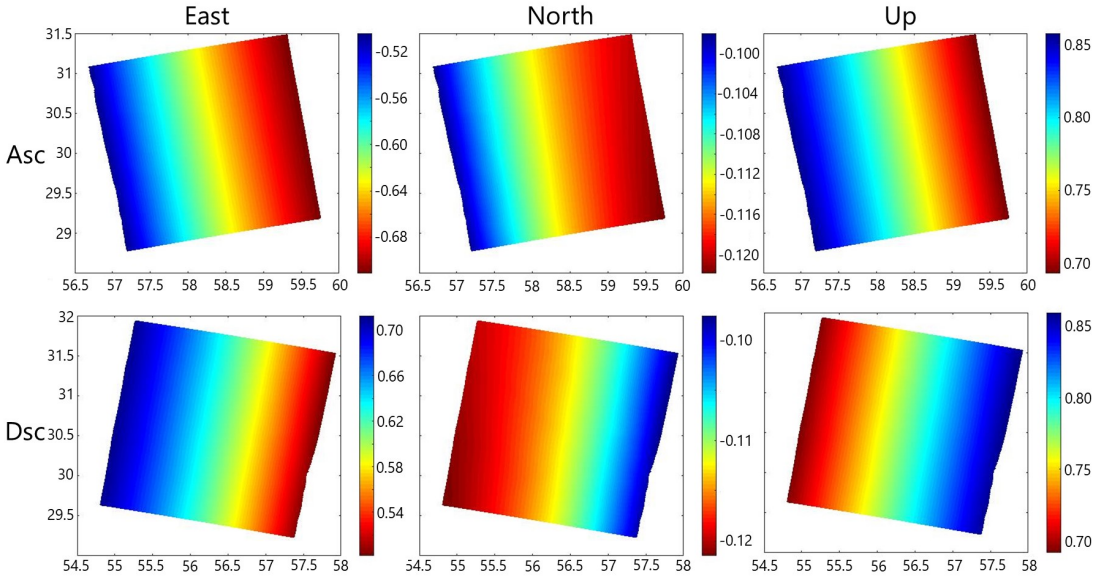

Figure 1.4: Directional cosines of a unit vector in the InSAR look angle direction for a Sentinel-1 IW scene. a.), b.), and c.) present values in N, E, and U components derived from ascending data. d.), e.), and f.) present the values derived from descending data. The detail of these examples is from SAR images over latitude 30°N.

However, the particularities of the TOPS mode in Sentinel-1 acquisitions offer a potential to extract the along-track displacement, which is greatly sensitive to the north-south motion (about 10° to be projected). Since the along-track scanning is continuously steered from backward to forward relative to the flight direction, the variable squint angle in the azimuth direction results in a greater sensitivity of the measurement to the along-track motion. The effect varies within a burst depending on the magnitude of squint angles (±0.4° and ±0.7° (Grandin et al., 2016)). Therefore, a constant azimuth displacement can cause a phase ramp over the burst in the TOPS image due to a variable sensitivity of the along-track measurement. Furthermore, the sensor acquires pixels at the burst edges with the largest squint angle. The backward and forward components correspond with the opposite senses of displacement so that the effect can cause a phase jump between the consecutive bursts. In Fig. 1.5, I present the sensitivities of pixels in a burst for the along-track measurement varied by the

squint angles and incidence angles. This feature of the Sentinel-1 shows us that the TOPS mode image contains information of both across and along-track displacements.

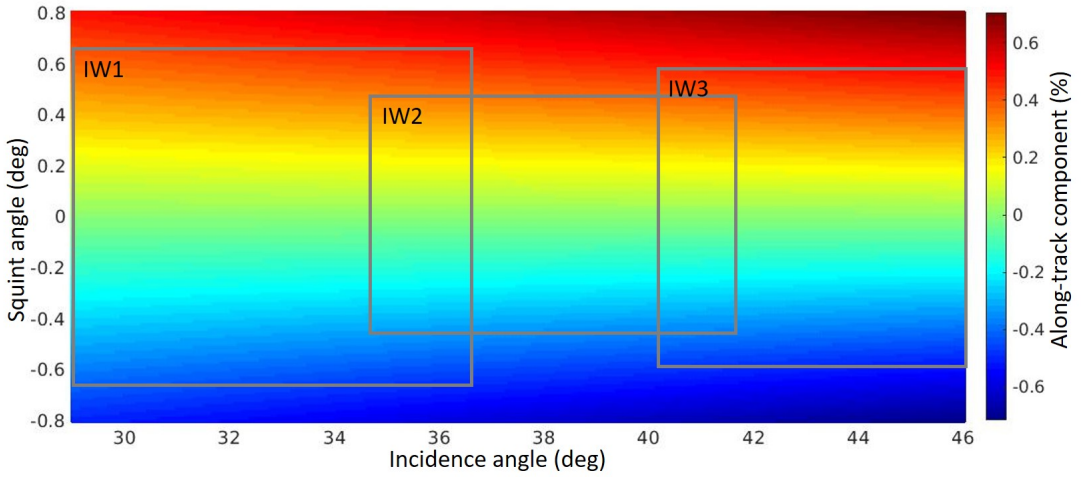

Figure 1.5: Percentages of along-track components that contribute to total line-of-sight displacements by defining the same magnitude of displacement in three dimensions (East, North, and Up). This map represents the sensitivity of the along-track motion varied by the diverse squint angles in the azimuth direction and variable incident angles in the range direction. The grey boundaries present the ranges of squint angles and incidence angles for each sub-swath.

Since TOPS mode acquires images with small burst overlap areas, pixels in these regions have redundancy of measurements. The same region is illuminated by different looks, forward- and backward-looking observations. These two observations have the same magnitude of sensitivities in across-track and vertical components. The difference in phase delay is a result of the separation of observational squint angles. Thus, we can analyse the interference of these two observational phases to extract displacement in the horizontal azimuth direction. However, as mentioned, this effect causes phase ramp over bursts and burst discontinuities in the mosaiced image processing for line-of-sight observation. Thus, we normally estimate and eliminate this azimuth shift in the coregistration step using Enhanced Spectral Diversity estimation (Prats-Iraola et al., 2012). Apart from the variable squint angle, pixels in a burst are also illuminated with a difference of central Doppler frequency, which is associated with a sensor steering and satellite velocity, varying along the azimuth direction. The ESD estimation applies a relationship of difference Doppler frequency and the double-difference phase in the burst overlap region to estimate the azimuth shift with the highest precision ever. Then, the estimated shift is applied in resampling a secondary image to the same alignment as a primary image and is precise enough to avoid the phase ramp and burst discontinuities in the interferogram.

On the other hand, the burst overlap InSAR analysis focuses on the estimated ESD value to extract the azimuth displacement. Indeed, in the previous paragraphs, I

describe the estimation associated with only the azimuth displacement component, but actually, the displacement is only one of the components that cause the misregistration shift. The double-difference phase actually includes an orbital error, ionospheric signal, and random noise. Even though this along-track measurement is difficult to achieve due to the high uncertainty of the technique, Grandin et al. (2016) and Spaans (2016) observed deformation associated with the Chile earthquake using single interferograms. This large deformation signal (∼0.4 m) can dominate the other nontectonic components comprised in the burst overlap phase. However, there is still a big challenge in measuring a subtle deformation such as interseismic displacements since the signal is saturated by noise. Thus, this study will apply the along-track measurement with a time-series approach assuming that the deformation is the only component with correlation in time. The methodology can filter out the disturbing components. Furthermore, this thesis also demonstrates the ionospheric mitigation applied with along-track measurement and proposes a strong multilooking to reduce decorrelation noise in order to enhance the interseismic signal.

1.4 Areas of study: West-Lut and Chaman faults

This thesis demonstrates the algorithm applied to Sentinel-1 SAR images to study deformations across the West-Lut fault in eastern Iran and the Chaman fault in Afghanistan. At the plate tectonic scale, both active faults are in the system of the Alpine-Himalayan belt (Fig. 1.6), one of the largest crustal tectonic systems. This seismic belt accounts for 17% of the world's largest earthquakes (USGS, 2014), but it is a result of 60% of overall fatalities (2 million) caused by earthquakes since 1900 (Walters, 2012). Series of mountain ranges comprised in this system over a length of more than 10,000 km are located at the southern part of the Eurasian plate. The deformation in this collision zone is mainly driven by the northward movement and subduction of the African, Arabian, and Indian plates relative to the stable Eurasian plate. In the number of tectonic structures along the system, the strike-slip West-Lut and Chaman faults respond to parts of this convergence by accommodating shear strains in a dominantly north-south direction.

Present-day deformation at the longitude of the West-Lut fault results from a collision of Arabia with Eurasia plates in a nearly north-south direction at 2.5 cm/yr approximately (Walpersdorf et al., 2014). In the east of the West-Lut fault, the convergence is absorbed by mostly the Makran subduction zone and mountain ranges in the north. Whereas, in the west of the fault, most compression localize along the Zagros mountain in the south, and the rest is building up in the Alborz and Kopeh Dagh mountain ranges in the north. The West-Lut fault is in the area of central Iran, surrounded by these dominant compression structures. A series of thrust and right-lateral faults with NNW-SSE to N-S strikes localize in this area and accommodate a part of the

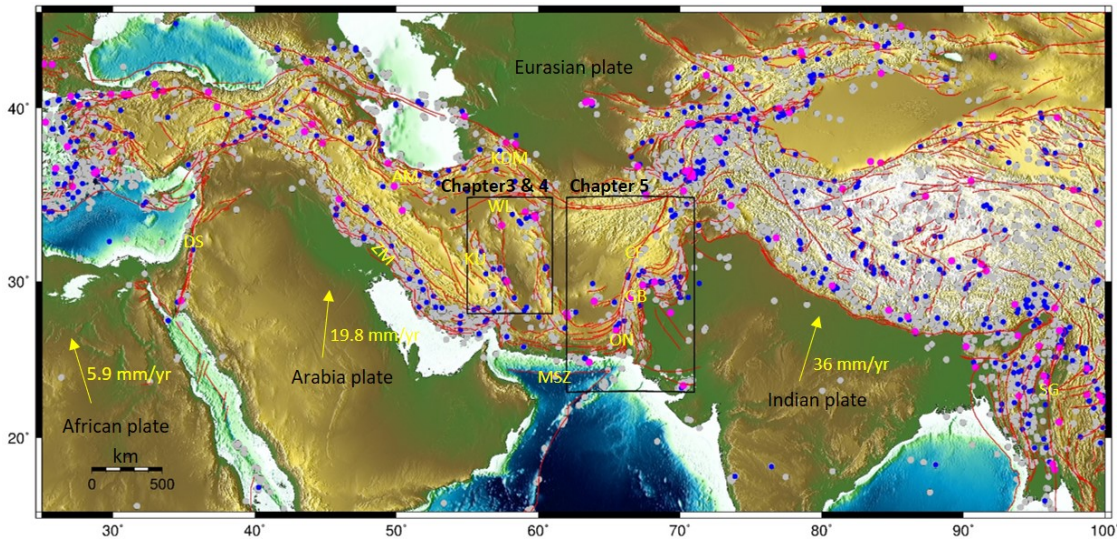

Figure 1.6: Location of study areas, denoted by black rectangles, for the following chapters. The red lines represent major faults (Styron and Pagani, 2020). The dots present major earthquakes that occurred between 1972 and 2020. Grey dots indicate earthquakes with magnitudes (Mw) between 5 and 6. Blue dots represent earthquakes magnitude (Mw) between 6 and 7. Pink dots present earthquakes that occurred with a magnitude (Mw) higher than 7. All data are from the USGS catalogue (source: https://www.usgs.gov/natural-hazards/earthquake-hazards/earthquakes). The plate velocities relative to the stable Eurasian plate are from the UNAVCO (source: https://www.unavco.org/software/geodetic-utilities/plate-motion-calculator/plate-motion-calculator.html). AM: Alborz mountain, CF: Chaman fault, DS: Dead Sea fault, GM: Ghazaband fault, KDM: Kopeh Dagh mountain, KU: Kubhanan fault, MSZ: Makran subduction zone, ON: Ornah Nal fault, SG: Sagaing fault, WL: West-Lut fault, ZM: Zagros mountain.

collision. The West-Lut fault is a right-lateral strike-slip fault that accumulates north-south shear strain with the highest rate (∼4 mm/yr) in this series of faults. The fault can be roughly divided into two segments by the complexity, comprising sub-parallel systems and reverse faulting structures, of fault in the southern segment and conversely a simple single segment comprising the northern part. Furthermore, at the transition between two segments, the active Kuhbanan fault appears to join the West-Lut fault; therefore, the strain accumulation is probably not constant, as expected, between the northern and southern segments. The GNSS study's contribution (Walpersdorf et al., 2014) has done well providing overall kinematics of faults in this region, but the network does not concentrate on the West-Lut fault. Thus, this variation of slip rate and also fault parameters has not been robustly reported.

The Chaman fault is a major left-lateral strike-slip fault accommodating a nearly north-south shear component (i.e., in the N20E direction) between Indian and Eurasian plates. In the south, the fault starts offshore at the triple junction of Arabian, Eurasian, and Indian plates. This area is at the eastern end of the Makran subduction zone. From the coastline to the north, the Ornah Nal fault strike in an almost north-south direction along with a series of east-west thrust faults in the west. Further to the north, this

segment comprises the Chaman fault and the Ghazaband fault sub-parallel to each other. The InSAR studies (Fattahi and Amelung, 2016) presented that the Ghazaband fault (∼16 mm/yr) accumulates a higher slip rate than the Chaman fault (∼8 mm/yr) at this latitude. The work in chapter 5 applies SAR images covering this segment and also the northern area of this segment. In the northern part, the Chaman fault is only a predominant structure to accommodate the strain. There is a discrepancy in the tectonic slip rate concluded from InSAR studies at this latitude. Fattahi and Amelung (2016) suggested that the Chaman fault is accumulating only a part of deformation (6 mm/yr) and proposed an unknown fault to accommodate another 6 mm/y. In contrast, Szeliga et al. (2012) proposed a ∼16 mm/yr of slip rate operate at this latitude and localize only at the Chaman fault without proposing another fault. Therefore, the along-track measurement in this thesis could contribute a useful part to this discussion.

The burst overlap InSAR technique has two main limitations, which are ionospheric signal and decorrelation noise. Since the SAR coherence for the area around the West-Lut fault is excellent, I start the experiment in Chapter 3 with the ionospheric mitigation for the West-Lut fault area. This could make the experiment to deal with the ionospheric signal easier by handling a significant problem at a time. Furthermore, the strike-slip deformation across the West-Lut fault is dominantly in the north-south direction, an insensitive component for the conventional line-of-sight InSAR observation. The 4 mm/yr of the fault slip rate corresponds to a variation of 0.5 mm/yr in the line-of-sight direction across the fault. This small magnitude of deformation signal is difficult to be distinguished from the other noise terms in the interferometric phase. Thus, the fault can be a great example to prove the efficiency of the burst overlap InSAR technique in measuring the slow slip rate. Also, the method could be able to detect the variation of deformation between the northern and southern segments of the West-Lut fault. Then, I apply the algorithm with the Chaman fault area, which has a lower level of SAR coherence. The tectonic slip rate in this area is higher than the West-Lut fault. Also, the along-track measurement could detect variation of slip rates between the northern segment that has only the Chaman fault and the southern segment that has both the Ghazaband and Chaman fault to accumulate strains. Furthermore, in this area, the number of observations could reach four observations from two along-track measurements and another two line-of-sight measurements, generated by images from ascending and descending passes. An overdetermined system is available to decompose ground velocities associated with interseismic deformation to three-dimensional displacements (i.e., east, north, and up).

1.5 Aims and overview of the thesis

As introduced in Section 1.1 and supported in Section 1.2-1.4, the space-based geodetic InSAR technique is a powerful tool to measure and monitor continental tectonic strain

rates. Furthermore, the particular observing characteristics of Sentinel-1 and great advances in post-processing, especially time-series analysis, increases our capacity to accomplish the observation of tectonic deformation globally for land surface areas. However, there is still a vital gap between the capabilities of the conventional methods of InSAR and the determination of global tectonic strain in all dimensions. The limitation is the detection of deformation concentrated in the north-south direction that previously has been challenging to achieve. Therefore, this thesis designates the main objective to decrease this gap using the burst overlap InSAR technique with a time-series approach as a key role.

In this thesis, I applied stacks of Sentinel-1 images as the main tools to investigate tectonic strain focusing on two strike-slip faults, in which the deformation is dominantly in the north-south direction: the West-Lut Fault in Eastern Iran and the Chaman Fault system. These two areas have different levels of coherence, senses of lateral slip, and magnitudes of slip rate. The subsequent chapters in this thesis are organized as follows:

- Chapter 2: In this chapter, I give the background information of the line-of-sight InSAR technique, which can be related to the principle of the burst overlap InSAR method. I describe the workflow of InSAR processing and the ESD technique (Prats-Iraola et al., 2012) that is used in the image coregistration. I also explain the interseismic model for active faulting and the Bayesian approach applied in the following chapters.

- Chapter 3: I start the work by proposing an ionospheric correction, which is a significant bias for the burst overlap InSAR technique, with a time-series approach. The main algorithm is adapted from the existing method, split-band in range technique (Gomba et al., 2017), and applied to correct for both line-of-sight and along-track measurement. Also, this chapter proposes a point selection with an adaptive threshold to avoid an unwrapping problem in the existing method, which can significantly bias results. Secondly, a fit-plane method is applied to reduce an edge problem that arises when a spatial filter with large window size, typical to reduce noise in the estimation, is performed. Even though all algorithms mentioned here were developed based on the Sentinel-1 features, the demonstration of an ionospheric correction with a time-series approach in Chapter 3 can be implemented to any other mission, apart from applying to the along-track measurement.

- Chapter 4: This chapter presents time-series results of line-of-sight and along-track observations covering the West-Lut fault in eastern Iran and also the tectonic interpretation for the area. The level of SAR coherence in this area is excellent. However, the West-Lut fault's interseismic slip rate is about 4 mm/yr of accumulated strain in a nearly pure north-south direction. This low strain rate

signal is significantly small relative to the decorrelation noise, which is particularly high and occurs to be another crucial problem for the burst overlap InSAR technique. This chapter proposes a strong multilooking and time-series analysis with the NSBAS approach to reduce the noise. Since the conventional line-of-sight measurement cannot detect the interseismic signal, this chapter will explain a limitation and prove the efficiency of the along-track process to examine the north-south low strain rate (4 mm/yr) compared to the level of noise, which is a requirement to satisfy the evaluation of seismic risk even with identified low-risk fault.

- Chapter 5: After proving the reliability of the analysis, the process is then applied to the Chaman fault, which has a lower level of SAR coherence than the West-Lut fault area. However, the along-track and across-track measurements are available from both ascending and descending passes in this area. Therefore, the number of InSAR observations for this area is allowed to decompose the velocity to the three-dimensional component. Furthermore, the analysis can reach the overdetermined system in the area, where four observations are overlapped, giving a better constraint for the estimation. This chapter presents the analysis to define the deformation in three dimensions. Furthermore, due to the high sampling in time of Sentinel-1 observation, this chapter presents some examples of temporal behaviours of fault surface creep to support that the InSAR observation now does not only have high resolution in space, but the temporal resolution is high enough to boost up the study of time-dependent tectonic deformation.
- Chapter 6: This chapter provides the summary of the thesis and lists the limitations that need further investigation, and also outlook for future study.

Chapter 2

Methods

In this chapter, I describe the InSAR background focused on the conventional line-of-sight InSAR, which can be related to detail in Chapter 3 and Chapter 4. I show the workflow of InSAR processing, including the time-series inversion approach (NSBAS) and ESD technique, which I apply to the along-track measurement in this thesis. I review an elastic-half space model for interseismic deformation and also a Bayesian approach used to extract further tectonic information from the measurements.

2.1 InSAR principle

Interferometric Synthetic Aperture Radar (InSAR) is principally identified as the technique that interferes two SAR images together. A SAR image is a radar image, but it is taken with the particular concept of Synthetic Aperture to achieve higher resolution. Although airborne (e.g., UAVSAR (Rosen et al., 2006)) and ground-based SAR (Monserrat et al. (2014) and Tarchi et al. (2003)) also exist for ground deformation studies, the SAR images that are employed broadly nowadays are SAR satellite images. Most of the SAR satellites are in near-polar orbits and repeat-pass missions on consistent ground tracks, orbiting in well constrained and actively managed orbital tubes. The sensors on the platforms transmit and receive radar signals with a side-looking geometry, and consequently the relative down and east-west look direction of the sensors. A number of bands with wavelengths ranging from several mm to a meter are operated with a variety of missions nowadays, for example, X band: Terrasar-X, C band: ERS1/2, Envisat, Radarsat, Sentinel-1, L band: JERS-1, ALOS1/2 (Table 2.1). The longer wavelength has a higher potential of penetration, but the phase is more dispersive in the ionospheric layer (Belcher, 2008). In the standard format, every pixel in SAR images contains amplitude and phase information, which is in complex number form (i.e., Single Look Complex, SLC). The amplitude, which represents the target's return intensity, can provide scattering properties of the objects localized in the pixel. The ob-

Table 2.1: Examples of SAR satellite with their properties

Satellite	Band	Wavelength (cm)	Frequency (GHz)
TerraSAR-X	X	3.09	9.7
ERS	C	5.66	5.3
RADARSAT-1	C	5.63	5.3
ENVISAT	C	5.60	5.3
Sentinel-1	C	5.55	5.4
ALOS1/2	L	23.62	1.3

served phase is a measurement of the distance between the sensor and ground; however, it is modulo by 2π, meaning that the phase varies from $-\pi$ to π. Thus, this wrapped phase does not represent the full range between the satellite and ground. A typical satellite altitude of 700 km gives a mid-range distance from the satellite to ground of 900 km, many integer multiples of the wavelength. Therefore, random fractional phases in a single SAR image cannot provide any information.

However, suppose there is another SAR image acquired over the same area either at different positions or at different times. In that case, interfering two SAR images can retrieve a phase difference between the first and second acquisitions. There are two main objectives expected from these phase differences. In the first case, the sensor acquires images at different positions. This component is proposed to be sensitive to the ground height, which can be developed to provide the Digital Elevation Model (DEM). This topographic phase was an initial early objective of InSAR processing, but the primary purpose of the InSAR phase has now been changed to extract a present-day surface deformation, the objective of the second case that interferes SAR images from a different time. A ground displacement during the time between two acquisitions can also cause a time delay, and consequently the phase difference between the first and second acquisitions. Due to a measurement of wavelength fraction, the displacement from InSAR observation has the potential to achieve centimetre to millimetre level precision. Furthermore, every pixel in the interferometric image can provide phase information, so the InSAR result has a very high spatial resolution even in remote areas. For example, the ScanSAR mode, which is the recent mode that can acquire extensive coverage in one track, of ALOS-2 operates at a spatial resolution of 100 m with 350-km wide coverage. TOPS images from Sentinel-1 with 250-km range extents provide pixel spacing at 2.3x14.1 m in range and azimuth, respectively. These are the reasons why the InSAR technique has contributed a significant part in studying the geophysical processes of surface deformation for the past couple of decades.

For an ideal InSAR deformation study, the sensor should acquire images at the same position to avoid the other components apart from the displacement contributing to the phase changes. Even though satellite orbital control in recent SAR systems has

been highly improved, for example, the orbital tube of Sentinel-1 being controlled by ESA, which aims for a baseline separation of about ±100 m, the satellite still acquires images at slightly different positions and geometries. Consequently, before generating the interferometric phase, one of the SAR images (i.e., secondary images) is needed to be coregistered and resampled to the other image (i.e., primary image) to align these two SAR images in the same geometrical framework. Initially, precise orbit information (ephemeris) and a DEM are used to calculate the position and geometry of images to apply a coarse coregistration. In particular, for Sentinel-1 processing, the Precise Orbit Ephemerides, an expected accuracy of Sentinel-1 orbit information at 5 cm (Fernández, 2011) (source: ESA, https://qc.sentinel1.eo.esa.int/aux_poeorb/), and the elevation from Shuttle Radar Topography Mission (SRTM), which can averagely provide a spatial resolution at 30 m, usually are implemented.

After performing this geometric coregistration, a slight shift between the primary and secondary images due to the limitation of orbit information accuracy and a displacement still exists. The level of the coregistration error at this step is as low as a fraction of pixel and can cause only phase noise in the interferogram image of Stripmap mode. Further processing with the cross-correlation technique can reduce the error and reach the requirement of Stripmap mode (i.e., ±0.125 pixels (Prats-Iraola et al., 2012)). However, this error will cause a critical effect if the SAR images are acquired with the ScanSAR or TOPS mode, operated by recent SAR missions (e.g., ALOS2 and Sentinel-1). The observational component of this mode is nonstationary, but it is rotated along the flight path. The products of theses two modes normally are multiple series of small images with varied squint angles. Therefore, the analysis requires higher accurate coregistration to achieve a final mosaiced image without phase ramp and discontinuity. Thankfully, the enhanced spectral diversity (ESD) (Scheiber and Moreira, 2000), (Prats-Iraola et al., 2012) has been proposed and enabled the system, such as the Sentinel-1 image. Basically, the technique applies different band interferometric images and interferes them together to estimate the small shift based on the spectral properties. This technique has proven to give much higher precision than the cross-correlation technique so that it can provide higher accuracy for the coregistration, satisfying the requirement (i.e., the precision of thousandth of a pixel, 0.001 pixels). Further detail of the ESD for Sentinel-1 image will be found in Chapter 2.3 and Chapter 3.3.

After two SAR images are in the same alignment, the interfering can be performed to generate an interferogram image by complex conjugate multiplication. Since the sensor acquires images with a non-zero baseline, the objects in the pixels are imaged by different geometry looking. This causes two components to arise in the interferometric phase. One of the components is the flat-earth phase, a result of the curvature of the earth. The second component is the topographic phase, which results from the height of the surface. These two terms can be estimated from the positions of the satellite

and external Digital elevation model (DEM) and, consequently, can be removed from the interferometric phase.

The workflow mentioned above is mostly generic steps of recent InSAR processing for deformation studies. All terms are correlated with the range, which physically depends on the geometry of the sensor and ground surface. In an ideal case, only the surface displacement in the line-of-sight direction (D_{LOS}) should induce the interferometric phase ($\triangle\phi_{InSAR}$) at this step using Eq. 2.1. However, in practice, apart from ground displacement signal ($\triangle\phi_{def}$), the interferometric phase is combined with several other nuisance terms (i.e., DEM error ($\triangle\phi_{DEM}$), orbital error ($\triangle\phi_{orb}$), tropospheric phase delay ($\triangle\phi_{trop}$), ionospheric phase advance ($\triangle\phi_{ion}$), and noise ($\triangle\phi_n$)). Nowadays, the methods to estimate or mitigate these terms are diverse and vary by different factors.

$$D_{LOS} = -\frac{\lambda}{4\pi}\triangle\phi_{InSAR} \tag{2.1}$$

$$\triangle\phi_{InSAR} = \triangle\phi_{def} + \triangle\phi_{DEM} + \triangle\phi_{orb} + \triangle\phi_{trop} + \triangle\phi_{ion} + \triangle\phi_n \tag{2.2}$$

Two of the error terms, DEM error ($\triangle\phi_{DEM}$) and orbital error ($\triangle\phi_{orb}$), are the results of removing the topographic and flattening phase. The inaccuracy in external DEM data causes the phase residual in topographic phase estimation, and the limitation of orbit information accuracy leads to a miscalculation of the sensor geometries. However, these two components should not dominate the other terms. The DEM error does not have a significant effect when it is converted to the residual topographic phase. Meanwhile, new SAR systems have succeeded in precise orbit information, which is as high as only a few centimetres (e.g., 5 cm for Sentinel-1). These two terms are unable to improve significantly by post-processing of the individual interferograms themselves. However, the time-series processing, which will be explained further below, uses a stack of SAR images to estimate the average displacement in one specific period and can decrease these two error terms.

The most significant term that biases the interferometric phase is the tropospheric signal ($\triangle\phi_{trop}$). Due to differences in atmospheric conditions at the time of primary and secondary acquisitions, transmitted signals have a different time delay, which results in an additional phase in the interferometric phase. The component due to the Zenith Hydrostatic Delay (ZHD) is large (i.e., ∼3.5 m (Doin et al., 2009)), scaling with the pressure of the atmosphere. Still, its impact on relative InSAR measurement is assumed to be less because the differences between two days result in dry delays that are long-wavelength signals. However, it is mostly water vapor in the troposphere that affects the interferometric observation and can contribute significant noise of 10s cm

at shorter wavelengths. This bias term has a temporal correlation, but the scale is too small, even with the 6-day revisit period of Sentinel-1. The delay also has a spatial correlation, which is inversely related to the distance. The typical correlation distance can vary from 10-100 km, which is difficult to predict. Furthermore, the area with a high variation of topography usually has a strong effect because the atmospheric phase delay highly correlates with the surface height, an effect which is commonly called stratified troposphere.

The mitigation of atmospheric phase delay for a single interferogram can be divided into two categories. The first category uses the phase itself to estimate the bias, such as linear correlation with topography and power-law estimation (Bekaert et al., 2015). The second category, which is widely used nowadays, applies external data (i.e., weather model and DEM) to determine the phase bias. For example, European Centre for Medium-Range Weather Forecasts (ECMWF) provides numerical weather information globally with the highest spatial and temporal resolution at 9 km and 6 hours, which could be incorporated with the InSAR technique. However, if a stack of the interferograms is available, the time-series processing can also mitigate the bias. The displacement correlates in time, but the atmospheric delay does not. This means that temporal averaging displacement can filter out the atmospheric delay. The weather model or even atmospheric phase correction for InSAR data (Yu et al., 2018) are almost available globally and tend to gain higher resolution and more accuracy. Consequently, more recent InSAR studies usually perform time-series analysis with the correction from external data together as routine.

2.1.1 Ionospheric signal

Apart from the tropospheric delay, the upper atmosphere, an ionospheric layer (above ∼70 km), can also cause another bias to the interferometric phase. In contrast, the ionized portion in the ionosphere contributes phase advances to the microwave rather than delay. Similar to the tropospheric delay, the factor that generates a bias to the interferometric phase is the variation of the different ionospheric conditions between primary and secondary acquisitions. Eq. 2.3 presents a relationship between the interferometric ionospheric phase ($\triangle\phi_{ion}$) and a difference of TEC (Total Electron Content) ($\triangle TEC$), representing a density of electron that radars travel through in the ionospheric layer

$$\triangle\phi_{ion} = \frac{-4\pi K}{cf_0}\triangle TEC \tag{2.3}$$

where c is the speed of light, f_0 is a carrier frequency, and constant K is 40.28 $m^3.s^{-2}$. Thus, the magnitude of the phase bias grows with the inverse of the carrier frequency (Meyer et al., 2006). Therefore, this ionospheric bias is a significant nuisance in low-frequency SAR images (e.g., L-band), which could be strong enough to dominate the

other terms. On the other hand, the bias is expected to have a slight effect on high-frequency images (e.g., C-band and X-band). However, Gomba et al. (2017) presented an interferogram, which covers the 2016 Taiwan earthquake, from the C-band Sentinel-1 image. This extreme case was covered with ionospheric variation about 50 cm within a range of 300 km south to north. Also, an example potentially influenced by the ionospheric signal in this work is shown in Fig. 2.1.

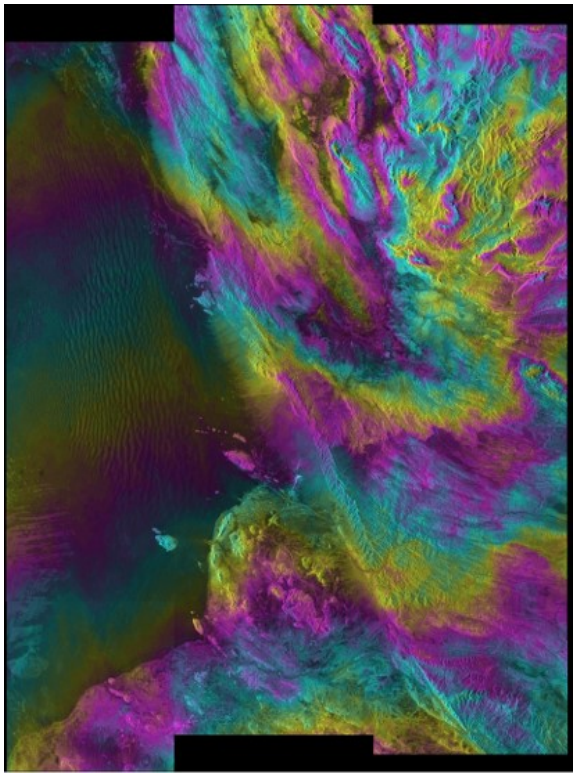

Figure 2.1: An example of interferogram potentially influenced by the ionospheric signal. The wrapped interferogram is generated from C-band Sentinel-1 images. 1-fringe cycle corresponds to 5.5 cm. The SAR images were acquired in ascending constellation around mid-latitude (∼30°N) in Afghanistan. Image ground width and length is ∼250 km.

Since the ionospheric effect is typically considered homogenous over the scale of 100 km approximately (Brcic et al., 2011), the effect could be identified as a long-wavelength signal or presented as a phase ramp over the image. Consequently, deramping is usually applied as it is the simplest and quickest way. However, this could remove the real tectonic signal associated with long-wavelength deformation, particularly the interseismic signal, of a few mm/yr over 100s km. Consequently, the general workflow of InSAR processing for every frequency should also incorporate an explicitly ionospheric correction. And the correction should be performed with more robust techniques, such as the split-spectrum in range (Gomba et al., 2017), which should probably aim for the global InSAR measurement. It not only benefits the standard line of sight InSAR, but it would also be significantly useful for the along-track displacement map. The ionospheric signal, which will be explained in Chapter 3, is a significant component in

the burst overlap InSAR technique.

2.1.2 Decorrelation noise

All nuisance terms mentioned above affect the accuracy of the interferometric phase, but the last term, the decorrelation noise, influences the result's precision instead. The magnitude of noise depends on the correlation of elements in the resolution cell between primary and secondary images. Ideally, if the scattering properties of every component in the pixel are absolutely consistent between two images, this decorrelation term is negligible. In practice, the sensor acquires two images with different position and look angle, so different incident angle causes the scattering properties to change. Thus, the influence increases by the perpendicular baseline, a distance between two positions of acquiring images. However, the geometric decorrelation is no longer a significant factor in the continued SAR systems with great constellation maintenance of orbits. On the other hand, temporal decorrelation is still crucial in recent InSAR processing, especially geophysical monitoring studies, which usually need to extract the small tectonic signal across a timespan of years. The temporal changes of elements between two acquisitions cause the difference in scattering properties in the resolution cell, such as vegetation growth, soil moisture, and snow. The decorrelation usually decays with time and with different patterns depending on the land cover type. Consequently, the type of land could be an initial factor in planning InSAR processing. For example, vegetated areas are much more difficult to process because they result in higher noise than dry and urban regions. Consequently, the areas, which are densely vegetated, usually lack InSAR studies of long-term deformation studies and are more restricted to short-period observations such as earthquake studies using L-band data.

Coherence (γ) is an index, which varies from 0 to 1, to represent pixel correlation. Coherence at 0 means that the pixel loses all phase information, whereas coherence at 1 is an ideal correlated case. The calculation of coherence is shown in Eq. 2.4. (Touzi et al., 1999) and depends on the similarity of the arbitrary pixel with its surrounding pixels. The regular operation is a two-dimensional boxcar method. N is a number of points in the specific window, whereas M and S represent phases of primary and secondary images, respectively. The bar indicates the complex conjugate. Since the noise characteristic is a gaussian distribution, one of the methods to reduce the noise is spatial averaging. Under the critical assumption that interferometric phases are consistent over a specific area, taking an average phase from local pixels can reduce the noise. This step, which is called Multilooking, operates with a complex number. The multilooked phase (ϕ) and the standard deviation (σ_ϕ) expected from the operation are presented in Eq. 2.5 and Eq. 2.6, respectively (Hanssen, 2001). The number of pixels (N), the number of looks, is the main parameter to reduce the noise. Since the spatial variation over the averaging area is lost, a tradeoff between the resolution

and noise level must be considered carefully. Especially in an area with high phase variation, multilooking may average phases over a fringe, wrapped phase cycle, and the multilooked phase is no longer consistent with the assumption.

$$\gamma = \frac{\left| \frac{1}{N} \sum_{i=1}^{N} M_i \cdot \bar{S}_i \right|}{\sqrt{\frac{1}{N}(\sum_{i=1}^{N} M_i \cdot \bar{M}_i \sum_{i=0}^{N} S_i \cdot \bar{S}_i)}} \tag{2.4}$$

$$\phi = \arctan\left(\frac{Im \sum_{i=1}^{N} M_i \cdot \bar{S}_i}{Re \sum_{i=1}^{N} M_i \cdot \bar{S}_i} \right) \tag{2.5}$$

$$\sigma_{\phi}^{2} = \frac{1 - |\gamma|^{2}}{2\,|\gamma|^{2}} \tag{2.6}$$

Again, if a stack of SAR images is available, time-series processing can avoid the limitation from decorrelation noise and consequently enhance the small surface displacement signal over the years timespans. The processing can be divided into two main categories. The first category is the Persistent Scatter method (e.g., Ferretti et al. (2001), Hooper (2006)). The principal concept of the technique is to find persistent scatter (PS) pixels. The PS pixel is the resolution cell for which one element dominates the back-scatter phase. The phase distribution of the PS pixel has been proven to be nearly stable and can provide phase information over time. In practice, the technique pairs all images to one common primary images, selecting the PS pixels by using amplitude or phase analysis, and then focusing on only the selected pixels.

The second cluster, which can take advantage of the recent InSAR missions, is small baseline processing (e.g., Berardino et al. (2002)). One SAR image pairs with multiple acquisitions in the stack with a focus on minimizing the perpendicular baseline separation of selected pairings. This is due to the sources of decorrelation, so the technique only generates interferograms with short temporal and spatial baselines to keep the correlation as high as possible. Each interferogram normally is multilooked to decrease the noise and data loading before time-series estimation. The small baseline technique is becoming a routine method nowadays since the new SAR systems can provide the data with a very short temporal baseline. Recently, there are new strategies (e.g., SqueeSAR (Ferretti et al., 2011)) that try to take advantage of all possible pairs of interferograms. The technique is a kind of extension from the small baseline technique. The method considers the points that have long time decay and take benefits from points that have a seasonal pattern or permanent scatter. The small baseline is principally a subset of this methodology. However, the time-series approach applied in this work is NSBAS (López-Quiroz et al., 2009), another extension of the small baseline approach. The regular analysis converts the observed small baseline phase to optimal

increment phases using the least-square method, Singular Value Decomposition (SVD) inversion. In some instances, a small baseline network has a gap, which means isolated clusters of interferograms, which normally due to a rejection of post-processing based on their criteria, such as an unwrapping problem, decorrelation noise, or absence of SAR operation itself resulting in a gap of data. Therefore, an additional constraint, which is deduced by the assumption of time-dependent deformation, is incorporated into the inversion. Specifically, this work has assumed and applied a linear displacement to the minimum constraint.

As mentioned above, the interferometric phase is the measurement of wavelength fraction, so the interferometric phase is a wrapped phase, which varies between -π to π. The ambiguity band is bounded by wavelength, such as ∼3.1 cm (X-band), ∼5.6 cm (C-band), ∼23.5 cm (L-band). Since the total number of ambiguities is not possible to realize, the InSAR observation can only retrieve relative displacement to reference point in the scene. The phase unwrapping relies on the assumption that the displacement phase between adjacent pixels does not exceed half of the ambiguity band. The processing cumulates the differential phase between all neighbouring pixels to gain relative displacement over the scene. Examples of unwrapping routines that are widely implemented are the minimum cost function (MCF) (Costantini and Rosen, 1999) and SNAPHU (Chen and Zebker, 2002). However, if the phase difference between the adjacent pixels is larger than $\pm\pi$ or phase noise is too large, unwrapping errors will occur.

2.2 Workflow of LiCSAR and LiCSBAS

The procedure of generating velocity maps from stacks of SLC SAR images in this thesis is mainly based on LiCSAR (Lazecky et al., 2020) and LiCSBAS (Morishita et al., 2020) packages. They both are open sources developed by COMET to generate InSAR Sentinel-1's products (e.g., velocity map) with an ability to be performed for large-scale studies. LiCSAR is the primary tool to produce a large stack of unwrapped interferograms, usually now higher than 100s images for an area with six years of the Sentinel-1 data archive. The process starts coregistrating all secondary SLC images into the same alignment as the primary SLC image. Due to a varied squint angle in acquiring TOPS mode images, after applying geometric coregistration with precise orbit and DEM information, the coregistration needs a refining step to avoid an error (i.e., phase ramp and burst discontinuity) due to the azimuth shift. Applying Enhanced Spectral Diversity (ESD) alone can already satisfy the required accuracy with a precision of 0.001 pixels, but the algorithm performs the estimation of intensity cross-correlation first due to an ambiguity technique of ESD.

After all images are in the same geometry framework, I generate a stack of interfero-

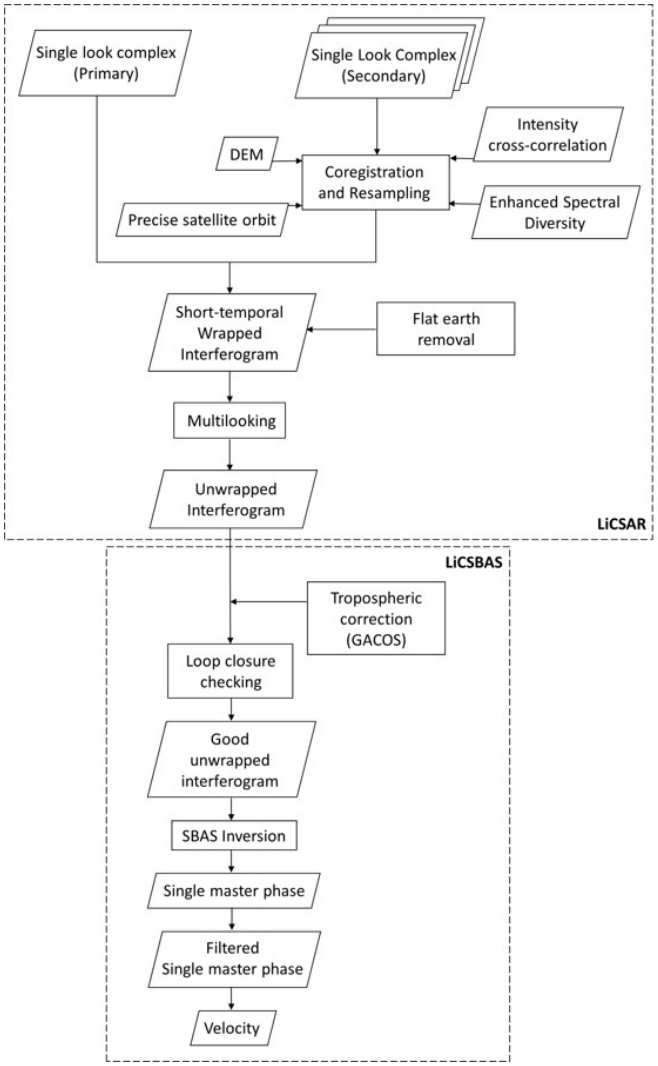

Figure 2.2: Workflow of LiCSAR (Lazecky et al., 2020) and LiCSBAS (Morishita et al., 2020) packages.

grams following the Small Baseline style with five consecutive acquisitions. One image pairs with five consecutive epochs, including acquisition before and after the epoch. The flat earth phase estimated from Shuttle Radar Topography Mission (SRTM) DEM is also removed during the interferogram generation. It should be noted that the criteria of generating interferograms still adhere to the principle of the typical small baseline analysis, which focuses on maintaining an interferometric coherence by limiting only short temporal baseline interferograms. However, according to a recent study (Ansari et al., 2020), the number of interferogram pairs and average temporal baseline in a time series should be increased to avoid systematic phase inconsistencies described in the study. The bias is defined as a short-lived or fading signal, which has a significant impact on the short temporal baseline interferogram. However, since a considerable parameter causing this effect is a variation in the moisture content (Ansari et al., 2021),

the bias probably has less impact on the two study areas in this thesis. Areas of the West-Lut fault in Iran and the Chaman fault in Afghanistan are devoid of vegetation and have relatively low rainfall rates and variations. Most of the areas are bare areas, desert, and dry. Quantitative research is still required; for example, figure 11 in Ansari et al. (2020) presents a comparison between the bias and land cover. The effect in a dry area is likely to be small relative to the other land cover type. After generating all interferograms in the network, I multilook wrapped interferograms with 5 looks in azimuth and 20 looks in range, which give approximately 70 m x 50 m for the spatial resolution. Then, I unwrap all interferograms using a statistical cost approach with the SNAPHU software. (Hooper (2010) and Chen and Zebker (2002)).

Then, LiCSBAS, an automated tool to generate InSAR time-series products and inherently suited with LiCSAR outcomes, corrects the tropospheric phase derived from the GACOS model (Yu et al., 2018), which is mainly based on the HRES-ECMWF weather model. LiCSBAS applies loop closure checking (Hussain et al., 2016) to identify an unwrapping error. The judgment is based on the assumption that the summation of the InSAR unwrapped phases from a set of interferograms that can form a closed polygon should be close to zero if there is no unwrapping occur. The algorithm will reject the interferogram with the unwrapping error. Then, LiCSBAS performs an inversion with an NSBAS approach (López-Quiroz et al. (2009), Doin et al. (2011)) to retrieve optimal single master phases. The NSBAS method, like the classic SBAS technique (Berardino et al., 2002), has the advantage of allowing for gaps in interferogram networks. The NSBAS technique, on the other hand, bridges this gap between isolated clusters of interferograms by including a constraint in the inversion instead of applying singular value decomposition (SVD) (Berardino et al., 2002). Using the SVD method will result in a zero InSAR incremental phase at the data gap and consequently cause a bias in the time-series estimation (López-Quiroz et al., 2009). On the other hand, the NSBAS approach uses information deduced from the other interferograms in the time series and a predefined displacement model to connect these separated image datasets.

The NSBAS method assigns a small weight to the constrained part in the inversion; therefore, its significance is trivial when the connected network is applied. The analysis solves increments of phase difference and then estimates average velocity from cumulative displacements derived from the incremental phases. The temporal information from time-series products with a high temporal sampling rate from Sentinel-1 can significantly contribute to geophysical process studies, particularly in the time domain. This thesis applies the NSBAS approach to derive the time-series InSAR phase difference for across- and also along-track measurements. I define a linear displacement as an additional constraint, which is written in the matrix form of linear inversion system

$(d = Gm)$ as

$$\begin{bmatrix} \phi_{12} \\ \phi_{13} \\ \phi_{14} \\ \phi_{15} \\ \phi_{23} \\ . \\ . \\ \phi_{n-1,n} \\ 0 \\ 0 \\ . \\ . \\ . \\ . \\ 0 \end{bmatrix} = \begin{bmatrix} \begin{bmatrix} 1 & 0 & 0 & . & . & . & . & | & 0 & 0 \\ 1 & 1 & 0 & . & . & . & . & | & 0 & 0 \\ 1 & 1 & 1 & . & . & . & . & | & 0 & 0 \\ 1 & 1 & 1 & 1 & . & . & . & | & . & . \\ 0 & 1 & 0 & 0 & . & . & . & | & . & . \\ . & . & . & . & . & . & . & | & . & . \\ . & . & . & . & . & 1 & 1 & | & . & . \\ . & . & . & . & . & 0 & 1 & | & 0 & 0 \end{bmatrix} \\ \gamma. \begin{bmatrix} 1 & 0 & 0 & 0 & . & . & 0 & | & -t_{1,2} & -1 \\ 1 & 1 & 0 & 0 & . & . & 0 & | & -t_{1,3} & -1 \\ 1 & 1 & 1 & 0 & . & . & 0 & | & -t_{1,4} & -1 \\ 1 & 1 & 1 & 1 & . & . & 0 & | & . & . \\ . & . & . & . & . & . & 0 & | & . & . \\ . & . & . & . & . & . & 0 & | & . & . \\ 1 & 1 & 1 & 1 & 1 & 1 & 1 & | & -t_{1,a} & -1 \end{bmatrix} \end{bmatrix} \begin{bmatrix} \hat{\phi}_{12} \\ \hat{\phi}_{23} \\ \hat{\phi}_{34} \\ \hat{\phi}_{45} \\ . \\ . \\ . \\ \hat{\phi}_{a-1,a} \\ v \\ c \end{bmatrix} \tag{2.7}$$

The constraint part (the lower portion in the G matrix) introduces the linear characteristic for the displacement. v and c are a velocity and a constant offset respectively in a linear model, estimated from cumulative displacements at time t. m and d are sets of model parameters and observations, respectively. The technique identifies a minimal weight in the co-variance matrix (γ) to this constrain part, for example, a thousandth of the measurement part. Therefore, this additional assumption will influence the estimation only when there is a data gap in the small baseline network. After retrieving the incremental phase, LiCSBAS applies 72-day temporal filtering with the single master phases and estimates averaged velocities.

2.3 Sentinel-1 TOPS mode with Enhanced Spectral Diversity (ESD)

The Sentinel-1 image, acquired with the characteristics of TOPS mode (Fig. 1.2), requires an extra step in the coregistration of the regular InSAR processing. Due to the high squint angle of the sensor's illumination direction, the look angle and the central Doppler frequency change abruptly around the overlap area (especially the pixels in the burst overlap region that are illuminated twice with the largest separation). The abrupt change can cause discontinuities between the bursts if misregistration greater than 0.001 pixels remains. Scheiber and Moreira (2000) reported that a constant time shift from misregistration adds a phase bias to the interferometric phase under the presence of a Doppler centroid. The error expectedly appears as a phase ramp over

the burst. Since the Doppler frequency varies in the azimuth direction, points are focused by different centre frequencies. Consequently, the points have different phase slopes. The shift causes a slight offset in the frequency domain between primary and secondary images, so the difference linear phase term still remains. They presented that the magnitude of phase bias (ϕ_{err}) depends on the doppler frequency.

$$\phi_{err} = 2\pi f_c \triangle t \tag{2.8}$$

Even though the time shift ($\triangle t$) is constant, the Doppler frequency (f_c) varies in the azimuth direction continuously. This makes the phase arise in the way of ramping over the burst in the azimuth direction. Therefore, the TOPS SAR images from Sentinel-1 require a shift estimation with an accuracy higher than 0.001 pixels to avoid this misregistration ramp.

Prats-Iraola et al. (2012) presented that the geometry coregistration, cross-correlation, and simple Spectral Diversity (Scheiber and Moreira, 2000) cannot satisfy the co-registration requirement for the TOPS images. The Spectral Diversity technique (Scheiber and Moreira, 2000) splits the original image (full bandwidth) into two sub-bands with different spectral looks. The method uses a double difference phase from two looks of primary and secondary images to identify the shift with high sensitivity. Furthermore, Prats-Iraola et al. (2012) proposed the Enhanced Spectral Diversity, based on the standard Spectral Diversity, but they use the natural full band images of backward and forward-looking in the burst overlap area instead of the synthetic sub-band. In contrast to split-bandwidth spectral diversity, the full bandwidth can be utilised, so noise levels remain the same as in the original interferogram. Moreover, due to the larger separation of Doppler frequency than the synthetic data, this high precision can be used to coregister more accurately than ever. The relationship between the double-difference phase ($\triangle\phi_{ovl}$) and the azimuth shift ($\triangle x_{az}$) are presented in Eq. 2.9

$$\triangle\phi_{ovl} = 2\pi\triangle f_{ovl}\triangle t_{az} = 2\pi\triangle f_{ovl}\frac{\triangle x_{az}}{\triangle x_s}(\triangle t_s) \tag{2.9}$$

$$\sigma_{ovl} = \frac{1}{2\pi\triangle f_{ovl}}\frac{1}{\sqrt{N}}\frac{\sqrt{1-\gamma^2}}{\gamma}\frac{1}{\triangle t_s} \tag{2.10}$$

where $\triangle f_{ovl}$ is the Doppler frequency difference, $\triangle t_{az}$ is a misregistration shift in time axis, $\triangle x_s$ is the azimuth pixel size (13.99 m), $\triangle t_s$ is the azimuth sampling (0.0020555s) per pixel. The theoretical uncertainty in the shift estimation (σ_{ovl}) is shown in Eq. 2.10, where N is a number of the sample averaged, γ is coherence. The conventional InSAR processing applies the ESD estimation to eliminate the misregistration offset between the primary and secondary images in resampling step. In addition, Fig. 2.4 presents

Table 2.2: Sentinel-1 TOPS Properties Described for Each Sub-Swath in IW mode (applied from Spaans (2016) and Grandin et al. (2016))

Sub-Swath	IW1	IW2	IW3
Steering squint angle (°)	±0.64	±0.47	±0.57
Doppler frequency difference (Hz)	4801	4035	4256
Ambiguity band (mm)	±710	±850	±800
Azimuth sampling (s)		0.0020555	
Azimuth pixel size (m)		13.99	
Orbit inclination (°)		98.2	
Ascending/Descending Heading (at equator)		N12W / N168W	

precision of the measurement with different numbers of looks (N), including the number I used in the following chapters for the burst overlap InSAR analysis.

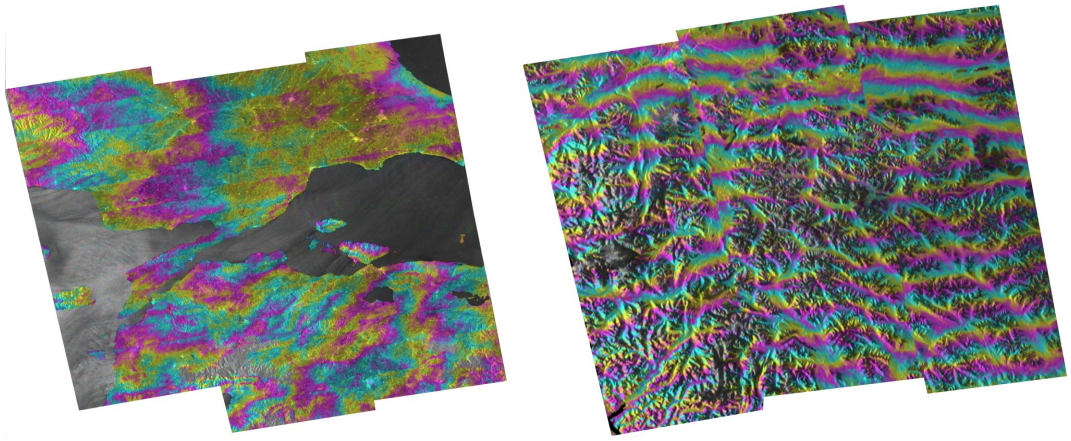

Figure 2.3: Examples of burst discontinuities due to the coregistraion error. The errors in the ESD estimation are probably result from strong variation of ionospheric signal and decorrelation noise.

2.4 An Elastic half-space model for interseismic deformation

In this thesis, I model surface deformation, InSAR measurements, associated with interseismic phase based on an elastic half-space model (Savage and Burford, 1973) of a vertical strike-slip fault. In the interseismic period, the upper part of the crust is locked while the lower crust and mantle still move by the plate tectonic movement. This causes crustal deformation and a strain accumulation at fault.

$$v(x) = \frac{s}{\pi} \arctan\left(\frac{x - f_i}{d}\right) + a \tag{2.11}$$

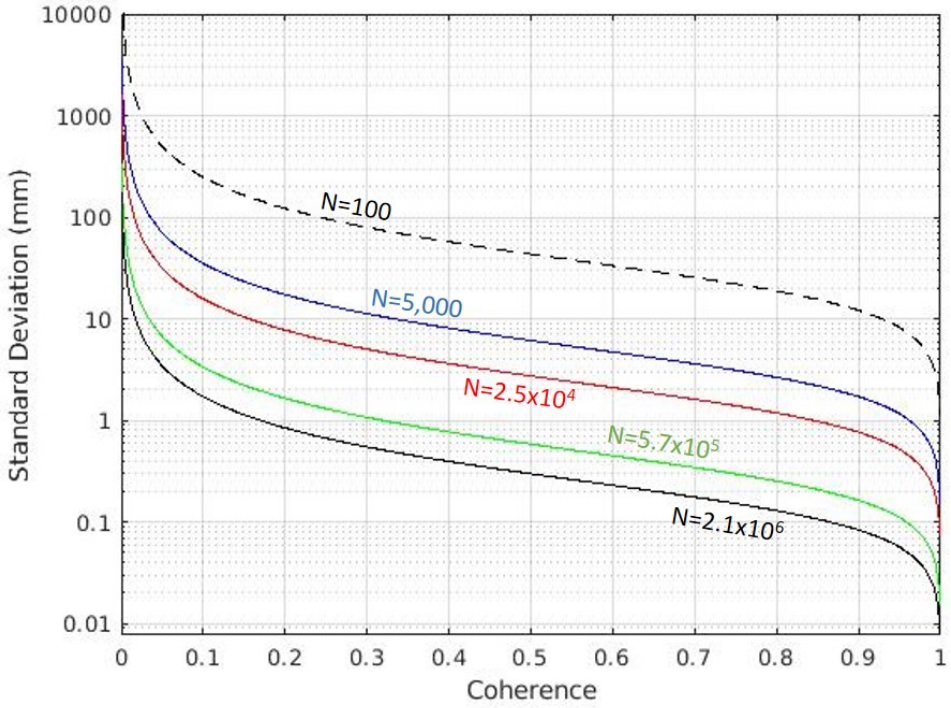

Figure 2.4: Standard deviation of the along-track measurement. The estimation is determined with coherence and the number of averaged pixels (N) Eq. 2.10. The black line is the precision when all pixels in burst overlap are averaged. The green line (570,000 pixels) and the red line (25,000 pixels) are the numbers of looks applied in Chapter 3 and Chapter 4, respectively.

Eq. 2.11 represents the responding of the surface movement, which we can observe, to the deforming process beneath the ground. The relationship is a 1D model, a function of fault-perpendicular distance from the fault trace (x) and the ground velocity (v). Due to a lock at fault, the ground surface deforms in an arctangent curve, where the velocity gradient, focused strain, localizes around the fault trace. In practice, we apply the arctangent shape, drawn from what we observe on the ground (i.e., x and v), to deduce the fault's parameters (i.e., depth of the locked part beneath the ground (d), deep fault slip rate across the fault (s), and offset (f) of the position of the shear zone at depth relative to the surface fault trace defining the profile zero location in x). The variable a is a relative offset nuisance parameter to account for the non-absolute measurement from InSAR observations and needs for an arbitrary reference point.

In some areas (e.g., Chaman fault (Fattahi and Amelung, 2016)), the fault does not accommodate strain across a fully locked depth interval from the locking depth to the surface. A shallow creep responds to a part of the strain as an aseismic slip. The dislocation occurs from the surface and extends to some depth, which is shallower than the locking depth (d). Thus, discontinuities can be observed at the fault trace in the InSAR velocities from this relative short-wavelength surface displacement. Therefore,

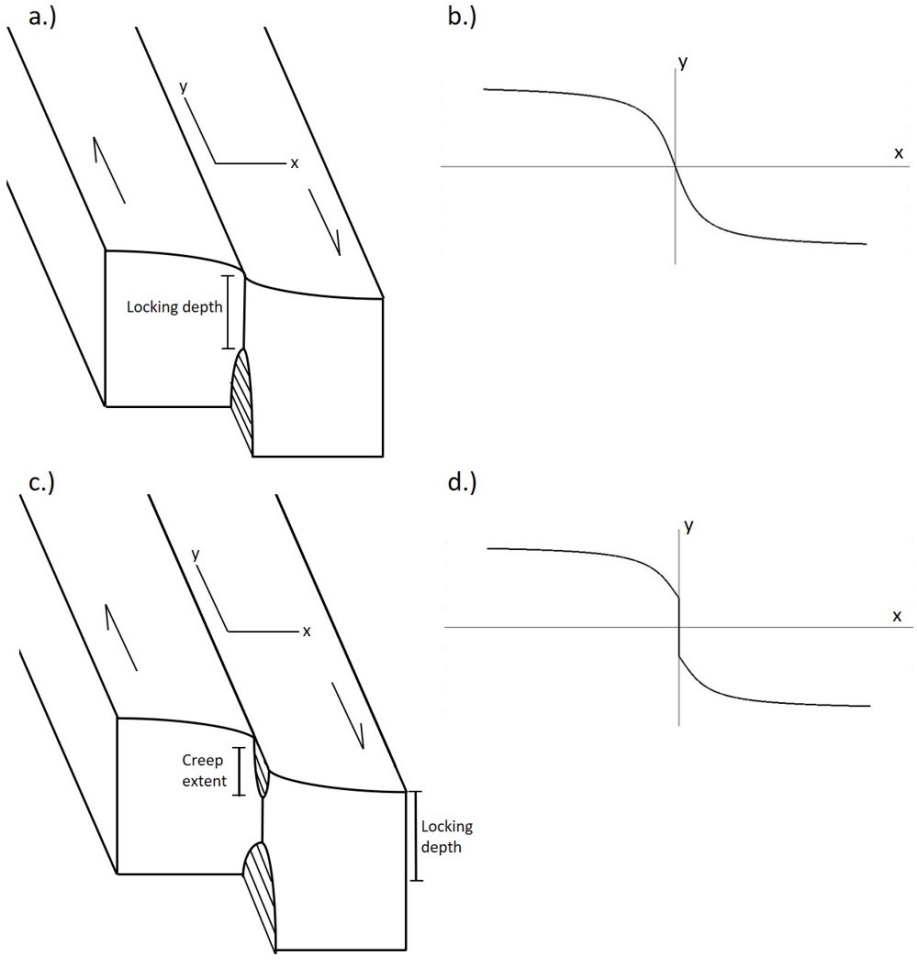

Figure 2.5: a.) Model of interseismic deformation across a strike-slip fault after (Savage and Burford, 1973) b.) Map view of a surface deformation that can be detected by InSAR observation. The displacement or velocity in a fault-parallel component has a smoothed arctangent curve. c.) Model of interseismic deformation across a strike-slip fault with a shallow creep d.) Map view of a surface deformation, which is a combination of arctangent shape and a displacement offset due to a surface creep

to model profile velocity with surface creep, I follow Fattahi and Amelung (2016), which applied InSAR observations to study fault creep along the Chaman fault, to represent a combination of long-wavelength interseismic deformation and a dislocation offset at fault (Eq. 2.12). c is a creep rate, and E is a depth of creep extent, i is a fault number. Since the Ghazaband fault is parallel to the Chaman fault with a separation distance of about 40-50 km, the modelling applied in this area needs to incorporate the displacements associated with the two faults together. Then, x distance is a perpendicular distance from the first fault.

$$v_p(x) = \frac{s}{\pi} \arctan\left(\frac{x - f_i}{d}\right) + \frac{c}{\pi} \arctan\left(\frac{E}{x - f_i}\right) + a \tag{2.12}$$

2.5 Bayesian approach (GBIS)

In this thesis, I apply a Bayesian approach for the inversion of InSAR results to infer the posterior probability density functions (PDFs) of fault model parameters of interseismic deformation (Eq. 2.11 and Eq. 2.12). The source parameters will be reviewed with statistical intervals by the posterior distribution and also a set of model parameters with a maximum likelihood. The method considers uncertainties of the observational data and a probability of prior models, which are defined by previous studies that apply geodetic observation with the West-Lut and Chaman faults. Based on the Markov Chain Monte Carlo method (MCMC), the algorithm starts sampling the posterior distribution with a set of model parameters referred from prior information and perform a random walk to define a new accepted set of parameters when the likelihood is higher than the initial value (based on the Metropolis-Hastings algorithm (Hastings (1970), Metropolis et al. (1953)). Furthermore, I apply the iteration of drawing posterior PDF following GBIS (Bagnardi and Hooper, 2018), which proposed an automatic step size selection. This modified method defines an optimal size of values added to each model by considering a time of convergence and avoiding a walk to struggle in a local maximum of likelihood. For each iteration, the algorithm deals with a residual of estimated observations deduced from trial model parameters and observational values. $p(\mathbf{d}|\mathbf{m})$ is a likelihood of model parameters (m) given the observations (d). G is a model function. C is the covariance matrix of the data, and p(m) the prior PDF of the model parameters.

$$p(\mathbf{d}|\mathbf{m}) = \exp\Big[-\frac{1}{2}(\mathbf{d}-\mathbf{G_m})^T\mathbf{C_d^{-1}}(\mathbf{d}-\mathbf{G_m})\Big] \tag{2.13}$$

At the end, samples from a huge number of iterations (500,000 iterations, excluding a burn-in period, in this thesis), clarifying the number by the convergence, can draw a posterior distribution of each fault parameter and also provide the optimal models.

Chapter 3

Ionospheric Mitigation for InSAR Using a Time Series Approach

In this chapter, I present an algorithm for mitigation of ionospheric disturbance, a significant limitation on the accuracy of the burst overlap InSAR technique. The algorithm is an extension of Gomba et al. (2017), which is based on the split-spectrum in range technique. I include a new method to identify unwrapping errors in the ionospheric phase estimation and a fit-plane method for low-pass filtering the ionospheric signal. I demonstrate the algorithm with the C-band Sentinel-1 image acquired over the West-Lut fault area to mitigate the ionospheric noise for both across- and along-track measurements with a time-series approach.

3.1 Introduction

Radar Interferometry (InSAR) has the potential to measure and monitor active tectonic deformation globally (Elliott et al., 2016, and reference therein). However, due to it being a space-based observation, changes to the phase during propagation of the microwave signal through the atmosphere significantly degrade the technique's accuracy (Hanssen, 2001). Methods to estimate or mitigate the phase bias from propagation through the lower layer of the atmosphere (i.e., troposphere) have been intensively proposed (Murray et al., 2019). The weather model or even tropospheric estimated phase for the InSAR correction is freely provided with nearly global coverage (e.g., GACOS Yu et al., 2018) and is upgrading with higher resolution and precision. Consequently, recent InSAR studies usually perform analysis with the tropospheric correction as a routine to improve the quality of the velocity map.

On the other hand, the ionospheric phase contribution, which comes from interaction with electrons in the upper layer of the atmosphere (>70 km), adds to the

ground displacement signal and affects the accuracy of the velocity map. The effect is strongest for low-frequency SAR (e.g., L-band). However, the effect can also be strong at C-band, e.g., Gomba et al. (2017) presents an interferogram covering the 2016 Taiwan earthquake from C-band Sentinel-1, which includes line-of-sight variation due to ionospheric variability of ∼50 cm from south to north. Additionally, since the ionospheric distribution is generally identified as a long-wavelength signal, the effect is frequently eliminated by normal deramping. However, this could lead to removing the long-wavelength tectonic signal. Consequently, ionospheric correction should be included in the general workflow of InSAR processing to improve the quality of the velocity map and to offer more sustainability to the InSAR technique.

Moreover, to image global tectonic strain, the azimuth displacement map is a key to access north-south tectonic deformations, a significant limitation of the InSAR line-of-sight technique. Burst overlap interferometry (Grandin et al., 2016 and Spaans, 2016) has proved an effective method to achieve the along-track displacement with the highest ever precision. However, the ionospheric variation, which is particularly sensitive to the technique, has a strong effect on the accuracy of the method, especially for studies with a long-term small tectonic signal. Consequently, ionospheric correction is essential for the azimuth velocity mapping.

In this chapter, I propose a technique that improves on the split-spectrum in range method (Gomba et al., 2017). Firstly, the technique should include a point selection in the analysis, especially to omit the point with unwrapping error, which is more severe than conventional InSAR due to the technique's high uncertainty. Furthermore, I present that the identification of unwrapping error needs to be performed with an adaptive threshold rather than a fixed criterion, which could disrupt low-pass filtering and consequently bias an estimated ionospheric screen. Secondly, I apply a small baseline approach to estimate time-series ionospheric phase. This reduces noise and better constrains the ionospheric contribution for each acquisition than a single interferogram. Finally, I present a new method for low-pass filtering. Due to the low precision of the technique, filtering with a large window size is required. However, standard gaussian filtering underestimates the ionospheric phase when the filter window falls off the scene edge because the operator accounts for only an average value instead of a trend. Furthermore, this inaccurate estimation can significantly bias the burst overlap InSAR measurement since the ionospheric variation is a major source of the ionospheric shift in the along-track measurement. To deal with this issue, I propose a technique to fit a planar surface to a sub-area of the ionospheric estimation and perform it as a moving window analysis.

In section 3.2, I explain the ionospheric effect on the conventional line-of-sight InSAR technique. Also, I basically describe sources of additional delay to the burst overlap InSAR technique and suggest how the ionospheric effect can impact the result

by different ionospheric conditions. In section 3.3, I explain the processing strategy applied in the processing. Section 3.4 demonstrates the experimental results from the West-Lut fault. The velocity maps from the line-of-sight and along-track direction in this area are biased by the ionospheric signal, even with the C-band time-series analysis. In section 3.5, I give a summary of the correction and the limitation of the technique.

3.2 Ionospheric effect

3.2.1 Conventional InSAR (Across-track measurement)

The disturbance on microwave propagation in the upper atmosphere, above ∼70 km, causes a bias to the interferometric phase. Specifically, the ionized portion in the ionosphere contributes a phase advance to the radar signal. The magnitude of the effect depends on the number of Total Electron Content (TEC) in the slant range that microwaves travel through. The factor that generates a signal to the InSAR measurement is the spatial variation of the TEC difference between primary and secondary acquisitions. Usually, the ionospheric bias has a strong effect in areas around the equator and at high latitudes (Fattahi et al., 2017). Also, the effect on the SAR image acquired in the afternoon of local time, for example, Sentinel-1 ascending image, is more variable than one acquired in the morning or night. The relationship between the ionospheric phase ($\triangle\phi_{ion}$) and the TEC difference ($\triangle TEC$) between two acquisitions can represent as in Eq. 3.1. c is the speed of light, f_0 is a carrier frequency, and constant K is 40.28 $m^3.s^{-2}$.

$$\triangle\phi_{ion} = \frac{-4\pi K}{cf_0}\triangle TEC \tag{3.1}$$

From Eq. 3.1, the relationship shows that the magnitude of phase bias varies inversely with the carrier frequency. As a result, this ionospheric component is a significant nuisance in low-frequency SAR processing (e.g., L-band). On the other hand, the bias is typically expected to be small on high-frequency images (e.g., C-band and X-band). However, the interferogram from C-band Sentinel-1 images (Gomba et al., 2017), which captured the 2016 Taiwan earthquake, was covered by an ionospheric variation of about 50 cm within a range of 300 km from south to north. This demonstrated that a general workflow of InSAR processing for all frequencies should include an ionospheric correction.

Since the ionospheric effect is typically considered homogenous over the scale of 100 km (Brcic et al., 2011), the distribution is considerably smooth. Most of the effect could be identified as a long-wavelength signal, presented as a phase ramp over an image, and the disturbance can be simply eliminated using normal deramping. This operation is probably valid for an application focusing on short-wavelength phenomena

such as land subsidence; however, this may result in the removal of the long-wavelength signal that is associated with tectonic deformation. Several techniques for directly estimating the ionospheric phase have been proposed; however, the most effective and sustainable methodology is probably split-spectrum in range (Gomba et al., 2017). Only the ionospheric phase is dispersive in the interferometric phase, whereas the others (e.g., displacement, tropospheric, and topographic phase) are not. In particular, only the ionospheric contribution varies with frequency. This technique takes advantage of this feature to distinguish the ionospheric bias. The method employs band-pass filtering to generate narrow-band images that are subdivided from full-band SAR images to high-frequency (f_H) and low-frequency (f_L) images. f_0 is a central frequency. $\triangle\phi_L$ and $\triangle\phi_L$ represent the split-band phases. Then, we can calculate the ionospheric phase ($\triangle\phi_{ion}$) using Eq. 3.2.

$$\triangle\phi_{ion} = \frac{f_L f_H}{f_0(f_H^2 - f_L^2)}(\triangle\phi_L f_H - \triangle\phi_H f_L) \tag{3.2}$$

3.2.2 Burst Overlap InSAR (Along-track measurement)

The burst overlap InSAR is the technique to retrieve ground displacements in the along-track direction using Enhanced Spectral Diversity (ESD), applied to the burst overlap area of Sentinel-1 TOPS mode images (Grandin et al. (2016), Spaans (2016), Hooper and Spaans (2017), and Yague-Martinez et al. (2019)). The original objective of ESD is to estimate a misregistration shift, composed of azimuthal ground movement and other terms, to eliminate an offset between primary and secondary images. This technique, on the other hand, focuses on retrieving the azimuth displacement from the ESD estimated shift.

The TOPS mode system scans the surface by acquiring discontinuously multiple small images, called bursts. During image acquisition, the sensor is continuously steered backward to forward in an along-track direction (i.e., flight direction) to illuminate one burst. The system acquires the same small areas between the consecutive bursts to avoid a gap in the final images; therefore, pixels in this overlap area are observed by both backward- and forward-looking geometries. For the extraction, the forward-looking interferogram is subtracted from the backward-looking interferogram to generate the double-difference interferogram. The subtraction removes most of the displacement component in across-track and vertical direction and leaves only the deformation signal in the horizontally along-track direction ideally. The two look measurements observe the pixels in the burst overlap region with different squint angles ranging from 0.94° to 1.28° and different Doppler frequencies around 4200-4800 Hz depending on the sub-swath (Table 4.2), resulting in larger separations than previous techniques (e.g., MAI). Therefore, ESD processing can provide the estimated shift with greater precision

than ever before. Eq. 3.3 express the relationship between the double-difference phase ($\triangle\phi_{ovl}$) and the azimuth shift ($\triangle x_{az}$). $\triangle t_{az}$ is Doppler frequency difference, $\triangle f_{ovl}$ is azimuth time shift, $\triangle x_s$ is the azimuth pixel size, $\triangle t_s$ is the azimuth sampling rate, N is the number of samples averaged, and γ is coherence in the latter.

$$\triangle\phi_{ovl} = 2\pi\triangle f_{ovl}\triangle t_{az} = 2\pi\triangle f_{ovl}\frac{\triangle x_{az}}{\triangle x_s}(\triangle t_s) \tag{3.3}$$

$$\sigma_{ovl} = \frac{1}{2\pi\triangle f_{ovl}}\frac{1}{\sqrt{N}}\frac{\sqrt{1-\gamma^2}}{\gamma}\frac{1}{\triangle t_s} \tag{3.4}$$

However, following the standard line-of-sight InSAR measurement, the estimated shift potentially includes other components, the nuisance terms that can bias the measurement. For the first instances, most of the topographic and flat-earth phases should be cancelled out in the second interfering since the particular pixels in backward- and forward-interferograms are at the same height, position, and distance in range direction. Similarly, a tropospheric phase, a significant component of the standard InSAR processing, affected by mostly water vapor in the tropospheric layer, contributes the phase delay to the observed interferometric phase. Conversely, the bias can be considered nearly negligible in the double-difference phase since the backward- and forward-looking observations have highly temporal and spatial correlations with the tropospheric effect. According to the geometry, the signals of backward- and forward-looking travel through the global mean height of water vapor, ∼1.4 km from the ground, with the largest separation only 30 m within a few seconds in time. These two values are considered in the tropospheric variation scale associated with Kolmogorov turbulence (Hanssen (1998) and Hanssen (2001)).

However, the inconsistency between the accuracy of the burst overlap technique and the expected precision was revealed in (Spaans, 2016) and (Hooper and Spaans, 2017), and was identified as a result of the ionospheric phase advance. As aforementioned, the TOPS mode acquires images in discontinuous bursts rather than continuously scanning like the Stripmap mode. After acquiring the forward-looking image, the satellite moves forward. The sensor acquires images in the other two sub-swaths before returning to take the backward-looking image at different positions. Therefore, the backward- and forward-looking observations have a different path of microwave propagation through the ionosphere. The bias caused by integration through different ionized portions introduces the residual phase into the along-track shift estimation. Thus, the measurement is a mixture of azimuthal displacement and the double-difference ionospheric phase.

Note, the magnitude of the ionospheric phase difference between primary and secondary images does not disrupt the along-track measurement directly. Instead, It is a spatial variation of the differential TEC in the azimuth direction. Fig. 3.1 presents

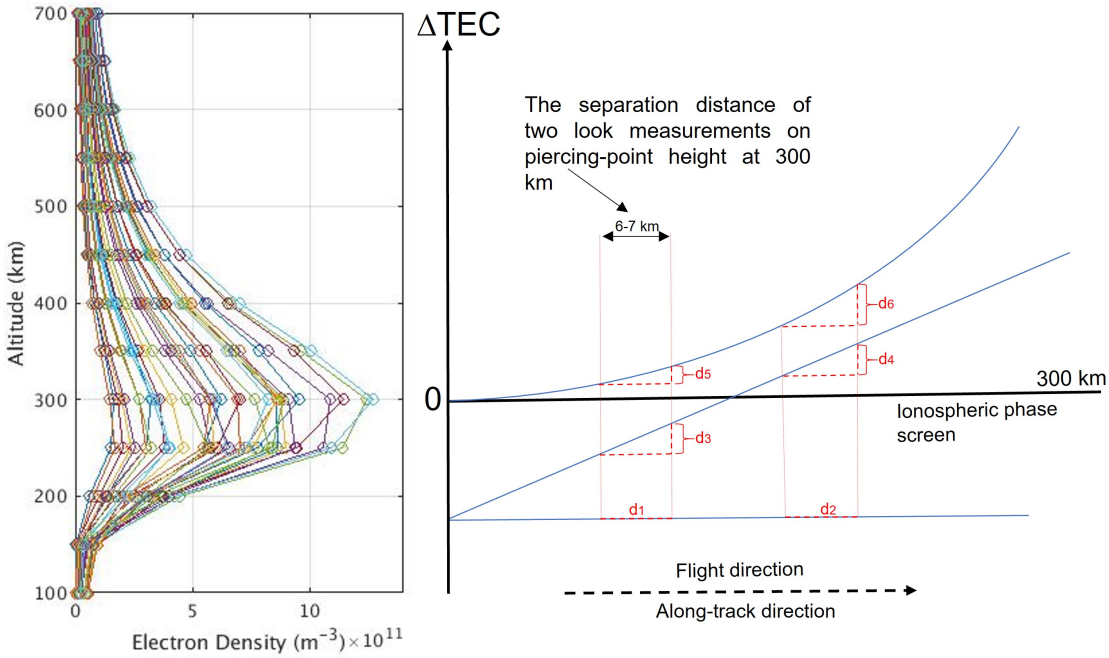

Figure 3.1: (Left.) The electron density profile against altitude. The sample data is from Bilitza et al. (2017) and represents the ionospheric condition in the West-Lut fault area at the SAR acquisition times. (Right.) The simplification of the ionospheric effect to the burst overlap InSAR phase. The variation of ionospheric difference ($\triangle TEC$) in azimuth direction is the main factor to bias the estimated ESD shift. The three simple ionospheric conditions (blue lines), which are stable, linear, and non-linear, are presented by the single-layer model with piercing-point height at 300 km. d represents the magnitude of bias to the ESD phase. If there is no displacement in this scenario, $d_1 = d_2 = 0$ and $d_5 < d_3 = d_4 < d_6$

simplifications of different cases that affect the observation with a single-layer model. Specifically, the TEC from satellite to ground in three dimensions is approximated as being all at a single height and is represented by a horizontally 2D plane illustrating the spatial distribution of the effect that microwave signal experiences along the line-of-sight direction. Based on the variation of the average TEC density with height in Fig. 3.1, this elevation-dependent layer is typically assumed to be 250-400 km from the ground. The height defines the atmospheric layer where the ionospheric effect is strongest. In this study, I define the ionospheric height at 300 km above ground.

In an ideal case, if both primary and secondary images have constant TEC across a scene, the ionospheric shift caused by the subtraction of the two look interferograms will be negligible. Second, if the ionospheric variation consists of only one constant gradient (i.e., linear trend), the ionospheric shift will be constant across the image. This component is identified as an absolute ionospheric phase, which typically could be estimated during a refining step in TOPS image coregistration. Nonetheless, the relative measurement is still effective because the bias is homogenous across all burst overlaps. However, any non-linear trend in TEC will result in a variable contribution to

the azimuth shift measurement. In fact, since the SAR scene for a tectonic application usually spans hundreds of kilometres in order to capture all active geophysical processes, the ionospheric condition cannot be expected to be stable or modelled by a single mathematical function across the scene. Moreover, the ionospheric effect also has high turbulence involved and consequently can cause a phase variation in a short distance.

Additionally, this issue appears to be significant for standard interferometric images, particularly at the burst overlap area, which has an abruptly different ionospheric path. However, the phase difference is very small in line-of-sight measurement and not severe enough to cause an error in the interferogram after filtering. It is only necessary to consider this possibility of burst discontinuities when analysing InSAR results with a high precision requirement. On the other hand, due to the great sensitivity of the ESD technique, this effect is visible and significant in azimuth displacement maps (Gomba et al. (2017), Grandin et al. (2016), and Spaans (2016)).

3.3 Processing Strategy

In this study, I propose a time-series approach to ionospheric estimation to improve the quality of velocity maps from both the conventional and burst overlap InSAR. The main workflow discussed in this section is an extension of the modified Split-Spectrum in range method proposed by Gomba et al. (2017), which works well with the Sentinel-1 image correction. This study considers the feature of the burst-mode acquisition; therefore, the concept can also benefit the along-track measurement. Specifically, an entire individual burst without mosaic needs to be applied in the analysis to exploit the ionospheric bias in the burst overlap area. However, I proposed an improved analysis that addresses some biases, to enable the technique in every case. The overall steps of the workflow are depicted in Fig. 3.2. The initial part of the workflow to estimate the ionospheric phase from TOPS images using split-spectrum in range is similar to Gomba et al. (2017). The important idea from the literature is that a non-linear ionospheric shift can cause a bias in the resampling step. Therefore, they proposed an analysis of ionospheric estimation to start with splitting burst-level SLC images and then performing a resampling to avoid the bias. Instead, I split the image after resampling and then estimate and remove the phase that is added in the resampling.

Since the burst version cannot be unwrapped, the unwrapped interferograms from a mosaiced image are used to guide the unwrapping for the burst version. Firstly, I resample full-band SLC images to one common master in a stack of images and generate the sub-band images of this mosaiced version. The algorithm divides the process into patches to mitigate bias introduced from different bandwidths between each sub-swath. The sub-band interferograms of each pair in the small baseline analysis are generated and multilooked by 8 looks in azimuth and 40 looks in range. Then, I perform the

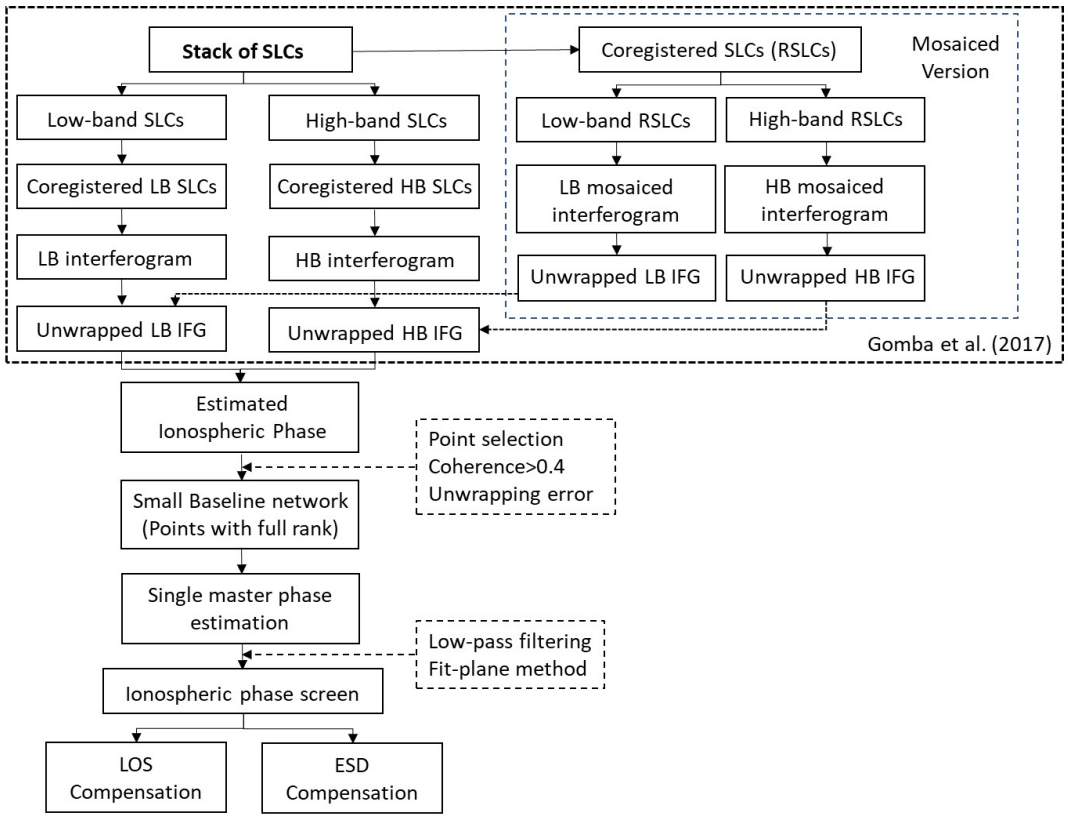

Figure 3.2: The algorithm workflow. The processing is divided into two parts. The initial part is to estimate the ionospheric correction using split-spectrum in range. The algorithm is similar to the main workflow proposed in Gomba et al. (2017) and takes into account a bias introduced during the resampling step due to ionospheric signal. I reject the points that have coherence lower than 0.4 and apply the adaptive threshold to reject points with unwrapping error. The small baseline approach is used with the points, which have the full rank, to analyse the time-series analysis. After achieving the ionospheric phase for every epoch, the low-pass filtering is performed by the fit-plane method. Then, the estimation is extracted to compensate for the line-of-sight and azimuth offset results.

unwrapping step using the SNAPHU software. For the unmosaiced version, the sub-band interferogram images are generated and also multilooked by 8 looks in azimuth and 40 looks in range. These interferogram images are rearranged with a new alignment to match and then added to the unwrapping image from the mosaiced version to produce an unwrapping interferogram with this unmosaiced version. In addition, the resampling information from full-band is projected to high- and low-band frequency and then is applied back to correct the bias.

3.3.1 Point selection

Before extracting the ionospheric dispersion phase, I propose a point selection step that should address two main problems. The first issue results from a typical decorrelation noise in the InSAR technique, but the effect is more severe than the standard line-of-sight InSAR measurement. Firstly, since the signal-to-noise ratio is lower, the sub-band

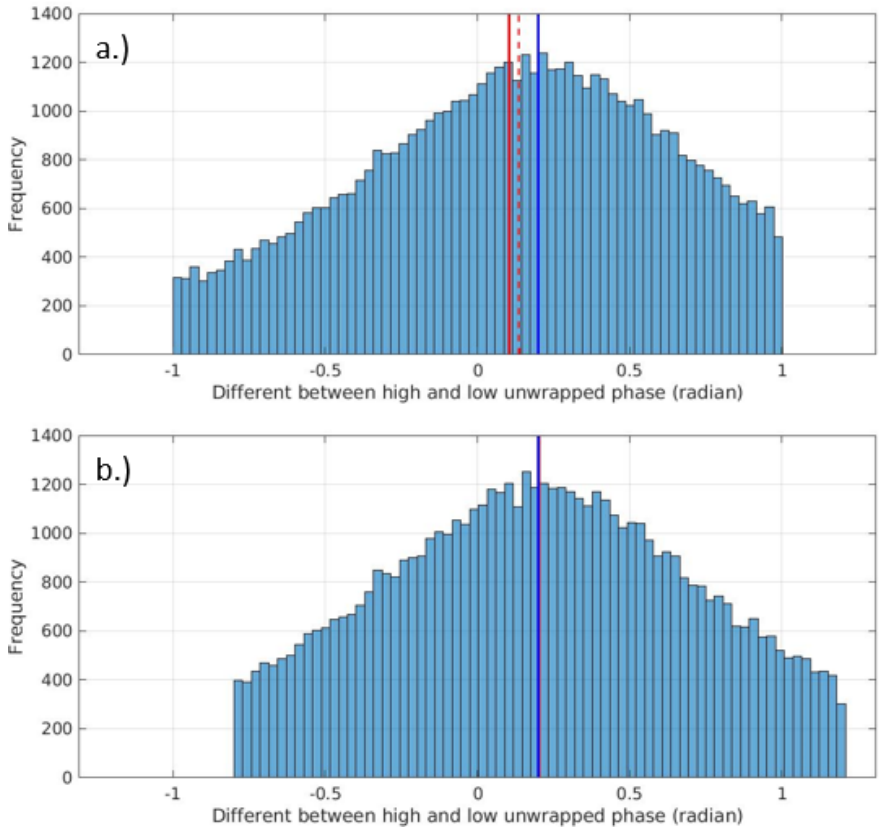

Figure 3.3: Simulation of phase difference (i.e., uwl-uwh). The number of points in the histogram is around 50,000 pixels. The actual value (blue lines) is at 0.2. a.) Histogram of pixels selected by a fixed threshold, between $\geq \pm 1$ radian. b.) Histogram of selected pixels using the adaptive threshold. The mean (red line) and median (red dashed line) values are different from the actual value less than 0.002 radians.

images have higher noise than an original full-band image. Additionally, the phase difference between high- and low-band images is amplified when it is converted to the ionospheric phase. Consequently, the level of noise in the estimation is notably high. Thus, I establish a criterion for selecting points with only coherence greater than 0.4 in both high- and low-band interferograms.

The second selection is to discard points with unwrapping errors. Moreover, the algorithm must be improved in identifying unwrapping errors in the existing method, which can bias the estimation. Outliers from the unwrapping problem, as well as bias from the typical selection, can disrupt low-pass filtering, and hereby the estimated ionospheric screen. I examine this unwrapping issue by taking the difference of the unwrapped phase between low- and high-band interferograms (i.e., uwl-uwh). I assume that the difference is close to zero, which can be used to reject the point with a large difference (e.g., $\geq \pm 1$ radian). Nonetheless, the difference is not completely zero due to the dispersion of the ionospheric signal, which is indeed the objective of the estimation. Furthermore, this difference, which will be inverted to the ionospheric phase, varies

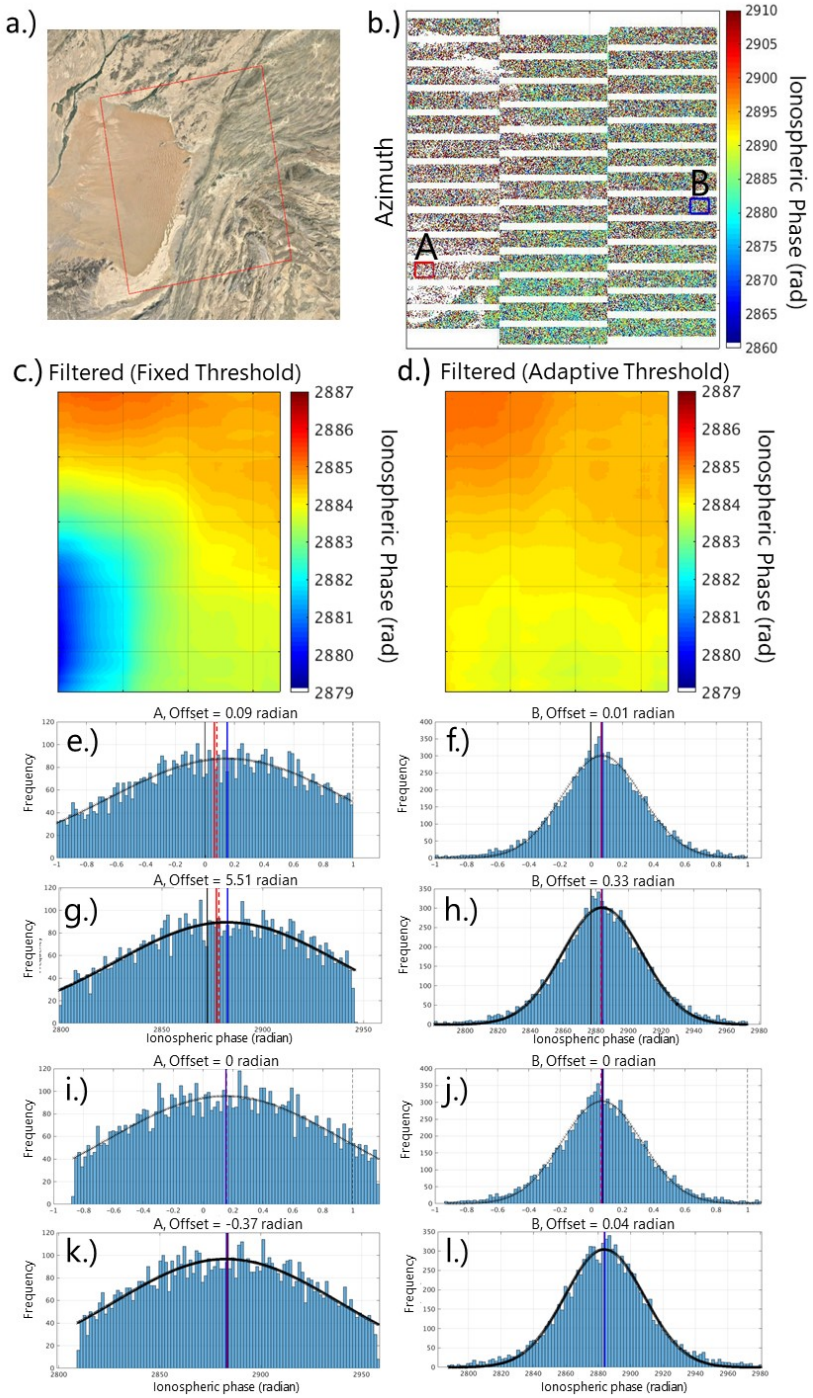

Figure 3.4: The effectiveness of the adaptive threshold. a.) present the area type of this example. b.) The estimated ionospheric phase which is projected to the piercing-point at 300 km from the ground. c.) is the ionospheric plane, which is applied the Gaussian filtering. The points in the west of the plane present a significant variation. This strong signal seems to correlate to the desert area in which is unreasonable for the ionospheric signal. d.) is the ionospheric plane by using the adaptive threshold. There is no bias in the desert area. e) and g.) present the bias to the point in the desert area to dd = uwl-uwh and ionospheric phase, respectively. f) and h.) present the bias in the area that have low noise, and show that the bias is not crucial in this low noise area. i.), j.), k.), and l.) are histograms of the same two areas, but the points are selected by the adaptive threshold. The blue lines are mode values, which are the peaks of the histograms. The red lines and red dashed lines are mean and median values, respectively. The black lines are the midpoints of the histograms.

across the scene. As a result, omitting points with a fixed threshold by using zero as a threshold's centre causes a bias in the set of selected points. In particular, the bias causes the phase difference distribution to be asymmetric. In other words, there is an offset between the peak and the middle value of a histogram. In the example shown in Fig. 3.3, 50,000 pixels are simulated with a phase difference of 0.2, and Gaussian noise added. Then, pixels with a phase difference between $\geq \pm 1$ radian are selected and plotted as a histogram. The mean (red line) and median (red dashed line) values are 0.09 and 0.1 radians, respectively. When the average filter is applied, there is a bias of about 0.11 radian from the actual value (blue line). Although this offset appears insignificant, this phase is significantly amplified when it is calculated to the ionospheric phase.

Fig. 3.4 presents an example of the ionospheric estimation with a fixed threshold. The ionospheric plane has a strong variation in the desert area. In the ionospheric investigation, this correlation is implausible. The Fig. 3.4e and Fig. 3.4f are the histograms of phase difference (uwl-uwh), which are selected by the ± 1 radian threshold. The histograms are plotted from unfiltered phases. The blue lines, which represent the mode value (i.e., the histogram's peak), are offset from the histogram's centres (black line). The mean value (red line) of the data in the low noise area is offset from the mode value by only about 0.01 radians because many points still cluster around the mean value. Conversely, the mean value of the data in the desert area, on the other hand, is offset from the mode value by about 0.09 radians. This bias is converted and has a 5.5 radian effect on the ionospheric phase (Fig. 3.4g). This enhances that using the fixed threshold will cause bias in areas with a low number of points or has a high noise.

To address this issue, I propose using a adaptive threshold to omit the point in a small area and operate the analysis with a moving window. In a small area, I apply the fixed window size of 20x20 km and estimate the actual mean value in this area using iterations of weighted mean. In the first iteration, I select the points with phase differences of -1<phase<+1 and calculate the mean value (μ_1) from these points. Second, I select the points with the phase difference of μ_1-1<phase< μ_1+1 and compute the average value (μ_2) from these points. This weighted mean can offset the average values closer to the peak of the histogram in every iteration. I keep repeating the iteration for 20 times, although I found from the experiments that the mean value usually presents the actual mean value at around the 6th-7th iteration. Then, I keep only the points with a phase difference of μ_{20}-1<phase< μ_{20}+1. For illustration, the algorithm is demonstrated using the simulated data (Fig. 3.3). The histogram distribution is symmetric, and the mean value calculated from these points is at 0.2024, which is offset from the actual value by about 0.0024 radians.

In practice, I skip the window, which has a number of points lower than 10000

pixels in the first iteration, because the flat histogram can make the method ineffective. Second, if most of the points in the specific area have the same unwrapping error value, the histogram's peak will be outside of $\pm\pi$. Therefore, before starting the iteration, I exclude the points with a difference greater than $\pm pi$ to prevent the weighted-mean walk from reaching the incorrect peak. Fig. 3.4d presents the ionospheric plane with the adaptive threshold. The strong variation in the desert area has disappeared. The histograms in Fig. 3.4i- 3.4l are symmetric, and the offset of the ionospheric phase between the mean values and mode values is less than 0.4 radians.

3.3.2 Time-series analysis

To estimate the time-series ionospheric phase, I proposed the small baseline technique instead of daisy-chain analysis to avoid an accumulation of decorrelation noise. This algorithm can provide a better constraint on estimating the ionospheric contribution for each acquisition than a single interferogram. After retrieving all of the selected points, I use Eq. 3.2 to extract the ionospheric dispersion phase for each interferometric pair in the small baseline network. One acquisition can pair with five consecutive acquisitions. Based on a single-layer model, I project the unmosaiced ionospheric phase to the ionospheric piercing-point height at 300 km, where the total electron content (TEC) is expected to peak.

Furthermore, since the mathematical function cannot predict the temporal characteristic of the ionospheric phase, I cannot define the constrain part in the G matrix of the NSBAS technique (Doin et al. (2011) and López-Quiroz et al. (2009)), which can be applied for the time-series network with the isolated clusters of interferograms. Thus, I only analyse points with full ranks. Moreover, since low-pass spatial filtering is one of the algorithm's significant issues, I analyse the time-series ionospheric phase using the unfiltered version to reduce the probability of filtering problems.

3.3.3 Low-pass Filtering

After obtaining the relative ionospheric phase for each epoch, I apply low-pass filtering to obtain the ionospheric phase screen. Due to a high magnitude of noise in the estimated ionospheric phase and the high sensitivity of the ESD relationship in burst overlap InSAR, strong filtering is required. Since the ionospheric effect is relatively smooth and a long-wavelength signal, a large number of window sizes can be used to trade spatial resolution for precision. However, the existing method has a significant problem at the scene edge because the filtering can only provide the mean value of the points in a window without accounting for a trend that continues outside of the scene. Consequently, the ionospheric phase screen produced by the averaging filter does not fit well with the points near the scene's edge and thus disrupt the accuracy of the result. Fig. 3.5 presents a simulation of the ionospheric phase in one dimension (blue points)

and the smoothed version (red points) using a Gaussian filter. Because the window size is 100 km, the filtered points closer to the edge than half the size of the filtering window (50 km) are biased by the edge problem. Moreover, as aforementioned, the source of ionospheric error in the burst overlap InSAR is a spatial variation of the different TEC. The mean filtering around the edge of the scene typically underestimates the ionospheric variation; therefore, the typical estimation is unable to represent the actual trend of the ionospheric screen, resulting in a bias in the along-track measurement.

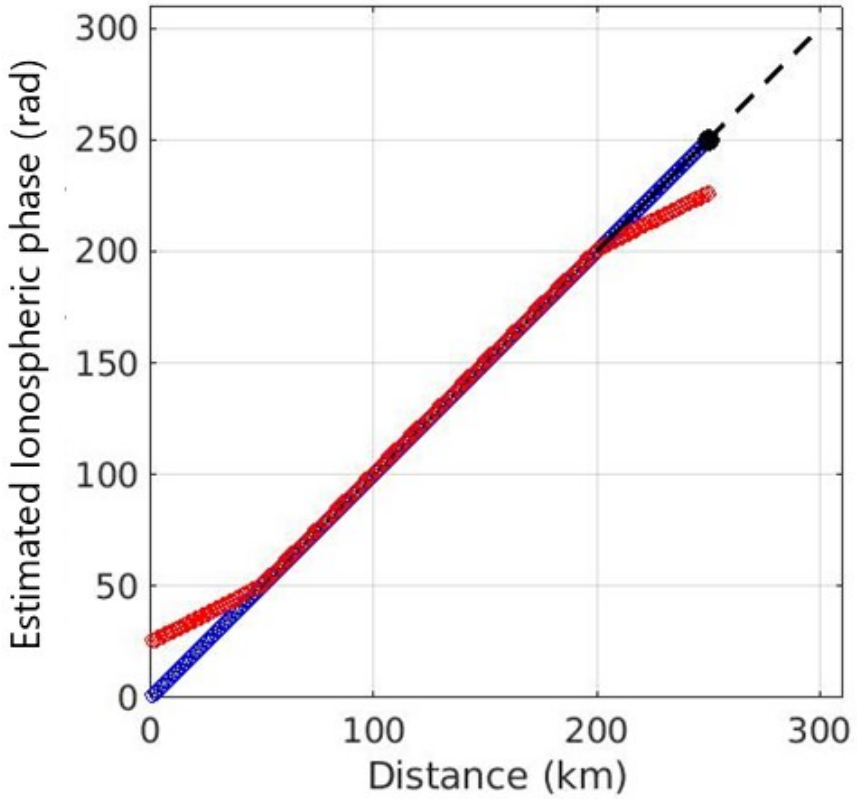

Figure 3.5: Simulation of ionospheric phase in one dimension. The ionospheric variation is simulated with a linear trend (blue points). The red points are filtered product of Gaussian filtering with 100 km window size. The black dot is the centre of the moving window, analysing at the last point. The black line and black dashed lines are the linear model fitted with pixels in the moving window, within 50 km from the centre point (black dot).

Therefore, I propose an algorithm for low-pass filtering based on a fitting plane with sub-area as moving window analysis. This methodology can be identified as an extension of the fit-function method to the ionospheric phase. The fit-function methodology does not have the edge problem because it accounts for a trend of the ionospheric phase. However, a single mathematics function cannot fit well with the actual ionospheric stage over the SAR scene associated with the tectonic study, which typically spans 100s km to capture all active processes. This proposed algorithm takes benefits from both the fitting function and moving window analysis. For example, according to the simulated data in Fig. 3.5, pixels 50 km from the centre are used to fit the linear line to estimate

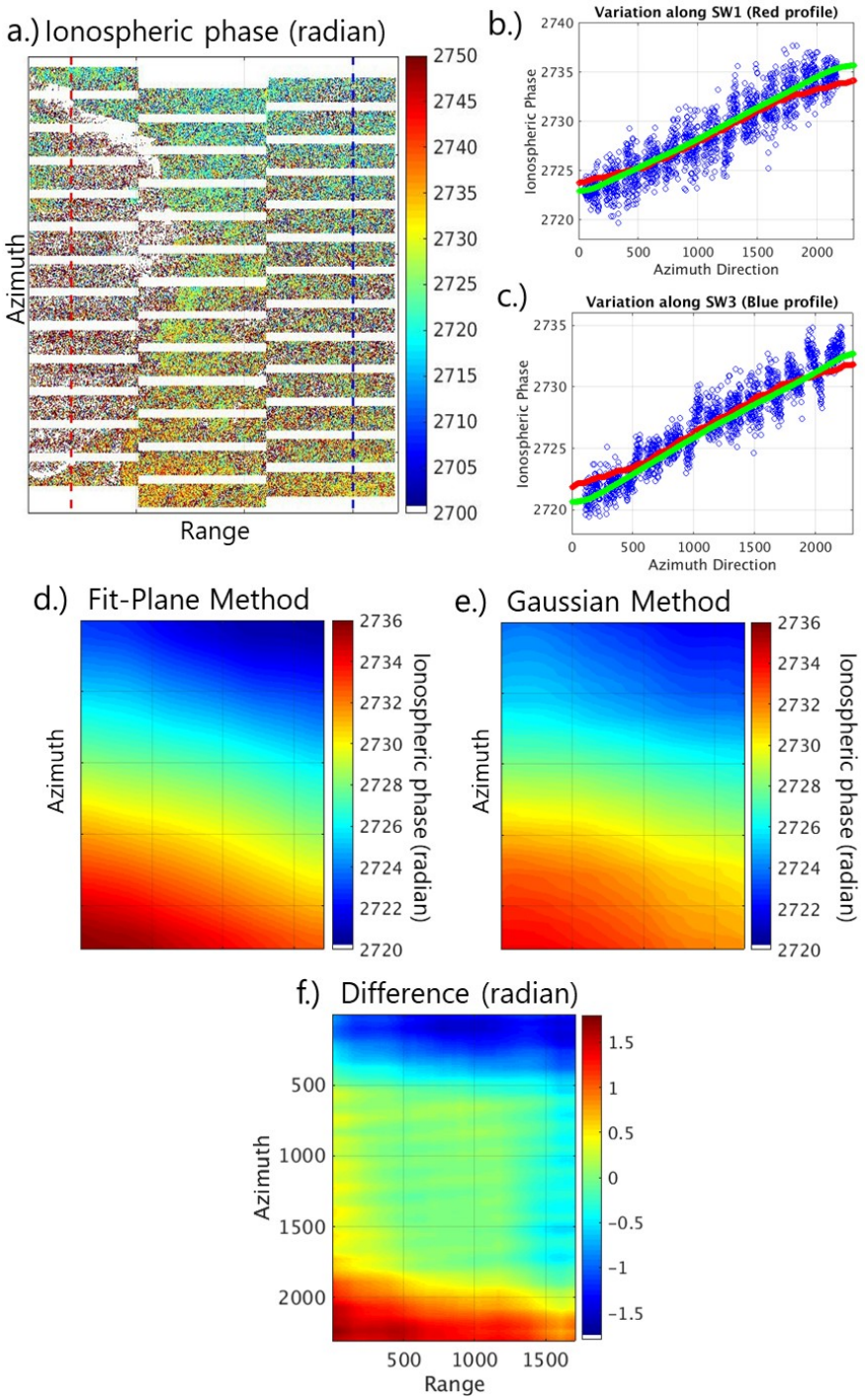

Figure 3.6: The effectiveness of the fit-plane filtering. a.) The estimated ionospheric phase which is projected to the piercing-point at 300 km from the ground. b.) and c.) are the variation of the fit-plane filtering (green) and Gaussian filtering (red) and the distribution of the ionospheric phase. d.) and e.) are the ionospheric screen from the fit-plane method and Gaussian filtering, respectively. f.) present the difference between two filterings.

the filtered point at the edge of the scene (black dot). As shown, since this algorithm considers the ionospheric trend rather than the average value, the estimated point from the linear model is consistent with the simulated ionospheric phase (blue point). In practice, for a two-dimensional problem, I select a particular sub-area and assign the gaussian weight to each point in the window based on its distance from the centre. I carry out a weighted fit to obtain a linear plane, estimate an ionospheric phase for the window's centre point, and then repeat this algorithm over the entire scene to retrieve the ionospheric phase screen.

Fig. 3.6 compares the fit-plane method to Gaussian filtering with a 100 km window size in an example from our interferogram stack. In the profiles, the fit-plane process can fit with the estimated ionospheric phase better than the mean filtering. As a result, I can improve the accuracy of low-pass filtering in the ionospheric phase estimation without the edge problem. After obtaining the ionospheric phase screen, I can apply the estimation to compensate for the ionospheric effect in line-of-sight measurements. Moreover, by analysing the estimation with the unmosaiced version, I can extract the ionospheric influence for the points in the burst overlap area. I can then subtract the difference ionospheric phase from a forward-looking area with a backward-looking area, inferred from the specified ionospheric piercing-point height, to retrieve the ionospheric shift that biases the along-track displacement map.

3.4 Experimental results

I applied the algorithm to a stack of SAR images over the West-Lut fault in eastern Iran. The fault, which lies between central Iran and Afghanistan, is one of the tectonic structures that accommodate a strain from the Arabia-Eurasia convergence. The fault can be divided into two segments by latitude 30.5°N. The northern section, a single trace with no complex structure, is identified as a strike-slip fault with a slip rate of 4 mm/yr in the north-south direction (Walpersdorf et al., 2014), whereas the tectonic structure is more complex in the south. At the transition zone, the Kubanan fault, which cumulates a 3-5 mm/yr strain, appears to terminate and join the West-Lut fault in this area. Therefore, I expect that the southern segment, the only major structure at this latitude, accumulates the strain of the West-Lut fault and the Kubanan fault together (i.e., 7-10 mm/yr).

I applied a time-series analysis with 90 Sentinel-1 images from the ascending track between November 2014 and May 2019. Since there was an absence of acquiring image between March 2017 and March 2018, the longest temporal baseline is one year. However, due to the area being dry and non-vegetated, the one-year interferograms still have high correlation.

For the line-of-sight measurement, I coregister SAR images to a single common

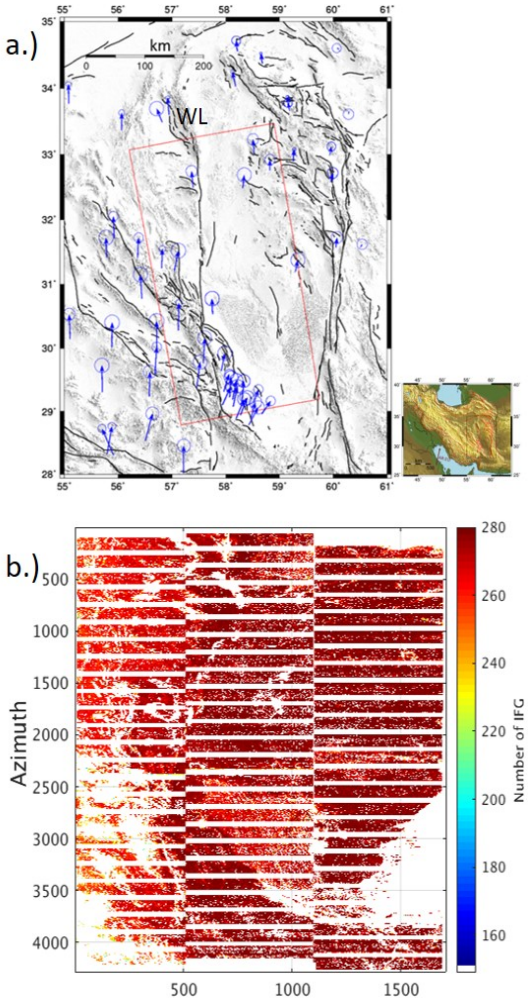

Figure 3.7: a.) The area of example. The ascending track 159 covers the West-Lut fault in eastern Iran. Blue arrows present GPS data Walpersdorf et al., 2014. b.) The distribution of selected points to be calculated in the small baseline time-series analysis. All the points have full ranks and are projected to ionospheric single-layer at height 300 km. The shading presents the number of interferograms in the small baseline networks.

master and generates 280 interferograms using the LiCSAR package (Lazecky et al., 2020), which is based on the GAMMA software. The unwrapping is done using a statistical cost approach with SNAPHU software (Hooper (2010) and Chen and Zebker (2002)). The tropospheric bias was corrected using the Generic Atmospheric Correction online service for InSAR data (GACOS) (Yu et al., 2018), which is based on the weather model and DEM data together. I performed the time-series analysis with the NSBAS approach using the LiCSBAS package (Morishita et al., 2020). One step in the procedure is to check the unwrapping error using loop misclosure checking and reject interferograms with significant problems. However, I found that most of the unwrapping problems in many interferograms occurred in the desert area, which lacks correlation. Consequently, I omitted these pixels before loop checking to maintain a number of selected interferograms and no gap in the network. This is why there is no

point on the line-of-sight velocity map in the desert area.

The average velocity from the 4-year data stack is presented in Fig. 3.8. The map shows a long-wavelength signal across the scene, obviously. I also plotted the velocity profile of InSAR points against the latitude. There is a variation of about 10 mm/yr from south to north in the line-of-sight direction. This strong signal cannot be identified as a deformation signal based on the slip rate of 4 mm/yr in the north-south direction. Furthermore, there is no significant variation in topography in this area; therefore, I expect the variation to be caused by the ionospheric effect.

Furthermore, I also exploit points in burst overlap areas from the resampled SLC images. Since the SAR images contain 25 bursts in each sub-swath, I have 24 burst overlap areas to measure in each sub-swath. Eq. 3.4 presents that the ESD technique is highly sensitive to the decorrelation noise. Consequently, I apply strong multilooking (∼570,000 pixels) to mitigate the effect. The theoretical precision of measurement should be better than 1.5 mm if the average coherence is greater than 0.2 (Fig. 2.4). Considering the high level of correlation in this study area, I assume that the decorrelation noise is insignificant, leaving only the ionospheric noise.

I apply the small baseline analysis with the double-difference interferograms and convert them using the ESD relationship (Eq. 3.4) to displacements. The velocity in the along-track direction is shown in Fig. 3.9. According to the profile, the along-track velocity varies by about 15 mm/yr from south to north. This variation is consistent with the line-of-sight result, which shows a strong gradient in the azimuth direction as well.

To correct these ionospheric biases, I apply the proposed algorithm to the stack of 280 interferograms. As proposed in section 3.3, I reject points based on coherence and unwrapping error, and select only the points with full ranks (i.e., equal to 90). I present the selected points that are projected to the modelled ionospheric layer at piercing height 300 km in Fig. 3.7. I used the small baseline approach to perform the time-series analysis and the fit-plane method to obtain ionospheric phase screens.

Fig. 3.8 presents the ionospheric correction for the line-of-sight result. The correction (Fig. 3.8c) has a similar trend as the variation of the estimated velocity. The standard deviations of the single master interferograms resulting from the small baseline conversion are calculated and presented in Fig. 3.8f. The compensation can help to reduce the cumulative noise by approximately 20 mm. The transect profile of the velocity map from south to north shows that the variation decreases from 10 mm/yr to 5 mm/yr. The long-wavelength has disappeared, leaving only a short-wavelength signal, which should be the remaining tropospheric delay from the correction. The results clearly show the 2017 Mw=6.0 Kerman earthquake and land subsidence in Kerman city.

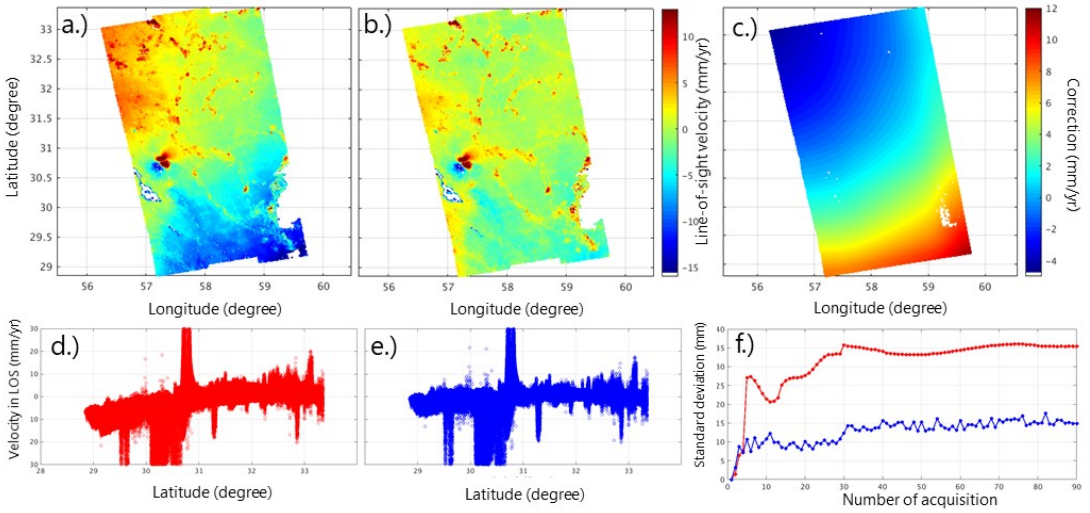

Figure 3.8: The ionospheric correction for the line-of-sight results. a.) the estimated velocity before the correction. It shows a long-wavelength signal across the scene. b.) the velocity map after compensation. c.) The difference between with and without correction. d.), e.) are the velocity profiles from south to north of before and after correction, respectively. f.) the standard deviation of the single master phases. Red and blue lines are from before and after correction, respectively.

Furthermore, the estimation is applied to mitigate the ionospheric bias in the along-track velocity results (Fig. 3.9). I select the ionospheric points, which represent the influence on the backward- and forward-looking phase in the burst overlap area, from the ionospheric screen. Then, I subtract them to obtain the ionospheric phase bias for the double-difference interferograms, and I apply the small baseline analysis to obtain single master ionospheric shifts. The along-track velocity was corrected and presented with standard deviation in Fig. 3.9b-3.9f. The compensation can reduce cumulative noise from the ionospheric effect by approximately 24 mm. The estimated velocity after the correction is more stable, particularly at points on the eastern side of the fault. The velocity map can present the variation between the area of single trace and complex structure more clearly than before the correction. The along-track velocities vary across the fault by about 4 mm/yr and 10 mm/yr in the northern and southern segments, respectively.

However, there is still a significant variation as a high-frequency signal remained in a few burst overlap areas; for example, the burst overlap near latitude 30.3°N in sub-swath 2 (i.e., middle sub-swath). This abrupt change is also visible in the result prior to correction and likely to have similar perturbation in the same burst overlap area. This variable of burst overlap is most likely caused by a short-wavelength ionospheric signal. However, due to the high uncertainty in ionospheric estimation, small changes in ionospheric conditions over short distances are difficult to identify. Furthermore, due to the high sensitivity of the ESD technique, a small error in ionospheric estimation can cause

a significant bias in the result. Thus, the correction for the along-track measurement must be performed cautiously to avoid adding bias to the measurement. Consequently, while the algorithm is effective at mitigating long-wavelength ionospheric signals over the scale of a hundred kilometres, it cannot remove short-wavelength ionospheric signals.

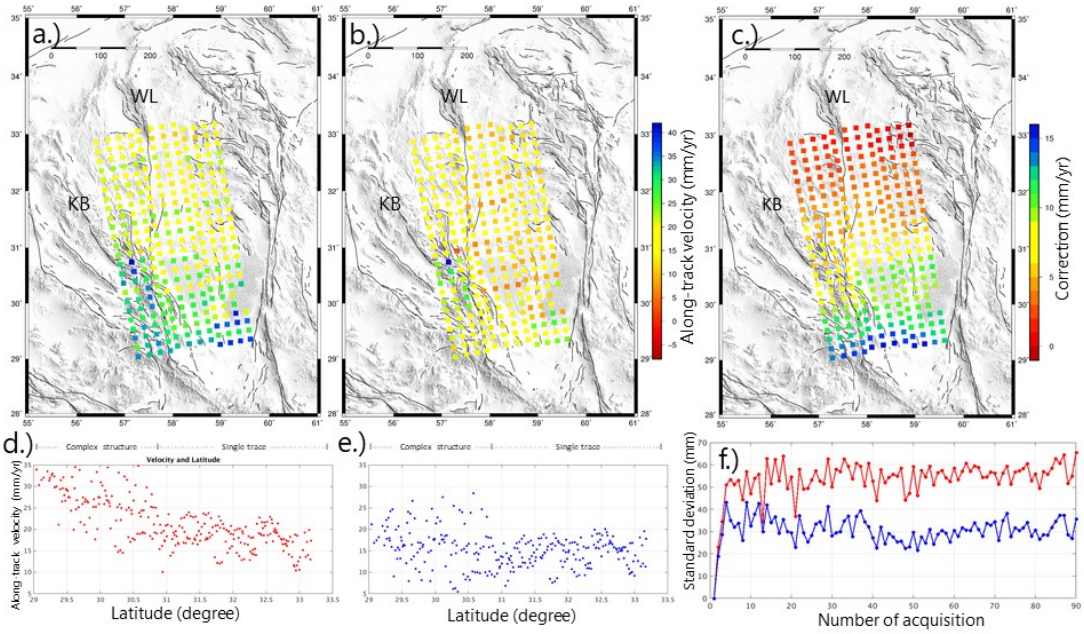

Figure 3.9: The ionospheric correction for the azimuth offset result a.) the average velocity in the along-track direction. Plus sign is the displacement to N168W. One burst overlap area is multilooked to 4 points to decrease the decorrelation noise. b.) the velocity map after the compensation c.) the difference between before and after correction. d.), e.) are the velocity profiles from south to north of before and after correction, respectively. f.) the standard deviation of the single master phases. Red and blue lines are from before and after correction, respectively.

3.5 Conclusion

This chapter proposes a time-series method to mitigate ionospheric bias in line-of-sight and along-track measurements. The algorithm is developed on the split-spectrum method, and two additional procedures are proposed to supplement the existing technique. Firstly, the adaptive threshold should be used to exclude the point with unwrapping error. This can help to avoid the bias caused by asymmetrical distributions of the estimated ionospheric phases, which are selected by a fixed threshold. Furthermore, I present the fit-plane method for low-pass filtering. Due to the significant noise in the estimation and high sensitivity of the ESD technique, strong filtering is required. The fit-plane method allows for a large window size (e.g., >100 km) to be applied without causing the edge problem.

I demonstrated the proposed algorithm with the data over the West-Lut fault area. Despite being analysed from a stack of C-band Sentinel-1 images, the estimated velocity in the line-of-sight direction has a strong gradient prior to the correction. For the along-track velocity results, I apply strong multilooking to reduce the decorrelation noise; therefore, the remaining variation should be due to ionospheric shifts only. The velocity map also shows a systematic bias as a linear trend from south to north.

The correction for the line-of-sight measurement can reduce the spatial distribution of the single-master interferometric phases by about 20 mm. The long-wavelength signal that disturbs the velocities is removed. This implies that we can mitigate the ionospheric bias by not using the deramping; therefore, we can achieve the velocity more accurately without risking eliminating tectonic signals. Furthermore, I extend the approach to mitigate ionospheric bias in the burst overlap InSAR technique. In the single-master analysis, the distributions of the double-difference phase were reduced by about 25 mm. The north-south trend from the bias has disappeared. The technique, however, is limited to retrieving the high-frequency ionospheric signal. As the ionospheric condition is expected to be homogeneous over 100 km, I expect spatial filtering between the burst overlap area can mitigate the short-wavelength signal. Therefore, this chapter shows that this ionospheric mitigation allows us to retrieve small deformations in both line-of-sight and along-track measurements more accurately.

In addition, for a future study, a recent research, Navarro Sanchez et al. (2021), presents a preliminary result from processing that applies an ionospheric estimation with the Persistent Scatter Interferometry (PSI) technique. The main idea is to trade off spatial coverage against accuracy to deal with the high uncertainty of ionospheric phase estimation. Following their suggestions, a quantitative clarification of the trade-off between pixel density and noise is required. Future research could determine how to achieve a high-precision ionospheric estimation without using the large spatial filtering used in this thesis.

Chapter 4

Measuring North-South Shear with Time-series TOPS Burst Overlap InSAR: The West-Lut Fault in Eastern Iran

In this chapter, I demonstrate the time-series analysis for the along-track measurement to study the north-south low strain rate (∼4 mm/yr) across the West-Lut fault. I also address the other nontectonic components included in the burst overlap InSAR phase apart from the ionospheric signal. This chapter presents the efficiency of the along-track measurement and also the limitation of the technique.

4.1 Introduction

There is a high correlation between where earthquakes occur and how fast strain is accumulating within the crust. Measuring the global strain rate is therefore one of the priorities for constraining earthquake hazards (Bird and Kreemer, 2015). The global strain rate map available now are conducted from the GNSS network distributed over the globe (e.g., Kreemer et al. (2014)). The campaign distribution is sparse compared to the global scale of continental deformation and often concentrates in a well-defined area with known high seismic risk in more economically developed countries. Thus, the map does not provide a good constraint for active faults that are defined as low risk or have never been exposed before perhaps due to the lack of recent major seismicity. The recent advances in the space-based geodetic technique of InSAR (Elliott et al. (2016), and references therein) have a high potential to accurately measure the global strain rate at a denser spatial sampling than currently achievable in many tectonically deforming

areas. However, a significant limitation in using these kinds of polar-orbiting satellite measurements, especially compared to those from other methods such as GNSS, is the sensitivity of surface motion that is greatest in the vertical and east-west directions, with much less constraint on a north-south displacement. The deformation signal in the interseismic period is typically small (of the order centimetre to millimetre per year) or nearly undetectable above the noise in the measurement of faults striking along the azimuthal direction of the satellite pass; therefore, the lack of study on these sub-optimally oriented faults needs to be addressed prior to achieving the aim of a dense global strain rate with InSAR. There are many north-south orientated strike-slip faults associated with the Alpine-Himalayan collision zone. Such major fault systems include the Dead Sea Transform, the Lut Fault system studied here, the Chaman Fault system of Pakistan and Afghanistan and the Sagaing Fault in Myanmar.

The TOPS mode of Sentinel-1, which acquires small discontinuous bursts with varying Doppler, offers the potential to partly resolve this problem; it is possible to use a spectral diversity technique to determine azimuth offsets in burst overlap areas with greater sensitivity than previously possible. Although this burst overlap interferometry has already been applied to extract large displacements at the metre scale in the north-south direction (Grandin et al. (2016), Spaans (2016)), there are significant noise contributions from decorrelation and propagation through the ionosphere that make it difficult to detect motion on the order of a few millimetres per year. Consequently, it is challenging to use this method to measure surface displacements associated with long-term interseismic deformation across active fault zones.

To address the current limitation, this chapter demonstrates a time-series approach with the burst overlap InSAR technique. A spatial multilooking with a particularly high number of looks is applied to reduce the effect of decorrelation noise, and the perturbation from the ionospheric signal is mitigated by the range split-spectrum method explained in Chapter 2 and spatial filtering. I test the algorithm with Sentinel-1 data over the 400-kilometre-long West-Lut fault in eastern Iran. The fault is a north-south strike-slip fault and accumulates about 4 mm/yr of dextral shear strain across it. However, at the latitude of the southern segment, below the conjunction of the Kuhbanan fault (Fig. 4.2), the area consists of complex structures, and the strain accumulation is not well-constrained by the previous geodetic study based upon sparse GNSS (Walpersdorf et al., 2014). I interpreted the results to refer fault slip rate parameters using a Bayesian approach and verified the validity of the results by comparing it with independent measurement (i.e., GNSS) from Walpersdorf et al. (2014) using the chi-square test.

The chapter is organized as follows. Section 4.2 firstly reviews InSAR techniques approaching the north-south measurement. Section 4.3 introduces the nuisance terms in the burst overlap interferogram, and then Section 4.4 describes the algorithm to

implement the non-tectonic components in the technique. Section 4.5 discusses the average velocity map and also interprets it within the tectonics of the region. Lastly, Section 4.6 gives a conclusion and suggestion for the further development of the method.

4.2 Along-track InSAR measurement

To complement the InSAR technique, many studies have tried to extract the north-south displacement from conventional InSAR, analysed based on independence measurements from multiple looking geometries. Wright et al. (2004) proposed that the analysis needs the satellite to operate in non-polar orbit with right- and left-looking to gain an efficient result. However, most of the standard mode of SAR satellites currently operating have only one-look direction operated, and their constellations are in a near-polar orbit. Therefore, it is difficult to acquire an accurate north-south surface motion from conventional InSAR processing. Following the methodology presented in Wright et al. (2004), I examined the Dilution of precision (DOP) in the east, north, and up components of surface displacement estimated from the Sentinel-1 operation. The DOP ratio is a parameter representing qualities of the decomposed results, calculated from an inversion, relating with the standard deviation of the observational data (i.e., the InSAR line-of-sight results). Fig. 4.1 shows the test result as I define the standard deviations of four looks angle at 1. The colour pixels represent an overlap area of four images with differing viewing geometries. Two of them are acquired on the ascending pass, and the other two are from the descending pass. They all are illuminated with the radar operating in a right-looking mode. The DOP in the east component is better than the observational data since the distribution of the look direction spreads well in four look directions. On the other hand, the north component's precision is about 27–29 times the observational data due to the poor constraint to the north-south direction.

Some other studies (e.g. Michel et al. (1999), Bechor and Zebker (2006), and Grandin et al. (2016)) proposed techniques that aim to observe the along-track crustal motion directly. This azimuth direction is parallel to the satellite track, which is much more sensitive to the north-south component, as typical ground track azimuth directions for polar-orbiting satellites such as Sentinel-1 are 348° on ascending and 192° on descending paths. First of all, the offset-tracking implements the cross-correlation of the amplitude image to extract offsets in the azimuth direction (Michel et al., 1999). The accuracy could reach 2.5% pixel in Fialko et al. (2001). This accuracy is comparable with the optimal case in Wright et al. (2004). However, this technique has an advantage that it does work with only a single interferogram and is available for recent SAR missions. A few years later, the analysis based on phase information instead of amplitude was proposed (Bechor and Zebker, 2006). The approach is well-known as the Multi-Aperture SAR Interferometry (MAI). They applied sub-aperture processing, which can obtain the partial signal of the antenna beamwidth, to generate backward- and forward-

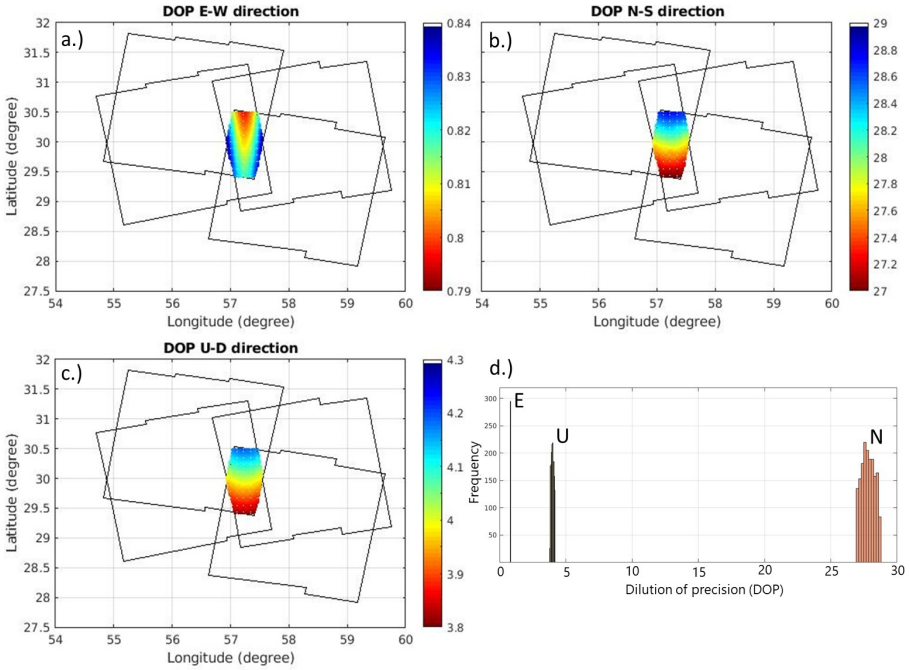

Figure 4.1: Relative errors (Dilution of precision, DOP) (Wright et al., 2004) in (a) east, (b) north, and (c) vertical components. The analysis is based on acquisitions in the standard IW Sentinel-1 operation. The colored pixels represent an area that is observed by four different look directions. All measurements are from a right-looking antenna. Two observations are from ascending pass, and another two are observed in descending constellation. Defining each measurement's standard deviation at one without a correlation, as shown in (d.), the mean DOP in east (E), north (N), and vertical (U) direction are 0.8, 28, and 4, respectively.

looking interferograms. The phase difference between two synthetic differential-looking interferograms is deduced to an along-track displacement phase. The accuracy of the improved MAI (Jung et al., 2009) is restricted at the decimetre level, which is slightly over 1% pixel of the ERS image. Feng et al. (2013) shows a comparison of the offset-tracking and MAI techniques, applied with ALOS images, for an earthquake. The result agrees well with each other, but the offset-tracking has larger uncertainties (i.e., 12-15 cm) than the MAI, which is about 8 cm and can reach 2 cm in high coherence areas.

Finally, the most recent and precise technique is to exploit the along-track displacement in burst overlap areas of TOPS mode images using Enhanced Spectral Diversity (ESD) (Prats-Iraola et al., 2012). The original objective of the ESD technique was initially developed to satisfy the particular accuracy TOPS mode requires in refining azimuthal misregistration shifts (i.e., 0.001 SAR azimuth pixel, which is about at the 1 cm shift level) between primary and secondary images. On the contrary, the burst overlap interferometry technique focuses on extracting the azimuthal ground displacement, which is one of the components in the estimated shift. The method follows the principle idea of MAI observation but uses the advantage of the Sentinel-1 acquiring image with

varied squint angle to produce the full-bandwidth interferograms from backward- and forward-looking directions. Consequently, the double-difference interferogram is generated from naturally different looking-angle images instead of synthetic images. The larger separation of the steering angle and doppler centroid separation result in higher precision than the offset tracking and the MAI approaches. The studies of the Chile earthquake (Grandin et al. (2016), Spaans (2016)) have shown that the technique is possible to achieve precision at a few centimetres, and the displacement agrees with the GNSS data at 3-6 cm level of accuracy.

4.3 Sentinel-1 TOPS image with Enhanced Spectral Diversity (ESD)

The Sentinel-1 mission expands the scope of InSAR technique in many ways, for instance, providing near-global land coverage, reduction in InSAR decorrelation from shorter repeat intervals, more rapid responding to hazards, or a potential to understand more temporally-variable deformation. The TOPS acquisition mode is the key to success in all these benefits. The sensor acquires discontinuously small images, called bursts, with three different look angles in one cycle to widen a swath in the range direction. This operation can obtain a wider image than typical Stripmap mode for 3–4 times in one orbit track and consequently achieve a much shorter revisit time (i.e., 6–12 days) at the expense of azimuthal resolution. During a burst acquisition, the sensor is continuously steered from backward- to forward-looking in an along-track direction (i.e., flight direction). This means that the line-of-sight looking is not permanently perpendicular to the flight direction, but the squinted geometry varies along the azimuth direction. This sensor steering is the principal factor that causes the Sentinel-1 processing requirement of a shift estimation with greater accuracy in coregistration. The precision of former processing strategies, composed of geometrical coregistration and cross-correlation technique, is limited at about 0.125 pixels, which is sufficient for the Stripmap mode. However, this relatively low level of refinement can cause a significant problem for the burst-mode image.

The primary source of the remaining shift after geometrical coregistration is the limitation of orbital information accuracy (Fattahi et al., 2017). The expected accuracy of ESA's orbital information is 5 cm (Fernández, 2011). Due to this limitation of accuracy, the residual causes a restriction to generate an interferogram with a completely zero baseline. Thus, this leads to those two images are acquired at different positions and geometries. The continued steering of the satellite antenna results in objects being illuminated with different squint angles, causing the variation of the additional phase, presented as phase ramp over the scene.

On the other hand, even though the sensor can perfectly acquire images at the same

position, a displacement in the azimuth direction can also cause a phase ramp. For instance, in the case of a whole block of land movement, the sensor illuminates objects for the entire burst with a variation of different squint angles. The sensitivity to detect azimuth displacement varies in an along-track direction (González et al., 2015) due to the beam steering. The additional azimuthal phase is nearly negligible at zero squint angle because the displacement vector is perpendicular to the measurement. On the contrary, pixels at the beginning and end of the burst obtain the largest additional phases but with the opposite sign since their squint angles are the most sensitive to the azimuth displacement. Consequently, the magnitude of time delay varies in the along-track direction, and the additional phases are added to the line-of-sight measurement varyingly. This variation causes the phase ramping and also phase discontinuity between the bursts due to abrupt change of squint angle.

Therefore, the shift estimation for TOPS images requires the ESD technique to refine the misregistration offset with an accuracy higher than 0.001 pixels (Prats-Iraola et al., 2012). The method extracts the azimuthal mismatch between the primary and secondary images by generating the double-difference interferogram in the burst overlap area. The pixels in this overlap area are acquired by both backward- and forward-looking geometry. These two measurements have different squint angles between 0.7-1.1 degrees and different doppler frequencies around 4200-4800 Hz depending on the sub-swath. In the interfering, the forward-looking interferogram is subtracted from the backward-looking interferogram. The subtraction removes most of the offset phase in an across-track direction since they should have the same effect in two difference-looking interferograms. Due to a difference of squint angle in the azimuth direction, the remaining phase ideally represents the offset phase in the horizontally along-track direction. The relationship between the double-difference phase ($\triangle\phi_{ovl}$) and the azimuth shift (x_{az}) is presented in Eq. 4.1, following Grandin et al. (2016), where $\triangle f_{ovl}$ is the Doppler frequency difference, $\triangle t_{az}$ is a misregistration shift in time axis, $\triangle x_s$ is the azimuth pixel size (13.99 m), $\triangle t_s$ is the azimuth sampling (0.0020555s) per pixel. The theoretical uncertainty in the shift estimation is shown in Eq. 4.2, where N is a number of the sample averaged, γ is coherence.

$$\triangle\phi_{ovl} = 2\pi\triangle f_{ovl}\triangle t_{az} = 2\pi\triangle f_{ovl}\frac{\triangle x_{az}}{\triangle x_s}(\triangle t_s) \tag{4.1}$$

$$\sigma_{ovl} = \frac{1}{2\pi\triangle f_{ovl}}\frac{1}{\sqrt{N}}\frac{\sqrt{1-\gamma^2}}{\gamma}\frac{1}{\triangle t_s} \tag{4.2}$$

Considering nuisance terms that bias the standard line-of-sight InSAR measurement, most of the topographic and flat-earth phases should be cancelled out in the interfering of the backward- and forward-looking interferograms because the two ob-

servations correspond to the same height, position, and distance in range direction. Similarly, the tropospheric phase, caused by a water vapor content in the tropospheric layer, contributes an additional delay to the observed interferometric phase and is a significant component of the standard InSAR processing. Conversely, the tropospheric contribution can be considered nearly negligible in the double-difference phase because the backward- and forward-looking observations have highly temporal and spatial correlations of the tropospheric effect. From the geometry, the signal from backward- and forward-looking travel through the global mean height of water vapour (i.e., 1.4 km) with the mean separation only around 0.03 km. Furthermore, the object is acquired by backward- and forward-looking with a few seconds separation in time. According to Hanssen (2001), the mean power spectra of atmospheric signal, related to Kolmogorov turbulence, can be inferred to distributions at 0.89, 0.70, and 0.88 mm in the along-track measurement for SW1, SW2, and SW3, respectively. These levels of distributions cannot be considered irrelevant in the measurement. However, the estimation of tropospheric turbulence within 30 meters is challenging to achieve, and the influence on the observed phase can be expected to be a Gaussian distribution. Consequently, I considered the variation of difference tropospheric delay as insignificant, which does not provide a systematic error, and specified this effect as random noise.

However, the obtained accuracy of the ESD phase was revealed inconsistency with the expected precision (Spaans (2016), Hooper and Spaans (2017)). The plausible explanation is from an ionospheric effect. Due to the different positions of acquiring images, the radars of backward- and forward-looking measurements experience different paths through the ionosphere. The ionized portion in the ionospheric layer causes the phase advance to the radio signal. Specifically, the phase bias introduces different time shifts to the backward- and forward-looking interferograms. Consequently, the ionospheric effect remains in the double-difference phase even after the double interfering.

Note that the ESD measurement is not disrupted by the magnitude difference of the ionospheric phase between the primary and secondary images directly. Instead, the main factor is a spatial variability of the ionospheric condition in the azimuth direction. Ideally, the ionospheric bias will be negligible if the differential ionospheric state is homogenous for the whole SAR scene. In the case of a linear trend, the bias influences only an absolute measurement, inducing the same effect over the scene, and therefore the relative observation is still effective. However, the long-wavelength ionospheric condition cannot be expected to be stable over the scale of tectonic applications, usually covering hundreds of kilometres to capture entire geophysical processes. A non-linear trend in the variation of the ionosphere, which is mostly the case, will lead to the variable contribution, resulting in perturbing the relative measurements.

In addition, I investigated the phase distribution, affected by the ionospheric noise, to the azimuth shifts in the data set. Since I applied a strong multilooking, explained in

the next section, to the double-difference phase for mitigating the decorrelation noise, the experiment is based on the multilooked properties. I firstly omitted the points with coherence lower than 0.5 and averaged the whole points in one burst overlap to estimate the mean offset. The mean offset will be considered if the number of remained pixels, having coherence higher than 0.5, is larger than 25 pixels. Consequently, the precision of the mean offset will be less than 1 mm (Fig. 4.5). Therefore, I can assume that there is only ionospheric noise significant for the phase distribution. I found that the mean standard deviation of the relative ionospheric signal is about 18 mm over an area of 200x300 km^2. Moreover, the ionospheric bias also has high turbulence involved and consequently causes the variation in a very short distance.

Therefore, I proposed that the misregistration shift is a mixture of azimuth displacement, orbital error, ionospheric noise, decorrelation noise, and random error (Eq. 4.3).

$$\triangle\phi_{ovl(az)} = \triangle\phi_{ovl(dis)} + \triangle\phi_{ovl(orb)} + \triangle\phi_{ovl(ion)} + noise \tag{4.3}$$

4.4 Processing strategy

I applied 90 ascending scenes acquired by the Sentinel-1 between November 2014 and May 2019 in order to analyse a time-series approach. The SAR scene has 25 bursts long in each sub-swath, covering the fault between the latitude of 29°N-33°N (Fig. 4.2), and can produce 24 burst overlap interferograms in each sub-swath. Due to the absence of any images being acquired between March 2017 and March 2018, the longest temporal baseline is one year to bridge this gap. However, as coherence in this area is excellent, one-year interferograms still have a high correlation. Unfortunately, descending scenes acquired over this area in the same time span as ascending data are perturbed by incoherent patches (Fig. A.1). The anonymous signal's effect is probably due to Radio-Frequency Interference (RFI) (Chojka et al., 2020). This disturbance is caused by another instrument in the area emitting radiation in the same frequency band as the Sentinel-1 C-band system. This anonymous signal should be removed before using these descending images; otherwise, the disturbance may cause the analysis to be misinterpreted. However, the interference seems to disappear after the acquisition in January 2020. This is probably due to a change in the processing (Instrument Processing Facility, IPF) of raw data (Level-0) to SLC image (Level-1) of this area. However, to my knowledge, I cannot find any specific mention of the change in the ESA's document yet; therefore, another possibility is that the ground-based radio source, which must be a powerful generator such as military-grade equipment, ceased operations after January 2020. Nonetheless, for our InSAR processing, the number of available descending images is still short to be performed with a burst overlap InSAR measurement, a high noise technique. As a result, I could not compare two independent InSAR measure-

ments, but I validated the ascending result with the GNSS data (Walpersdorf et al., 2014) instead.

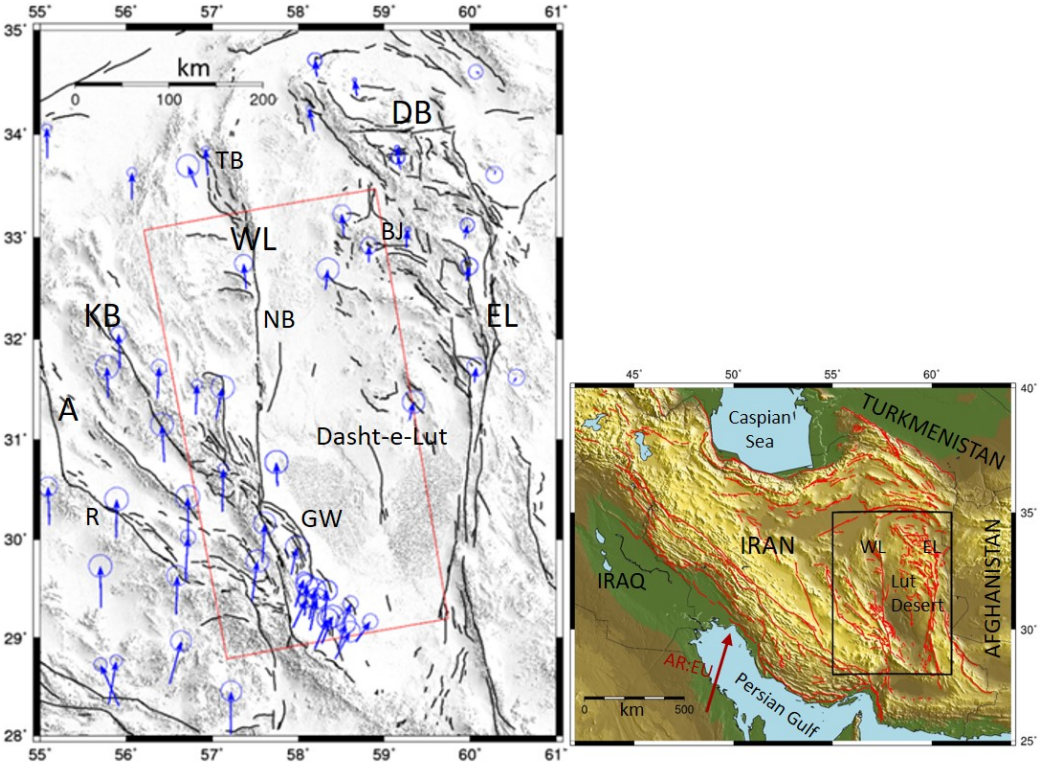

Figure 4.2: (Left) The area of West-Lut fault. Black lines represent faults (Walker et al., 2013). The ascending track 159 covers the West-Lut fault (WL) in eastern Iran. The West-Lut fault comprises with Gowk (GW), Nayband (NB), and Tabas (TB) segments. The Kuhbanan fault appears to join the West-Lut fault around latitude 30.2°N. Further to the west, the Anar fault (A) and Rafsanjan fault (R) are nearly parallel to the strike of Kuhbanan fault. On the east of Dasht-e-Lut block, the East-Lut fault (EL) is a major fault stiking nearly north-south. Also, the secondary fault lying in an east-west direction are Dasht-e-Bayaz fault (DB) and Birjand fault (BJ). The red rectangle is the coverage of the Sentinel-1 SAR data, applied in this chapter. Blue arrows present GNSS velocities with respect to a stable Eurasia from Walpersdorf et al. (2014). (Right) Map of Iran with major faults denoted by red lines (Styron and Pagani, 2020).

I coregistered every scene to one common primary image (i.e., scene acquired in September 2016) by using the LiCSAR package (Lazecky et al., 2020), based on GAMMA software. Since the ESD technique is an ambiguous measurement, the shift estimation is limited by phase modulo 2π. Consequently, in the coregistration procedure, to ensure that an initial error is within the ambiguity band, it performs a rough coregistration with orbital information before refining the azimuth shift by cross-correlation and then ESD techniques. Due to the great sensitivity of the method, the estimated shift has particularly high uncertainty, depending on coherence and the number of measurements (Eq. 4.2); therefore, the decorrelation noise is handled meticulously in the estimation. Commonly, the average ESD from every pixel in the burst overlap

is usually applied. Furthermore, interferograms typically include a large area where multiple bursts are required to study a tectonic deformation. Consequently, to achieve the highest precision, the technique also uses the mean shift from every burst overlap to minimize the significant effect of decorrelation noise.

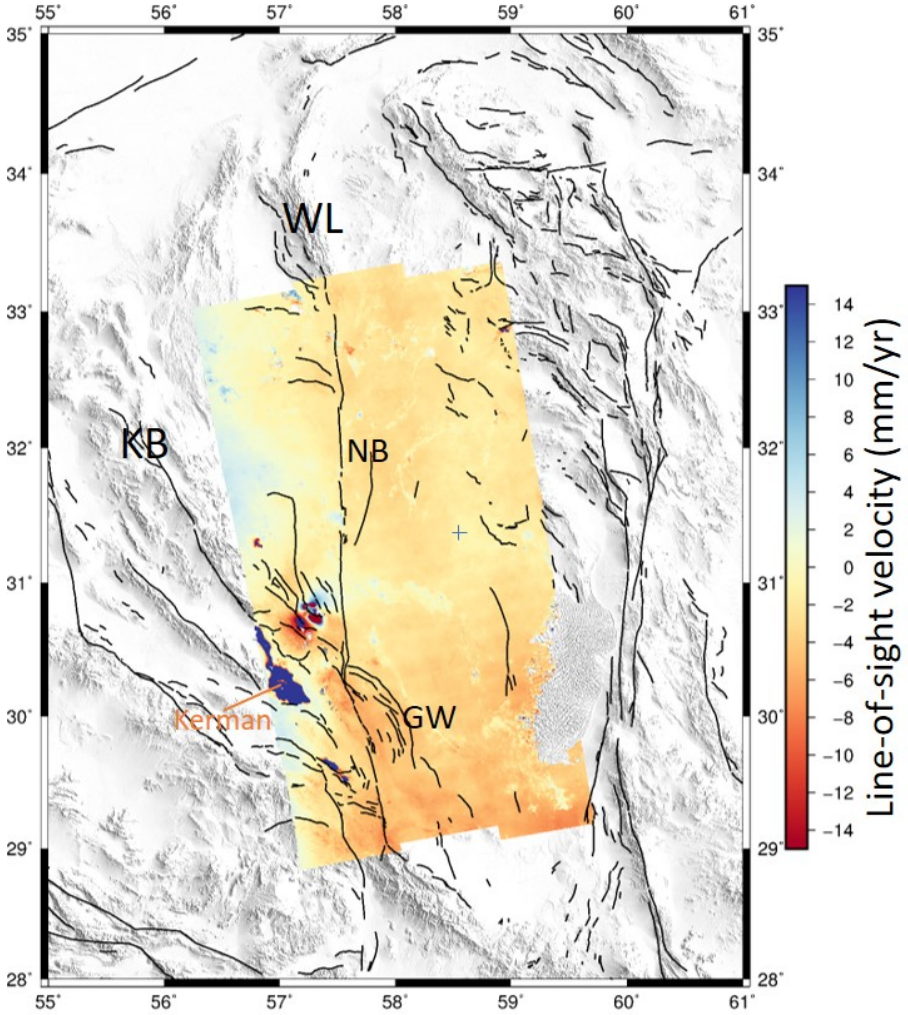

Figure 4.3: Line-of-sight velocity map. Points are multilooked by 8 looks in azimuth and 40 looks in range. The velocities were analysed by the NSBAS time-series approach (Morishita et al., 2020). The result presents the earthquake rupture in the NNE of Kerman city (30.7°N, 57.3°E). In the time-series analysis, I found that earthquakes that cause the slip present in the map occurred during March 2017 and March 2018. This low constrain is a result of the one-year gap of acquiring image. In this area, there are more ten earthquakes with moment magnitude (Mw) 4.5-6.0 in December 2017 recorded in the earthquake catalog (USGS). WL: West-Lut Fault, KB: Kuhbanan Fault. The blue cross sign, shown at latitude 31.30°N, longitude 58.65°E, represents the reference area of the InSAR result. Black lines represent faults (Walker et al., 2013).

As the estimated shift is an average value from a number of burst overlaps, all components involved in the misregistration shift are reduced by their mean values. Generally, the orbital shift can be assumed as a constant over the scene because of the parallel orbit and the small orbital tube of the Sentinel-1. The subtraction of

the averaged value in the resampling step can eliminate most of the timing error in SAR instruments and also actual misregistration from limited orbital accuracy. On the other hand, the azimuth displacement and the ionospheric term cannot be considered constants. The shift can represent only the averaged values of these two components. Due to being an unambiguity problem, the estimation of the displacement term can be referred to as the averaged deformation for the whole block of study area if there is no outlier displacement to dominate the averaging, for example, earthquake. Similarly, the estimation of the ionospheric component could represent only a scene-level ionospheric state. However, the residual is considerably small and not severe enough to disrupt the actual signal in filtered line-of-sight interferogram, even a large azimuthal movement. After retrieving the estimated shift, the secondary image was resampled to the common primary image. At this stage, the misregistration shift is typically smaller than 0.001 pixels, and the line-of-sight interferograms should be performed without the phase ramp and the phase discontinuity between bursts.

For the across-track measurement, I produced 280 interferograms and then unwrapped them by a statistical cost approach with SNAPHU software (Hooper (2010) and Chen and Zebker (2002)). The Generic Atmospheric Correction online service for InSAR data (GACOS) (Yu et al., 2018) was used to mitigate the tropospheric signal. The correction can reduce the standard deviation of the interferometric phase in each interferogram by about 20% averagely for this work. Points in the desert area were omitted to avoid rejecting interferograms in a loop-closure checking for unwrapping error. Then, I performed a time-series analysis with the NSBAS approach based on the LiCSBAS package (Morishita et al., 2020). As shown in Chapter 3, the line-of-sight velocity map firstly showed a long-wavelength ionospheric signal across the scene about 10 mm/yr from south to north. Thus, I employed the ionospheric correction with a time-series approach based on the applied split-spectrum method. The mitigation can remove most long-wavelength signals and reduce the north-south variation to approximately 5 mm/yr (Fig. 4.3). The result shows a number of short-wavelength tectonic signals, such as the three M_w ~6.0 Kerman earthquakes in December 2017, and land subsidence in Kerman city (Fig. 4.4). However, the average velocity does not show any long-wavelength signal that can be referred to as the interseismic tectonic deformation across the fault. Assuming that there is no relative deformation in normal or vertical components, the line-of-sight signal influenced from the north-south strike-slip component should be at 0.5 mm/yr (Fig. A.3), estimated by average look angle at 38° and heading angle at N10.3W.

For the along-track measurement, to maximize coherence, I generate double-difference interferograms from pixels in burst overlap areas of the coregistered SLC images. Note these resampled images are generated using LiCSAR (Lazecky et al., 2020); however, I employ my script based on Matlab for the subsequent processing. As previously dis-

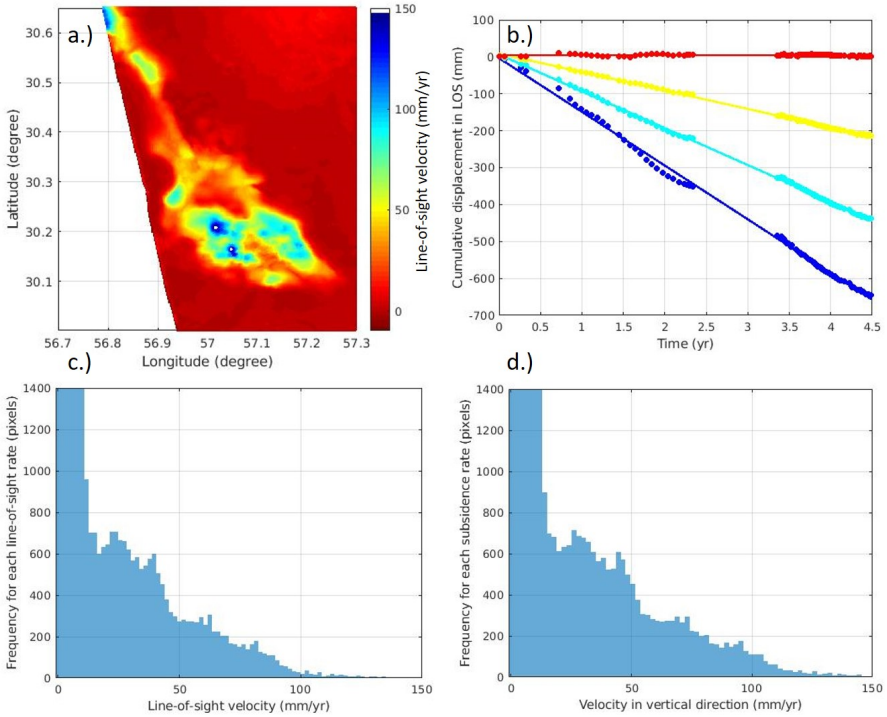

Figure 4.4: a.) Land subsidence map of an area in Kerman city (marked in Fig. 4.3). b.) Time-series deformation derived by line-of-sight InSAR analysis. Red, yellow, cyan, and blue colors present the ground moving away from the satellite at rates 0, 50, 100, 140 mm/yr approximately. The linear model appears to fit well with the InSAR data, so the subsidence seems to occur steadily. c.) The histogram presents an overall line-of-sight displacement rate. d.) The histogram illustrates a vertical displacement rate, assuming that there is no horizontal deformation. The bin width is 1.8 mm/yr.

cussed, despite the subtraction of the averaged ESD shift during coregistration, the residual phase due to local displacement and local ionospheric effect still remains in the double-difference phase.

For a practical illustration, Spaans (2016), which studied the 2015 Illapel, Chile earthquake by using Sentinel-1 images, mentioned the existence of the local shift after the resampling. They also applied the averaged ESD shift for the coregistration and constructed displacement maps in both line-of-sight and along-track direction. The gradient of displacement (i.e., ∼60 cm) was detected over multiple burst overlaps in the along-track measurement by both ascending and descending data. The shift estimation works efficiently, even with this large displacement in the azimuth direction. The phase ramp and phase discontinuity do not appear for most bursts in the line-of-sight interferometric images. However, they still found small burst discontinuities in the area where line-of-sight and along-track measurements detected the largest deformation. The residual displays that the coregistration by average shift does not remove all local shifts, but the resampling only offset the distribution to have zero mean. Furthermore, after the resampling, the residual offset still maintains the displacement information

with the sense of relative movement, even though the points are in different burst overlaps.

Although, in general, I can apply the double-difference interferograms generated from resampled images to study relative ground velocities directly, in this thesis, I still need to add back the azimuth shifts applied in the coregistration, both from cross-correlation and ESD estimates to the double-difference phases. It is due to that standard processing in LiCSAR employs image processing independently based on a predefined frame basis, with 13-burst long on each of three sub-swaths. To cover the West-Lut fault, the deformation studies in this thesis need to process two LiCSAR frames, consisting of 25 bursts long for each sub-swath (one burst in common between consecutive frames). Specifically, the coregistration analysis is carried out on an individual basis. The estimated shift from coregistration is a mixture of actual misregistration resulting from orbit accuracy limitations, ionospheric bias deduced from the scene level, and average azimuthal displacement of the entire scene. As a result, the averaged azimuth shifts estimated separately from two frames are subtracted and consequently cause an offset in the measurements across the frames.

Therefore, after adding the estimated azimuth shift back, the total double-difference phases represent the azimuth shift between primary and secondary images just after the geometry coregistration with orbit information. At this stage, the offset caused by frame-based estimation should be disappeared, and consequently, I apply a single reference point to the measurements of both frames. The procedure can maintain coherence, avoid phase discontinuities in resampled images used for line-of-sight measurements, and avoid phase offset between consecutive frames.

Due to the greater sensitivity, the decorrelation noise has more effect on the burst overlap interferometry technique than the line-of-sight measurement. Specifically, the ambiguity band of the double-difference phase is more than $\pm$700 mm, whereas the conventional InSAR is $\pm$14 mm in C-band analysis. Consequently, the presence of even small levels of noise can cause a significant perturbation to the along-track measurement. In order to reduce the effect from the decorrelation component, after generating every double-difference interferogram in the small baseline network, phases were multilooked to 1.5 km in azimuth and 0.5 km in range (i.e., $\sim$110x230 looks). The number of total pixels used in this spatial averaging is 25,000, which is very high compared to the traditional number of looks in conventional InSAR.

Since this study monitored a slow tectonic process with a high temporal resolution from the Sentinel-1 (i.e., short revisit time), this strong multilooking is valid for the burst overlap InSAR technique with an assumption that displacements in each interferogram are not over one phase cycle (i.e., $\pm$700 mm). On the other hand, the line-of-sight phase varies much sensitively to the displacement; therefore, the strong

multilooking cannot be performed with a wide area. To design the number of looks, I considered an acceptable level of precision and retained enough information as possible to infer the fault interseismic parameters. The azimuthal length of one burst overlap area (i.e., 1.5 km) is relatively small compared to the north-south tectonic deformation. Furthermore, the noise of the technique is particularly high. Consequently, I assume that the variation of along-track velocity within one small burst overlap area is probably unable to detect and cannot provide much useful information. Thus, the number of total azimuth width of the burst overlap area is applied in multilooking to increase precision rather than spatial resolution. On the other hand, 0.5 km resolution in the range direction, which corresponds to 0.8 km of ground pixel spacing averagely, should be sufficient to present a gradient of strain accumulation across the fault in an east-west direction.

The distributions of the multilooked phase related to coherence are shown in Fig. 4.5 comparing with the theoretical precision (Eq. 4.2). The test was conducted by calculating phase differences and separation distance between pixels, with the same particular range of coherence, within the same burst overlap area. Then, at each range of separation distance, I estimated the mean standard deviation from every possible pair of estimation from all of the interferograms. The standard deviations at the smallest separation distance were picked to refer to the distribution of the particular coherence. The estimation of neighbouring pixels within the same burst overlap can reduce the ionospheric effect since the bias should be similar in the same burst overlap. The deformation signal in the interseismic period should not be significant with short temporal baseline interferograms. Thus, the distribution should be a result of decorrelation noise only. From the figure, the distribution is inconsistent with the theory. The distribution between coherence 0.1 and 0.3 seems to agree with the theoretical estimation. However, the estimated errors with coherence higher than 0.3 are larger than the theory.

After multilooking the double-difference phase for every interferogram, I applied the ionospheric estimation from the time-series split-spectrum method to mitigate the noise. The algorithm estimates the ionospheric phase based on the unmosaiced version; therefore, I can extract the ionospheric signal that affects the backward- and forward-interferograms. The mitigation can reduce the cumulative ionospheric noise in the time-series analysis about 25 mm. However, the study in Chapter 3 suggested that the correction can detect only a long-wavelength ionospheric signal. The variation in a short distance, which I identified as a short-wavelength ionospheric signal, still affects the analysis. In this work, I applied the spatial-filtering between the burst overlap area to mitigate this short-wavelength signal. I assumed that the phase has a Gaussian distribution, and the ionospheric condition is homogeneous over 100 km (Brcic et al., 2011).

The next step is to apply the small baseline time-series approach to the corrected

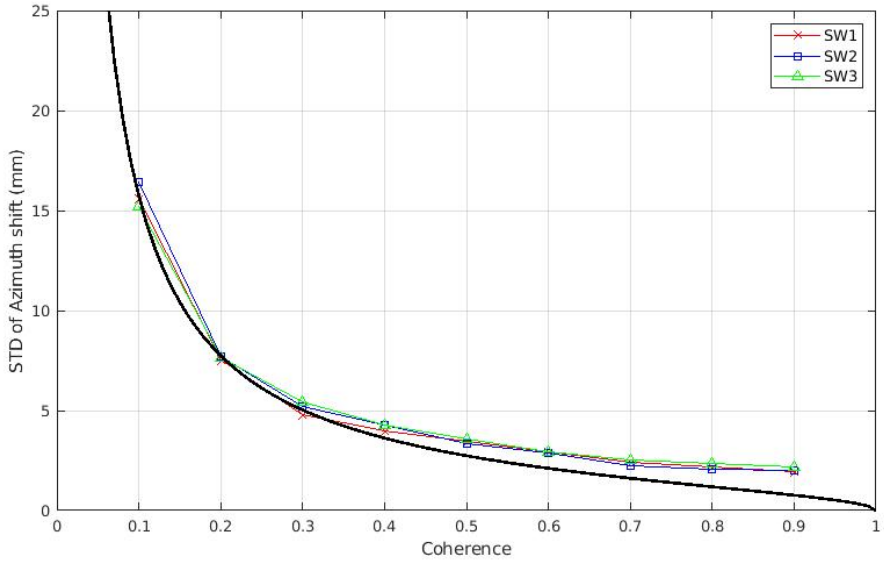

Figure 4.5: Standard deviation of phase multilooked by ∼25,000 pixels against coherence. The estimated error of SW1, SW2, and SW3 are presented with red, blue, and green lines, respectively. The estimation appears to agree with the theoretical precision (black line), calculated from Eq. 4.2, with coherence lower than 0.3. However, the estimated errors with coherence higher than 0.3 are larger than the theory.

double-difference phase. Note that I applied the analysis with the wrapped phase. Since the ambiguity band (±700 mm) is particularly large relative to the slow-moving process, forming double-difference interferograms only between acquisitions separated by a short time interval, the phase unwrapping can be dismissed for this algorithm. Additionally, I have also investigated the inversion with a daisy-chain approach. I found that the analysis accumulates noise along the time-series, and therefore the average velocity encounters large bias and noise. This bias is expectedly a result of cumulative decorrelation noise. It probably also exists in the line-of-sight analysis, but the effect could be insignificant. However, owing to the high sensitivity, the bias is obviously shown in the ESD technique. I found that the small baseline approach can constrain the noise accumulation, and the scatter of the average velocity has less distribution.

Nevertheless, some outliers of the velocity still exist, even with the small baseline analysis. In the time-series, I discovered that the problem always occurs at the period that interferogram lost correlation (i.e., coherence<0.1). These outliers are considered the point with high coherence in most timespan, but there are only some short periods that lose phase information. Thus, the time-series analysis obtains a negative effect on inversion performance if these low coherence points are included in the analysis. Consequently, in each point, I omitted the interferogram with coherence lower than 0.1 and then applied NSBAS using a minimum norm constraint as a linear velocity in order to link isolated clusters of interferograms.

In addition, the SqueeSAR (Ferretti et al., 2011) and phase linking (Ansari et al., 2018) algorithms, which have a strategic idea to exploit information from every possible interferogram in time series, are fascinating to use with the analysis. Including a larger number of interferograms can reduce noise and provide more robust results. However, for the burst overlap InSAR analysis, these approaches need to employ the wrapped phase in the inversion; therefore, when using SqueeSAR or phase linking methods, the ambiguity band must be carefully considered. The investigation to enable the two methods with along-track measurements is beyond the scope of this thesis; however, I suggest that the method needs to incorporate an algorithm to identify a pixel with a phase exceeding the ambiguity band.

After retrieving a single master phase from time-series inversion, there is a method called periodogram applied in Yague-Martinez et al. (2019) to estimate an averaged along-track velocity based on a stack of ESD phases. This approach also employs estimation with wrapped phase and pick averaged velocity that gives a minimal residual between observation and velocity model using a complex domain. However, in this thesis, I apply a least-squares fitting linear model to the cumulative phase. The basic idea is the same: find an averaged velocity with the smallest residual. As a result, the investigation to clarify a specific detail of the difference between the conventional line fitting and periodogram is required. Thus, I still apply a conventional method in this thesis.

Moreover, I have also investigated the maximum contribution from earth tide to the relative azimuth movement. Following Xu and Sandwell (2020), the earth tide influencing InSAR measurement was decomposed into three components. The first component is an absolute tide, which does not affect the relative measurement, because the effect is homogenous over the scene. Specifically, the earth tide is a long-wavelength signal with a spatial scale over 100 km. Secondly, the variation of the tide effect resulting from the change in look angle across the scene can cause a phase ramp in range direction. On the contrary, it does not affect the burst overlap InSAR since the subtraction of the backward- and forward-interferograms can cancel out most of the variation. Lastly, this component is a result of a variation of the tidal effect directly. The SAR scenes longer than 100s km are regularly deployed nowadays owing to the Sentinel-1 satellite. The change of tide signal in the along-track direction biases the relative measurement of the line-of-sight InSAR and the along-track InSAR since the tide is one of the real deformation signals in the measurement.

To verify the influence of earth tide on the result, I considered the tide variation in azimuth direction referred from the solid tide model (Milbert, 2018) between the latitude of 29°N and 34°N along the longitude of 59°E at the 90 SAR acquisition times. I found that the effect of tide variation with the range of 400 km for an interferogram can reach ±9 mm in the along-track deformation signal. This level of influence could

be significant to the velocity estimation despite relative measurement. However, I estimated the tide velocity, calculated from only the tide displacement. The rate varies less than 0.3 mm/yr from latitude 29°N to 34°N and is quite stable in longitude direction; therefore, the influence of earth tide can be verified as insignificant to the results.

4.5 West-Lut Fault

The Arabia-Eurasia collision is a major source of most of the driving forces that govern the observed crustal deformation kinematics in the Iranian territory. The convergence produces an overall shortening in a nearly north-south direction at this latitude. Previous GNSS data from the global model, together with a regional network, presented the convergent rate at 25-26 mm/yr (Vernant et al., 2004). The Zagros mountain in SW of Iran accommodates part of this shortening rate at 10-12 mm/yr, whereas the rest of the dextral shear is taken up by the active fault system lying between central Iran and Afghanistan (Walker and Jackson, 2004). The geodetic GNSS deformation field from Walpersdorf et al. (2014) indicates that each of the major faults accommodates part of the plate convergence in a distributed sense, with increasing rates observed going from west to east.

The West-Lut Fault is one of the most significant faults in the shear zone system. The fault is the western boundary of the Dash-e-Lut block with an overall length of ∼700 km and strikes dominantly in the north-south direction with a right-lateral sense of strike-slip motion. The West-Lut fault is also called the Gowk-Nayband fault, which is named after the constituent fault segments. Likewise, I also analysed the tectonic deformation by splitting the West-Lut fault into two segments. The Nayband segment, comprising the northern part, has a single trace and is interpreted to connect with the Tabas fault system in the north around latitude 33°N. On the contrary, the Gowk segment, the segment accounted from southward of latitude 30.5°N, is much more complex with sub-parallel fault systems and reverse faulting structures.

4.5.1 The results of along-track measurement

The West-Lut fault has previously been reported to accumulate a slip rate of ∼4 mm/yr (Walpersdorf et al., 2014) based upon block models for the region constrained with GNSS observations. The velocity map of the along-track measurement across the fault is presented in Fig. 4.6. The points with mean coherence along the time-series lower than 0.2 were omitted. The choice of this threshold is selected to remove the noisy pixels located in the desert dune area in the east without removing the points in the more stable areas where a consistent along-track measurement can be made. However, there are high values in the southeast but these signals are probably associated with sand dune migration. For the result, the positive sign indicates a ground movement

toward the north with an azimuth of N10.3W, an average heading angle of the scene. Note I present a variation of heading angles of the SAR scene in Fig. A.4. The variation range about 1.6° across the scene. However, if I assume the relative displacement at 10 mm/yr across the scene, the maximum relative bias of projecting the displacement into the north component is about 0.05 mm/yr. Since this value is minor compared to the other nontectonic noise, I assume that this value is insignificant in the study. Nevertheless, this variation is more important to consider in higher latitude areas. As shown in the figure, the interseismic signal cannot be readily seen from the velocity map. Moreover, the result obviously shows a high-frequency variability between the burst overlap. I suspect that it is an influence of short-wavelength ionospheric signals since points in the same burst overlap have similar characteristics of perturbation.

For the difference between burst overlaps, the variation along the azimuth direction appears to be stronger than the variation along the range direction. Even though a quantitative study is still required, I suspect that, as introduced in Chapter 3, the main source of bias in burst overlap InSAR measurement is a non-linear variation of differential ionospheric phase advance in the azimuth direction. On the other hand, not any variation in the range direction causes a bias in the burst overlap InSAR measurement since the range variation causes the same magnitude of phase advance to the backward- and forward-looking interferometric phases. Specifically, a bias in relative burst overlap InSAR measurement in the range direction results from a difference of an azimuthal trend in the range direction. Furthermore, besides the smooth variation of TEC in the ionosphere, one of the ionospheric perturbations, traveling ionospheric disturbance (TID), causes a high-frequency variation to the ionospheric phases. In particular, the TID characteristic is one of the factors that can be used to reveal a short-wavelength ionospheric bias in the burst overlap InSAR measurement. TID can be calculated by dense a GNSS network that can continuously provide ionospheric data (TEC) in the time domain, and the measurement of a difference between a particular TEC and spatially smoothed TEC plane is defined as TID. As the TID characteristics are identified as being similar as a waveform, despite the fact that more research for a robust theory is needed, the daytime TID alignments studied by Jonah et al. (2018) and a literature review in the research (Kotake et al. (2007), Tsugawa et al. (2007), Otsuka et al. (2011), and Otsuka et al. (2012)), are in a northeast-southwest direction. As a result of these demonstrations, as well as the supposition that TEC variations in the longitude direction are small within a scale of 10° (Ding et al. (2007), Jonah et al. (2018)), I expect to see variations along the azimuth direction more frequently than in the range direction.

However, assuming that the slip rate is constant along the segment, the expected velocity signal can be further enhanced by multiple burst overlap averaging, which should mitigate the effect of short-wavelength ionospheric signals. In the northern

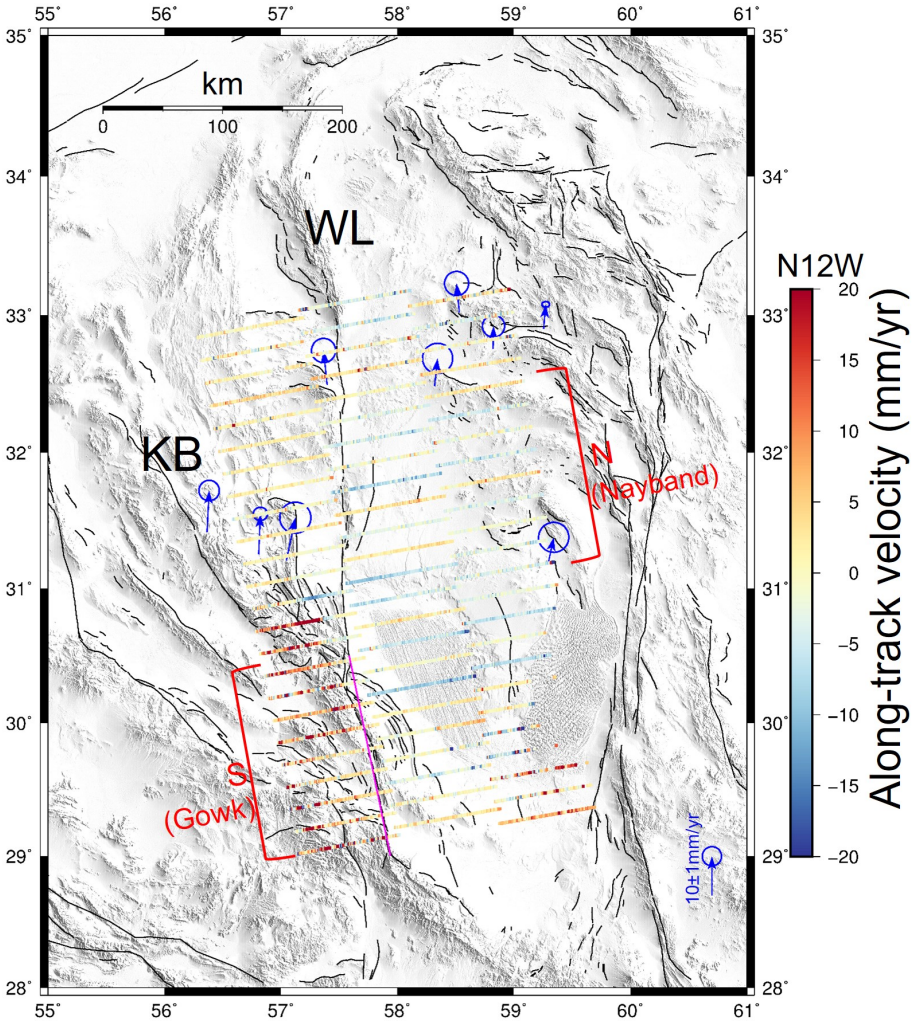

Figure 4.6: Along-track velocity map obtained from Sentinel-1 ascending data, covering the northern and southern West-Lut fault (Nayband and Gowk segments, respectively). All the points were applied by strong multilooked (1.5x0.5 km), and were estimated using time-series azimuth offset on the burst overlap areas. The points with an averaged coherence lower than 0.2 were omitted. The positive sign represents ground movements in the direction of N10.3W. Blue arrows are the locations of the 9 sites of GNSS data (Walpersdorf et al., 2014) used in validation of the interseismic deformation for Nayband segment. The red bracket show burst overlap applied in present transect profile for Nayband (N) and Gowk (S) segments. Black lines represent faults (Walker et al., 2013). The pink straight line represents a simplified surface trace for the southern half of the fault (the Gowk segment), which is used in the modelling (Fig. 4.9). The strike of the simplified fault segment is on average 347°.

segment, I present a transect of the velocity points between latitude 31N-32.5N, covering the area with only a single trace, and also a mean velocity profile averaged from every 2-km bin in Fig. 4.7. I avoid including the data between 30.5°N-31°N due to the short-wavelength signal of 2017 Kerman earthquakes (Fig. A.5), which include an impact of a strong displacement (0.4 m) in the along-track direction from the interferogram, paired from images acquired in March 2017 and March 2018. As demonstrated in the profile, we can see a dextral strain localized within a narrow zone close to the fault location, as illustrated by the change in velocity from 1-2 mm/yr in the west, to -2 mm/yr in the east, over a fault perpendicular distance of about 50 km.

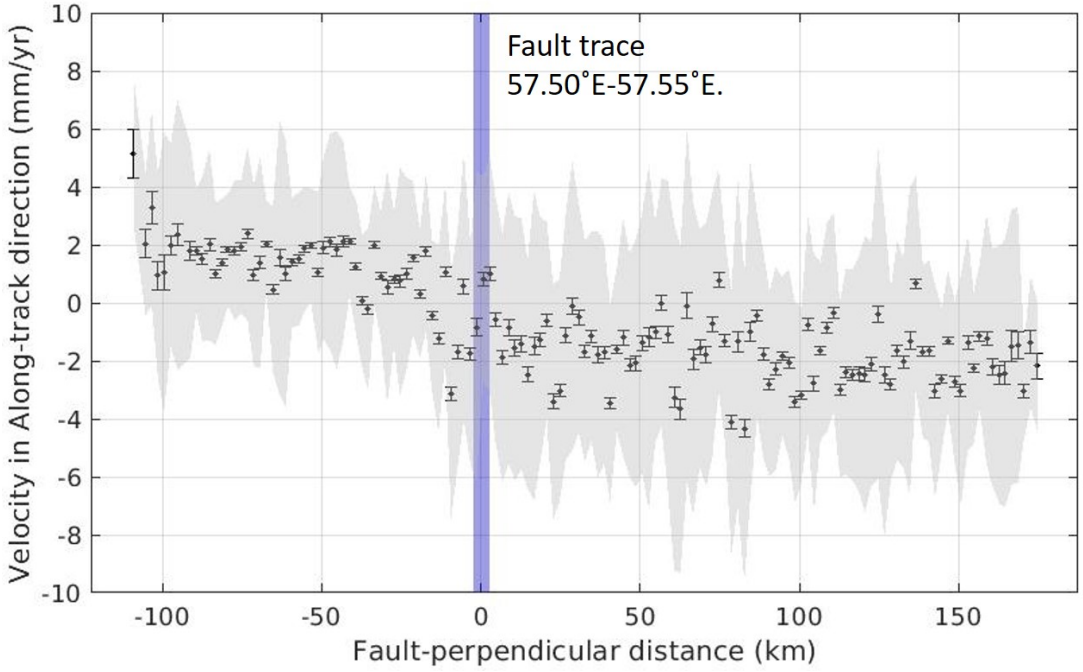

Figure 4.7: Transect profile showing the derived along-track velocity field. Points are from 9 burst overlap areas (∼150 km) in each sub-swath, covering the northern single surface trace segment of the fault (surface position denoted by the purple shaded vertical band) with a range of longitude between 57.50°E and 57.55°E, in an area between latitude 31°N and 32.5°N (Fig. 4.6). The zero fault-perpendicular distance on the x-axis is at longitude 57.525°E. Black circles and error bars are mean velocities and their standard deviations using a bin width of 2 km. The grey shaded area represents the one standard deviation of the burst overlap InSAR points.

To validate the accuracy of the measurement, I projected the GNSS data (Walpersdorf et al., 2014) into the along-track component direction (N10.3W). Although the GNSS data applied to the verification were operated in 1997-2008, which is different from the time period of InSAR data acquired in 2014-2019, the validation is still applicable due to the absence of large earthquakes in the time gap of data. I compared the result as a one-dimensional product by statistically comparing the GNSS data and the mean velocity of InSAR points located in one kilometre from the GNSS sites in the longitude direction by the chi-square test. I offset the GNSS data by the station

Table 4.1: The optimal model parameters from different observations. The models are estimated from Bayesian approach using 9 GNSS sites from Walpersdorf et al. (2014) (Fig. 4.6) and along-track InSAR measurement. Note 0−100 km of optimal fault locking depth of GNSS data is a range I bound the Bayesian analysis. 9 GNSS data cannot provide a good constraint for referring to a robust interseismic deformation model's arctangent curve. The posterior distribution of the locking depth parameter with a range of 0−100 km cannot reveal a peak of Gaussian distribution (Fig. A.7). The optimal value determined by Bayesian analysis appears to be greater than 100 km.

Parameter	GNSS	InSAR	GNSS+InSAR
Number of data points	9	140	149
Slip rate (mm/yr)	6.6±1.7	4.3±0.5	4.2±0.4
Locking depth (km)	0−100	17.9±9.7	19.5±7.9
Fault location (km)	5.2±36	-13.6±5	-13.5±4

at longitude 56.8°E, RAVR station in Walpersdorf et al. (2014), to match with the InSAR results. I estimated the semivariogram of the one-dimensional InSAR points and obtained a sill variance at 17.2 mm^2/yr^2 without a statistical correlation (Fig. A.6). Note that there is the covariance between InSAR points in the same burst overlaps due to a similar ionospheric condition, but it is disappeared by the compression from two-dimension to one-dimension in spatial filtering. I tabulate all the values verified by the chi-square test in Table 4.4. The chi-square estimation is only 2.92 indicating the statistical agreement between InSAR and GNSS measurements with 95% confidence and 7 degrees of freedom, which the p-value is at 12.59.

I also applied a Bayesian approach to infer interseismic modelling parameters based on the elastic half-space model (Savage and Burford, 1973). I assumed that the West-Lut fault is a vertical strike-slip fault and locked from the surface without a creeping according to a lack of discontinuity observed on the fault trace in the line-of-sight velocity map. The inversion algorithm from GBIS (Bagnardi and Hooper, 2018) is applied to a transect of the mean velocity profile, which is prior projected into the north-south direction, parallel to the fault trace. In the analysis, I set the upper bound of slip rate and locking depth parameters at 20 mm/yr and 100 km, respectively. The location of the fault can vary ±100 km from the fault trace at latitude 57.55°. The variance of each mean velocity point is defined from 17 mm^2/yr^2 divided by the number of averaged InSAR points, mostly at 17 points, so most of the mean points have a standard deviation around 1.1 mm/yr. The model parameters of the best-fitting interseismic model to InSAR data only, GNSS data only, and two data sets together (Fig. 4.8) are reported in Table 4.1.

As a result of higher spatial resolution, the models inferred from InSAR data have a smaller standard deviation than the model from the GNSS only. Most of the misfit between the InSAR model and the GNSS velocity occurs at three easternmost GNSS

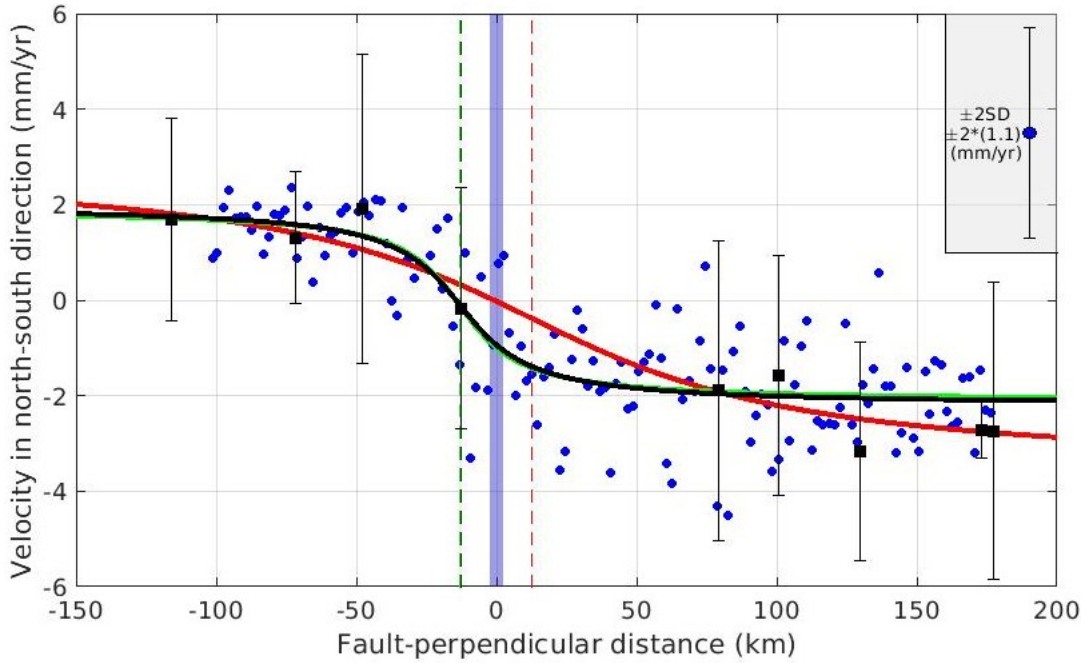

Figure 4.8: The best-fitting model of the interseismic strain accumulation using the optimal parameters from the Bayesian approach shown in Table 4.1 applied with GNSS (red), InSAR (green), and GNSS+InSAR (black) data for the northern segment. Nine GNSS stations applied in this validation are shown in Fig. 4.6. The mean azimuth velocities in Fig. 4.7, averaged from 9 burst overlaps pointed with the N bracket in Fig. 4.6, were projected into the north-south direction (the fault-parallel direction). Two-sigma error bars represent the northern component of the GNSS velocity data. They are referenced to the InSAR profile by using the site at a longitude of 56.8°E. The purple shaded vertical band represents a fault trace with a range of longitude between 57.50°E and 57.55°E. The zero fault-perpendicular distance on the x-axis is at longitude 57.525°E. Blue points, which are mean velocity profiles with 2 km bin width, were used in the inversion. The black dashed line represents the location of the West-Lut fault estimated from the InSAR and InSAR+GNSS modellings. The modelled fault position offsets 10 km to the west of the fault trace (∼57.55°E), identified by Walker et al. (2013). The vertical red dashed line shows the estimated fault location calculated from GNSS modelling. At the top right, a two-sigma errorbar with a blue point presents the mean uncertainty of InSAR points. They are all similar, approximately at 1.1 mm/yr.

Table 4.2: The optimal model parameters for the Northern and Southern fault segment transects. The model parameters are estimated from Bayesian approach using data points in burst overlaps shown in Fig. 4.6.

Segment	Slip Rate (mm/yr)	Locking Depth (km)	Fault Location (km)
Northern	4.3±0.5	17.9±9.7	-13.6±5
Southern	7.5±0.5	9.8±3.0	-9.8±2

sites. These stations are in the area above the Birjand fault. This zone has a series of secondary structures, which are not well-defined. Walpersdorf et al. (2014) proposed that they probably are active and responsible for a part of the kinematics in the region. Furthermore, due to a lack of a GNSS station close to the fault, the interseismic model cannot be well constrained by the GNSS data only, especially the locking depth parameter. The 100-kilometer bound of locking depth parameter is not enough to show a gaussian distribution in the posterior histogram (Fig. A.7). The distribution does not reveal the histogram's peak in the $0-100$ km range, and the optimal value seems to be deeper than 100 km. This estimate appears to be significantly higher than 14 ± 7 km, which was calculated using a compilation of interseismic deformation studies in Wright et al. (2013). This large estimated value of locking depth also results in a trade-off with the slip rate producing a large estimate for this parameter also. Finally, the model from InSAR only is almost the same as the model from both InSAR and GNSS together. According to the variance calculation above, the standard deviation of most InSAR points is 1.1 mm/yr, which is as good as the standard deviation from the GNSS data. Consequently, the inversion is dominated by the InSAR data, which has a 15 times higher number of observations than GNSS data in this objective, even with the one-dimensional product that has been through many downsampling steps.

Moreover, I can observe that the southern West-Lut fault accommodates a higher strain accumulation than the northern part. The optimal model was referred from a transect of the mean velocity profile from points between latitude 29°N-30.5°N (Fig. 4.9). The tectonic structure in this latitude has more complexity than the northern part, and coherence is not as high as the area in the north. Due to the technique's uncertainty, which is not precise enough to allow the measurement to detect the highly variable structure from multiple closely spaced sub-parallel fault segments, we assumed that only a single fault accommodates the interseismic deformation across this region. The inversion revealed that the mean velocity profile is most consistent with a 7.5 mm/yr slip rate. The strain accumulation is almost twice as high as the northern segment's. Most of the variation occurs on the western side of the fault, especially around the latitude of 30.5°N, the region of intersection with the Kuhbanan fault. Conversely, the velocity on the eastern side of the fault slightly increases from north to south by only about 1-2 mm/yr.

4.5.2 Tectonic interpretation

I summarized the slip rate of the two West-Lut fault segments estimated from different methodologies in Table 4.3. The West-Lut fault has a long-term Holocene slip rate estimated from dated fault offset features at 1.4 ± 0.5 mm/yr and 3.8 ± 0.7 mm/yr on the Nayband segment and Gowk segment, respectively (Walker et al., 2010). The lower slip rate estimated for the Nayband segment has a discrepancy rate estimated from with

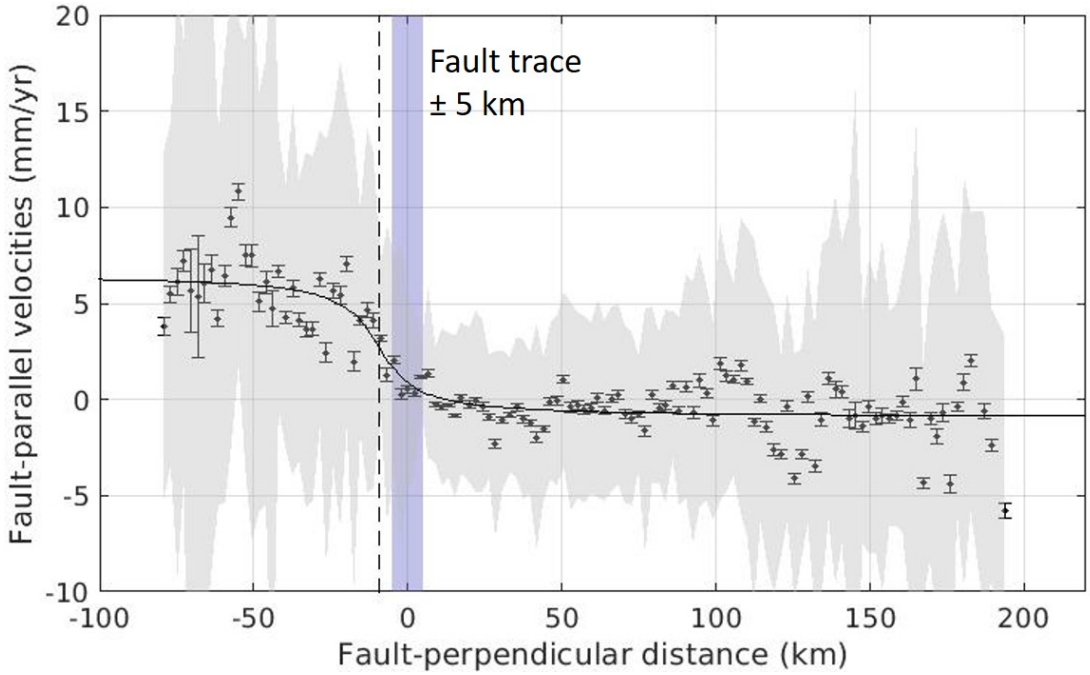

Figure 4.9: Transect showing the north-south velocity field. Points are from 9 burst overlap areas (∼150 km) in each sub-swath, covering the southern segment of the West-Lut fault, between latitude 29°N-30.5°N. The mean azimuth velocities were projected into the fault-parallel direction (347°). Since the fault traces of the Gowk fault is complicated and distributed, the purple shaded vertical band represents a surface trace with a range of ±5 km from simplified fault segment, presented as a pink straight line in Fig. 4.6. Error bars are mean north-south velocities and their standard deviations using a bin width of 2 km. The grey shaded area represents the one standard deviation of the burst overlap InSAR points. The black line represents the best-fitting model of the interseismic strain accumulation using the optimal parameters from the Bayesian approach. Due to the technique's high uncertainty, the assumption that only a single fault accommodates the interseismic deformation across this region is made. This work modeled a fault as a fully locked fault above a freely slipping fault dislocation because no discontinuity is observed in the line-of-sight result to indicate shallow surface creep. The black vertical dashed line is the fault location at 57.53°E from the model.

the present-day geodetic data. The GNSS study (Walpersdorf et al., 2014) proposed a slip rate of 4.4±0.4 mm/yr from their rigid block model and 4.7±1.7 mm/yr from taking a rate difference of the mean velocity from both sides of the fault (Walpersdorf et al., 2014). Likewise, the along-track measurement of InSAR in this paper is consistent with a 4.3±0.5 mm/yr slip rate in the interseismic model.

However, I roughly compared the GNSS velocities only on the western side of the fault (e.g., RAIN (13.55 mm/yr) and NYBD (8.81 mm/yr) stations in Walpersdorf et al. (2014)) and found the variation between the segments at approximately 5 mm/yr, which agrees with the InSAR measurement here. Secondly, at the transition zone between the Nayband and Gowk segments, the Kuhbanan fault appears to join the West-Lut fault and terminate at this conjunction. The slip rate of the Kuhbanan fault at 3–5 mm/yr estimated from the GNSS deformation field suggests that the slip rate

Table 4.3: Slip rate values of the northern and southern segments from different methods (Walker et al. (2010), Walpersdorf et al. (2014)) and this study

Segment	Latitude	Geological Trenching	GNSS	InSAR
Northern	>30.5°N	1.4±0.5	4.4±0.4	4.3±0.5
Southern	<30.5°N	3.8±0.7	4.4±0.4	9.2±0.5

varies by increasing from NW to SE along the fault (Walpersdorf et al., 2014). Therefore, the Gowk segment, the only major tectonic feature at this latitude, is expected to accumulate the strain of the West-Lut fault and the Kuhbanan fault together. The combined slip rate is 6–10 mm/yr depending on whether the values are taken from the rigid block model or the average velocity method (Walpersdorf et al., 2014). However, due to the assumption, this work made to compensate for the limitation of detecting the highly variable structure, this work cannot conclude that the relative motion localizes only along the Gowk fault. Indeed, the idea that the strain distributes over the complex zone could explain the discrepancy of the InSAR measurement and the geological trenching.

In addition, the fault locations estimated from the interseismic modeling are likely too far to the west to the fault trace (Styron and Pagani, 2020). In the southern segment, the shift of 9.8±2 km from the fault trace can be explained by the complexity of the area that comprises bundles of ill-defined secondary structures. These complex structures on the west of the West-Lut fault probably accumulate a part of the tectonic strain. However, due to the limitation of the burst overlap InSAR technique, I cannot take a high variation of deformation in a short distance into account in the modeling. Therefore, the assumption I made that only the single West-Lut fault accumulates the tectonic strain at this latitude might not be valid. Moreover, the western area of the segment is an adjoining area between the West-Lut fault and the Kubanan fault, Anar, and also Rafsanjan faults (Fig.4.2). Even though this work proposes, for the first time, that the Gowk segment accommodate a strain at a similar magnitude to the Nayband segment and Kubanan fault together, a further study on clarifying a structural form of distributed shear beneath these structures is still required.

However, in the northern segment, only the West-Lut fault is clearly a tectonic structure in this area. The fault-parallel velocity deduces the fault location, a horizontal shift of the shear zone at depth to the surface trace, at around 13.6±5 km west of the fault trace. Given where the surface fault trace is accurate, these modeled fault parameters, including a locking depth, indicate the locked portion of the fault dipped ∼60° to the west. However, there is no displacement in a normal component reported or a compressional structure around this latitude. The explanation might be that a fault deformation is in the north-south horizontally, even with a fault dip. Nevertheless,

I propose that the problem is from a limitation of the InSAR observation. The main factor that defines the locking depth and fault location parameters is a variation of ground velocity across a shear zone at the surface. I propose that the technique's precision together with the number of InSAR points in a shear zone are too low to depict an accurate result relative to a gradient of 4 mm/yr interseismic arctangent model. Furthermore, the observational data using in modeling is from an average profile with a length of 140 km section. However, the estimated far-field velocity, which is a long-wavelength signal, is still efficient. I also employed a Bayesian approach with the interseismic model to infer the fault parameters with a fixed fault location at longitude 57.55° (Fig.A.11), a location of fault trace (Styron and Pagani, 2020). I find that the best fit far-field parameter is still the same, and the fault plane locking depth increases. Still, the overall model appears to agree well with the InSAR data. The objective of this study is to clarify the efficiency of the burst overlap InSAR technique. Also, due to an uncertainty of the fault trace and the effect of averaging such a large segment, arbitrarily fixing location can affect the locking depth, which is a factor in seismic hazard evaluation. Thus, in this thesis, I still apply fault parameters that incorporate fault location as a modeled parameter because this model best fits the gradient of the current observational InSAR data. I expect that reducing decorrelation and short-wavelength ionospheric noise enable the technique to provide results with a higher resolution and consequently a more robust model.

For the seismicity, the historical and instrumental earthquake records present bundles of the past seismic events in Tabas and Gowk segments (Fig. 4.10). In contrast, the Nayband segment, the only visible tectonic feature likely that between the Tabas and Gowk segments could transmit the strain, is also only the quiescent part of the West-Lut fault (Walker and Jackson, 2004). For this reason, the earthquake potential on the Nayband segment is of concern given the accumulation of strain along this long straight strike-slip fault segment. However, the level of hazard posed by this fault is mitigated by the low level of population density in this desert region which results in a lower risk due to reduced exposure to any potential ground shaking. This paper proposed one of the possible explanations that the Gowk segment accumulates the higher strain rate two times the Nayband segment. Consequently, this could cause the number of earthquakes significantly higher than it should be compared to the Nayband's number. I expected that most of the unbalanced strain accumulation is released over the multiple secondary faults in the complex zone. Since the velocity from the line-of-sight measurement does not show the discontinuity on the fault, I proposed that the fault has accumulated the strain as fully locked without aseismic slip. The paleoseismic investigation on the Nayband segment reported that the most recent event appears to occur during the last 800 years (Foroutan et al., 2014); therefore, the potential slip for the next rupture is just over 3 m approximately given an accumulation rate of $\sim$4

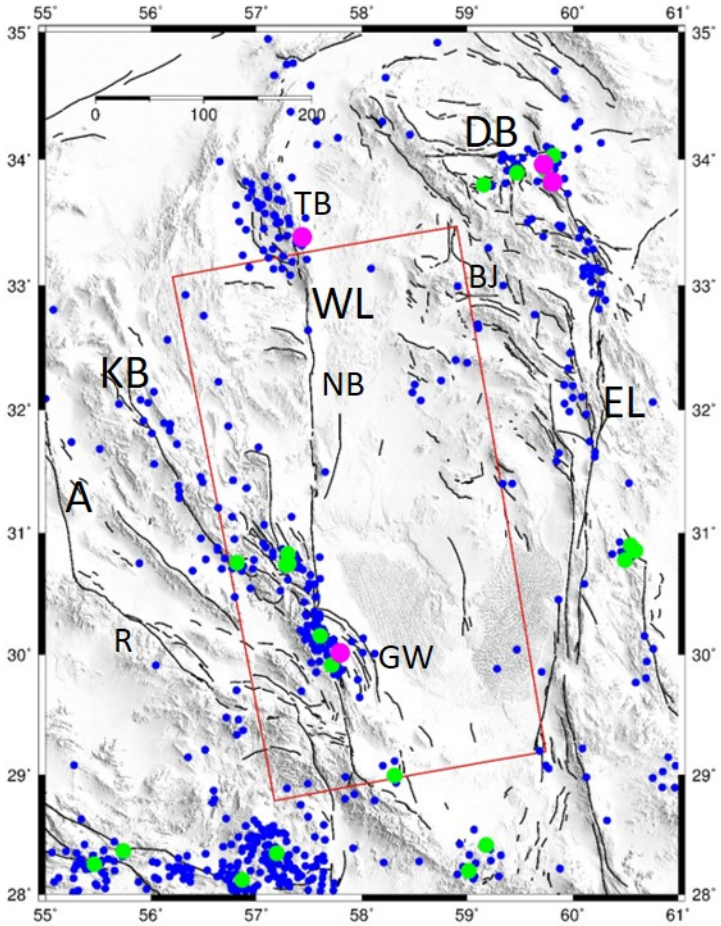

Figure 4.10: Map of major earthquakes in the West-Lut fault region. All data are from USGS catalog (source:https://www.usgs.gov/natural-hazards/earthquake-hazards/earthquakes), which present major earthquake occurred between 1972 and 2020. Blue points represent earthquakes with magnitudes (Mw) between 4.5 and 6. Green dots presents earthquakes magnitude (Mw) between 6 and 7. Pink dots indicate earthquake occurred with magnitude (Mw) higher than 7. The red rectangle denotes the are of coverage from Sentinel-1 used in this study. Black lines represent faults (Walker et al., 2013). Fault names as in Fig. 4.2

mm/yr over that interval, and that all of the previous strain accumulation was released in the last earthquake..

From these recent geodetic results, I estimated the potential earthquake's magnitude of the Nayband segment based on the slip deficit and fault modelling parameters from the inversion. I proposed the seismic moment (M_0) of strike-slip fault and moment magnitude (M_w) using Eq. 4.4 and Eq. 4.5, respectively. The seismic moment is in units of Newton-meters. Where μ is the fault rigidity, assumed at 3.3 x 10^{10} Pa. A is the fault area (m^2), calculated from the fault width (w) estimated from the modelled locking depth and the fault length (l), assumed to be in range of 120-200 km by considering the extent of the Nayband segment. I proposed a fault slip (S), deduced by the accumulated slip deficit. The deficit has built up with a slip rate (s) of 4.3±0.5 mm/yr since the last

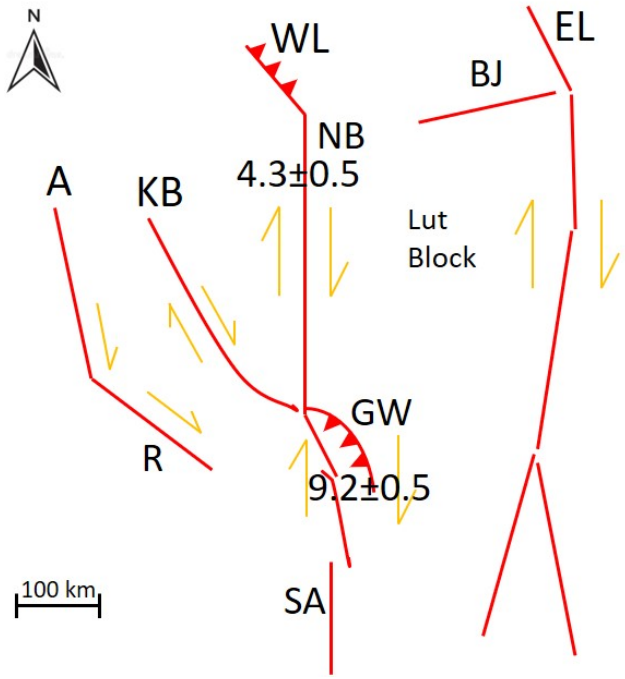

Figure 4.11: A Schematic of tectonic deformation along the West-Lut fault. Red lines approximate major faults in the region around the West-Lut fault (WL). They all accommodate right-lateral shear strain. This figure highlights a variation of the tectonic slip rate between the Nayband segment (NB) and Gowk segment (GW). I suspect that the Gowk segment appears to accommodate a strain rate equal to the northern latitude with both the West-Lut fault and the Kuhbanan fault (KB) accommodate the tectonic strain. A:Anar fault, EL:East-Lut fault, R:Rafsanjan fault, SA:Sabzevaran fault.

earthquake, which reportedly occurred 800 years ago (t) with a 100 years uncertainty, defined for the precision of historical report. I present histograms of the estimation with their uncertainties in Fig. 4.12 and propose the magnitude of potential earthquake at M_w=7.6±0.1.

$$M_0 = \mu \times A \times S = \mu \times wl \times st \tag{4.4}$$

$$M_w = \frac{2}{3}(log_{10}M_0 - 9.1) \tag{4.5}$$

4.6 Conclusion

This chapter has demonstrated the implementation of the algorithm to estimate the low strain rate of the north-south strike-slip fault in Eastern Iran by exploiting the burst overlap area of Sentinel-1 data with a time-series approach. The two main sources of error were taken into account; the strong multilooking reduces the effect of decorrela-

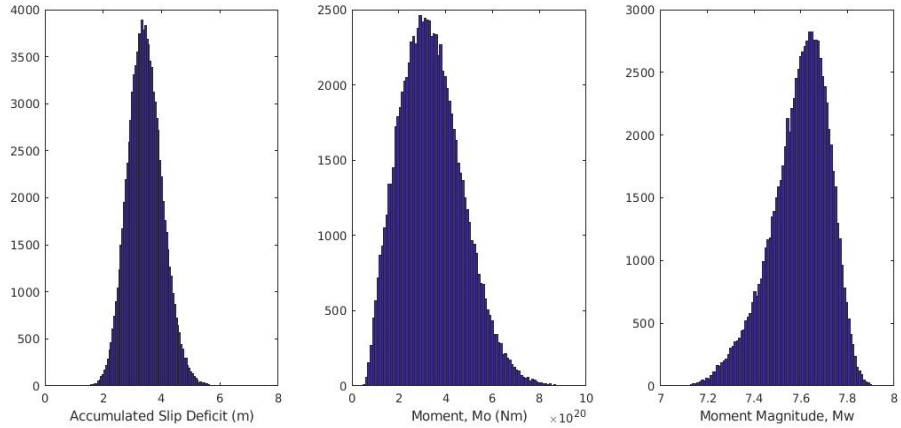

Figure 4.12: Histograms of the accumulated slip deficit since the last earthquake 800 years ago (left), the calculated potential seismic moment given the fault area and slip deficit (middle), and the equivalent moment magnitude (right) of the Nayband segment estimated based on fault modelling parameters shown in Table 4.3

tion noise, and the ionospheric bias is mitigated by applying split-spectrum in range. Since the technique can invert the double-difference interferograms network as an unambiguity analysis, I can apply the NSBAS approach to the wrapped phase without additional process. Although the velocity map cannot clearly present the tectonic strain, the mean velocity profile across the West-Lut fault shows the strain accumulation with a typical arctangent pattern expected of a locked strike-slip fault above a shearing zone at depth. Specifically, in the spatial filtering, averaging from multiple burst overlaps to one-dimensional profile, I exchanged the azimuthal resolution on the order of hundred kilometres to reduce the short-wavelength ionospheric signal, which the current ionospheric correction cannot estimate. The result statistically agrees with GNSS data by using the chi-square test. Moreover, for the tectonics of this region, the results can detect the variation of slip rates between northern and southern portions of the West-Lut faults. I suggest that the southern part probably accumulates a higher strain rate caused by the combined slip of the West-Lut and the adjoining Kuhbanan faults at this southern extent.

The along-track measurement with the accuracy of a few mm/yr from this work presents the potential to address the particular limitation of InSAR measurement to accomplish the measurement of tectonic strain globally, including strike-slip faults orientated along the azimuthal direction of polar orbiting SAR satellites (i.e. in the north-south direction). Furthermore, the descending data for this area, unfortunately, are disturbed by incoherent patches; therefore, analysing these perturbed images needs further investigation on the influence on the InSAR phase or ESD estimation. However, suppose data from ascending and descending are available. In that case, two more components from exploiting points in the burst overlap area can allow the InSAR

Table 4.4: Chi-sq test comparing the along-track InSAR velocities of the northern profile with 7 GNSS sites Walpersdorf et al. (2014). N is a number of along-track InSAR points which are in 1 km in longitude direction from GNSS stations. v (InSAR) mean velocity from N points. SD (InSAR) is a standard deviation of the mean velocity sqrt(17/N). I assumed that the InSAR point has a variance of 17 mm/yr without correlation, estimated from the semivariogram. v (GNSS) is the velocity of the GNSS data in the along-track direction. SD (GPS) is the standard deviation of GNSS data in the along-track direction, calculated from the error ellipse. I estimated a Chi-square distribution from the Residual between two observations by applying the InSAR and GNSS Variance as a Weight. All values in this comparison are in mm/yr.

	InSAR				GNSS					Residual
Station	N	velo	sd	var	velo	sd	var	Variance	Weight	(mm/yr)
1	22	0.3	0.9	0.8	0.4	1.3	1.6	2.3	0.43	-0.1
2	17	2.1	1.0	1.0	1.8	1.6	2.6	3.6	0.28	0.3
3	3	-3.2	2.4	5.7	-2.6	1.6	2.4	8.1	0.12	-0.6
4	5	-1.1	1.8	3.4	-2.4	0.3	0.1	3.5	0.29	1.3
5	17	-2.1	1.0	1.0	-2.7	1.2	1.3	2.3	0.43	0.6
6	19	-3.3	0.9	0.9	-1.0	1.3	1.6	2.5	0.40	-2.3
7	19	-2.2	0.9	0.9	-1.6	1.6	2.5	3.4	0.30	-0.6

technique to constrain the full three-dimensional motion.

Chapter 5

Three-dimensional Deformation along the Chaman Fault from InSAR

In this chapter, I analyse line-of-sight and along-track measurements applied with TOPS Sentinel-1 images acquired over the Chaman fault area in both ascending and descending passes. I demonstrate an algorithm to decompose InSAR velocities to the east, north, and up components. The method includes long-wavelength constraints of the line-of-sight and burst overlap InSAR observations. The algorithm benefit in referencing InSAR velocities to the GNSS reference frame and mitigate the ionospheric disturbance. I also present evolution of surface fault slips during 2014-1018.

5.1 Introduction

In chapter 4, I demonstrated that the burst overlap InSAR technique applied to TOPS Sentinel-1 images is effective in measuring velocities for slow tectonic processes concentrated in the north-south direction. This means that we can use InSAR measurements to provide observations with high sensitivity to all three dimensions. With two independent measurements added to the conventional InSAR, ascending and descending line-of-sight measurements, we can solve directly for all three components where burst overlaps from ascending and descending tracks overlap.

Furthermore, the short revisit time of Sentinel-1 enables more investigation on temporal variation of the geophysical process. This higher frequency of observation benefits not only capturing the time-dependent deformation but also lowering InSAR noise (e.g., APS, orbital error, ionospheric disturbance) in the time-series analysis to enhance a signal of tectonic displacement for sub-periods. Time-series InSAR analysis is used to

study a slow tectonic process by providing a velocity field that represents the averaged deformation over many years. In this chapter, I present the temporal characteristics of surface creeps, including seismic and aseismic fault slips, for segments of the Chaman fault. I demonstrate that modeling the surface creep as a time-dependent process can better explain Sentinel-1's InSAR observation than a single linear analysis.

This chapter applies InSAR data from ascending and descending data to analyse time-series line-of-sight and burst overlap InSAR measurements to estimate the averaged velocities over four years from 2014 to 2018. SAR images cover the area about 400 km along the Chaman Fault in Afghanistan. The fault is a strike-slip fault lying 12°N-35°N dominantly. The InSAR velocities in line-of-sight and along-track components are decomposed into three-dimensional components (i.e., east, north, and up directions). Also, I exploit seismic and aseismic slips for segments of the Chaman fault using time-series products to expand their temporal evolution of surface creep.

5.2 Chaman Fault System

At the continental scale, the Chaman fault system is an on-land segment on the western boundary of the Indian plate. According to the literature, the nearly north-south shear component of 24-28 mm/yr, driven by the India-Eurasia relative motion (i.e., 30 mm/yr at latitude 28°N (Altamimi et al., 2016)), is localized in this transition zone. With a length of more than 900 km long, the fault system comprises a suite of predominant north-south sinistral strike-slip faults. From the shoreline to the latitude 28°N, the Ornah-Nal fault is a major tectonic structure to accommodate the shear component together with a brunch of secondary east-west thrust faults in the west (i.e., Hoshab Fault, Panjgur Fault, and Siahan Fault) (Szeliga et al. (2012) and Fattahi and Amelung (2016)). Further to the north, the Chaman and Ghazaband fault traces are clearly seen. These two faults are parallel to each other with a strike orientation of N22E approximately. At the latitude 30.7°N, the Ghazaband fault trace, referred from the global active faults (Styron and Pagani, 2020), disappears and leaves only the Chaman fault as the only major tectonic at this segment with a higher degree of bending to the east (i.e., N34E). The single fault trace connects with the Gardez fault at around latitude 33°N and terminates around the latitude 35°N (Styron and Pagani, 2020).

Geological studies (Lawrence et al. (1992) and Ul-Hadi et al. (2013)) and global plate tectonic models, such as Kreemer et al. (2014) and Altamimi et al. (2016), propose that the Chaman fault system accommodates most part of the strain accumulation. However, the modern geodetic observation (Szeliga et al. (2012) and Fattahi and Amelung (2016)) presented that the strain is not accommodated by only a single fault. Still, it is distributed over multiple tectonic structures in the region. The first geodetic study (Szeliga et al., 2012) presented a heterogeneous characterization of the

strain accumulation along the fault. In the southern segment, the study applied the GNSS data from a campaign around latitude 26°N and proposed that the Ornah-Nal fault accommodates a strain around 13.4-16.9 mm/yr with a shallow locking depth of about 3 km. Further to the north, in the area where two major faults are parallel to each other, from 7 GNSS stations around latitude 30°N, they presented a slip rate of the Chaman fault around 6.8-10.3 mm/yr with also a shallow locking depth at 3 km. This slip rate broadly agrees with InSAR observation from Fattahi and Amelung (2016), which applied a time-series approach with seven years (i.e., 2004-2011) of Envisat data. Moreover, due to a greatly higher spatial resolution, the InSAR studies (Fattahi and Amelung (2016) and Barnhart (2017)) can detect velocity discontinuities implied to aseismic surface creep on the fault trace. They also presented a variation of fault coupling comprising locking and creeping segments and proposed the creeping rate from 2 to 11 mm/yr. In addition, for the short-wavelength displacement, Furuya and Satyabala (2008) presents an afterslip, a post-seismic deformation, following the 2005 Mw=5.0 Kalat, Afghanistan earthquake.

For the Ghazaband fault, the sub-parallel fault, the InSAR result (Fattahi and Amelung, 2016) presented a slip rate at 16 mm/yr without surface creep. However, the interseismic deformation cannot be detected by the GNSS campaign (Szeliga et al., 2012) around latitude 30°N. This disagreement was explained by Barnhart (2017) that the GNSS stations are located at the fault terminus, and they consequently suggested a variation of strain accumulation associated with the Ghazaband fault. Meanwhile, a transect profile from InSAR measurement around latitude 29°N showed a strain accumulation across two faults at 24 mm/yr, composed of 8±3.1 mm/yr and 16±2.3 mm/yr from the Chaman and Ghazaband fault, respectively. Their interseismic model is consistent with a locking depth of the Ghazaband fault around 10±2 km, and also a locking depth of the Chaman fault around 27±8.7 km, which is much deeper than the estimation from GNSS data.

In the northern segment, where the Chaman fault is the only predominant tectonic structure to accommodate the shear strain, a transect profile of InSAR observation across the fault around latitude 32°N showed a variation of velocity around 10-14 mm/yr explained by a 6.1±1.1 mm/yr accumulated by the Chaman fault and a 6.2±1.1 mm/yr accommodated by an arbitrary fault potentially located 60 km to the west of the Chaman fault. The profile is consistent with a locking depth of the interseismic model at 10 km and a creeping rate along the Chaman fault at 5 mm/yr. On the contrary, the InSAR data from Szeliga et al. (2012), analysed from a set of four-year Envisat data, presented a strain accumulation across the fault at 16.8±2.7 mm/yr localized only on the Chaman fault with a shallow locking depth at 5.4±2.4 km. I suspect that the disagreement of the locking depth between the two studies results from that Szeliga et al. (2012) did not take the existence of the creeping parameter into account.

However, the model and a tectonic interpretation at this latitude are still ambiguous and need further investigation. I suspect that this is a result of an incompatible of the line-of-sight measurement to the fault-parallel velocity.

Despite the high rate at the plate boundary zone (Kreemer et al. (2014) and Altamimi et al. (2016)), the facts from the recently geodetic measurements that the strain is distributed to many structures across the region cause the earthquake potential on the Chaman fault system released from high risk. Furthermore, it is less intense due to the surface creep (Fattahi and Amelung, 2016) and the afterslip (Furuya and Satyabala, 2008), which could give a plausible reason for only five major earthquakes that occurred in the last 200 years along this 1000-km-long fault. Nevertheless, the locking depth is one of the factors to be considered for the magnitude estimation. Also, the interpretation of the strain accumulation, which varies along latitude, is still not unique. Consequently, this study will apply the conventional line-of-sight InSAR together with the along-track measurement, more compatible with the fault geometry, to contribute more proficient data to the Chaman fault system.

5.3 Time-series InSAR Measurement

To study the slow strain accumulation across the Chaman fault system, I conduct a time-series analysis of four years of data between January 2015 and December 2018. I apply two Sentinel-1 SAR image stacks, one with 65 ascending images and one with 64 descending images. The scene coverage is the region between latitude 28.5°N-32.5°N (Fig. 5.1), which includes the southern segment where the Chaman and Ghazaband faults are parallel to each other, as well as the northern segment where the Chaman fault is the only major tectonic structure to accommodate the shear strain.

The fault strike (i.e., N12E-N35E) is almost parallel to the descending ground track direction, ∼190°, so the line-of-sight component in the descending pass is nearly perpendicular to the Chaman fault. Because the majority of the horizontal motion, strike-slip deformation, is parallel to the fault, the line-of-sight velocity contains very little horizontal movement. As a result, line-of-sight displacement detected in descending data is likely to be due to vertical motion. However, the double-difference phase in the along-track direction is highly sensitive to strike-parallel motion and is better suited for observing the strain accumulation across the Chaman strike-slip fault. In addition, I processed an independent measurement from the ascending track with N10.3W heading direction for both line-of-sight and along-track measurements. Note that the ascending data covers an area slightly to the south of the descending data, but most areas are still in common (Fig. 5.1).

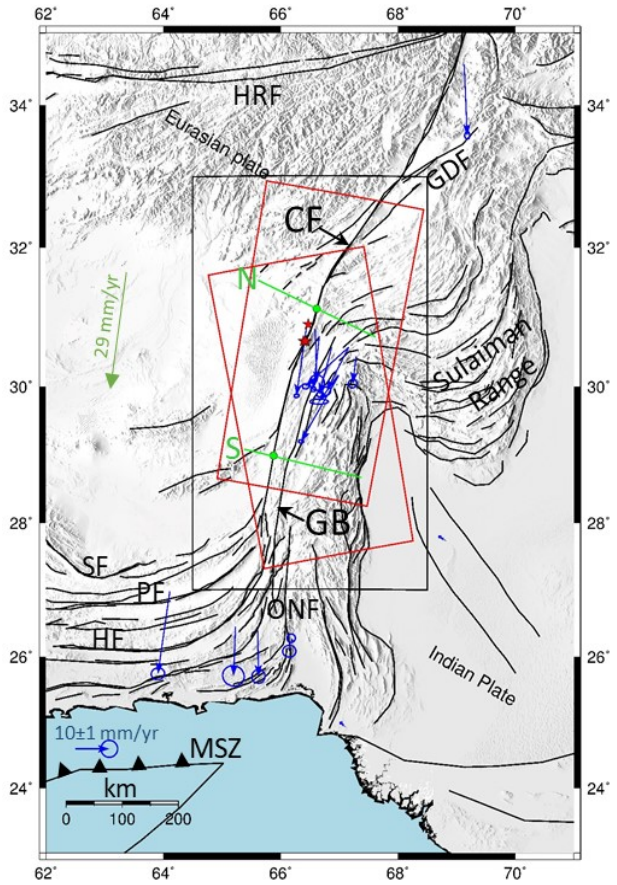

Figure 5.1: Chaman fault study area, denoted by the black rectangle, a boundary that will be used for the following figures to present InSAR results. The red rectangles present the coverages of SAR images from both ascending (∼350°) and descending (∼190°) passes. The green arrow is the velocity of the Eurasian plate relative to the stable Indian plate from the UNAVCO (source: https://www.unavco.org/software/geodetic-utilities/plate-motion-calculator/plate-motion-calculator.html). The blue arrows represent the GNSS data from Szeliga et al. (2012) relative to the Indian plate. The black lines represent faults. CF: Chaman fault, GB: Ghazaband fault, GDF: Gardez fault, HF: Hoshab fault, HRF: Herat fault, MSZ: Makran subduction zone, ONF: Ornach Nal fault, PF: Panjgur fault, SF: Siahan fault. Green lines represent transect profiles, as implemented in the following sections, across a northern segment (N) at latitude 31.1°N and a southern segment (S) at latitude 29°N of the Chaman fault system. The red stars indicate the epicentres of intermediate earthquakes (Mw ∼5.5) that ruptured on 13^{th} May 2016 at latitude 30.66°N and on 11^{th} July 2016 at latitude 30.84°N. These two earthquakes are analysed in more detail in Section 5.5.

5.3.1 Conventional InSAR (Line-of-sight measurement)

I estimate the average velocity of deformation in the line-of-sight direction for 2015-2018 using a small baseline approach. I generate interferogram stacks with the LiCSAR framebatch package (Lazecky et al., 2020). All SAR images are coregistered and resampled to the same alignment with a common primary image, the scenes that were acquired in September 2016. The coregistration procedure consists of rough coregistration based on orbit information and refining coregistration using cross-correlation and ESD techniques (Prats-Iraola et al., 2012). Then, I produce every pair of interferograms in the small baseline network, and the interferograms are multlooked by 8 looks in azimuth and 40 looks in range, which give approximately 100x100 m^2 for the spatial resolution. For each interferogram, I use the GACOS (Generic Atmospheric Correction Online Service for InSAR), which is based on the ECMWF weather model (Yu et al., 2018) to mitigate tropospheric effects.

However, in this study, I cannot obtain an accurate estimate to correct the ionospheric disturbance. This area does not have coherence as high as the West-Lut fault area in Chapter 3. Many interferograms include significant noise, particularly in the desert area, the area to the west of the fault between latitudes 29.5°N-31.5°N, and the mountain area on the east. In the ionospheric estimation, I need to omit points in those areas in many low coherence interferograms. Lack of points in many areas leads to extending the window size in the Fit-plane method, applied in Chapter 3, to extrapolate the ionospheric trend from the existing pixels. Appling the extrapolated model to correct the ionospheric signal can introduce additional bias into measurements, particularly for along-track measurements, which include amplification when converting ESD phase to displacement. According to the line-of-sight velocity fields (Fig. 5.2), the long-wavelength signal, typical of the ionospheric effect, appears to be present only on the ascending data. The descending data does not show a trend across the area for both line-of-sight and along-track velocities. Nevertheless, I mitigate the disturbance in the line-of-sight results using plane referencing (Hussain et al. (2018) and Weiss et al. (2020)). The ionospheric disturbance is mitigated during the step of transforming the line-of-sight velocities into a GNSS reference frame. Long-wavelength signals in InSAR velocities will be constrained based on the GNSS data. I will explain the approach in the next section after achieving the velocity fields from InSAR observations in all components.

The time-series analysis is based on the LiCSBAS package (Morishita et al., 2020), with the inversion performed using an NSBAS approach (López-Quiroz et al. (2009), Doin et al. (2011)). In the procedure, there is a loop closure checking (Hussain et al., 2016) to identify unwrapping errors and discard interferograms with a significant problem, as determined by the percent error, from the network. However, in this Chaman study, most interferograms have unwrapping errors in the southeast areas of

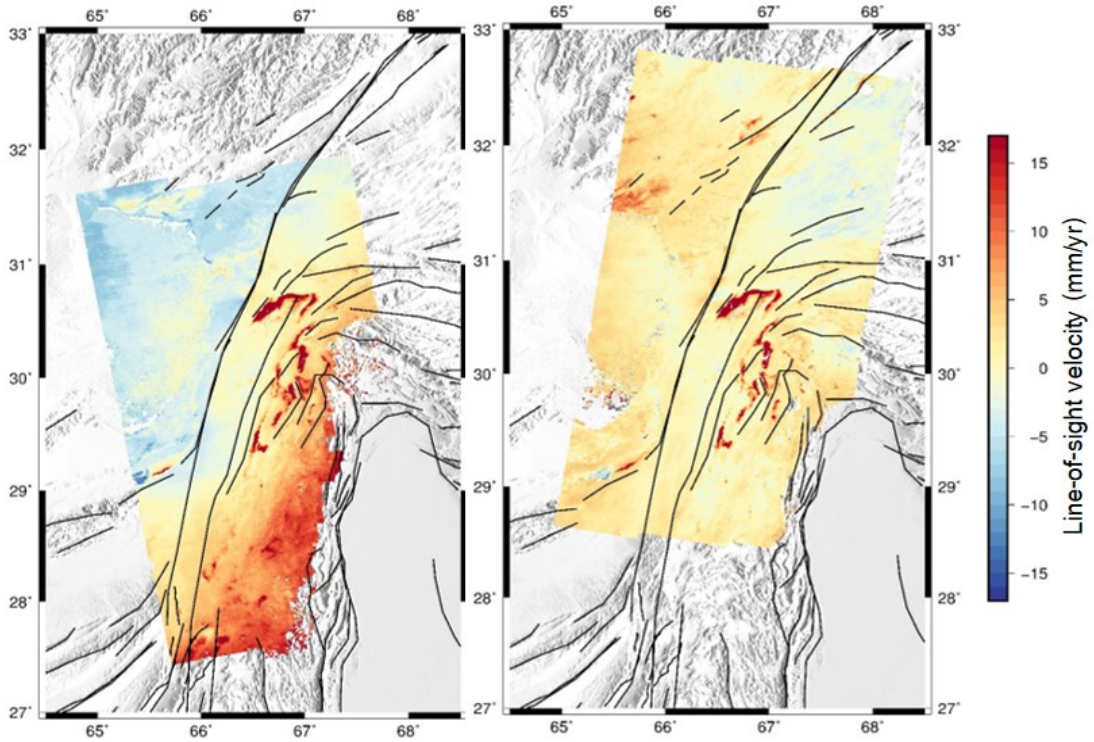

Figure 5.2: Line-of-sight velocities across the Chaman fault area. The results are derived from Sentinel-1 SAR images acquired in ascending (left) and descending (right) passes. The warm shade (red) represents the movement of the ground away from the satellite, while the cool shade (blue) depicts the displacement toward the satellite.

the scene. The issue probably results from a high variation of the topography and the tropospheric signal and leads to the removal of many interferograms from the time-series network. Since the unwrapping problem area is far from the fault trace, I decided to omit pixels in this area before loop closure checking to maintain the number of interferograms and keep the level of redundancy high. As a result, there is no point in the area in the line-of-sight velocity field (Fig. 5.2). Then, I perform the inversion to retrieve single master phases and fit a linear model to the cumulative displacement for each pixel to obtain the average velocities in the line-of-sight direction over four years (i.e., 2015-2018).

5.3.2 Burst overlap InSAR (Along-track measurement)

In order to exploit burst overlap regions, the procedure is the same as demonstrated in Chapter 4. I generate double-difference interferograms from the coregistered SLC images to optimize a correlation. The coregistration includes geometry coregistration, based on orbit information, and refining coregistration that eliminates misregistration offsets estimated by cross-correlation and ESD techniques (Prats-Iraola et al., 2012). The ascending and descending SAR scenes are 25 bursts long in each sub-swath. Then, I can examine 24 burst overlaps for each sub-swath by subtracting backward-looking

phases from forward-looking phases. Due to the particularly low precision of the ESD technique, I apply a strong multilooking to the observed phase with the number of looks approximately 25,000 pixels, giving 1.5 km in azimuth and 0.8 km in range, to decrease decorrelation noise. The expected distribution of the multilooked phase, presented in Chapter 4, is lower than 8 mm for the point with averaged coherence higher than 0.2.

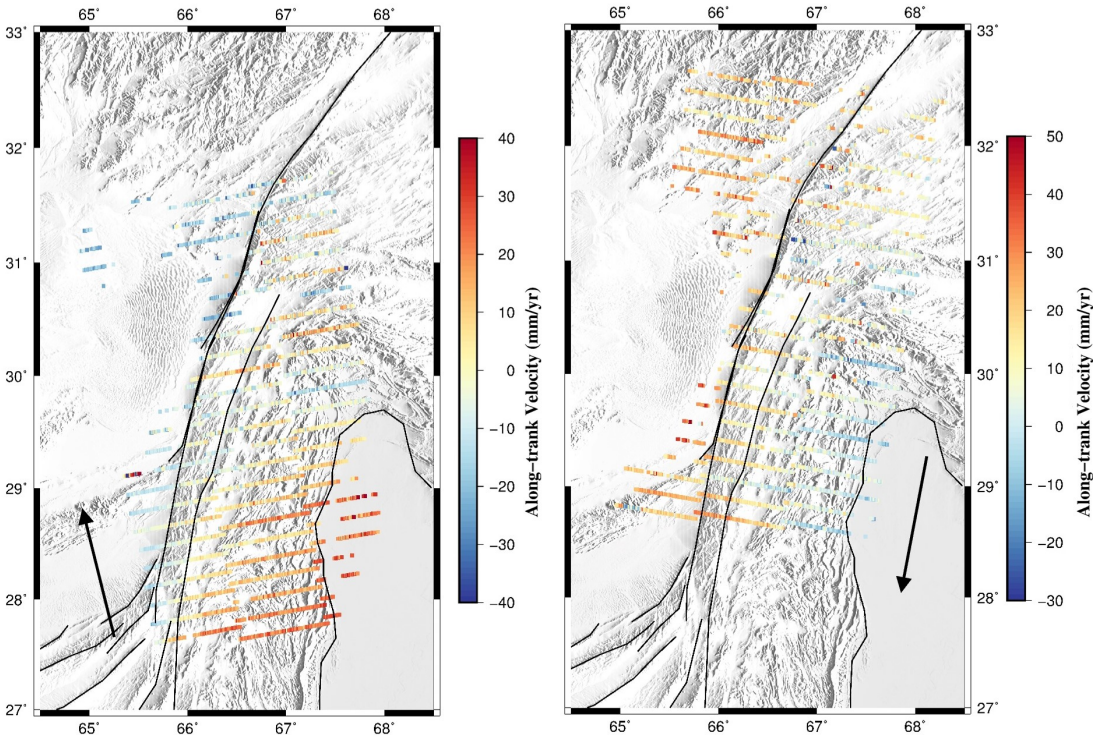

Figure 5.3: Along-track velocities across the Chaman fault area. The plus sign indicates that the ground moves horizontally in the direction of the satellite heading angle (black arrows): a.) the ascending pass (349.7°) and b.) the descending pass (190.3°).

According to the results of the investigation in Chapter 4, I omit the multilooked pixels with coherence lower than 0.2 in each interferogram before applying an inversion. I perform a time-series analysis with an additional constraint to address the potential problem from a discontinuity of the interferogram network. I assume that the inter-seismic deformation progress steadily over four years, so I define linear displacement in the constraint part. After achieving the optimized phase, I fit a straight line to the cumulative displacements and propose a slope as averaged velocity over four years. Note that the inversion is analysed with a wrapped phase under the assumption that there is no displacement greater than the ambiguity band, which is equal to ±710 mm, in a short-temporal interferogram. I present the averaged velocities in the along-track component in Fig. 5.3.

5.4 Three-dimensional deformation

Due to extraction of both line-of-sight and burst overlap InSAR results from the data in ascending and descending passes, this results in that, in certain regions, we observe a ground displacement 3–4 times with different looking components. This redundancy in the overlapping areas between observations allows estimating the surface displacements in three dimensions. In this section, I demonstrate an analysis of velocity decomposition from the InSAR along-track and across-track measurements and also GNSS data (Szeliga et al., 2012). Although the GNSS network across this region is not dense enough to verify the interseismic deformation, the GNSS data is needed for referencing and constraining the long-wavelength signal of the InSAR observations.

Because the line-of-sight InSAR measurements are in individual reference frames, I first use a GNSS network (Szeliga et al., 2012) to transform the line-of-sight velocities to an Indian-fixed reference frame following the method applied in Hussain et al. (2018) and Weiss et al. (2020). The methodology works by constraining a long-wavelength signal in the line-of-sight InSAR velocity field to be consistent with the smoothed long-wavelength displacements derived from GNSS data. Firstly, I project the 7 GNSS velocities (Fig. 5.1), which are located inside InSAR coverage, in horizontal east-west and north-south components into the InSAR-looking direction. Then, I estimate linear planes that best fit the projected GNSS data (Fig. 5.4). Note that Weiss et al. (2020) derived this long-wavelength analysis with second-order polynomial. However, due to the sparse and poor distribution of the GNSS network across this region, I cannot estimate non-linear smoothed displacements precisely.

Then, I fit a linear plane to InSAR line-of-sight velocity fields. Because there is no long-wavelength or systematic vertical displacement in this area, the estimated plane should only infer the horizontal displacement, which is consistent with the GNSS estimates. However, as mentioned in the previous section, ramps remain in the line-of-sight velocities, especially the measurement in ascending pass. I suspect that the long-wavelength signal across the scene is primarily due to the ionospheric disturbance, for which I cannot provide a correction properly. Thus, the long-wavelength signal in the measured line-of-sight velocities (P_{LOS}) comprises signals from a tectonic deformation referenced to the Indian plate (P_{GNSS}), a variation due to different reference frameworks, and noise (mainly the ionospheric signal) ($P_{ref+ion}$).

$$P_{LOS} = P_{GNSS} + P_{ref+ion} \tag{5.1}$$

Therefore, this reference frame transformation, which constrains the long-wavelength signal of InSAR velocity field, can also benefit in mitigating the ionospheric disturbance, which appears as a ramp over the scene. I perform the transformation by removing

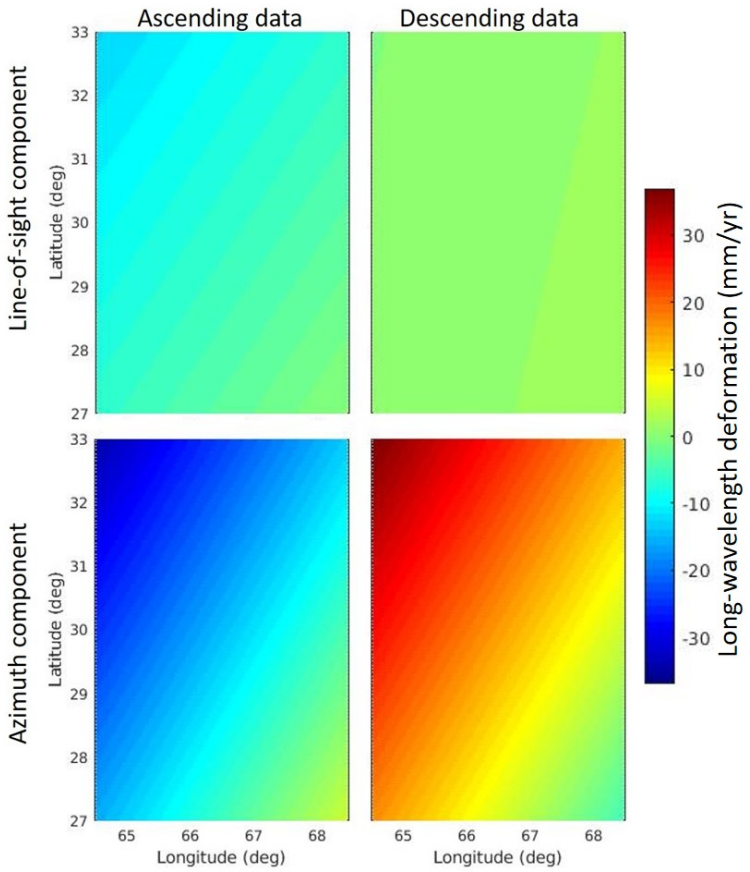

Figure 5.4: The best-fitting linear planes through the GNSS displacements (Szeliga et al., 2012) in four different InSAR observational components. The variations represent long-wavelength signals of horizontal deformation across the Chaman fault. GNSS-derived line-of-sight planes are estimated from 7 GNSS sites within InSAR coverage. GNSS-derived along-track planes are calculated from 18 GNSS stations across the region.

the plane difference (Fig. 5.5) estimated between the GNSS and InSAR data from the InSAR line-of-sight velocity field. The line-of-sight velocities are constrained to the relative motion with the stable Indian plate after subtraction. This long-wavelength subtraction should have no effect on a short-wavelength tectonic signal (e.g., velocity gradients localized close to the fault at the ∼10-km length scale (Weiss et al., 2020)), but the algorithm can improve the long-wavelength constrain to the InSAR velocities, which were disturbed by the ionospheric signal.

For the velocity decomposition, I divided the regular grid with a 10-km grid space to correspond with the spatial resolution of the along-track measurement (0.8x1 km) and calculated mean values of pixels that reside in the grid for each measurement. I assign weight based on the mean uncertainty of the measurements without a correlation. The general form of least square inversion ($d = Gm$) is expressed in the equation as a matrix

form below

$$\begin{bmatrix} LOS_{asc} \\ LOS_{dsc} \\ Az_{asc} \\ Az_{dsc} \end{bmatrix} = \begin{bmatrix} \sin(\theta)\cos(\alpha) & -\sin(\theta)\sin(\alpha) & -\cos(\theta) \\ \sin(\theta)\cos(\alpha) & -\sin(\theta)\sin(\alpha) & -\cos(\theta) \\ \sin(\alpha) & \cos(\alpha) & 0 \\ \sin(\alpha) & \cos(\alpha) & 0 \end{bmatrix} \begin{bmatrix} V_E \\ V_N \\ V_U \end{bmatrix} \tag{5.2}$$

where θ is a local radar incidence angle, α is the azimuth satellite heading angle (e.g., 349.7° on ascending and 190.3° on descending paths at this latitude). d matrix is organized by line-of-sight measurements acquired in ascending and descending tracks, then by the burst overlap InSAR observations from ascending and descending data. The line-of-sight part in the transformation matrix follows Weiss et al. (2020). The plus sign represents the displacement away from the satellite in line-of-sight observations and indicates horizontal ground motion in the direction of the flight path for along-track measurements. The along-track elements are not sensitive to the vertical motion as most of the signals are canceled out in the double interfering. I employ only grids with three or four InSAR measurements for the inversion.

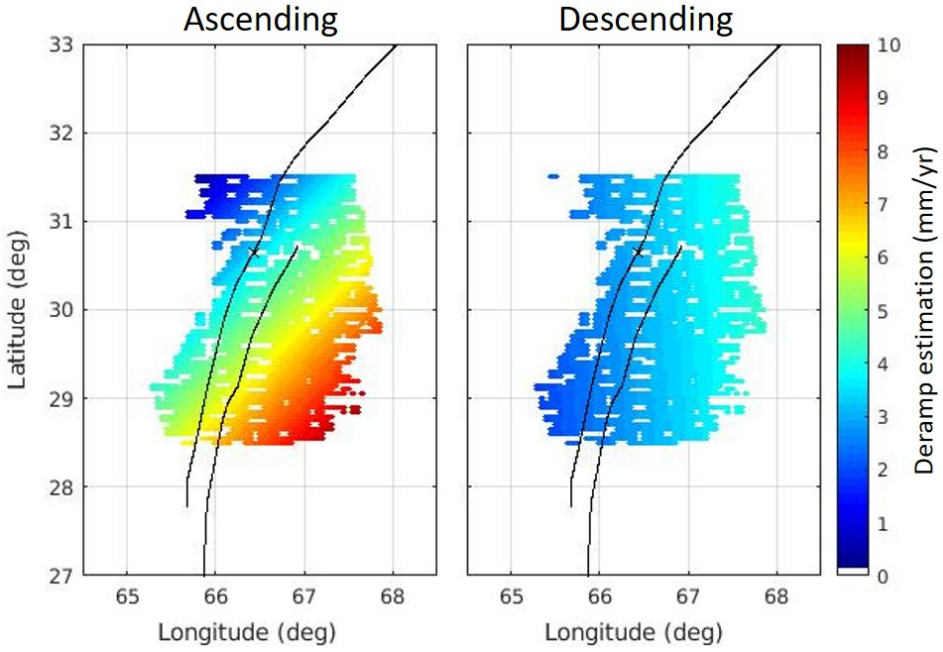

Figure 5.5: Residuals between best-fitting linear planes through GNSS and InSAR line-of-sight velocities. They are planes that I sutract from the line-of-sight velocities to transform the velocity rate map into the stable Indian reference frame before the inversion. They are in the form of a resampled 10 km by 10 km grid.

Again, since I cannot retrieve the accurate ionospheric estimation to mitigate the bias, the burst overlap InSAR results still have the ionospheric effect left in the measurements. The remaining long-wavelength signal influences the inversion by introducing

ramps to the decomposed velocities. Therefore, in addition to the tectonic deformation, I include a part of linear plane estimation into the inversion to respond with the additional long-wavelength signal. I assume that the signal detected in the burst overlap InSAR measurements comprise horizontally along-track motions, variation due to a difference of reference frames and additional long-wavelength signals (mainly ionospheric signal), similar to the assumption for the line-of-sight observations. However, I found that the inversion overestimates the plane and the ground displacements after including the plane estimation. The E-W and vertical velocities estimated from the inversion include ramps over the scene. The rates of E-W and vertical estimation are remarkably high, which is consistent with the planes being overestimated. On the other hand, the N-S velocities still show reasonable rates of displacements. This is most likely due to the along-track measurements provide good constraints on the horizontal north-south displacements.

In the investigation, I found that the fundamental issue is a vertical component in the line-of-sight measurements. The inversion attempts to analyse the additional planes to be consistent with the short-wavelength vertical signal to minimize the residual. Since the plane estimations I include in the inversion are freely independent, I need to provide a better constraint to the plane estimation, using the GNSS velocities field, similar to the approach used with the line-of-sight measurements. I project the 18 GNSS velocities, which are located both inside and outside InSAR coverage (Fig. 5.1), to the burst overlap InSAR components and then estimate the best fitting linear plane to the projected GNSS deformation. Also, I calculate the long-wavelength planes derived from the along-track InSAR observations. Then, I add the difference calculated between the two modeled planes as additional observations in each grid. However, since this additional constraint should influence only the plane estimate, I define a standard deviation of the additional observations in the inversion at 1000 mm/yr to prevent affecting the estimation of three-dimensional displacements. The general form of least square inversion ($d = Gm$) is shown in the equation as a matrix form below (Eq. 5.3).

$$\begin{bmatrix} LOS_{asc} \\ LOS_{dsc} \\ Az_{asc} \\ P_{Aza-GNSSa} \\ Az_{dsc} \\ P_{Azd-GNSSd} \\ GNSS_N \\ GNSSE \end{bmatrix} = \begin{bmatrix} \sin(\theta)\cos(\alpha) & -\sin(\theta)\sin(\alpha) & -\cos(\theta) & 0 & 0 & 0 & 0 & 0 & 0 \\ \sin(\theta)\cos(\alpha) & -\sin(\theta)\sin(\alpha) & -\cos(\theta) & 0 & 0 & 0 & 0 & 0 & 0 \\ \sin(\alpha) & \cos(\alpha) & 0 & lon & lat & 1 & 0 & 0 & 0 \\ 0 & 0 & 0 & lon & lat & 1 & 0 & 0 & 0 \\ \sin(\alpha) & \cos(\alpha) & 0 & 0 & 0 & 0 & lon & lat & 1 \\ 0 & 0 & 0 & 0 & 0 & 0 & lon & lat & 1 \\ 1 & 0 & 0 & 0 & 0 & 0 & 0 & 0 & 0 \\ 0 & 1 & 0 & 0 & 0 & 0 & 0 & 0 & 0 \end{bmatrix} \begin{bmatrix} V_E \\ V_N \\ V_U \\ aA \\ bA \\ cA \\ aD \\ bD \\ cD \end{bmatrix} \tag{5.3}$$

The observational matrix, d, contains measurements from line-of-sight (LOS), along-track (Az) InSAR measurements, and also GNSS observations. P denotes the constraint part, which is addressed using a long-wavelength displacement signal derived from GNSS data. On the right-hand side of the equation, there is a part that is the same as Eq. 5.2, which estimates velocity in three dimensions (V_E, V_N, and V_U). The addition is a GNSS component, as I present an example of a 10x10 km grid cell that contains a GNSS station. Note vertical motion from GNSS measurement is not available so that I can only include observations for horizontal displacement. Another main part is the additional plane (mostly a signal of long-wavelength ionospheric disturbance and a difference between reference frames) for the burst overlap InSAR observations. These inverted additional planes of ascending and descending data are represented in the m matrix by linear plane model coefficients (a, b, and c). *lat* and *lon* represent center latitude and longitude of the grid cell. The example represents the grid points where GNSS data is available. After constructing the full matrix with every grid point, I perform the inversion to estimate the decomposed velocities and plane coefficients for every grid point at the same time.

Fig. 5.6 presents the three-dimensional displacements estimated from the inversion relative to the Indian plate. There are still short-wavelength signals inherited from the along-track measurements. Specifically, the effect is a jump of the velocities , which are seen in a shape of the burst overlap region, such as the area around longitude 66°E-67°E at latitude 30°N. However, the overall decomposed velocities show that the deformation across the Chaman fault region is mainly concentrated in the north-south component with a left-lateral sense. The east-west velocities are also consistent with the left-lateral strike-slip motion with the fault strike to NNE direction. The vertical displacements can reveal land subsidences in cities of Pishin district, of Balochistan province, Pakistan. The analysis does not seem to overestimate the displacements as the inversion without the additional constraint. The best-fitting planes derived from the inversion, which could be referred to as the ionospheric mitigation, are presented in Fig. 5.7 in the along-track components.

I show the transect profiles through the observational InSAR velocities across the Chaman fault at latitude 31°N in Fig. 5.8. The profile at this latitude illustrate the deformation of the area that the Chaman fault is the only predominant tectonic structure to accommodate strain. Since the burst overlap InSAR includes a high variation induced by the short-wavelength ionospheric signal, the noise also contributes to the decomposed velocities. Thus, I need to enhance the deformation signal by incorporating areas that cover multiple burst overlaps in each sub-swath to be projected to the transect profile. This spatial filtering works well with nine burst overlap averaging in Chapter 4. However, with a higher slip rate of the Chaman fault, incorporating five burst overlaps, corresponding about 80 km long in the north-south direction, could be

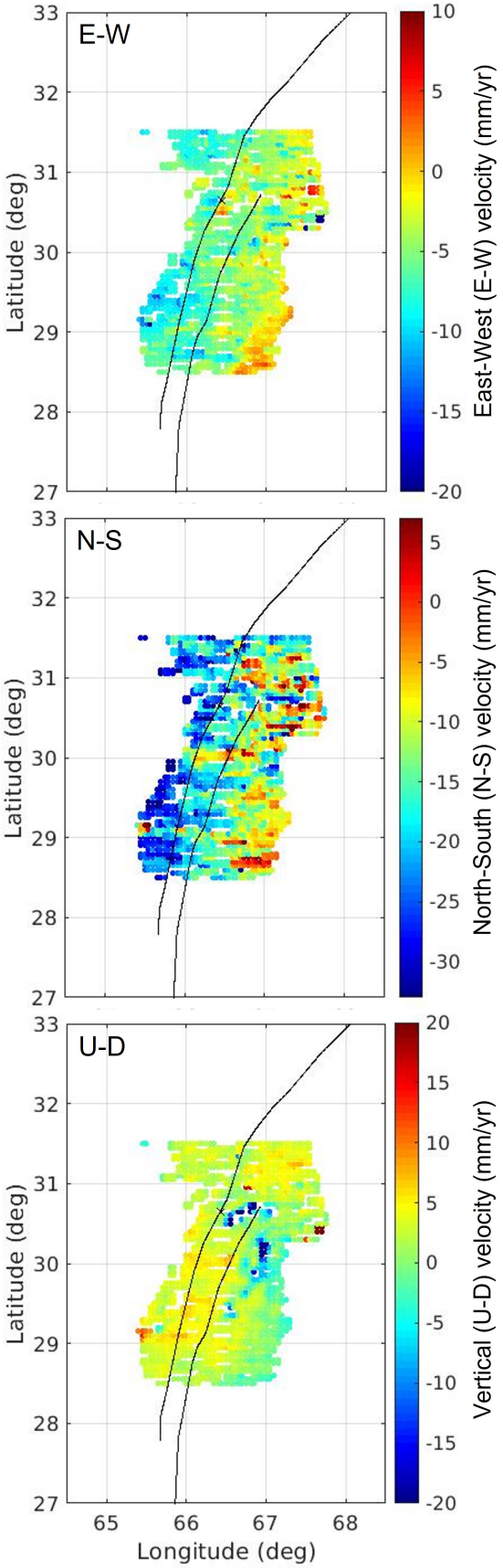

Figure 5.6: Decomposed velocities in east, north , and up directions. The black lines display the locations of the Chaman fault (west) and the Ghazaband fault (east) (Styron and Pagani, 2020).

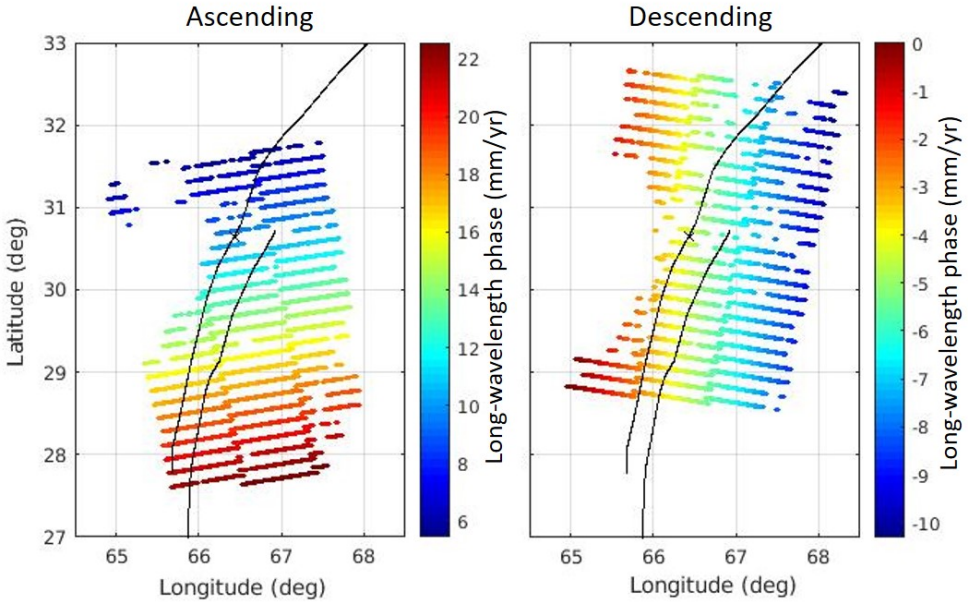

Figure 5.7: Long-wavelength phase estimated from the inversion. They present the additional values removed from the burst overlap InSAR during the inversion to order to minimize residuals in velocity decomposition. The values are calculated from the linear plane parameters for burst overlap InSAR pixels. a.) is the plane for the ascending data observation. b.) is the estimated plane for the descending data. The coefficients of linear polynomial surface models are shown in Table 5.1.

enough to enhance the deformation signal. To evaluate the transect profile with this particular width, I use a least-square inversion to fit a line to the fault surface coordinates (Styron and Pagani, 2020) between latitude 30.7°N-31.5°N and estimate the fault strike over the 80-km segment. I assume that the estimated line represents the fault trace. The average fault strike of this segment is at 24°.

Fig. 5.8c and 5.8d present the line-of-sight velocity profiles after applying the deramp based on the GNSS data to the line-of-sight measurement (Fig. 5.8a and 5.8b). The plus sign denotes that the ground moves away from the SAR sensor. The along-track velocity profiles are shown in Fig. 5.8e and 5.8f. The plus sign indicates the motion in the direction of the satellite heading angle.

Fig. 5.9 presents the transect profile through the decomposed velocities. The plus sign indicates the ground move to the east, north, and up directions. Fig. 5.9d shows the horizontal fault-parallel velocities derived from E-W and N-S deformations. To infer interseismic modeling parameters, I use a Bayesian approach with the GBIS algorithm (Bagnardi and Hooper, 2018) on the mean velocity profile based on the elastic half-space model (Savage and Burford, 1973). I assume that this segment is fully locked since the spatial resolution (10 km x 10 km) of the estimation is limited to detect high variable displacement, a fault surface creep in this study. I display the best-fitting model to the fault-parallel velocities derived from the three-dimensional estimation in

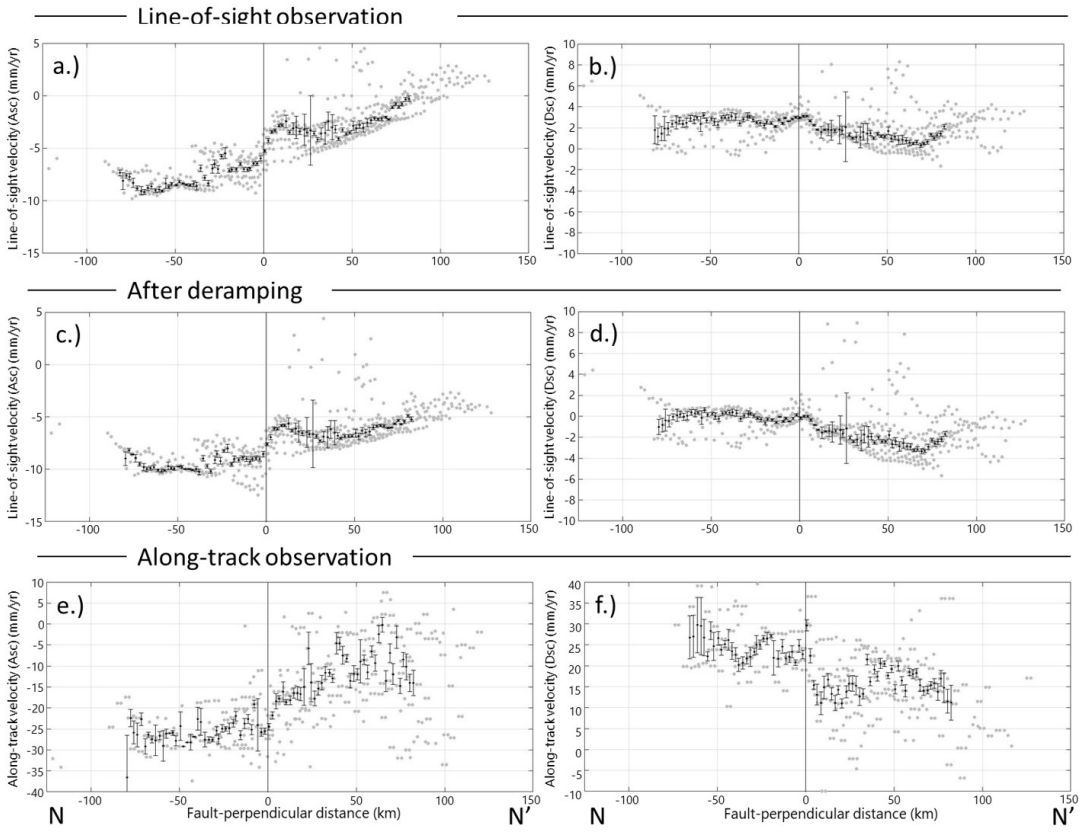

Figure 5.8: Transect profiles through the InSAR observational grid points. The transect profile is located at latitude 31°N, profile (N-N') in Fig. 5.1, and perpendicular to the strike of the simplified fault segment (24°). The vertical line represents the Chaman fault trace (Styron and Pagani, 2020). The grey dots show the averaged velocities of each grid point projected within ±40 km from the perpendicular profile. The errorbars present mean velocity profiles averaged from every 2-km bin. The lengths of the errorbars define one standard deviation of the mean velocities analysed on the number of InSAR points in each bin. a.) and b.) present the line-of-sight velocities before the deramping. c.) and d.) are the profiles after the ramp has been removed. The plus sign depicts the displacement away from the satellite. e.) and f.) present the along-track InSAR velocities. The plus sign indicates that the ground move in the same direction as the satellite's heading angle (i.e., 349.7° on ascending and 190.3° on descending passes).

Fig. 5.10 and present the optimal fault parameters with the interval from posterior distributions in Table 5.2.

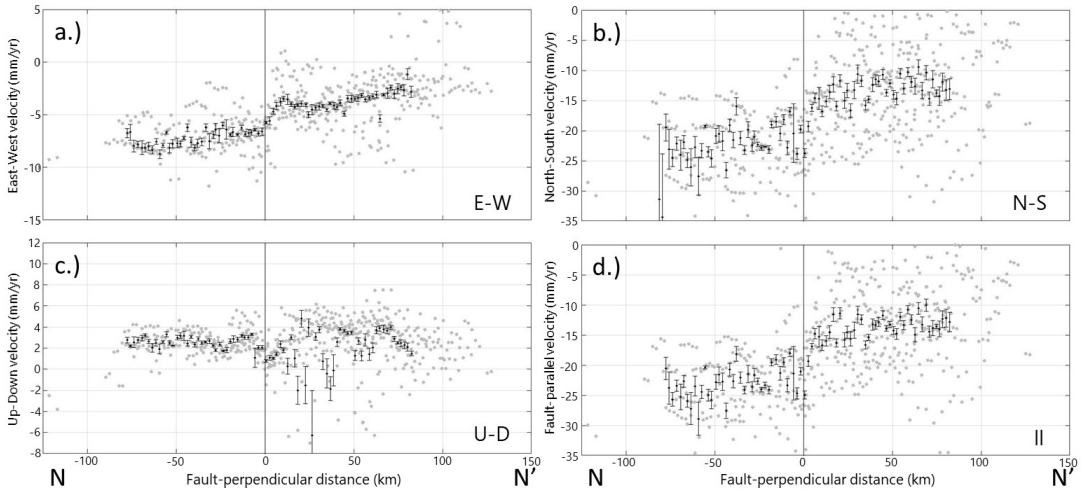

Figure 5.9: Transect profiles through the decomposed velocities estimated from the InSAR observations (Fig. 5.8) at latitude 31°N, profile (N-N') in Fig. 5.1. The vertical line represents the Chaman fault trace (Styron and Pagani, 2020). The grey dots are the average of decomposed velocities of each grid point projected from within ±40 km from the perpendicular profile. The errorbars present mean velocities averaged over each 2-km bin. The lengths of the errorbars define one standard deviation of the mean velocities analysed on the number of InSAR points in each bin. The deformation is shown in a.), b.), and c.) in the east, north, and up directions, respectively. d.) shows the velocity profile in the fault-parallel component.

In comparison with Fattahi and Amelung (2016), this profile is about 100 km south of the profile in Fattahi and Amelung, 2016; however, these two profiles present the deformation of segments where only Chaman fault is prominent in accumulating tectonic strain. The fault slip rate, which is at 10.4±0.4 mm/yr, is still consistent within the levels of precision with the 12±1.5 mm/yr strain rate proposed in Fattahi and Amelung (2016) with the profile at nearly latitude 31.8°N. Nevertheless, they suggested that the slip rate is composed of 6.1±1.1 mm/yr along the Chaman fault and another 6.2±1.1 mm/yr on the unknown fault 60 km to the east of the Chaman fault. Nevertheless, the results presented in this chapter are unable to detect the proposed fault and imply that all strain accumulation is localized only along the Chaman fault.

In the southern segment, I show a transect profile across the Chaman fault in the area around latitude 29°N (Fig. 5.11), where the Ghazaband fault parallels to the Chaman fault. I also perform the same analysis as the northern profile to simplify the fault segment. I fit a straight line to the fault coordinate between latitude 28.6°N and 29.5°N, and use a local fault strike at 12°N to project the decomposed velocities locate from within ±40 km from the profile to the fault-perpendicular distance. In the figure, I present the location of the Chaman fault at 0 km and propose the Ghazaband fault at 24 km using the fault coordinates from Styron and Pagani (2020). Note that

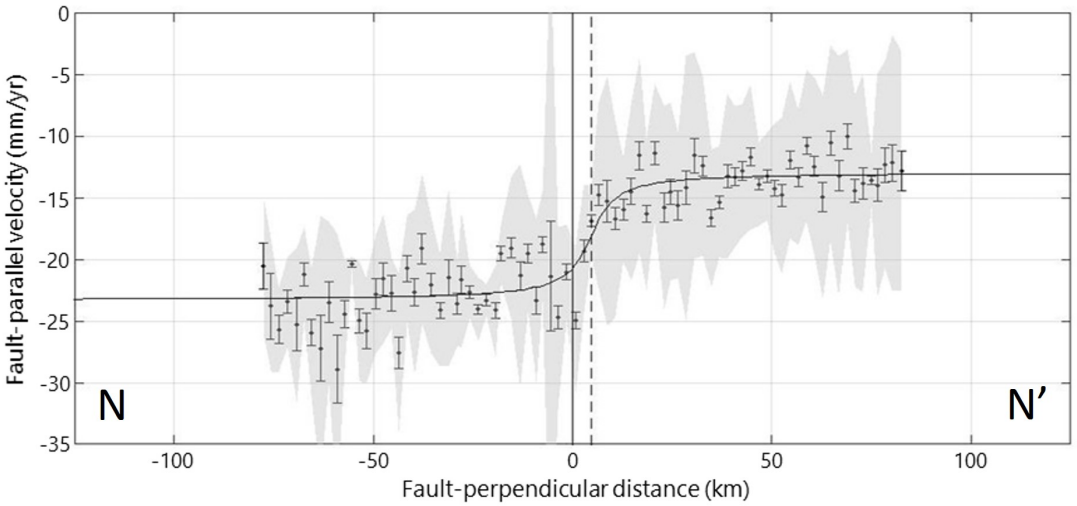

Figure 5.10: The best-fitting model of the interseismic strain accumulation across the Chaman fault at latitude 31°N, profile (N-N') in Fig. 5.1. The optimal source parameters are determined using a Bayesian approach, applied with a mean fault-parallel velocity profile (Fig. 5.9d) calculated from each 2-km bin. The grey shaded area represents one standard deviation of InSAR point scatters for each bin. The errorbars represent the mean velocities in a fault-perpendicular direction of each 2-km bin. The lengths of the errorbars define one standard deviation of the mean velocities analysed on the number of InSAR points in each bin. The model is most consistent with a slip rate of 10.4±0.4, locking depth at 4.6±1.8, fault location at 4.6±0.8, and averaged velocity of 18.1±0.1 mm/yr to the southwest.

Fattahi and Amelung (2016) modeled profile velocity across the faults at the same latitude at 29°N and proposed the location of the Ghazaband fault at 40 km away from the Chaman fault. The decomposed velocities reveal that the deformation is concentrated in the north-south component, with a significant variation across two faults (Fig. 5.11). However, due to omitting points with unwrapping error in the line-of-sight InSAR ascending measurements, there are not enough points to estimate far-field velocities in the mountain area east of the Ghazaband fault. Nonetheless, since the burst overlap InSAR measurement does not have the unwrapping problem, the along-track observations are still useful in this area.

Therefore, I use the along-track measurements to estimate the interseismic model at this latitude 29°N. Firstly, I estimate and remove planes from the along-track observations using the linear polynomial models (Fig. 5.7), inferred from the inversion. This subtraction can reduce the ionospheric disturbance in the measurements while also constraining the most long-wavelength signal of the along-track observations. I still use the same simplified fault segment and properties of transect profiles that I used previously with the decomposed velocities. I project all the burst overlap InSAR points located from within 40 km from the profile to the transect distance. Since the observational component of the along-track descending measurement (190.3°) is almost parallel to the fault strike (12°), the observation is most sensitive to fault-parallel

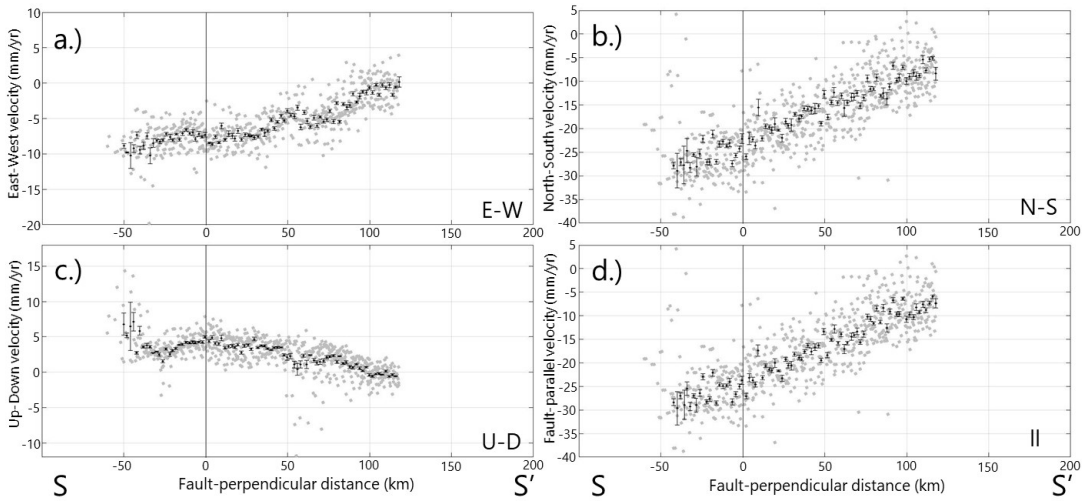

Figure 5.11: Transect profiles through the decomposed velocities estimated from the InSAR observations at latitude 29°N, profile (S-S') in Fig. 5.1. The vertical line represents the Chaman fault trace (Styron and Pagani, 2020). The grey dots are mean values of decomposed velocities of each grid point projected from within ±40 km from the perpendicular profile. The errorbars present mean velocities averaged over each 2-km bin. The lengths of the errorbars define one standard deviation of the mean velocities analysed on the number of InSAR points in each bin. a.), b.), and c.) show displacements in east, north, and up directions, respectively. d.) presents the velocity profile in the fault-parallel component.

Table 5.1: The coefficient of the linear polynomial surface model estimated from the inversion. $z = ax + by + c$ where x is longitude in degree and y is latitude in degree

Data	a	b	c
Ascending	0.89	-4.1	76.4
Descending	-3.23	0.14	205.8

displacements. On the other hand, the ascending observational component (349.7°) diverts from the fault strike about 22°, so the measurements also include deformation in a normal component. Thus, I estimate the displacement in the fault-perpendicular direction from the decomposed velocities. Fig. 5.12 shows the transect profile, which has the same profile properties as above, through the velocities (blue points) in the normal component and the mean velocity with a 2-km bin width (red line). Then, I project them into the ascending along-track component and subtract these averaged normal displacements from the ascending along-track measurements before converting the measurement to the fault-parallel component (Fig. 5.13a). Specifically, the residual of ascending measurements after the subtraction should only indicate the fault-parallel deformation. Fig. 5.13b presents the transect profiles through the descending along-track observations. The profile reveals a similar trend and benefits in having points in the transect distance between 100-150 km to constrain the far-field velocities.

I take advantage of measurement redundancy by plotting the observations from

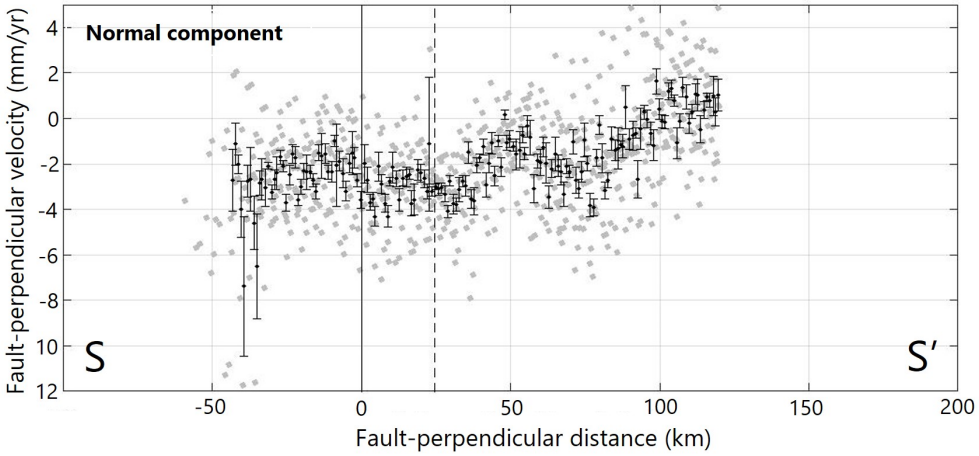

Figure 5.12: Transect profile of the fault-perpendicular velocities (normal component) across the Chaman and Ghazaband faults at latitude 29°N, profile (S-S') in Fig. 5.1. The displacement (grey dots) are projected from the decomposed velocities into 282°, which corresponds to the local fault strike 12°. The vertical line represents the Chaman fault trace (Styron and Pagani, 2020). The dashed line represents the approximate location of the Ghazaband fault, based on fault trace coordinates from Styron and Pagani (2020). The errorbars represent the mean velocity with a bin width 2 km. The lengths of the errorbars define one standard deviation of the mean velocities analysed on the number of InSAR points in each bin.

ascending and descending passes together and estimating the mean velocity with 1-km bin width from both of the data (Fig. 5.13c). The variation of mean velocities shows a total slip rate of roughly 20 mm/yr across this region, with left-lateral slip. I also estimate the fault parameters associated with the interseismic model using a Bayesian approach modified by Bagnardi and Hooper (2018). I define the model with two faults that run parallel to each other, and are both fully locked. I bound ±30 mm/yr for slip rate, ±50 km for locking depth, and ±200 km for fault locations to constrain parameters of two faults. I present the best-fitting model with the observations in Fig. 5.14 and show the model parameters in Table 5.2. The magnitude of slip rates across the Chaman fault are slightly lower than the estimation of 8.1±3.2 mm/yr in Fattahi and Amelung (2016), but they still agree within the level of precision. On the other hand, the locking depths are significantly different. This probably a result of modeling the fault without the surface creep parameter in this study. Furthermore, the modeling is most consistent with the fault location of the Ghazaband fault being roughly 63 km away from the Chaman fault trace, while the locations of the Ghazaband fault are proposed at 25 km and 40 km from the Chaman fault from Styron and Pagani (2020) and Fattahi and Amelung (2016), respectively. I suspect that there probably be other tectonic structures than the Chaman and Ghazaband faults associated with the strain accommodation in this area. The technique's most significant limitation is a low spatial resolution, which makes it difficult to identify high variable deformation. If we can reduce noise in the along-track measurement, we can eliminate and resolve this

Table 5.2: The best fitting Model Parameters for the Northern (latitude 31°N) and Southern (latitude 29°N) fault segment transects across the Chaman fault. The model parameters are estimated from Bayesian approach using data points in burst overlaps shown in Fig. 5.10 and Fig. 5.14.

Model parameters	Northern profile	Southern profile
Chaman Fault		
Slip Rate (mm/yr)	10.4±0.4	5.5±0.8
Locking Depth (km)	4.6±1.8	4.0±2.6
Fault Location (km)	4.6±0.8	3.3±1.7
Offset (mm/yr)	18.1±0.1	16.7±0.1
Ghazaband Fault		
Slip Rate (mm/yr)	-	15.5±0.9
Locking Depth (km)	-	14.9±1.9
Fault Location (km)	-	67.7±1.3

disagreement.

In addition, I present the InSAR observation after constraining the long-wavelength signals in Fig. 5.15 and Fig. 5.16. All velocities are referenced to an Indian-fixed reference frame.

5.5 Aseismic and seismic fault slip along the Chaman fault

Shallow creep along the Chaman fault was identified by (Fattahi and Amelung, 2016), and the spatial variation of creep rate was investigated by (Barnhart, 2017). In the InSAR measurement, the displacement associated with subtle motion is normally assumed to progress steadily over years of time span. However, Jolivet et al. (2013) demonstrated that we can investigate surface creep as an episodic process rather than linear displacement using InSAR measurement. To take advantage of the high-temporal resolution of Sentinel-1's observation, I also review temporal evolutions of fault slips from time-series analysis on particular profiles. I infer the episodic line-of-sight displacements using the estimated phase evolution, the single-master phase, from the NSBAS inversion. Since the burst overlap InSAR still has limitations in detecting the highly variable deformation, the ascending line-of-sight result is more compatible with detecting the Chaman's surface creep due to higher resolution and precision than the along-track measurements.

For a particular transect profile, I select line-of-sight measurements 10 km from the fault trace and use least-square analysis to fit lines to points on each side of the fault. For example, in Fig. 5.18(a), I fit lines to fault-parallel velocity profile, which is divided into points on the western (blue) and eastern (red) sides of the fault by the fault trace (vertical dashed line). The offset of the two lines at the fault trace can

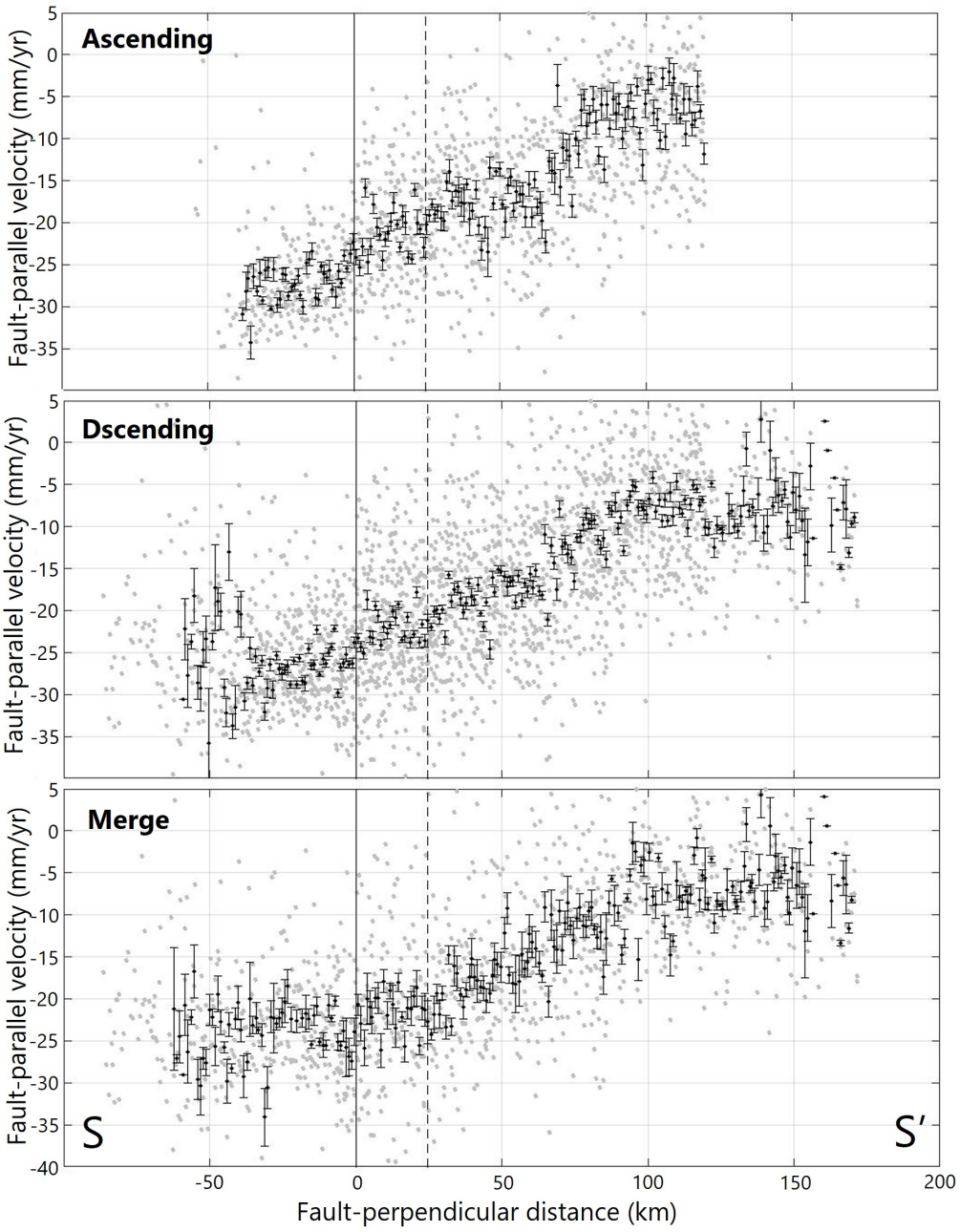

Figure 5.13: Transect profiles through the fault-parallel velocities estimated from burst overlap InSAR measurements after deramping at latitude 29°N, profile (S-S') in Fig. 5.1. The vertical line represents the Chaman fault trace (Styron and Pagani, 2020). The dashed line represents the approximate location of the Ghazaband fault relative to the Chaman fault, based on fault trace coordinates from Styron and Pagani (2020). The grey dots are the along-track InSAR measurements projected to the fault-parallel direction (∼12°). The velocities are in the Indian-fixed reference frame. The errorbars present mean velocities averaged over each 1-km bin. The lengths of the errorbars define one standard deviation of the mean velocities analysed on the number of InSAR points in each bin. a.) and b.) present the observations from the ascending and descending passes, respectively. c.) present the InSAR points and the mean fault-parallel velocities of both ascending and descending observations together.

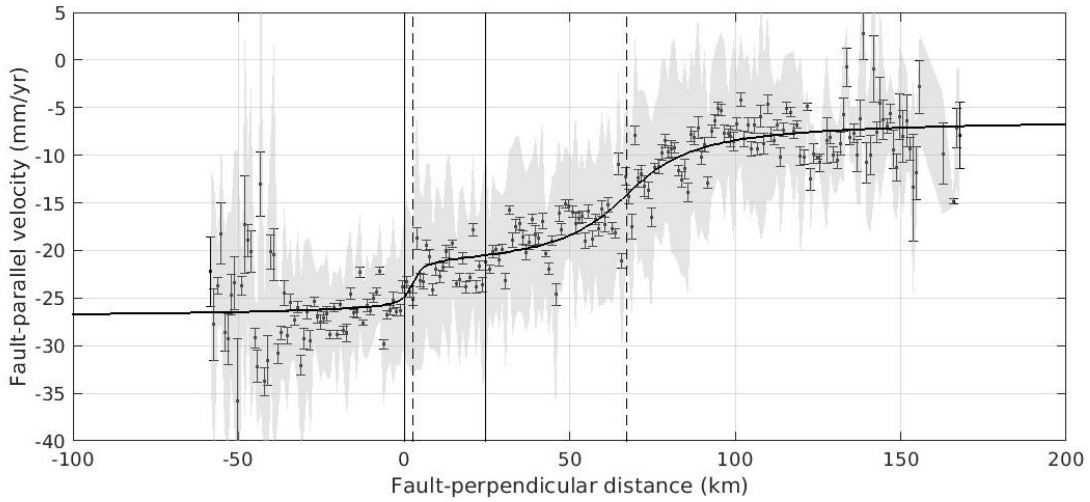

Figure 5.14: The best-fitting model of the interseismic strain accumulation across the Chaman and Ghazaband faults at latitude 29°N. The optimal source parameters are determined using a Bayesian approach, applied with the mean fault-parallel velocity profile (Fig. 5.13c) calculated from each 1-km bin. The errorbars represent the mean velocities of each 1-km bin in fault-perpendicular direction. The lengths of the errorbars define one standard deviation of the mean velocities analysed on the number of InSAR points in each bin. The grey shaded area displays one standard deviation of the InSAR point scatters for each bin. The vertical lines at 0 km and 24 km represent the Chaman and Ghazaband fault traces, respectively, approximated using (Styron and Pagani, 2020). In comparison, the dashed lines present the fault location determined by the inversion (at 1.1 km for the Chaman fault and 68.1 km for the Ghazaband fault). For the Chaman fault, the model is most consistent with a slip rate of 5.1±0.4 mm/yr, locking depth at 2.89±1.2 km, fault location at 1.1±1.1 km, and averaged velocity of 16.7±0.1 mm/yr to the southwest. The best-fitting model for the Ghazaband fault gives the fault parameter with a slip rate of 15.4±0.6 mm/yr, locking depth at 16.9±1.8 km, and fault location at 68.1±1.2 km.

be interpreted as an averaged creep rate over four years of data. On the other hand, I do the same thing, but with the single-master phase from the NSBAS inversion at each epoch rather than average velocities, and determine the evolution of displacement offsets over time. In Fig. 5.18(b), I present the cumulative fault slip at each epoch, with the first acquisitions as a reference. Since the selected InSAR points have the largest separation at 20 km, the long-wavelength signal (e.g., ionospheric disturbance) should not significantly bias the fault offset. Furthermore, due to the lack of highly topographic variation, the tropospheric contribution should only be associated with turbulence. This distribution can be mitigated by the estimation of the fault offset using a fitting line to the points on each side of the fault. The analysis can also absorb the long-wavelength signal, which is unrelated to fault creep but still influences this short distance. However, the short-wavelength effect still remains in the cumulative offset, as we can see by the scattering of the red points in Fig. 5.18(b). Note that I derive the phase evolutions which are smoothed by the temporal filter with a 72-day window size and spatial filtering to estimate the cumulative fault offsets. Thus, the

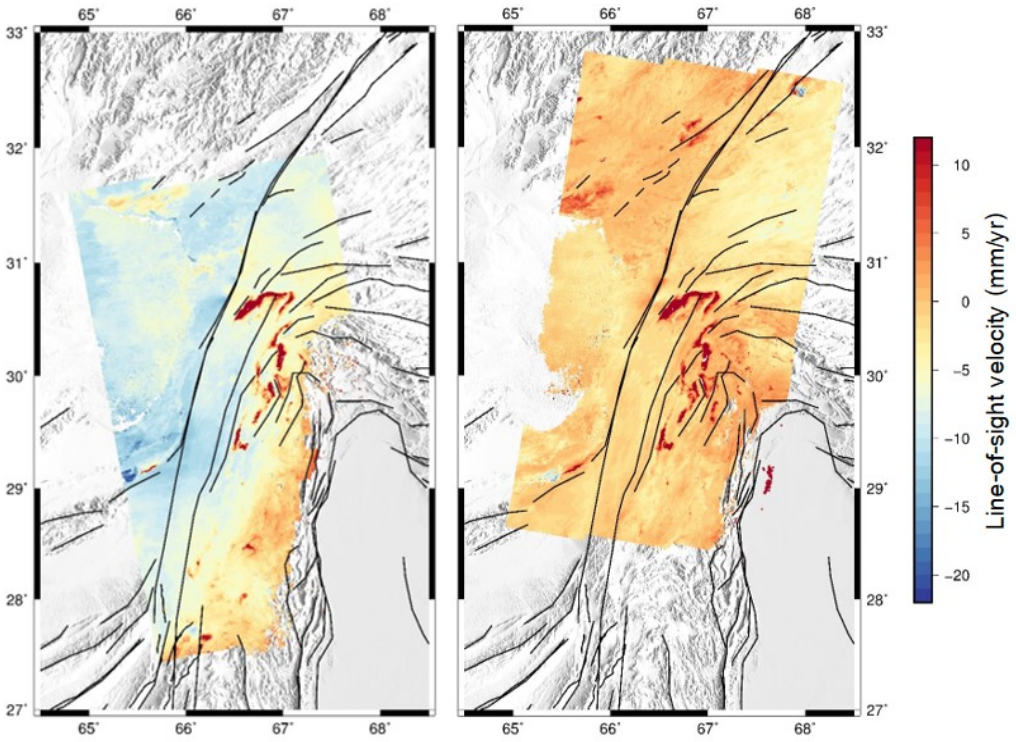

Figure 5.15: Line-of-sight velocities across the Chaman fault area after removing long-wavelength plane. The results are derived from Sentinel-1 SAR images acquired in ascending (left) and descending (right) passes. The warm shade (red) represents the movement of the ground away from the satellite, while the cool shade (blue) depicts the displacement toward the satellite.

actual observed offset includes more noise than the estimation, and there is a bias from the filtering. Then, the work that requires a precise displacement magnitude needs to consider the effect of this temporal filtering. However, the performance of temporal filtering can enhance clearer signals and reveal trends of displacement.

During the period 2014-2018, two intermediate earthquakes occurred along the Chaman fault segment studied in this study. I found that there are profiles influenced by these earthquakes, even segments that are 10s km away from the epicentres. Thus, I include these ruptures in the figures by presenting the first event with magnitude (Mw) 5.5 that occurred on 13^{th} May 2016, as the vertical line at 533 days from the first epoch. I plot the second earthquake, which occurred on 11^{th} July 2016 with magnitude (Mw) 4.7, as the dashed line at 592 days after the first acquisition. As the cumulative offsets still have noise disturbed, I enhance the displacement signals by fitting linear lines (blue lines in Fig. 5.18(b)) and propose the slopes as creep rates for sub-periods, which are divided by the earthquakes.

In Fig. 5.18, two profiles represent the temporal characteristics of fault slips from two transect profiles plotted with lowercase letters in Fig. 5.17. The offset processes

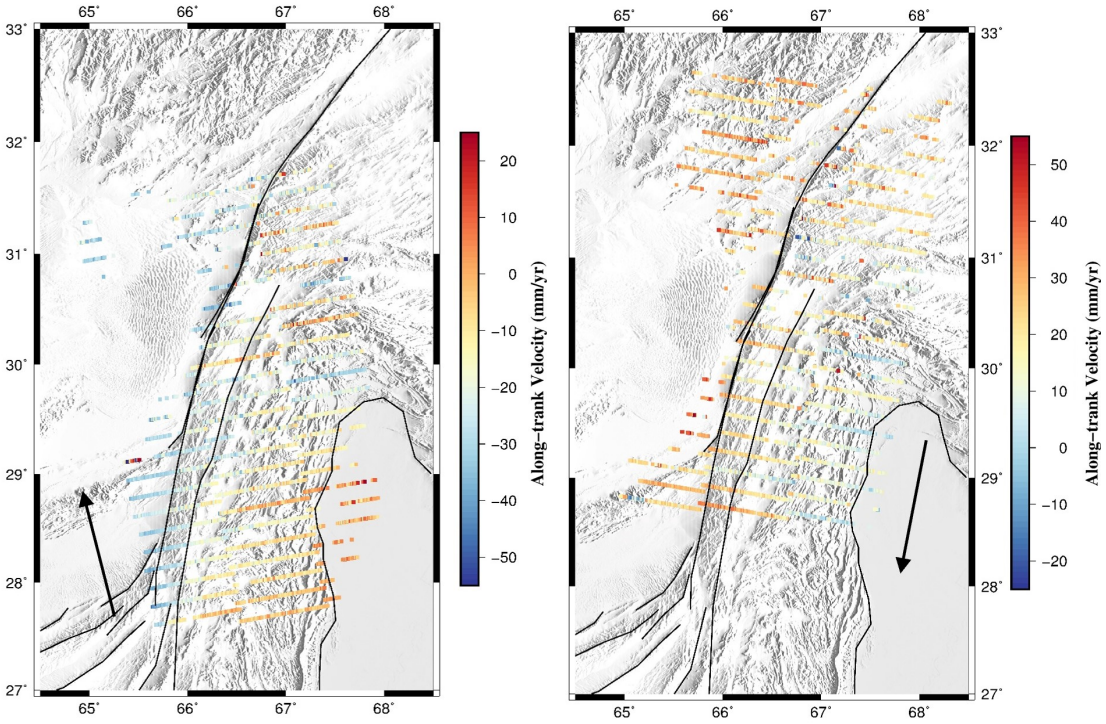

Figure 5.16: Along-track velocities across the Chaman fault area after removing long-wavelength plane. The plus sign indicates that the ground moves horizontally in the direction of the satellite heading angle (black arrows): a.) the ascending pass (349.7°) and b.) the descending pass (190.3°).

appear to be consistent with a linear trend. Creep rates before and after the earthquake are not significantly different. The linear regression, a typical operation of InSAR analysis that provides averaged velocities over time, can fit these scatter plots fairly well. The cumulative offset of 12 mm over 4 years (Fig. 5.18(b)) is consistent with the 3 mm/yr offset at the fault trace in the velocity profile (Fig. 5.18(a)). Considering a variation of creep rate for sub-periods, on the other hand, is possible and can provide more information on how the fault slip evolves, for example, profiles in Fig. 5.19, which are plotted with uppercase letters in Fig. 5.17. The transect profiles, presented in Fig. 5.19(a) and Fig. 5.19(c), are about 100 km and 50 km to the north of the two earthquakes, respectively; however, the surface creeps at these two segments appear to be influenced by the ruptures. The offset rates after the earthquakes in profile A (Fig. 5.19(b)) decrease from 5.13±0.6 mm/yr to nearly half of the creep rate before the rupture (at 2.36±0.3 mm/yr), the displacement rate decreases significantly from 5.21±0.7 mm/yr to 1.57±0.2 mm/yr in profile B (Fig. 5.19(d)). Also, at the segment of profile D (Fig. 5.19(g) and Fig. 5.19(h)), which is located about 50 km to the south of the first event, the trend of fault offset appears to change at the period of earthquakes. The fault slip decreases from 3.59±0.5 mm/yr to 1.1±0.2 mm/yr. In contrast, profile C (Fig. 5.19(e) and Fig. 5.19(f)), which is about 15 km to the south of the first event, does not show a clear variation at the time of rupture. The observation shows that the

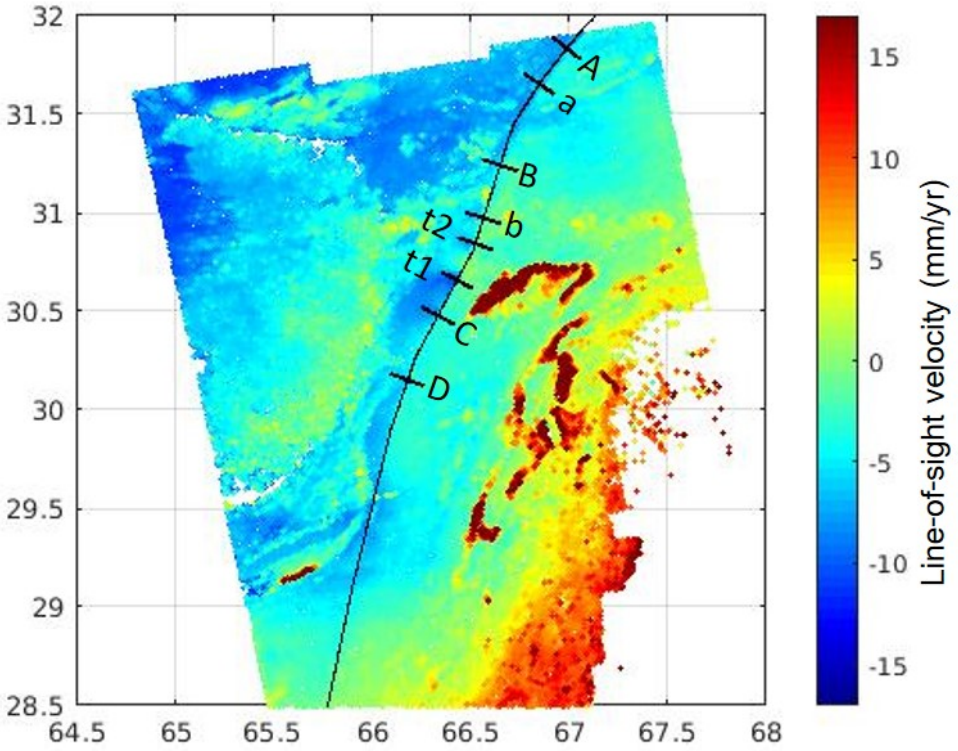

Figure 5.17: Location of exampled transect for seismic and aseismic fault slip

cumulative offsets progress gradually for the first three years, but fault creep appears to accelerate to a much higher rate (i.e., 15.38±1.9 mm/yr) in the final year.

The transect profiles t1 and t2 (Fig. 5.20), plotted with the letter t in Fig. 5.17, present the displacement across the fault segments close to the epicentres of the two earthquakes. The constant velocity over the 2014-2018 period clearly does not depict the actual fault slips for these areas. For these two profiles, I omit the acquisitions close to the dates of the two earthquakes in the estimation of creep rate since the outliers of surface ruptures can cause biases in the temporal filtering, as mentioned above. In the segment of profile t1, located near the epicentre of the first rupture, the estimation presents that there was no significant surface creep detected prior to the earthquake and suggests that the offset occurred steadily with a creep rate of 2.65±0.3 mm/yr after the second rupture about 200 days. For the segment of profile t2 that is close to the epicentre of the second earthquake, The time-dependent fault slip can detect that the aseismic slip rate (2.38±0.3 mm/yr), after the rupture, is higher than the average before the event (1.45±0.5 mm/yr).

However, the 300-day period during the earthquakes occurred cannot represent the displacement by the smoothed phase evolution. The 72-day temporal filtering perturbs the estimated phase and biases the actual offset magnitude during the ruptures. I then present the displacement in the period covering the ruptures by the profile along the

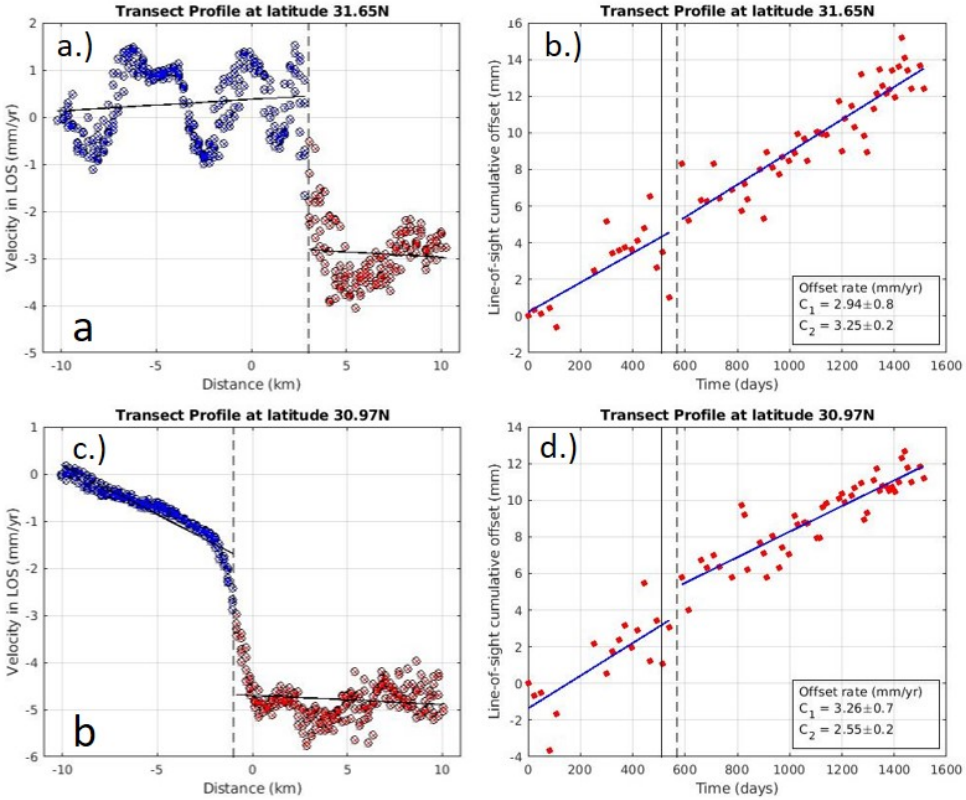

Figure 5.18: Velocity profiles and cumulative offset displayed surface fault creep for areas that fault slip progress steadily. They are presented as the lowercase letters (i.e., a and b) in Fig. 5.17. The fault creep for these segments appears to progress steadily during 2014-2018. The vertical line and dashed lines illustrate the earthquakes that occurred on 13^{th} May 2016 and 11^{th} July 2016, respectively. The C_1 and C_2 in legend denote the creep rate in the period before and after the earthquake, respectively.

fault trace about 100 km covering the segments close to the two epicentres in Fig. 5.21. The x-axis counts from the south to north along the fault trace from latitude 30.3°N to latitude 31°N. I depict the fault slip from the single master phase without temporal filtering. The vertical line represents the location of the first rupture, and the vertical dashed line is at the location of the second rupture. I present the time domain in colour, with reference to the date 24th of April 2016, the last date of acquisition before the earthquake. Even though the random noise is greater than in the smoothed phase evolution, the rupture signals can dominate the other components. At the segment close to the epicentre of the first event, the largest displacement (15 mm offset in line-of-sight direction), associated with a seismic slip, occurred during 0-24 days. However, the cumulative displacement shows that the magnitude of aseismic fault slip is also about 15 mm over 200 days after the event. Moreover, half of the aseismic slip (7-8 mm) occurred during the same time period as the second earthquake (48-96 days) in an area 20 km to the north. On the other hand, the fault slip after the rupture in the area close to the second event is difficult to distinguish between the displacement signal

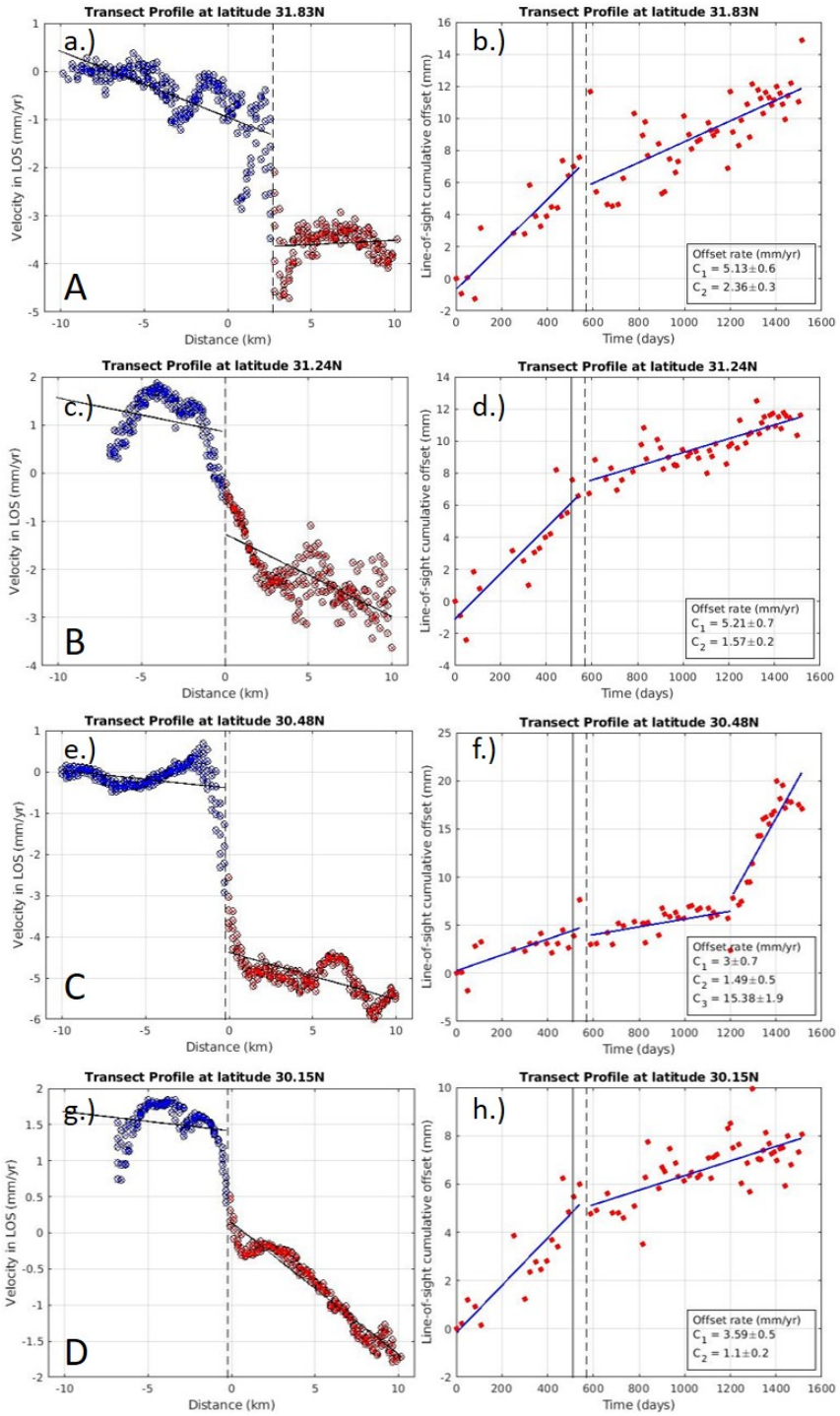

Figure 5.19: Velocity profiles and cumulative offset displayed surface fault creep for areas that fault slip progress with periodic variation. The profiles are presented with uppercase letters (i.e., A, B, C, D) in Fig. 5.17. The fault creep for these segments develops with periodic variations. The vertical line and dashed lines illustrate the earthquakes that occurred on 13^{th} May 2016 and 11^{th} July 2016, respectively. The C_1 and C_2 in legend denote the creep rates in the period before and after the earthquake, respectively, except the profile C (e, f), which is divided into three sub-periods.

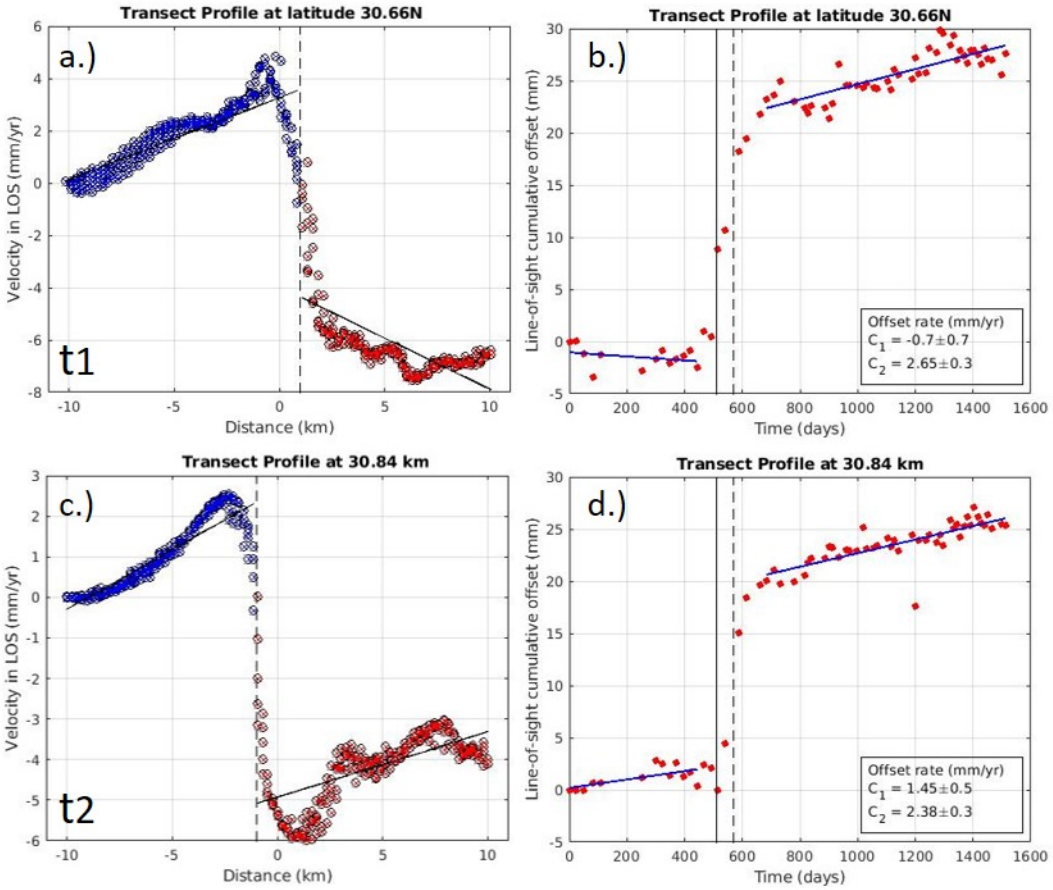

Figure 5.20: Velocity profiles and cumulative offset displayed surface aseismic and seismic fault slips for areas associated with fault ruptures. The transect profiles are at the segments that show the peaks of surface ruptures. They are presented with "t" letter lines in Fig. 5.17. a.) and b.) The profiles present the fault offset located close to the first rupture presented as a vertical line (13^{th} May 2016). c.) and d.) The profiles show the fault offset located near the second rupture presented as a dashed line (11^{th} July 2016). Since the cumulative displacements were applied temporal filters with 72 days window size, the bias needs to be considered when performing the analysis with high precision required. The C_1 and C_2 in legend denote the creep rate in the period before and after the earthquake, respectively.

and noise.

Furthermore, no significant offset in the line-of-sight ascending component across the fault is seen in the displacement profiles in the area between two events. This undetected signal of the seismic slips is probably a result of vertical motion associated with this segment. However, the fault offset estimated by the descending data shows significant discontinuities 3 km to the east of the fault trace. The signal is potentially the deformation associated with the normal component since the strike-slip component is incompatible with the look direction of the descending data. Since its line-of-sight component is almost perpendicular to the horizontal fault-parallel deformation, the observed phase should be significantly a result of the normal component. This could be easier to understand by considering the cumulative displacements map, focusing on the

deformation area around the earthquakes (Fig. 5.22 and Fig. 5.23). The measurements present the displacement away from the satellite in both ascending and descending observations. Although Barnhart (2017) proposed that there is no significant normal-fault displacement along the Chaman fault, this estimation in this section detects some noteworthy vertical movement referred from the measurement of descending data. However, the analysis needs further investigation to distinguish between the normal and strike components. Thus, all observed line-of-sight displacement from ascending data cannot simply be converted to the fault-parallel deformation.

However, the aseismic fault slips observed in this thesis agree with Furuya and Satyabala (2008), which presents a significant slip along the Chaman fault following the 2005 Mw=5.0 Kalat, Afghanistan earthquake. Even though the epicenters locate ∼100 km to the north of two events presented in this section, characteristics of post-seismic deformation are still the same. The spatial pattern of surface displacements presents an afterslip pattern dominantly and does not reveal significant visco-elastic relaxation or poro-elastic process. The slow slip signal can be detected over 50 km and last for nearly a year, which is slightly longer than the proposed 200 days in this thesis. Note they are different fault segments. This recurring pattern of deformation, intermediate earthquake followed by a significant afterslip for both segments, as well as surface creeps that can be observed in many segments of the Chaman fault, indicate that the fault accumulates only a portion of the plate tectonic strain. At this latitude, the tectonic shear strain is distributed into interseismically locked Chaman fault, sub-parallel faults (e.g., the Ghazaband fault, arbitrary fault at 68.1 km from the Chaman fault), fault surface creep, and also occasionally intermediate earthquake together with a particular slow slip.

5.6 Conclusion and outlook

As a result of additional measurements (burst overlap InSAR technique), I can decompose InSAR velocities into the three-dimensional components (i.e., east, north, and up). The decomposed velocities show that the deformation across the Chaman fault is concentrated in the north-south component. Even though the results still are influenced by short-wavelength variations, which is probably a result of ionospheric signals influencing the along-track measurement, the impact appears to be lower than the pure along-track observation, which does not have the additional constraint of line-of-sight measurements.

Additionally, the primary goal of this research is to define subtle ground velocities in three dimensions using only geodetic InSAR observations. The long-wavelength ionospheric signal should be corrected by phase-based ionospheric estimation, such as the split-band in range technique, and the redundancy of four InSAR measurements

estimating three unknowns (E, N, and U), which can also mitigate the effect.

Unfortunately, due to a large data gap in the desert area, this study does not have a good condition to perform the ionospheric correction; therefore, the long-wavelength signal is still present in the data. As a result, this work cannot yet achieve the final purpose, so the investigation to provide decomposed velocities in this chapter is only one step toward the final goal. Due to the limitations caused by decorrelation and ionospheric noises, I still need to rely on external GNSS data by following the long-wavelength constraint method (Hussain et al. (2018) and Weiss et al. (2020)), which have already proved efficient with line-of-sight measurements, to the burst overlap InSAR results. Moreover, this study proposes incorporating the long-wavelength plane estimation of the non-tectonic signal into the inversion estimating decomposed velocities. This work intends to include this non-tectonic long-wavelength estimation in the inversion into future work, which will be applied with only InSAR observations. The measurements can still be interfered with by some long-wavelength noise, but the redundancy of the observations will mitigate the effect. As a result, we do not need to incorporate the long-wavelength constraint from the GNSS data in the analysis.

However, as mentioned, I need to constrain this additional part with GNSS data because I cannot perform ionospheric correction correctly. Consequently, the long-wavelength bias appears to be significant for both ascending line-of-sight and along-track measurements. Furthermore, because I need to demonstrate the efficiency of applying the mitigation with long-wavelength displacement constraint at the same time during the inversion, I first correct the line-of-sight InSAR results using the same method as Hussain et al. (2018) and Weiss et al. (2020). Since the algorithm applied with a line-of-sight result has already been proved efficient, I assume that the line-of-sight results are correct and can focus on clarifying the method with the along-track measurements.

According to the results in this chapter, the method is efficient with the burst overlap InSAR technique. As a result, in the following step, we can incorporate the inversion to estimate decompose velocities and long-wavelength non-tectonic signals from line-of-sight and along-track InSAR observations simultaneously. Furthermore, toward the final objective, extending the time series and estimating phase-based ionospheric correction, possibly for another area, may allow the algorithm to achieve a high-resolution three-dimensional deformation based solely on InSAR observations. The future result could be an independent measurement to complement or validate the geodetic GNSS data, allowing for a more robust evaluation of tectonic deformation.

Furthermore, in this chapter, I discuss the southern part, which consists solely of sub-parallel Chaman and Ghazaband faults. However, Dalaison et al. (2020), a recent study, presents line-of-sight velocities estimated from time-series Sentinel-1 im-

ages across this region and proposes that this area probably comprises three major parallel faults at the latitude by proposing an unknown fault located 65-75 km east of the Chaman fault. Further study is needed in the future to provide a more precise conclusion, but this concept can now better explain the variation in the southern velocity transect profile. In my opinion, the results in Fig.5.14 can present a variation at Chaman fault trace, 25-35 km, and 65-75 east of the Chaman fault, as proposed in Dalaison et al. (2020). However, noise still disturbs the deformation signal to approve a concrete conclusion. As previous studies, including this thesis, have done, I propose that the next study consider this segment with more than two major structures (Chaman and Ghazaband faults).

Furthermore, I examine the temporal evolution of shallow creep using the estimated time-series product. The high temporal resolution of Sentinel-1 operation enables the InSAR technique to capture particular features of aseismic and seismic fault slip along the Chaman fault. With many years of Sentinel-1 operation to come, this episodic displacement could be more robust, useful, and significant for researching the geophysical process. This point of view can benefit post-seismic studying and other work that is a time-dependent process.

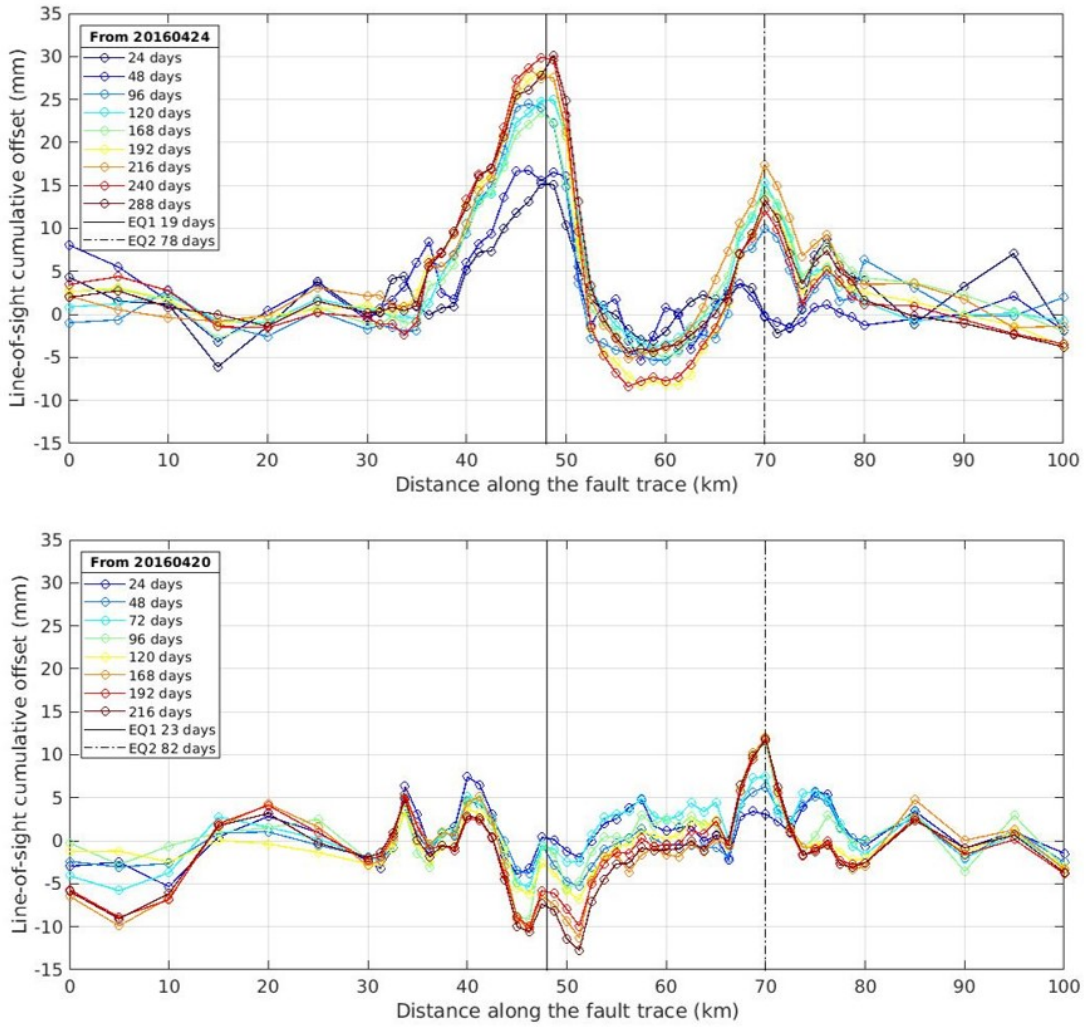

Figure 5.21: Cumulative offsets in line-of-sight direction. The distance on the x-axis starts counting along the fault trace and from latitude 30.3°N to 31°N. These profiles focus on the segment covering two intermediate earthquakes on 13^{th} May 2016 and 11^{th} July 2016. The profile covers almost the same area as presented as maps in Fig. 5.22 and Fig. 5.23. The time domain is referenced to the date 20^{th} April 2016 and is presented in colour. The vertical line represents the location of the first rupture, and the dashed line presents the location of the second rupture.

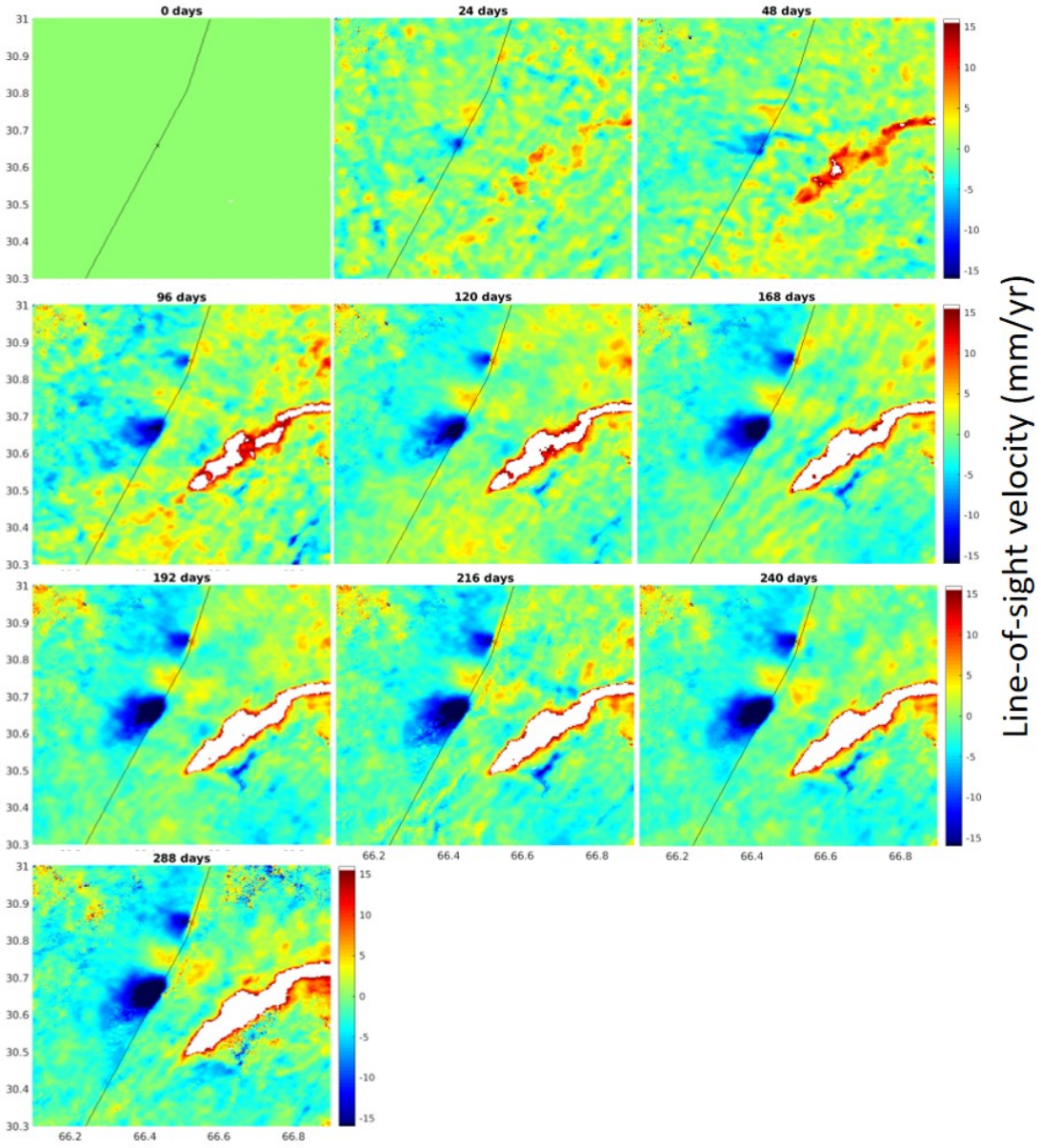

Figure 5.22: Maps of cumulative deformation focusing on the period after the earthquakes from ascending data. The plus is a displacement away from the satellite. The evolution starts accumulating from 24^{th} April 2016, which is the date of acquisition before the first event. Earthquakes occur on 19 and 78 days from the reference. The cross symbols represent the epicentres, applied from the USGS catalogue, but they have relocated the longitude to the fault trace. To the east of the fault trace, the observation presents strong deformation associated with land subsidence, which is an area of Gulistan, Qila Abdullah, and Pishin cities.

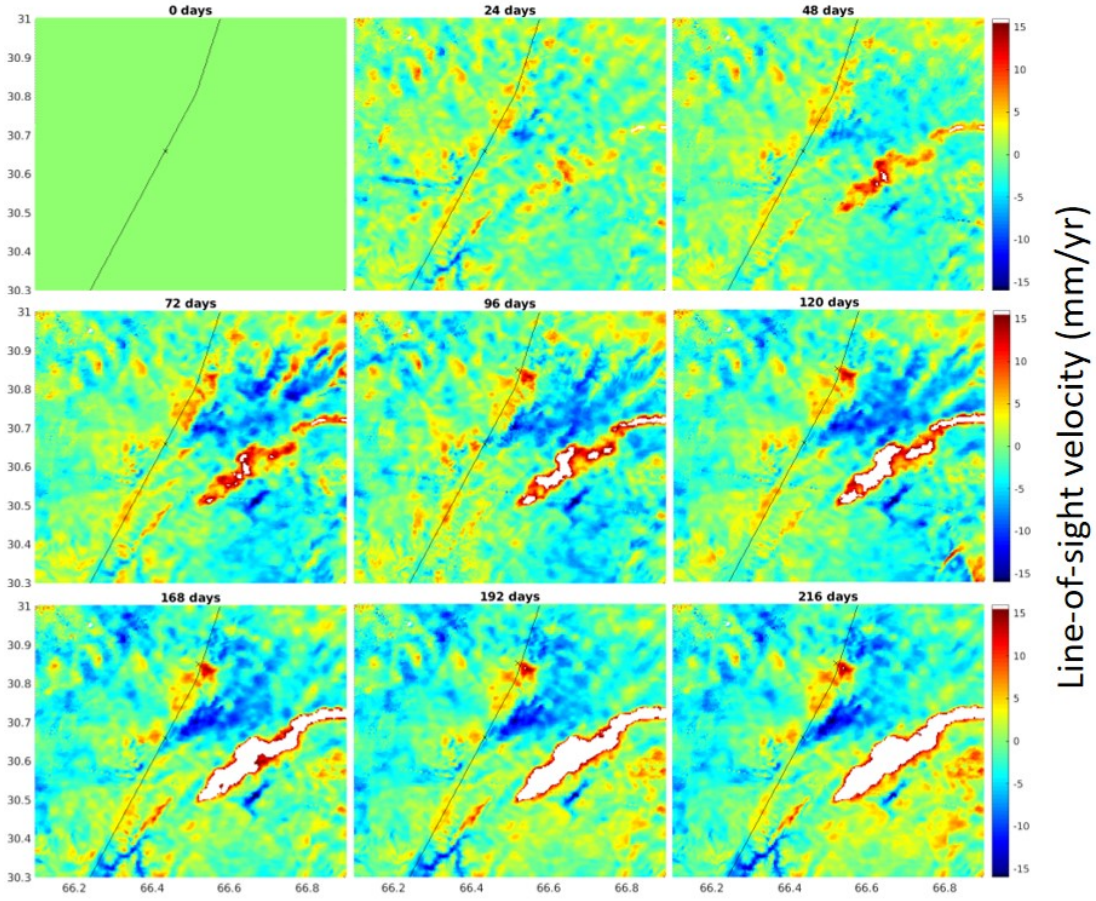

Figure 5.23: Maps of cumulative deformation focusing on the period after the earthquake from descending data. The plus is a displacement away from the satellite. The evolution starts acumulating from 20^{th} April 2016, which is the date of acquisition before the first event. Earthquakes occur on 23 and 82 days from the reference. The cross symbols represent the epicentres, applied from the USGS catalogue, but they have relocated the longitude to the fault trace.

Chapter 6

Conclusion and Outlook

6.1 Summary

The main aim of this thesis is to implement the recent InSAR measurement to accomplish strain rates globally. Since there are still challenges to be verified toward the goal, the valid objective of this thesis is to measure a slowly ground deformation that is concentrated in the north-south component, which is insensitive to line-of-sight InSAR observations. The time-series burst overlap technique used with the European Space Agency's Sentinel-1 satellites is crucial in overcoming the limitation. The ability to measure a north-south displacement allows InSAR observations to be sensitive to all types of fault slips.

To begin with, in Chapter 3, I started with an experiment to reduce the ionospheric noise, which is a significant bias in the burst overlap InSAR measurement. The split-spectrum in range method is applied to estimate the ionospheric phase screen at the piercing-point height. This chapter presents that this typical algorithm to mitigate the ionospheric effect for line-of-sight measurement can also extract ionospheric bias for the burst overlap analysis. The inferred ionospheric signal affecting the backward- and forward-looking interferograms are applied to correct the double-difference interferograms. These estimations are analyzed using a time-series approach with a small baseline style. The ionospheric estimation is analyzed from multiple interferograms, yielding lower noise than daisy chain evaluation. Furthermore, to eliminate the prior bias in the existing method, two additional steps are added: unwrapping identification with adaptive threshold and the Fit-plane method for low-pass filtering.

I applied the proposed algorithm to Sentinel-1 images covering the West-Lut fault, a north-south strike-slip fault. The ionospheric correction works well in this area, which has excellent coherence. As a result, noise in both time-series line-of-sight and along-track measurements can be effectively reduced by removing the long-wavelength signal

across the scene that is not associated with the tectonic signal. I present the corrected burst overlap velocities with strong multillooked pixels (4 points in one burst overlap), which can eliminate most of the effect from decorrelation noise and leave only the ionospheric signal dominated. However, the estimation can only detect the long-wavelength signal. The high-frequency variable from the short-wavelength ionospheric signal still composes in the observation. The bias appears to be consistent within the same burst overlap but varies significantly between them. This short wavelength of the ionospheric signal is a crucial limitation to assess seismic hazards more precisely. The limitation also affects the rest of the thesis. The method to estimate this short-wavelength ionospheric signal should be validated as soon as possible. However, the ionospheric estimation is another method that is remarkably low precision. The short-wavelength correction must be performed carefully because even a minor bias can add significant error to the along-track measurement. Specifically, the estimation is amplified again during the conversion from the ESD phase to displacement.

In Chapter 4, I present the result of time-series burst overlap InSAR, which is still applied with the West-Lut fault region. The north-south strain accumulation of the fault (i.e., 4 mm/yr) is remarkably low when compared to the precision of the ESD technique. The goal of the chapter is to prove the technique's efficiency even with a subtle motion. Also, I investigate the precision of the multilooked ESD phase with a spatial resolution of 1.5x0.8 km. This strong multilooking, which is only efficient due to the particularity of the ESD technique, can reduce the decorrelation noise, another challenge in measuring slow movement. I investigated that multilooked precision with coherence higher than 0.3 is inconsistent with the theory, verified with coherence and the number of InSAR points averaged. The bias, lower than 3 mm corresponding to 0.008 radians, is most likely the result of a very high-frequency signal with a wavelength shorter than 1.6 km, such as a very short ionospheric signal, a part of tropospheric turbulence that may not cancel out completely, or random noise. I also conducted additional experiments with the time-series analysis. I discovered that using NSBAS analysis can reduce noise and especially can be used with the wrapped phase due to the particularity of the ESD phase.

According to the result, the velocity map from the burst overlap InSAR cannot present an interseismic signal across the fault, which is accumulating 4 mm/yr of slip deficit. However, I estimate the mean velocities profile from 9 burst overlaps, which corresponds to >100 km in the north-south direction. The averaged transect profiles present the expected right-lateral sense with a typical arctangent curve of the deformation gradient localized at the location of the fault trace. The magnitude of slip rate is statistically consistent with prior GNSS data. Furthermore, the measurement proposed a variation of slip rate across two fault segments. The fault parameter was reviewed for the first time because the GNSS coverage is insufficient to provide a reliable estimate.

This time-series analysis in this chapter has proved efficient in detecting a slow tectonic process associated with the interseismic signal. However, the methodology requires a spatial filtering "between the different burst overlap" in order to enhance the tectonic signal. The main goal of filtering is to reduce the short-wavelength ionospheric signal. The effect causes a similar bias to pixels in the same burst overlap, but the impact can be mitigated by averaging across the burst overlap. Even though the averaging can mitigate this effect, the observation is limited in its application to measuring the slow variation of the deformation in the azimuthal direction. In this study, I exchange a spatial resolution to achieve a highly accurate result. However, the improved methodology to reduce decorrelation noise is still required, and again, the methods to estimate the high-frequency ionospheric signal are primarily required. Nevertheless, incorporating more Sentinel-1 images that will be acquired in the future into the time-series analysis is probably able to enhance a deformation signal to dominate the ionospheric impact.

Chapter 5 presents the InSAR measurements observing the ground displacement in line-of-sight and azimuth components with data from both ascending and descending passes across the Chaman fault. 3-4 InSAR measurements are available in certain areas, and consequently, the InSAR observation for this area is now sensitive to all three-dimensional components. Due to the low coherence and unwrapping issues in many SAR scenes, I cannot achieve an accurate estimation of the ionospheric phase in this study. However, in this chapter, I demonstrate an algorithm to decompose InSAR velocities, for which long-wavelength signals are constrained by independent GNSS data. The method can mitigate the effect of ionospheric disturbance while also referencing the InSAR velocities to the GNSS reference frame. Due to the short-wavelength ionospheric variation from the burst overlap InSAR measurements, the decomposed velocities still show velocity jumps in certain areas. The overall result, however, shows that the deformation across the Chaman fault region is primarily concentrated in the north-south component. The horizontal velocities are consistent with a left-lateral sense of slip.

Again, the main limitation that needs to be addressed as soon as possible is the mitigation of short-wavelength signals. I need to exchange a spatial resolution in order to reduce noise and enhance the displacement signal associated with the interseismic deformation in the modeling. Consequently, this low measurement resolution limits the ability to detect high variable tectonic deformation. For example, the fault location of the Ghazaband fault inferred from the modeling is inconsistent with the literature. I suspect that there is another tectonic structure is associated with the deformation at this latitude, but due to the sparse spatial sampling, I am unable to address this disagreement. However, the study shows that we can estimate displacement in slowly deforming areas in three dimensions using InSAR measurements. Although I need to constrain the long-wavelength signal based on the independent GNSS data, this type

of sparse GNSS network is now available in most parts of the world. Therefore, the method has the potential to be applied globally. Due to the rapid growth of the geodetic observations (i.e., InSAR and GNSS techniques), we can achieve the global stain rate in the near future.

The time-series products from line-of-sight measurement in Chapter 5 present benefits from Sentinel-1's short revisit time, which optimizes radar coherence and increases the temporal sampling rate to capture temporal behaviors more precisely, for example, evolutions of surface creep along the Chaman fault. With the Sentinel-1 and other SAR missions operating for years to come, vast knowledge of the temporal behaviors of surface deformation will be rapidly advanced, with typically dense spatial sampling of InSAR observations covering nearly the entire globe. In the coming years, the InSAR technique will probably accelerate the geophysical study.

6.2 Next step toward measuring tectonic strain accumulation globally

In this thesis, the burst overlap InSAR technique has proved effective in providing a north-south subtle deformation, and results can be derived with line-of-sight InSAR measurements to decompose ground velocities into three dimensions. The next step toward achieving the global strain rate is to figure out how to apply the burst overlap InSAR method with large-scale processing. Despite the fact that there are still issues to be clarified, this section is willing to contribute ideas gathered throughout this thesis for implementing the analysis on a global scale. Recently, one of the most advanced systems in processing InSAR large-scale coverage with time-series analysis is LiCSAR, developed by the Looking Inside the Continents from Space (LiCS) project of Centre for the Observation and Modelling of Earthquakes, Volcanoes, and Tectonics (COMET). This COMET-LiCSAR system has a strategic goal to automate process InSAR products of deforming regions with a global-scale coverage, and it has already demonstrated robust proof of its capability to do so. LiCSAR currently, for the seismic focus, can provide free use interferograms covering almost the entire Alpine-Himalayan belt. As a result, applying the burst overlap InSAR analysis to this existing system can be advantageous. Also, the operation can provide line-of-sight velocities, so a combination of four InSAR observations (plus GNSS) to achieve 3-D deformation can be more convenient. Specifically, we can focus on decomposing ground velocities of the Alpine-Himalayan belt area using the LiCSAR existing interferograms and provide a high-resolution interseismic strain map of the Alpine-Himalayan belt as a first practical result.

6.2.1 Decorrelation noise

In the processing, firstly, I propose that the operation generate double-difference interferograms of burst overlap pixels from resampled images, which are coregistered with rough (orbital information) and refine (ESD) offsets, to maximize coherence, and that the process can also work alongside the existing procedure. In addition, I propose a strong multilooking to reduce decorrelation noise, which is one of the significant limitations of the burst overlap InSAR technique. The strong multilooking, which is only valid with this large ambiguity technique (±700 mm), has proved effective, and their precision (number of pixel ∼25,000 pixels) has already been investigated in this thesis. I decrease the spatial resolution to 0.5 km in range and 1.5 km in azimuth, which is the total azimuth length of the burst overlap area, to increase the precision, as variation in such a short distance, to my knowledge, cannot provide much useful information for the global-scale tectonic analysis.

Spatial filtering that can keep a high number of InSAR pixels is another option for reducing decorrelation noise. However, more research is needed to clarify the relationship between spatial window size and precision. Also, as presented in Chapters 4 and 5, I propose a spatial averaging of velocities to reduce a short-wavelength ionospheric signal, so the research should include an examination of error propagation to the estimated velocities. As a result of the filtering, adjacent velocity pixels would have a level of correlation. On the contrary, the precision of averaging multiple velocities derived from the strong multilooked pixels is straightforward, and also the method can reduce the file size significantly. This can help save disk storage, and processing time to perform an analysis is short, making it more flexible to trial for another research.

Moreover, as a pixel-wise basis, I propose applying strong multilooking together with excluding pixels with a correlation less than a specific coherence threshold (i.e., coherence <0.1 applied in this thesis). This procedure can keep the decorrelation noise low. This approach, according to a precision investigation presented in Chapter 4, allows employing wrapped phases with time-series analysis. Operating an unwrapping algorithm in a small burst overlap area is difficult, and phase unwrapping across different burst overlap areas is nearly impossible, to my knowledge. Note the investigation in Chapter 4 focuses on precision only, so any real strong deformation/ionospheric signals (>1.5 m in a short temporal baseline) can still cause a double-difference phase to exceed an ambiguity band. We need to take this limitation into account when broadly employ the processing. In other words, the processing cannot employ interferograms with displacement greater than ∼1.5 m.

6.2.2 Time-series analysis

I propose the NSBAS approach to the time-series analysis since the omitting point with low coherence in the previous section can cause a gap in the interferogram network. Due to an investigation, I suggest that the NSBAS approach with omitting low coherence points provides velocity results with less noise than the conventional small baseline and daisy-chain analysis. The NSBAS time-series inversion can provide an optimal displacement time series from a simple least-square analysis. The product can reveal time-dependent deformation and also can be used to estimate averaged velocities for sub-period or entire time series. This analysis can use the benefit of 6 years (2014–2020) of high temporal sampling data from Sentinel-1. Also, massive data from many years to come with the same sampling rate could help to reduce noise caused by a short-wavelength signal. Additionally, because the time-series burst overlap analysis in this thesis only focuses on reducing noise in space with a low-pass filter, I propose the processing to include a high-pass filter in time, similar to a typical line-of-sight process. However, more research is needed to determine how effective the temporal filtering for the burst overlap InSAR measurement is. Furthermore, an alternative method, the time-series analysis that has a strategic idea to exploit every possible pair of interferograms in the time series, such as SqueeSAR (Ferretti et al., 2011) or any phase-linking analysis, is fascinating to be applied with this along-track measurement. However, the analysis needs to consider the issue of ambiguity band ($\pm$700 mm) carefully.

6.2.3 Ionospheric correction

The ionospheric correction with a split-band in range technique demonstrated in Chapter 3 and Chapter 4 is definitely a great method for reducing an ionospheric signal, which is another significant bias in the burst overlap InSAR technique. This approach can provide additional independent measurements to derive three-dimensional deformation, whereas the method demonstrated in Chapter 5 that constrains a long-wavelength InSAR signal requires an additional GNSS network. Thus, the availability of GNSS data limits the latter approach. In the global-scale context, however, I would recommend using a GNSS constraint rather than the split-band in range method because estimating ionospheric phase with consideration of bias introduced in a resampling step (Gomba et al., 2017) requires the technique to perform the image splitting at the full resolution (i.e., single look complex). Due to the current capacity of operation, this can be a significant limitation to provide an ionospheric estimate for global coverage. Therefore, I propose using the GNSS constraint first and then applying the split-band in range technique to the data covering areas that lack a GNSS network. Furthermore, a study to compare these two methods as well as a global TEC model, would provide a robust idea for identifying the suited technique for a specific area. The research should determine the technique's accuracy while taking into account a variation in the number of

GNSS sites and the maximum distance of a GNSS site included in the analysis with a different type and magnitude of tectonic deformation. Even though the objective of this research cannot lead to introduce the processing split-band in range globally, due to the limitation of computer resources, the study can identify the level of accuracy of the final result.

6.2.4 Absolute ground surface velocity

As mentioned in Chapter 4, during the coregistration process, the estimated cross-correlation and averaged ESD phases contain information of ionospheric bias averaged at a scene level and averaged azimuthal displacement of a land block covered by a frame. More precisely, the movement of the land block can be referred to as the plate tectonic movement of a particular area. This proposed algorithm summed this averaged shift back to the phase containing a local shift; therefore, the displacement component in the total shift is in the absolute sense. However, in this thesis, this absolute context is lost after I offset the result with a local reference point. Instead, we can assume that the displacement is the only component that correlates in time, even though the distribution is particularly high due to orbital uncertainty and ionospheric disturbance. The time-series analysis should be able to mitigate the other nontectonic signal. As a result, the average velocity derived from this algorithm can be organized in an absolute sense, no-net rotation, related to the ITRF Altamimi et al. (2012). This concept has been validated and presented in Hooper et al. (2020). The time-series frame-averaged ESD velocities agree well with the displacement from ITRF global plate model.

However, further explication of error sources that affect absolute estimates is required. The research should include investigations such as systematic orbital error or ionospheric signal in an absolute sense, which, in this thesis, I take advantage of being a local study and ignore all long-wavelength signals in which the effect is larger than a frame scale. As mentioned in the previous section, the global TEC model, with its high accuracy but low spatial resolution, may not be useful for a local framework, but this external data could be useful at this global scale. In addition, the processing should consider the effects of global-scale earth tides as well as variations in the satellite's heading angle at high latitudes.

For this proposed absolute product, as evidenced by the work presented in Weiss et al. (2020), it has been demonstrated that the line-of-sight InSAR can employ with a regional scale and analyzed based on a geodetic reference frame. Furthermore, the along-track measurement has been demonstrated in Hooper et al. (2020) that the technique can automatically provide a result with an absolute sense despite cooperating with a large noise. In my expectation, the error potentially can be reduced with much more data stream to come with the Sentinel-1 lifetime. Ambitiously, the subtle three-dimensional deformation with an absolute sense derived from InSAR measurement

could play a significant role in evaluating earthquake hazards with high resolution globally.

Appendix A

Supplementary materials for Chapter 4

Table A.1: The velocities derived from earth tide model (Milbert, 2018). I estimated the velocity around the West-Lut fault area from displacement associated with earth tide at the time of 90 SAR acquisitions, applied in the West-Lut fault work. All the values are in along-track component.

Velo	Longitude					Variation
Latitude	56	57	58	59	60	in longitude
35	1.33	.	.	1.30	1.29	0.04
34	1.38	.	.	1.35	1.34	0.04
33	1.43	.	.	1.40	1.38	0.05
32	1.47	.	.	1.44	1.43	0.04
31	1.52	.	.	1.48	1.47	0.05
30	1.56	.	.	1.52	1.51	0.05
29	1.60	.	.	1.56	1.55	0.05
Variation in latitude	0.27	.	.	0.26	0.26	(mm/yr)

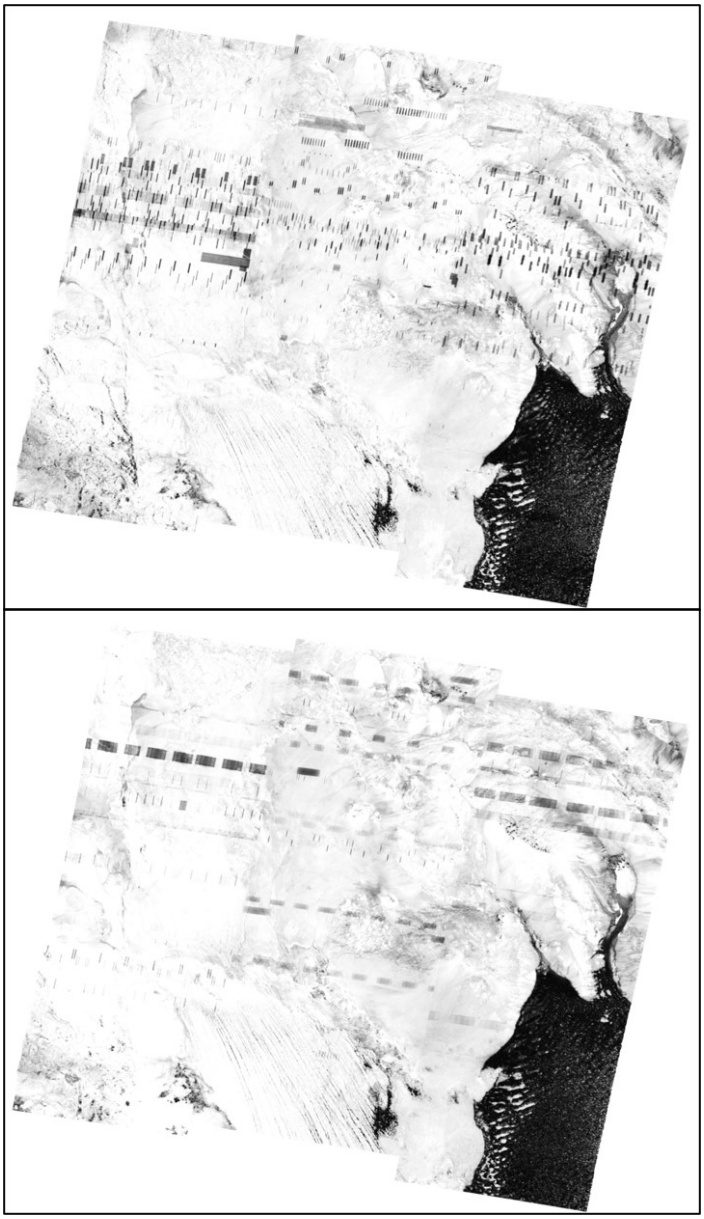

Figure A.1: Coherence images showing unexpected signal disturbing descending data over the West-Lut fault. The InSAR coherence are from interferogram acquired in October 2014 (20141012 and 20141105) and September-October in 2018 (20180921 and 20181027). The exampled images are from LiCSAR portal (source, https://comet.nerc.ac.uk/comet-lics-portal/) with frame number 093D_05874_131313. There are disturbed signal, incoherent patches, for most images over this area.

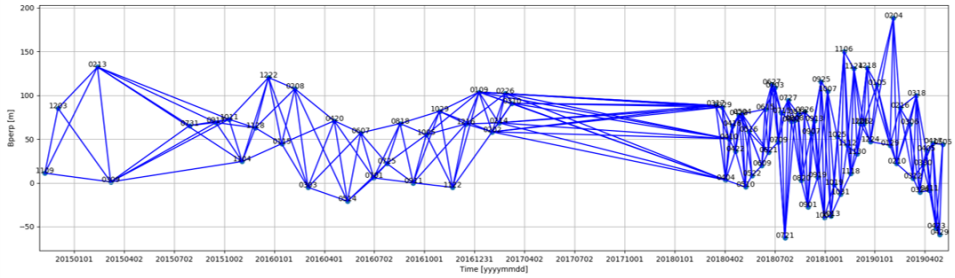

Figure A.2: Small Baseline network of InSAR processing along the West-Lut fault. The blue lines represent interferomitric pairs. Black dots present dates of SAR acquisitions.

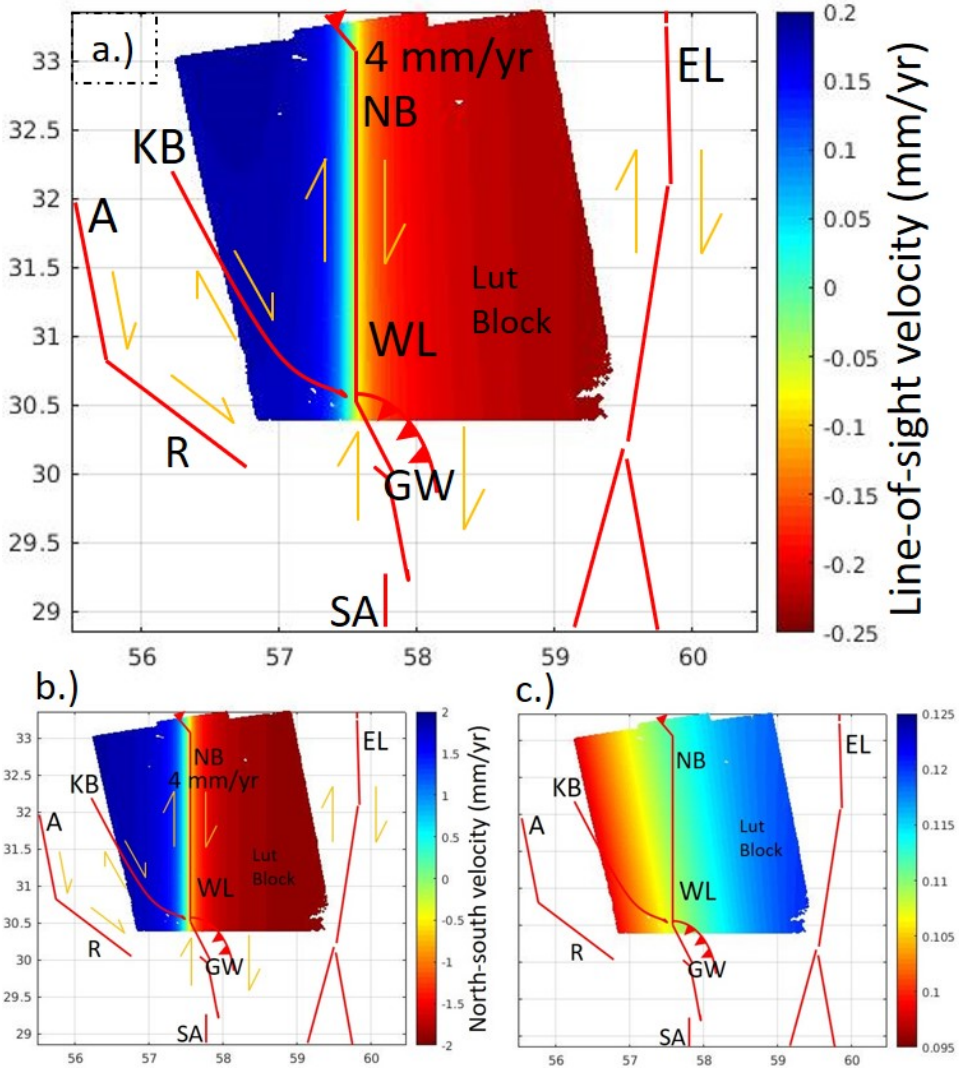

Figure A.3: a.) Map of the forward model of line-of-sight displacements. I calculated the north-south velocities (b.) from the interseismic model (Savage and Burford, 1973) using a 4 mm/yr slip rate across the Nayband segment (NB), the northern segment of the West-Lut fault, and define the locking depth at 10 km, approximated value in Walpersdorf et al. (2014). Due to a compatible look component, presented by directional cosine of a unit vector in the north component (c.), the line-of-sight measurement needs to extract an arctangent shape with a 0.45 mm/yr difference at the far-field.

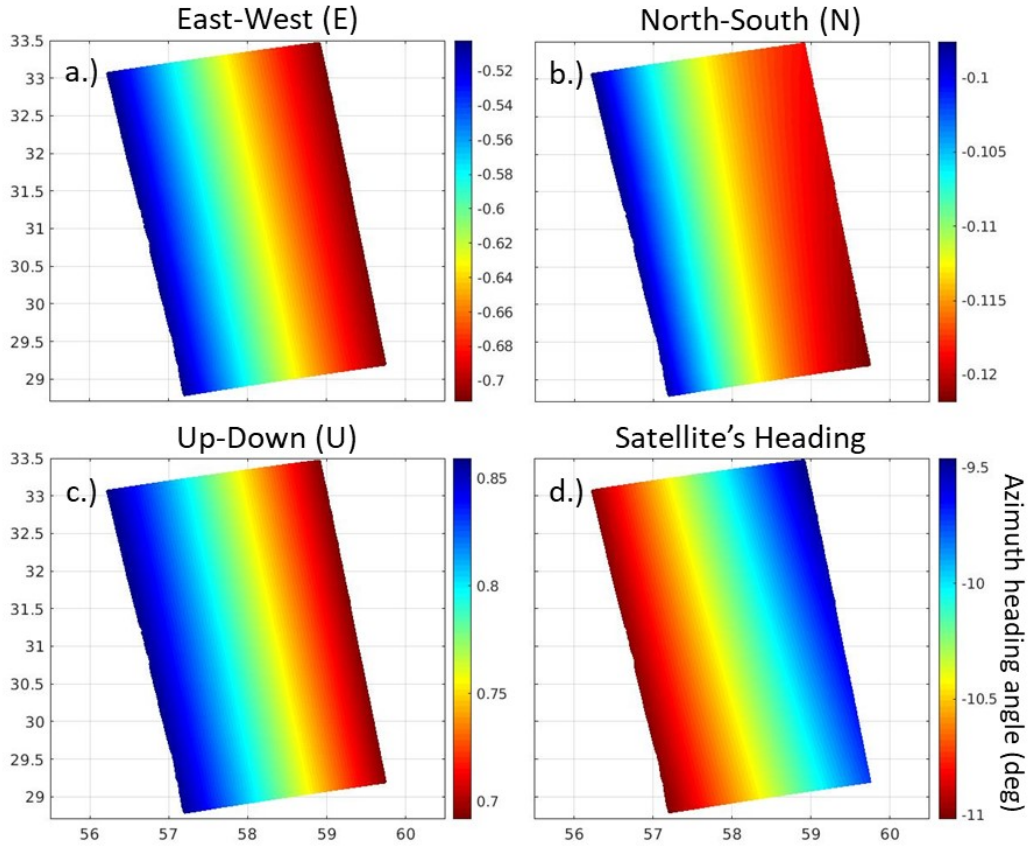

Figure A.4: a.), b.), and c.) present directional cosines of a unit vector in the InSAR look angle direction for Sentinel-1 images acquired over the West-Lut fault. The look vectors point toward the sensor and are estimated by a look_vector command in GAMMA software using Sentinel-1 imaging and DEM data. However, please note that these values are only an approximation because the estimation does not account for the slight variation, antenna steering backward and forward of the TOPS acquisition, within each individual burst. d.) display a satellites' heading component at each map pixel. The heading direction is calculated from a relationship in Eq. 5.2 (Weiss et al., 2020). I simply estimate the magnitude of the heading angle using an arctangent($\frac{N}{E}$) output. As a result, variation in range direction is greater than variation in along-track direction. To investigate the bias caused by variation, I define the relative displacement is at 10 mm/yr across the scene. The maximum relative bias in projecting displacement into the north-south component is approximately 0.05 mm/yr. Since this value is minor compared to the other nontectonic noise, I assume it is insignificant in the study. I analyzed the along-track results in this thesis using N10.3W as the value is an average of the West-Lut fault scene.

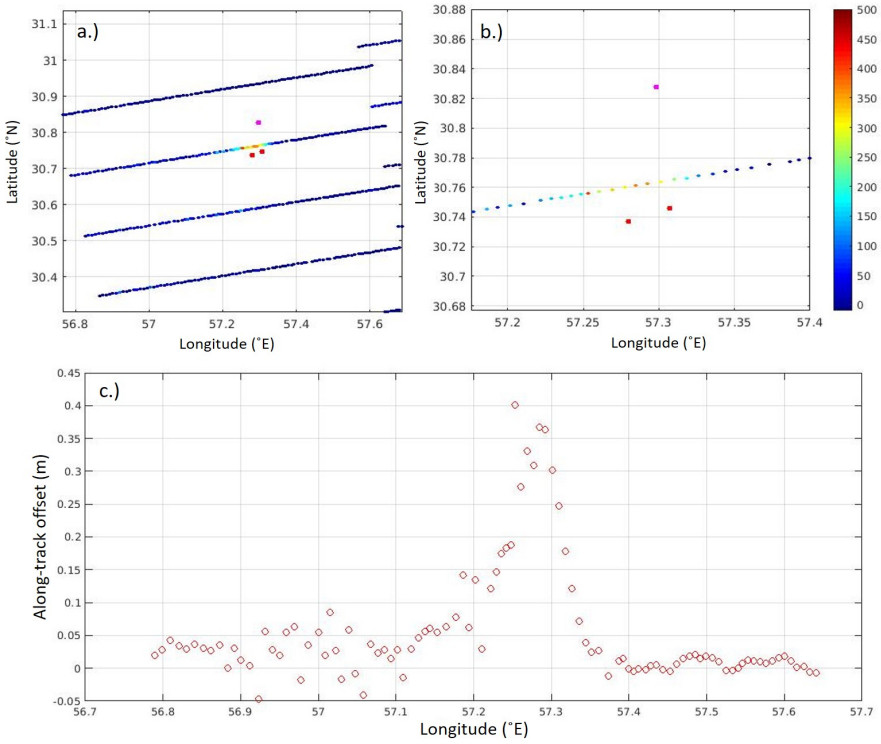

Figure A.5: Ground displacement associated with Kerman earthquakes in December 2017 . I present the location of burst overlap InSAR points with earthquake epicenters (red and pink dots) (Savidge et al., 2019). Earthquakes occurred on 1st and 12th December 2017. Unfortunately, there is a data gap between March 2017 and March 2018, so I cannot distinguish these three earthquakes. 0.4 meters is the total displacement of the three ruptures in the along-track component. However, since the third earthquake (red dot) is shallower than the other two, the detected deformation is probably dominated by this rupture.

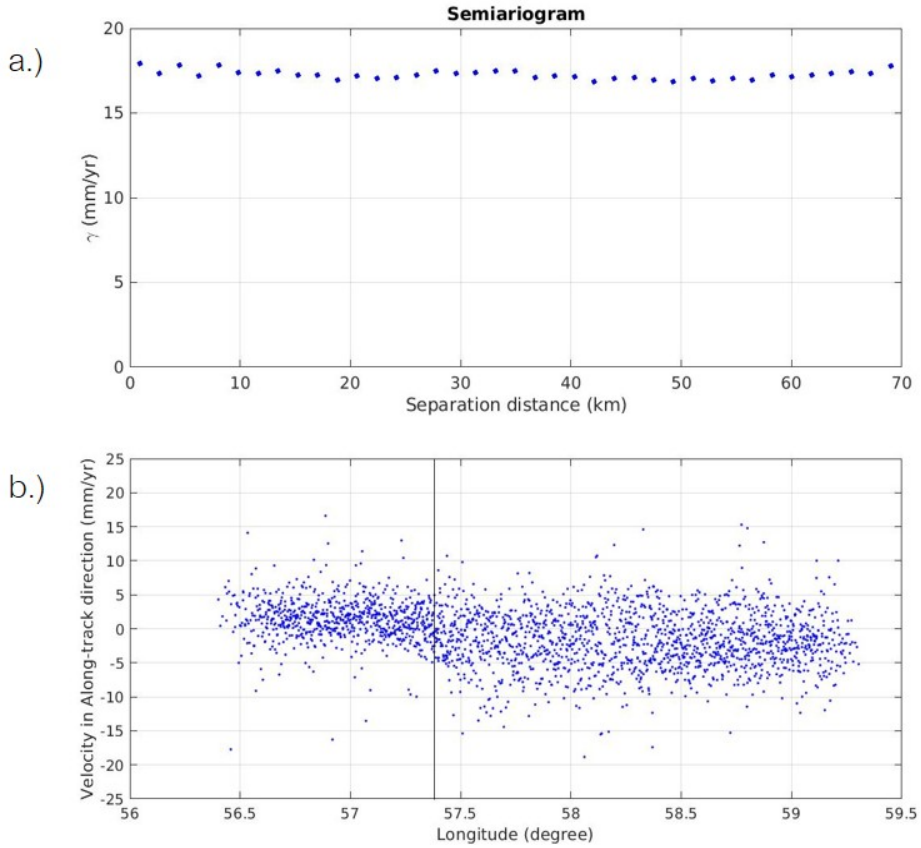

Figure A.6: a.) Semivariogram of the b.) one-dimensional InSAR points, transect profile of the along-track velocity across the Nayband segment of the West-Lut fault. InSAR points are from 9 burst overlaps, corresponding to 150 km in the north-south direction (Fig.4.6). An estimated sill variance is at 17.2 mm/yr without a correlation.

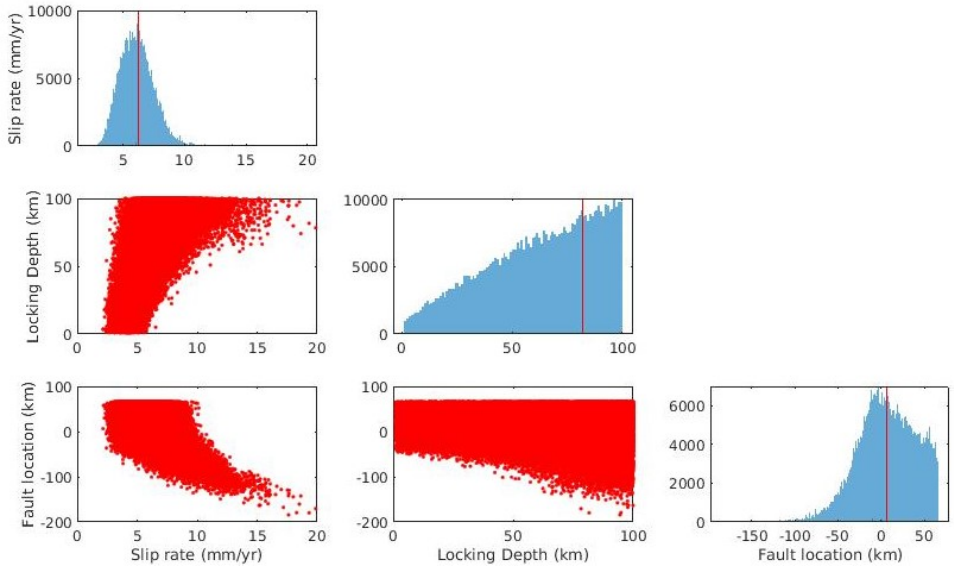

Figure A.7: Posterior distribution of a modeling interseismic parameters determined from GNSS measurements (Walpersdorf et al., 2014) observing the Nayband segment. Red vertical lines in histogram present the optimal model parameters analyzed with Baysian approach. Red points figure present the correlation between the paramenters (i.e. slip rate (mm/yr), lonking depth (km), location of the fault (km) relative to longitude 57.525°E.

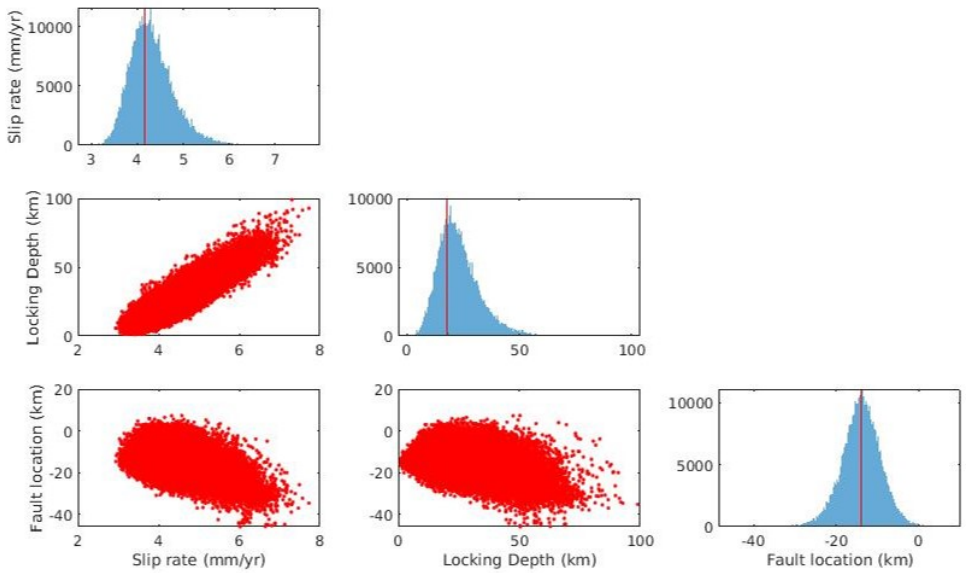

Figure A.8: Posterior distribution of a modeling interseismic parameters determined from burst overlap InSAR measurements observing the Nayband segment. Red vertical lines in histogram present the optimal model parameters analyzed with Baysian approach. Red points figure present the correlation between the paramenters (i.e. slip rate (mm/yr), lonking depth (km), location of the fault (km) relative to longitude 57.525°E.

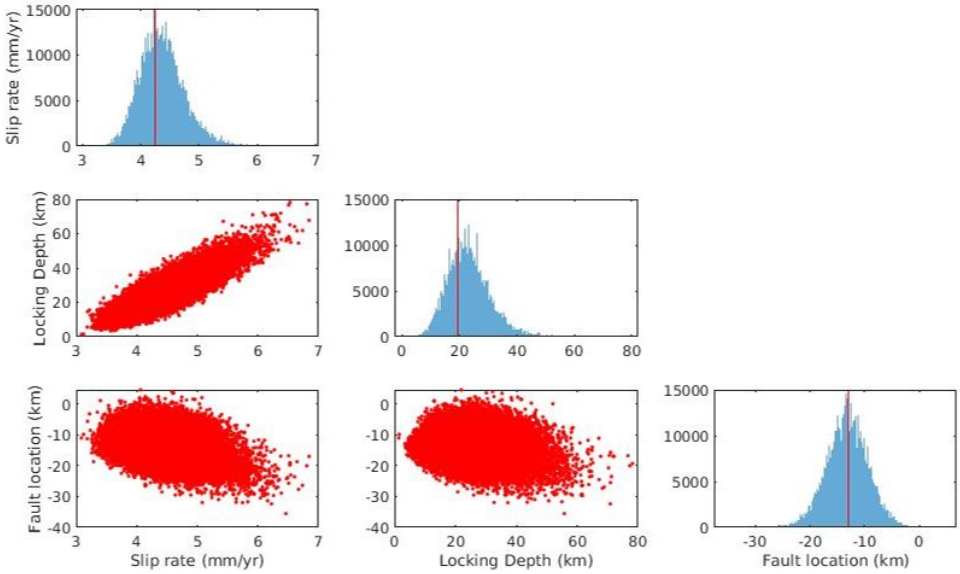

Figure A.9: Posterior distribution of a modeling interseismic parameters determined from GNSS (Walpersdorf et al., 2014) and burst overlap InSAR measurements observing the Nayband segment. Red vertical lines in histogram present the optimal model parameters analyzed with Baysian approach. Red points figure present the correlation between the paramenters (i.e. slip rate (mm/yr), lonking depth (km), location of the fault (km) relative to longitude 57.525°E.

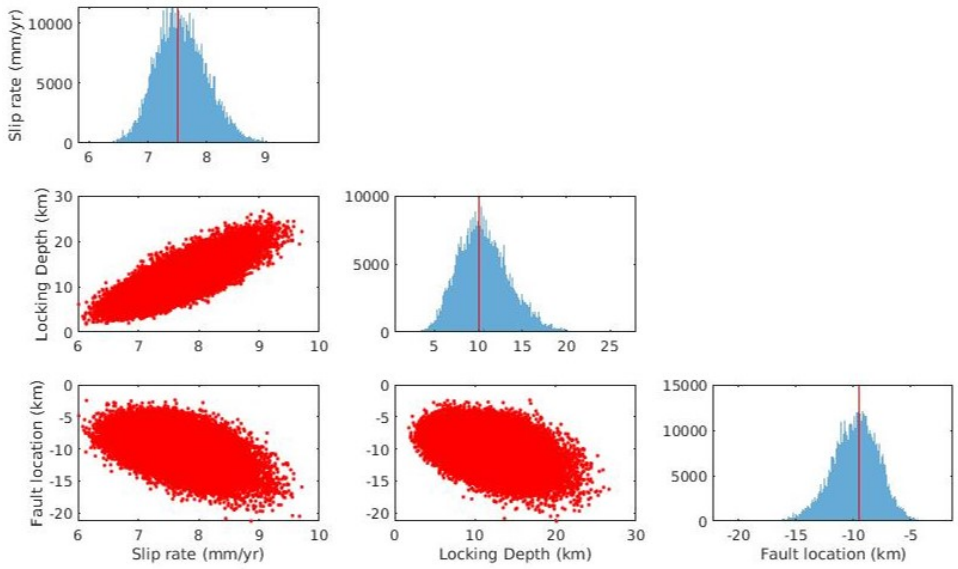

Figure A.10: Posterior distribution of a modeling interseismic parameters determined from burst overlap InSAR measurements observing the Gowk segment. Red vertical lines in histogram present the optimal model parameters analyzed with Baysian approach. Red points figure present the correlation between the paramenters (i.e. slip rate (mm/yr), lonking depth (km), location of the fault (km).

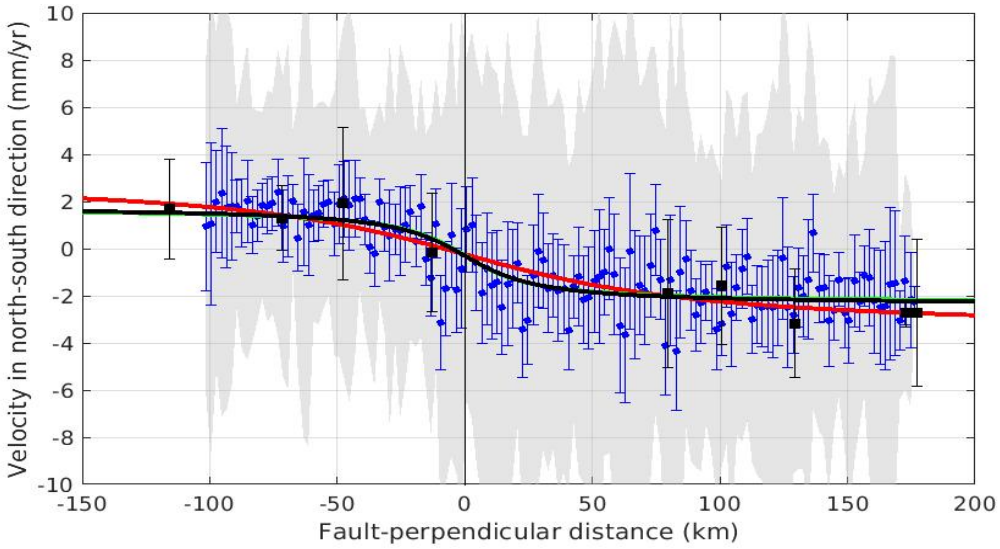

Figure A.11: The best-fitting model of the interseismic strain accumulation using the optimal parameters from the Bayesian approach applied with GNSS (red), InSAR (green), and GNSS+InSAR (black) measurements. All data are the same as applied in Fig.4.8, but I fixed the fault location at a surface fault trace (57.55°E). Blue points with one-sigma errorbars present the mean north-south velocities averaged from 9 burst overlaps over the Nayband segment. The grey shaded area represents the two standard deviation of the burst overlap InSAR points. All other symbols are the same as in Fig.4.8. From the inversion, in comparison to the model that does not fix the fault location, the far-field velocity is still similar around 4.3±0.3 mm/yr, but the locking depth increase to 25.3±7.4 km. However, the model still appears to agree with the observation even with the model that fixes fault location.

Appendix B

Supplementary materials for Chapter 5

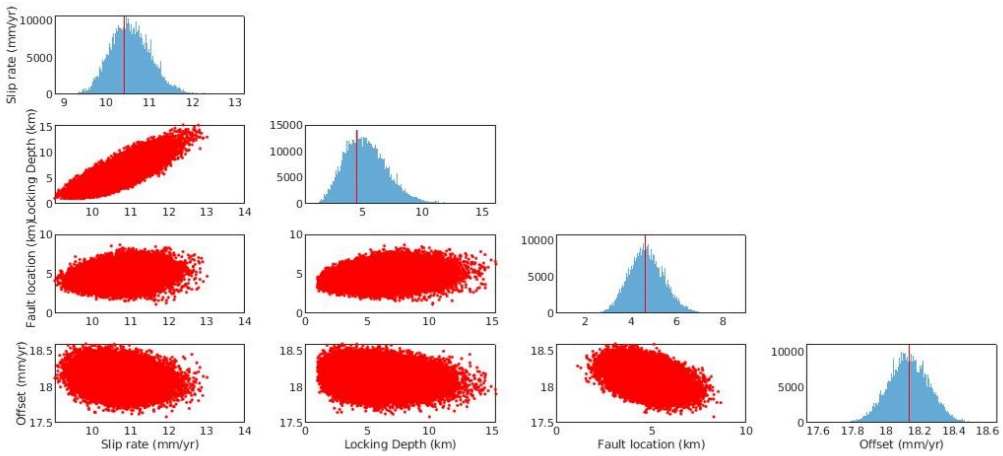

Figure B.1: Posterior distribution of a modeling interseismic parameters derived from decomposed velocities observing the northern segment of the Chaman fault at latitude 31°N. Red vertical lines in histogram present the optimal model parameters analyzed with Baysian approach. Red points figure present the correlation between the paramenters (i.e. slip rate (mm/yr), lonking depth (km), location of the fault at depth (km).

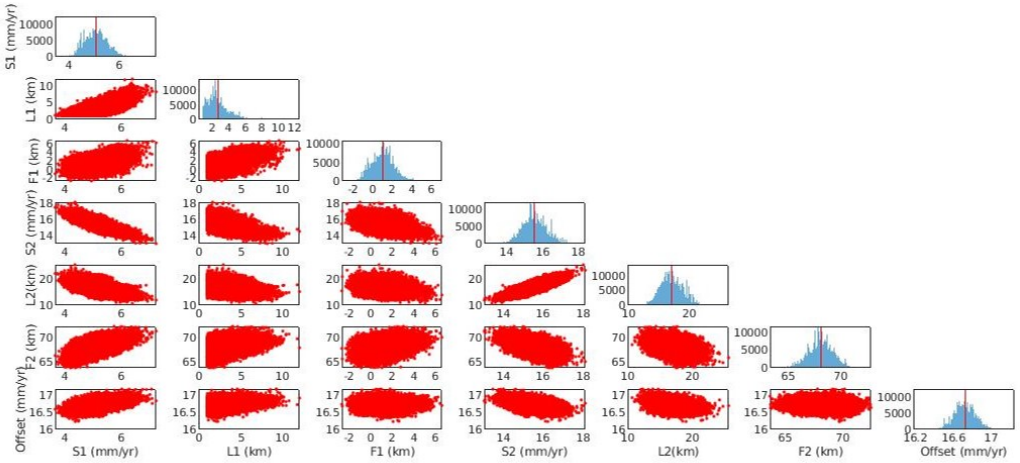

Figure B.2: Posterior distribution of a modeling interseismic parameters derived from along-track velocities observing the southern segment of the Chaman (1) and Ghazaband (2) fault at latitude 29°N. Red vertical lines in histogram present the optimal model parameters analyzed with Baysian approach. Red points figure present the correlation between the paramenters (i.e. slip rate (s) (mm/yr), lonking depth (L) (km), location of the fault (f) (km) relative to Chaman fault trace.)

References

Altamimi, Zuheir, Laurent Métivier, and Xavier Collilieux (2012). "ITRF2008 plate motion model". In: *Journal of Geophysical Research: Solid Earth* 117.B7.

Altamimi, Zuheir, Paul Rebischung, Laurent Métivier, and Xavier Collilieux (2016). "ITRF2014: A new release of the International Terrestrial Reference Frame modeling nonlinear station motions". In: *Journal of Geophysical Research: Solid Earth* 121.8, pp. 6109–6131.

Ansari, Homa, Francesco De Zan, and Richard Bamler (2018). "Efficient phase estimation for interferogram stacks". In: *IEEE Transactions on Geoscience and Remote Sensing* 56.7, pp. 4109–4125.

Ansari, Homa, Francesco De Zan, and Alessandro Parizzi (2020). "Study of systematic bias in measuring surface deformation with SAR interferometry". In: *IEEE Transactions on Geoscience and Remote Sensing* 59.2, pp. 1285–1301.

— (2021). "Fading signals in multilooked interferograms and deformation velocity maps". In: `https://www.youtube.com/watch?v=czDSZo2wJRk&t=1825s`.

Bagnardi, Marco and Andrew Hooper (2018). "Inversion of Surface Deformation Data for Rapid Estimates of Source Parameters and Uncertainties: A Bayesian Approach". In: *Geochemistry, Geophysics, Geosystems* 19.7, pp. 2194–2211. DOI: `10.1029/2018GC007585`. eprint: `https://agupubs.onlinelibrary.wiley.com/doi/pdf/10.1029/2018GC007585`. URL: `https://agupubs.onlinelibrary.wiley.com/doi/abs/10.1029/2018GC007585`.

Barnhart, William D (2017). "Fault creep rates of the Chaman fault (Afghanistan and Pakistan) inferred from InSAR". In: *Journal of Geophysical Research: Solid Earth* 122.1, pp. 372–386.

Bechor, Noa BD and Howard A Zebker (2006). "Measuring two-dimensional movements using a single InSAR pair". In: *Geophysical research letters* 33.16.

Bekaert, DPS, A Hooper, and TJ Wright (2015). "A spatially variable power law tropospheric correction technique for InSAR data". In: *Journal of Geophysical Research: Solid Earth* 120.2, pp. 1345–1356.

Belcher, DP (2008). "Theoretical limits on SAR imposed by the ionosphere". In: *IET Radar, Sonar & Navigation* 2.6, pp. 435–448.

Berardino, Paolo, Gianfranco Fornaro, Riccardo Lanari, and Eugenio Sansosti (2002). "A new algorithm for surface deformation monitoring based on small baseline differential SAR interferograms". In: *IEEE Transactions on geoscience and remote sensing* 40.11, pp. 2375–2383.

Bilitza, D, D Altadill, V Truhlik, V Shubin, I Galkin, B Reinisch, and X Huang (2017). "International Reference Ionosphere 2016: From ionospheric climate to real-time weather predictions". In: *Space Weather* 15.2, pp. 418–429.

Bird, Peter and Corné Kreemer (2015). "Revised tectonic forecast of global shallow seismicity based on version 2.1 of the Global Strain Rate Map". In: *Bulletin of the Seismological Society of America* 105.1, pp. 152–166.

Brcic, Ramon, Alessandro Parizzi, Michael Eineder, Richard Bamler, and Franz Meyer (2011). "Ionospheric effects in SAR interferometry: An analysis and comparison of methods for their estimation". In: *Geoscience and Remote Sensing Symposium (IGARSS), 2011 IEEE International*. IEEE, pp. 1497–1500.

Chen, Curtis W and Howard A Zebker (2002). "Phase unwrapping for large SAR interferograms: Statistical segmentation and generalized network models". In: *IEEE Transactions on Geoscience and Remote Sensing* 40.8, pp. 1709–1719.

Chojka, Agnieszka, Piotr Artiemjew, and Jacek Rapiński (2020). "RFI Artefacts Detection in Sentinel-1 Level-1 SLC Data Based On Image Processing Techniques". In: *Sensors* 20.10. ISSN: 1424-8220. DOI: 10.3390/s20102919. URL: https://www.mdpi.com/1424-8220/20/10/2919.

Costantini, M and Paul A Rosen (1999). "A generalized phase unwrapping approach for sparse data". In: *IEEE 1999 International Geoscience and Remote Sensing Symposium. IGARSS'99 (Cat. No. 99CH36293)*. Vol. 1. IEEE, pp. 267–269.

Dalaison, Manon, Romain Jolivet, Elenora van Rijsingen, and Sylvain Michel (2020). "The Distribution of Aseismic Slip and Partitioning of Deformation on Multiple Parallel Strike-slip Faults in the Chaman Fault System from InSAR". In: *AGU Fall Meeting Abstracts*. Vol. 2020, G017–11.

Ding, F, W Wan, B Ning, and M Wang (2007). "Large-scale traveling ionospheric disturbances observed by GPS total electron content during the magnetic storm of 29–30 October 2003". In: *Journal of Geophysical Research: Space Physics* 112.A6.

Doin, M-P, Cécile Lasserre, Gilles Peltzer, Olivier Cavalié, and Cécile Doubre (2009). "Corrections of stratified tropospheric delays in SAR interferometry: Validation with global atmospheric models". In: *Journal of Applied Geophysics* 69.1, pp. 35–50.

Doin, Marie-Pierre, S Guillaso, R Jolivet, C Lasserre, F Lodge, Gabriel Ducret, and Raphael Grandin (2011). "Presentation of the small baseline NSBAS processing chain on a case example: the Etna deformation monitoring from 2003 to 2010 using Envisat data". In: *Proceedings of the Fringe symposium*. ESA SP-697, Frascati, Italy, pp. 3434–3437.

Elliott, JR, RJ Walters, and TJ Wright (2016). "The role of space-based observation in understanding and responding to active tectonics and earthquakes". In: *Nature communications* 7.1, pp. 1–16.

Fattahi, Heresh and Falk Amelung (2016). "InSAR observations of strain accumulation and fault creep along the Chaman Fault system, Pakistan and Afghanistan". In: *Geophysical Research Letters* 43.16, pp. 8399–8406.

Fattahi, Heresh, Mark Simons, and Piyush Agram (2017). "InSAR time-series estimation of the ionospheric phase delay: An extension of the split range-spectrum technique". In: *IEEE Transactions on Geoscience and Remote Sensing* 55.10, pp. 5984–5996.

Feng, Wanpeng, Zhenhong Li, John R Elliott, Yo Fukushima, Trevor Hoey, Andrew Singleton, Robert Cook, and Zhonghuai Xu (2013). "The 2011 MW 6.8 Burma earthquake: fault constraints provided by multiple SAR techniques". In: *Geophysical journal international* 195.1, pp. 650–660.

Fernández, C (2011). "Sentinels POD service file format specifications". In: *Eur. Space Agency, Paris, France, Tech. Rep. GMESGSEG-EOPG-FS-10-0075*.

Ferretti, Alessandro, Alfio Fumagalli, Fabrizio Novali, Claudio Prati, Fabio Rocca, and Alessio Rucci (2011). "A new algorithm for processing interferometric data-stacks: SqueeSAR". In: *IEEE transactions on geoscience and remote sensing* 49.9, pp. 3460–3470.

Ferretti, Alessandro, Claudio Prati, and Fabio Rocca (2001). "Permanent scatterers in SAR interferometry". In: *IEEE Transactions on geoscience and remote sensing* 39.1, pp. 8–20.

Fialko, Yuri, Mark Simons, and Duncan Agnew (2001). "The complete (3-D) surface displacement field in the epicentral area of the 1999 Mw7. 1 Hector Mine earthquake, California, from space geodetic observations". In: *Geophysical Research Letters* 28.16, pp. 3063–3066.

Foroutan, Mohammad, Bertrand Meyer, Michel Sébrier, H Nazari, AS Murray, Kristell Le Dortz, MA Shokri, M Arnold, G Aumatre, D Bourls, et al. (2014). "Late Pleistocene-Holocene right slip rate and paleoseismology of the Nayband fault, western margin of the Lut block, Iran". In: *Journal of Geophysical Research: Solid Earth* 119.4, pp. 3517–3560.

Furuya, M and SP Satyabala (2008). "Slow earthquake in Afghanistan detected by InSAR". In: *Geophysical Research Letters* 35.6.

Gomba, G., F. Rodríguez González, and F. De Zan (2017). "Ionospheric Phase Screen Compensation for the Sentinel-1 TOPS and ALOS-2 ScanSAR Modes". In: *IEEE Transactions on Geoscience and Remote Sensing* 55.1, pp. 223–235.

González, Pablo J, Marco Bagnardi, Andrew J Hooper, Yngvar Larsen, Petar Marinkovic, Sergey V Samsonov, and Tim J Wright (2015). "The 2014–2015 eruption of Fogo volcano: Geodetic modeling of Sentinel-1 TOPS interferometry". In: *Geophysical Research Letters* 42.21, pp. 9239–9246.

Grandin, Raphael, Emilie Klein, Marianne Métois, and Christophe Vigny (2016). "Three-dimensional displacement field of the 2015 Mw8. 3 Illapel earthquake (Chile) from across-and along-track Sentinel-1 TOPS interferometry". In: *Geophysical Research Letters* 43.6, pp. 2552–2561.

Ul-Hadi, Shams, Shuhab D Khan, Lewis A Owen, Abdul S Khan, Kathryn A Hedrick, and Marc W Caffee (2013). "Slip-rates along the Chaman fault: Implication for transient strain accumulation and strain partitioning along the western Indian plate margin". In: *Tectonophysics* 608, pp. 389–400.

Hanssen, Ramon F (2001). *Radar interferometry: data interpretation and error analysis*. Vol. 2. Springer Science & Business Media.

Hanssen, Raymond Franciscus (1998). *Atmospheric heterogeneities in ERS tandem SAR interferometry*. Delft University Press.

Hastings, W Keith (1970). "Monte Carlo sampling methods using Markov chains and their applications". In: *Biometrika.* 57(1), pp. 97–109.

Hooper, Andrew (2010). "A statistical-cost approach to unwrapping the phase of InSAR time series". In: *Proceedings of the International Workshop on ERS SAR Interferometry, Frascati, Italy*. Vol. 30.

Hooper, Andrew, Pawan Piromthong, John Elliott, Jonathan Weiss, and Milan Lazecky (2020). "The improvement to high-resolution maps of interseismic strain accumulation from incorporating Sentinel-1 along-track measurement". In: `https://agu.confex.com/agu/fm20/meetingapp.cgi/Paper/752857`.

Hooper, Andrew and Karsten Spaans (2017). "Sentinel-1 along-track InSAR for global strain rate estimation". In: `http://fringe2017.esa.int/files/presentation523.pdf`.

Hooper, Andrew John (2006). *Persistent scatter radar interferometry for crustal deformation studies and modeling of volcanic deformation*. Stanford University.

Hussain, Ekbal, Tim J Wright, Richard J Walters, David Bekaert, Andrew Hooper, and Gregory A Houseman (2016). "Geodetic observations of postseismic creep in the decade after the 1999 Izmit earthquake, Turkey: Implications for a shallow slip deficit". In: *Journal of Geophysical Research: Solid Earth* 121.4, pp. 2980–3001.

Hussain, Ekbal, Tim J Wright, Richard J Walters, David PS Bekaert, Ryan Lloyd, and Andrew Hooper (2018). "Constant strain accumulation rate between major earthquakes on the North Anatolian Fault". In: *Nature communications* 9.1, pp. 1–9.

Ingleby, T and TJ Wright (2017). "Omori-like decay of postseismic velocities following continental earthquakes". In: *Geophysical Research Letters* 44.7, pp. 3119–3130.

Jolivet, Romain, Cécile Lasserre, M-P Doin, G Peltzer, J-P Avouac, Jianbao Sun, and R Dailu (2013). "Spatio-temporal evolution of aseismic slip along the Haiyuan fault, China: Implications for fault frictional properties". In: *Earth and Planetary Science Letters* 377, pp. 23–33.

Jonah, OF, A Coster, S Zhang, L Goncharenko, PJ Erickson, ER de Paula, and EA Kherani (2018). "TID observations and source analysis during the 2017 Memorial Day weekend geomagnetic storm over North America". In: *Journal of Geophysical Research: Space Physics* 123.10, pp. 8749–8765.

Jung, Hyung-Sup, Joong-Sun Won, and Sang-Wan Kim (2009). "An improvement of the performance of multiple-aperture SAR interferometry (MAI)". In: *IEEE Transactions on Geoscience and Remote Sensing* 47.8, pp. 2859–2869.

Kotake, Nobuki, Yuichi Otsuka, Tadahiko Ogawa, Takuya Tsugawa, and Akinori Saito (2007). "Statistical study of medium-scale traveling ionospheric disturbances observed with the GPS networks in Southern California". In: *Earth, planets and space* 59.2, pp. 95–102.

Kreemer, Corné, Geoffrey Blewitt, and Elliot C Klein (2014). "A geodetic plate motion and Global Strain Rate Model". In: *Geochemistry, Geophysics, Geosystems* 15.10, pp. 3849–3889.

Lawrence, RD, S Hasan Khan, and T Nakata (1992). "Chaman Fault, Pakistan-Afghanistan". In: *Ann. Tectonicae* 6, pp. 196–223.

Lazecky, Milan, Karsten Spaans, Pablo J Gonzalez, Yasser Maghsoudi, Yu Morishita, Fabien Albino, John Elliott, Nicholas Greenall, Emma Hatton, Andrew Hooper, et al. (2020). "LiCSAR: An automatic InSAR tool for measuring and monitoring tectonic and volcanic activity". In: *Remote Sensing* 12.15, p. 2430.

López-Quiroz, Penélope, Marie-Pierre Doin, Florence Tupin, Pierre Briole, and Jean-Marie Nicolas (2009). "Time series analysis of Mexico City subsidence constrained by radar interferometry". In: *Journal of Applied Geophysics* 69.1, pp. 1–15.

Metropolis, Nicholas, Arianna W Rosenbluth, Marshall N Rosenbluth, Augusta H Teller, and Edward Teller (1953). "Equation of state calculations by fast computing machines". In: *The journal of chemical physics* 21.6, pp. 1087–1092.

Meyer, Franz, Richard Bamler, Norbert Jakowski, and Thomas Fritz (2006). "The potential of low-frequency SAR systems for mapping ionospheric TEC distributions". In: *IEEE Geoscience and Remote Sensing Letters* 3.4, pp. 560–564.

Michel, Rémi, Jean-Philippe Avouac, and Jean Taboury (1999). "Measuring ground displacements from SAR amplitude images: Application to the Landers earthquake". In: *Geophysical Research Letters* 26.7, pp. 875–878.

Milbert, Dennis (June 7, 2018). *SOLID EARTH TIDE*. URL: `https://geodesyworld.github.io/SOFTS/solid.htm` (visited on 10/28/2020).

Misra, Pratap and Per Enge (2006). "Global Positioning System: signals, measurements and performance second edition". In: *Global Positioning System: Signals, Measurements And Performance Second Editions* 206, p. 43.

Monserrat, O, M Crosetto, and G Luzi (2014). "A review of ground-based SAR interferometry for deformation measurement". In: *ISPRS Journal of Photogrammetry and Remote Sensing* 93, pp. 40–48.

Morishita, Yu, Milan Lazecky, Tim J Wright, Jonathan R Weiss, John R Elliott, and Andy Hooper (2020). "LiCSBAS: An Open-Source InSAR Time Series Analysis Package Integrated with the LiCSAR Automated Sentinel-1 InSAR Processor". In: *Remote Sensing* 12.3, p. 424.

Murray, Kyle D., David P.S. Bekaert, and Rowena B. Lohman (2019). "Tropospheric corrections for InSAR: Statistical assessments and applications to the Central United States and Mexico". In: *Remote Sensing of Environment* 232, p. 111326. ISSN: 0034-4257. DOI: https://doi.org/10.1016/j.rse.2019.111326. URL: http://www.sciencedirect.com/science/article/pii/S0034425719303451.

Navarro Sanchez, Victor, Giorgio Gomba, Francesco De Zan, and Karsten Kretschmer (2021). "Compensation of ionospheric effects for InSAR stacks by means of a split-spectrum method". In: *EUSAR 2021; 13th European Conference on Synthetic Aperture Radar*, pp. 1–4.

Okada, Yoshimitsu (1992). "Internal deformation due to shear and tensile faults in a half-space". In: *Bulletin of the seismological society of America* 82.2, pp. 1018–1040.

Otsuka, Y, N Kotake, K Shiokawa, T Ogawa, T Tsugawa, and A Saito (2011). "Statistical study of medium-scale traveling ionospheric disturbances observed with a GPS receiver network in Japan". In: *Aeronomy of the Earth's Atmosphere and Ionosphere*. Springer, pp. 291–299.

Otsuka, Yuichi, Kazuo Shiokawa, Takuya Tsugawa, and Michi Nishioka (2012). "GPS Observations of Medium-Scale Traveling Ionospheric Disturbances over Europe". In: *39th COSPAR Scientific Assembly* 39, p. 1416.

Prats-Iraola, Pau, Rolf Scheiber, Luca Marotti, Steffen Wollstadt, and Andreas Reigber (2012). "TOPS interferometry with TerraSAR-X". In: *IEEE Transactions on geoscience and remote sensing* 50.8, pp. 3179–3188.

Reid, Harry Fielding (1910). "The mechanics of the earthquake". In: *The California Earthquake of April 18, 1906, Report of the State Earthquake Investigation Commission*.

Rosen, Paul A, Scott Hensley, Kevin Wheeler, Greg Sadowy, Tim Miller, Scott Shaffer, Ron Muellerschoen, Cathleen Jones, Howard Zebker, and Soren Madsen (2006). "UAVSAR: A new NASA airborne SAR system for science and technology research". In: *2006 IEEE Conference on Radar*. IEEE, 8–pp.

Savage, JC and RO Burford (1973). "Geodetic determination of relative plate motion in central California". In: *Journal of Geophysical Research* 78.5, pp. 832–845.

Savidge, Elena, Edwin Nissen, Majid Nemati, Ezgi Karasözen, James Hollingsworth, Morteza Talebian, Eric Bergman, Abdolreza Ghods, Manouchehr Ghorashi, Ehsan Kosari, et al. (2019). "The December 2017 Hojedk (Iran) earthquake triplet—sequential rupture of shallow reverse faults in a strike-slip restraining bend". In: *Geophysical Journal International* 217.2, pp. 909–925.

Scheiber, Rolf and Alberto Moreira (2000). "Coregistration of interferometric SAR images using spectral diversity". In: *IEEE Transactions on Geoscience and Remote Sensing* 38.5, pp. 2179–2191.

Spaans, Karsten (2016). "Near-real time volcano monitoring and modelling using radar interferometry". PhD thesis. Unversity of Leeds, pp. 1497–1500.

Styron, Richard and Marco Pagani (2020). "The GEM global active faults database". In: *Earthquake Spectra* 36.1_suppl, pp. 160–180.

Szeliga, Walter, Roger Bilham, Din Mohammad Kakar, and Sarosh H Lodi (2012). "Interseismic strain accumulation along the western boundary of the Indian subcontinent". In: *Journal of Geophysical Research: Solid Earth* 117.B8.

Tarchi, Dario, Nicola Casagli, Riccardo Fanti, David D Leva, Guido Luzi, Alessandro Pasuto, Massimiliano Pieraccini, and Sandro Silvano (2003). "Landslide monitoring by using ground-based SAR interferometry: an example of application to the Tessina landslide in Italy". In: *Engineering geology* 68.1-2, pp. 15–30.

Thatcher, Wayne et al. (1993). "The earthquake cycle and its role in the long-term deformation on the continental litosphere". In: *Annali di Geofisica* 36, pp. 13–24.

Touzi, Ridha, Armand Lopes, Jérôme Bruniquel, and Paris W Vachon (1999). "Coherence estimation for SAR imagery". In: *IEEE Transactions on Geoscience and Remote Sensing* 37.1, pp. 135–149.

Tsugawa, Takuya, Y Otsuka, AJ Coster, and A Saito (2007). "Medium-scale traveling ionospheric disturbances detected with dense and wide TEC maps over North America". In: *Geophysical Research Letters* 34.22.

USGS (2014). *Where do earthquakes occur?* URL: `https://web.archive.org/web/20140805134145/http://www.usgs.gov/faq/categories/9831/3342` (visited on 03/30/2021).

Vernant, Ph, F Nilforoushan, D Hatzfeld, MR Abbassi, C Vigny, F Masson, H Nankali, J Martinod, A Ashtiani, R Bayer, et al. (2004). "Present-day crustal deformation and plate kinematics in the Middle East constrained by GPS measurements in Iran and northern Oman". In: *Geophysical Journal International* 157.1, pp. 381–398.

Walker, Richard and James Jackson (2004). "Active tectonics and late Cenozoic strain distribution in central and eastern Iran". In: *Tectonics* 23.5.

Walker, RT, EA Bergman, JR Elliott, EJ Fielding, A-R Ghods, M Ghoraishi, J Jackson, H Nazari, M Nemati, B Oveisi, et al. (2013). "The 2010–2011 South Rigan (Baluchestan) earthquake sequence and its implications for distributed deformation and earthquake hazard in southeast Iran". In: *Geophysical Journal International* 193.1, pp. 349–374.

Walker, RT, M Talebian, RA Sloan, A Rasheedi, M Fattahi, and C Bryant (2010). "Holocene slip-rate on the Gowk strike-slip fault and implications for the distribution of tectonic strain in eastern Iran". In: *Geophysical Journal International* 181.1, pp. 221–228.

Walpersdorf, A, I Manighetti, Z Mousavi, F Tavakoli, M Vergnolle, A Jadidi, D Hatzfeld, A Aghamohammadi, A Bigot, Y Djamour, et al. (2014). "Present-day kinematics and fault slip rates in eastern Iran, derived from 11 years of GPS data". In: *Journal of Geophysical Research: Solid Earth* 119.2, pp. 1359–1383.

Walters, Richard John (2012). "Geodetic observation and modelling of continental deformation in Iran and Turkey". PhD thesis. University of Oxford.

Weiss, Jonathan R, Richard J Walters, Yu Morishita, Tim J Wright, Milan Lazecky, Hua Wang, Ekbal Hussain, Andrew J Hooper, John R Elliott, Chris Rollins, et al. (2020). "High-resolution surface velocities and strain for Anatolia from Sentinel-1 InSAR and GNSS data". In: *Geophysical Research Letters* 47.17, e2020GL087376.

Wright, Tim J (2002). "Remote monitoring of the earthquake cycle using satellite radar interferometry". In: *Philosophical Transactions of the Royal Society of London. Series A: Mathematical, Physical and Engineering Sciences* 360.1801, pp. 2873–2888.

— (2016). "The earthquake deformation cycle". In: *Astronomy and Geophysics* 54.7, pp. 4–20.

Wright, Tim J, John R Elliott, Hua Wang, and Isabelle Ryder (2013). "Earthquake cycle deformation and the Moho: Implications for the rheology of continental lithosphere". In: *Tectonophysics* 609, pp. 504–523.

Wright, Tim J, Barry E Parsons, and Zhong Lu (2004). "Toward mapping surface deformation in three dimensions using InSAR". In: *Geophysical Research Letters* 31.1.

Xu, X. and D. T. Sandwell (2020). "Toward Absolute Phase Change Recovery With InSAR: Correcting for Earth Tides and Phase Unwrapping Ambiguities". In: *IEEE Transactions on Geoscience and Remote Sensing* 58.1, pp. 726–733. DOI: 10.1109/TGRS.2019.2940207.

Yague-Martinez, Nestor, Pau Prats-Iraola, Muriel Pinheiro, and Marc Jaeger (2019). "Exploitation of burst overlapping areas of tops data. Application to sentinel-1". In: *IGARSS 2019-2019 IEEE International Geoscience and Remote Sensing Symposium*. IEEE, pp. 2066–2069.

Yu, Chen, Zhenhong Li, Nigel T Penna, and Paola Crippa (2018). "Generic atmospheric correction model for Interferometric Synthetic Aperture Radar observations". In: *Journal of Geophysical Research: Solid Earth* 123.10, pp. 9202–9222.